SZKOŁA DOKTORSKA
BioMedChem
Uniwersytetu Łódzkiego
i Instytutów Polskiej
Akademii Nauk w Łodzi

INSTYTUT ERCE BiolMed

Serafin Alexander Zawadzki

Praca doktorska:

Charakterystyka i ocena potencjału dendrymerów karbokrzemowych jako nośników siRNA przez modelową barierę krew–mózg

Doctoral thesis:

Characterization and evaluation of the potential of carbosilane dendrimers as siRNA carriers across a model of the blood–brain barrier

• Promotor/Supervisor
dr hab. Katarzyna Miłowska, prof. UŁ
Wydział Biologii i Ochrony Środowiska
Uniwersytet Łódzki

PODPIS ZAUFANY
SERAFIN
ZAWADZKI
07.05.2026 03:04:31 GMT+0200
Dokument podpisany elektronicznie
podpisem zaufanym

Łódź, 2026

Składam serdeczne podziękowania Promotorce mojej rozprawy
dr hab. Katarzynie Miłowskiej, prof. UŁ
za stworzenie znakomitych warunków do rozwoju naukowego, nieocenione wsparcie, życzliwość, zaangażowanie, liczne dyskusje, które były dla mnie źródłem wiedzy i motywacji.

Ogromne podziękowania kieruję do
Koleżanek i Kolegów z Katedry Biofizyki Ogólnej
za motywację do działania, inspirujące dyskusje oraz humor, które dodawały mi codziennie energii.

Szczególnie chciałabym podziękować mojej
Rodzinie**, a w szczególności **Mamie** i **Babci
za umożliwienie mi rozwijania pasji i nieustanne wsparcie, które było dla mnie źródłem siły i motywacji do dalszej pracy.

Spis treści

Wykaz stosowanych skrótów		**4**
I.	**Źródła finansowania**	**9**
II.	**Współprace z krajowymi i zagranicznymi instytucjami naukowymi**	**10**
III.	**Spis prac wchodzących w skład rozprawy doktorskiej**	**11**
IV.	**Wprowadzenie**	**13**
V.	**Założenia i cel pracy**	**18**
VI.	**Materiały**	**20**
VII.	**Metody**	**24**
VIII.	**Omówienie prac wchodzących w skład rozprawy doktorskiej**	**28**
IX.	**Perspektywy przyszłych badań**	**37**
X.	**Podsumowanie i wnioski**	**39**
XI.	**Streszczenie**	**40**
XII.	**Abstract**	**41**
XIII.	**Literatura**	**42**
XIV.	**Aktywność naukowa i organizacyjna**	**45**
XV.	**Prace wchodzące w skład rozprawy doktorskiej**	**52**
XVI.	**Oświadczenia współautorów prac wchodzących w skład rozprawy doktorskiej**	**203**

Wykaz stosowanych skrótów

^{1}H-NMR	–	protonowy magnetyczny rezonans jądrowy (ang. proton **n**uclear **m**agnetic **r**esonance)
AB	–	bariera pajęczynówki (ang. **a**rachnoid **b**arrier)
AC	–	astrocyty (ang. **a**strocyte **c**ells)
AD	–	choroba Alzheimera (ang. **A**lzheimer's **d**isease)
AFM	–	mikroskopia sił atomowych (ang. **a**tomic **f**orce **m**icroscopy)
AGS	–	suplement wzrostu dla astrocytów (ang. **a**strocyte **g**rowth **s**upplement)
ALS	–	stwardnienie zanikowe boczne (ang. **a**myotrophic **l**ateral **s**clerosis)
APP	–	białko prekursorowe amyloidu (ang. **a**myloid **p**recursor **p**rotein)
APOE4	–	apolipoproteina E4 (ang. **apo**lipoprotein **E4**)
aPTT	–	czas częściowej tromboplastyny po aktywacji (ang. **a**ctivated **p**artial **t**hromboplastin **t**ime)
Aβ	–	amyloid β (ang. **a**myloid **β**)
BA	–	bazofile (ang. **ba**sophils)
BACE1	–	enzym tnący APP w miejscu β 1 (ang. **b**eta-site **a**pp **c**leaving **e**nzyme **1**)
BBB	–	bariera krew–mózg (ang. **b**lood-**b**rain **b**arrier)
BCSFB	–	bariera krew–płyn mózgowo-rdzeniowy (ang. **b**lood-**c**erebro**s**pinal **f**luid **b**arrier)
BSCB	–	bariera krew–rdzeń kręgowy (ang. **b**lood-**s**pinal **c**ord **b**arrier)
CBF	–	mózgowy przepływ krwi (ang. **c**erebral **b**lood **f**low)
CD	–	dichroizm kołowy (ang. **c**ircular **d**ichroism)
CI	–	indeks komórkowy (ang. **c**ell **i**ndex)
CMT	–	transport za pośrednictwem nośników (ang. **c**arrier–**m**ediated **t**ransport)
CNS	–	ośrodkowy układ nerwowy (ang. **c**entral **n**ervous **s**ystem)
CVO	–	narządy okołokomorowe (ang. **c**ircum**v**entricular **o**rgans)
Cy-5	–	cyjanina-5 (ang. **cy**anine-**5**)

DAMPs	–	struktury molekularne związane z uszkodzeniem (ang. **d**amage-**a**ssociated **m**olecular **p**atterns)
ddPCR	–	kropelkowo-cyfrowa reakcja łańcuchowa polimerazy (ang. **d**roplet **d**igital **p**olymerase **c**hain **r**eaction)
DIC	–	rozsiane wykrzepianie wewnątrznaczyniowe (ang. **d**isseminated **i**ntravascular **c**oagulation)
DLS	–	dynamiczne rozpraszanie światła (ang. **d**ynamic **l**ight **s**cattering)
DMT	–	terapie modyfikujące przebieg choroby (ang. **d**isease-**m**odifying **t**herapies)
DPH	–	1,6-difenylo-1,3,5-heksatrien (ang. 1,6-**d**i**p**henyl- 1,3,5-**h**exatriene)
EC	–	komórki śródbłonka (ang. **e**ndothelial **c**ells)
ECGS	–	suplement wzrostu komórek śródbłonka (ang. **e**ndothelial **c**ell **g**rowth **s**upplement)
EMA	–	Europejska Agencja Leków (ang. **E**uropean **M**edicines **A**gency)
EO	–	eozynofile (ang. **eo**sinophils)
FBS	–	płodowa surowica bydlęca (ang. **f**etal **b**ovine **s**erum)
FDA	–	Agencja Żywności i Leków (ang. **F**ood and **D**rug **A**dministration)
FHA	–	szybki test halo (ang. **f**ast **h**alo **a**ssay)
FITC	–	izotiocyjanian fluoresceiny (ang. **f**luorescein **i**so**th**io**c**yanate)
FP	–	polaryzacja fluorescencji (ang. **f**luorescence **p**olarization)
GalNAc	–	triantenarna n-acetylogalaktozamina (ang. triantennary **n**-**ac**etyl**gal**actosamine)
GBM	–	błona podstawna kłębuszka nerkowego (ang. **g**lomerular **b**asement **m**embrane)
H_2DCF-DA	–	dioctan dichlorodihydrofluoresceiny (ang. **dic**hloro**dih**ydro**f**luorescein **d**i**a**cetate)
HCT	–	hematokryt (ang. **h**emato**cri**t)
HD	–	choroba Huntingtona (ang. **H**untington's **d**isease)
HGB	–	hemoglobina (ang. **h**emo**g**lo**b**in)
HSA	–	albumina surowicy ludzkiej (ang. **h**uman **s**erum **a**lbumin)

IATA	–	zintegrowane podejścia do badań i oceny (ang. **i**ntegrated **a**pproaches to **t**esting and **a**ssessment)
IFNα2	–	interferon α 2 (ang. **i**nter**f**ero**n α 2**)
IL-10	–	interleukina 10 (ang. **i**nter**l**eukin **10**)
IL-12p40	–	podjednostka p40 interleukiny 12 (ang. **i**nter**l**eukin **12** beta chain **p40**)
IL-6	–	interleukina 6 (ang. **i**nter**l**eukin **6**)
IL-8	–	interleukina 8 (ang. **i**nter**l**eukin **8**)
ISF	–	płyn śródmiąższowy (ang. **i**nter**s**titial **f**luid)
ITC	–	izotermiczna kalorymetria miareczkowa (ang. **i**sothermal **t**itration **c**alorimetry)
ITS	–	zintegrowane strategie badań (ang. **i**ntegrated **t**esting **s**trategies)
IVIS	–	system obrazowania in vivo (ang. ***in v****ivo* **i**maging **s**ystem)
KI	–	wbudowanie genu (ang. **k**nock-**i**n)
LC-MS	–	chromatografia cieczowa sprzężona ze spektrometrią mas (ang. **l**iquid **c**hromatography–**m**ass **s**pectrometry)
LY	–	limfocyty (ang. **ly**mphocytes)
MAF	–	wskaźnik niedokrwistości mikrocytarnej (ang. **m**icrocytic **a**nemia **f**actor)
MCHC	–	średnie stężenie hemoglobiny w krwince czerwonej (ang. **m**ean **c**orpuscular **h**emoglobin **c**oncentration)
MCV	–	średnia objętość krwinki czerwonej (ang. **m**ean **c**orpuscular **v**olume)
MFI	–	średnia intensywność fluorescencji (ang. **m**ean **f**luorescence **i**ntensity)
MO	–	monocyty (ang. **mo**nocytes)
MPS	–	układ fagocytów jednojądrzastych (ang. **m**ononuclear **p**hagocyte **s**ystem)
MPV	–	średnia objętość płytek krwi (ang. **m**ean **p**latelet **v**olume)
MWM	–	labirynt wodny Morrisa (ang. **M**orris **w**ater **m**aze)
NCI	–	znormalizowany indeks komórkowy (ang. **n**ormalised **c**ell **i**ndex)
NDF	–	współczynnik dyfuzji jądrowej (ang. **n**uclear **d**iffusion **f**actor)
NE	–	neutrofile (ang. **ne**utrophils)
NFTs	–	sploty neurofibrylarne (ang. **n**euro**f**ibrillary **t**angles)

NIR – bliska podczerwień (ang. **n**ear-**i**nf**r**ared)

NMDA – N-metylo-D-asparaginian (ang. **N**-**m**ethyl-**D**-**a**spartate)

NOR – test rozpoznawania nowego obiektu (ang. **n**ovel **o**bject **r**ecognition test)

NRC – znormalizowany parametr konfluencji fluorescencji czerwonej (ang. **n**ormalised **r**ed **c**onfluence)

NVU – jednostka neuro-naczyniowa (ang. **n**euro**v**ascular **u**nit)

OFT – test otwartego pola (ang. **o**pen **f**ield **t**est)

P/S – penicylina–streptomycyna (ang. **p**enicillin–**s**treptomycin)

PAMPs – wzorce molekularne związane z patogenami (ang. **p**athogen-**a**ssociated **m**olecular **p**atterns)

PBMC – komórki jednojądrzaste krwi obwodowej (ang. **p**eripheral **b**lood **m**ononuclear **c**ells)

PBS – buforowany roztwór soli fosforanowej (ang. **p**hosphate **b**uffered **s**aline)

PC – perycyty (ang. **p**ericyte **c**ells)

PCT – prokalcytonina (ang. **p**ro**c**alci**t**onin)

PD – choroba Parkinsona (ang. **P**arkinson's **d**isease)

PDW – wskaźnik zróżnicowania objętości płytek (ang. **p**latelet **d**istribution **w**idth)

PEG – glikol polietylenowy (ang. **p**oly**e**thylene **g**lycol)

PGS – suplement wzrostu perycytów (ang. **p**ericyte **g**rowth **s**upplement)

PLL – poli-L-lizyna (ang. **p**oly-**L**-**l**ysine)

PLTC – liczba płytek krwi (ang. **pla**t**e**lets **c**ount)

PLTs – płytki krwi (ang. **pla**t**e**lets)

PRRs – receptory rozpoznające wzorce (ang. **p**attern **r**ecognition **r**eceptors)

PT – czas protrombinowy (ang. **p**rothrombin **t**ime)

QFA – ilościowe oznaczenie fibrynogenu (ang. **q**uantitative **f**ibrinogen **a**ssay)

RBCC – liczba erytrocytów (ang. **r**ed **b**lood **c**ells **c**ount)

RBCs – krwinki czerwone (ang. **r**ed **b**lood **c**ells)

RDW – wskaźnik zróżnicowania objętości erytrocytów (ang. **r**ed cell **d**istribution **w**idth)

RES	–	układ siateczkowo-śródbłonkowy (ang. **re**ticuloendothelial **s**ystem)
RMT	–	transcytoza zależna od receptora (ang. **r**eceptor-**m**ediated **t**ranscytosis)
RNAi	–	interferencja RNA (ang. **RNA i**nterference)
ROS	–	reaktywne formy tlenu (ang. **r**eactive **o**xygen **s**pecies)
RTCA	–	analiza komórek w czasie rzeczywistym (ang. **r**eal-**t**ime **c**ell **a**nalysis)
siRNA	–	małe interferujące RNA (ang. **s**mall **i**nterfering **RNA**)
SMA	–	rdzeniowy zanik mięśni (ang. **s**pinal **m**uscular **a**trophy)
TEER	–	przezśródbłonkowy opór elektryczny (ang. **t**rans**e**ndothelial **e**lectrical **r**esistance)
TEM	–	transmisyjna mikroskopia elektronowa (ang. **t**ransmission **e**lectron **m**icroscopy)
Tf	–	transferyna (ang. **t**rans**f**errin)
TJ	–	połączenia ścisłe (ang. **t**ight **j**unctions)
TMA-DPH	–	1-(4-trimetyloaminofenylo)-6-fenylo-1,3,5-heksatrienu (ang. 1-(4-trimethylammoniumphenyl)-6-phenyl-1,3,5-hexatriene)
TNFα	–	czynnik martwicy nowotworów α (ang. **t**umor **n**ecrosis **f**actor **α**)
TT	–	czas trombinowy (ang. **t**hrombin **t**ime)
WBCC	–	całkowita liczba leukocytów (ang. total **w**hite **b**lood **c**ells **c**ount)
WBCs	–	krwinki białe (ang. **w**hite **b**lood **c**ells)
ZO-1	–	zonula occludens-1 (ang. **z**onula **o**ccludens-**1**)
ΔΨm	–	potencjał błony mitochondrialnej (ang. mitochondrial membrane potential)

I. Źródła finansowania

Badania zostały wykonane w ramach projektów:



Międzynarodowy projekt badawczy M-ERA.NET 2019-2023 „Nanoparticle transfer through endothelial barrier" UMO-2018/30/Z/NZ1/00911 finansowany przez Narodowe Centrum Nauki oraz Komisję Europejską w ramach programu Horizon 2020.



Międzynarodowy projekt badawczy realizowany w ramach programu Narodowej Agencji Wymiany Akademickiej (NAWA) wspólne projekty badawcze pomiędzy Rzeczpospolitą Polską a Republiką Słowacką pt. „Dendrymery fosforowe jako potencjalne czynniki wspomagające proces gojenia ran”, nr BPN/BSK/2021/1/00053/U/00001.

II. Współprace z krajowymi i zagranicznymi instytucjami naukowymi

Katedra Chemii Organicznej i Chemii Nieorganicznej, Uniwersytet w Alcalá de Henares, Alcalá de Henares, Hiszpania

Katedra Fizyki Jądrowej i Biofizyki, Uniwersytet Komeńskiego, Bratysława, Słowacja

Katedra Neuromedycyny i Neuronauki, Wydział Medycyny i Nauk o Życiu, Uniwersytet Łotwy, Ryga, Łotwa

Łotewskie Centrum Badań i Studiów Biomedycznych, Ryga, Łotwa

Katedra Chemii Fizycznej, Zakład Chemii Biofizycznej, Wydział Chemii, Uniwersytet Łódzki, Łódź, Polska

Zespół Struktury Powierzchni Materii Miękkiej, Centrum Badań Molekularnych i Makromolekularnych, Polska Akademia Nauk, Łódź, Polska

Uniwersyteckie Laboratorium Naukowe CoreLab, Uniwersytet Medyczny w Łodzi, Łódź, Polska

Zakład Cytobiologii i Proteomiki, Wydział Nauk o Zdrowiu, Uniwersytet Medyczny w Łodzi

III. Spis prac wchodzących w skład rozprawy doktorskiej

Prace doświadczalne:

(I) Zawadzki S., Martín-Serrano Á., Okła E., Kędzierska M., Garcia-Gallego S., López P.O., de la Mata F.J., Michlewska S., Makowski T., Ionov M., Pędziwiatr-Werbicka E., Bryszewska M., Miłowska K., **Synthesis and biophysical evaluation of carbosilane dendrimers as therapeutic siRNA carriers.** Sci. Rep. 2024, 14, 1615. https://doi.org/10.1038/s41598-024-51238-w

Punkty MNiSW$_{2024}$: 140

IF$_{2024}$: 3,9 (2-letni); 4,3 (5-letni)

(II) Zawadzki S., Okła E., Michlewska S., Makowski T., Buczkowski A., O. López P., de la Mata F.J., Ionov M., Bryszewska M., Miłowska K., **Structural and conformational rearrangements of human serum albumin, transferrin, and blood plasma induced by carbosilane dendrimer therapeutic delivery system.** Sci. Rep. 2025, 15, 39650. https://doi.org/10.1038/s41598-025-23355-7

Punkty MNiSW$_{2024}$: 140

IF$_{2024}$: 3,9 (2-letni); 4,3 (5-letni)

(III) Zawadzki S., Suty S., Okła E., Ortega López P., de la Mata F.J., Waczulikova I., Ionov M., Bryszewska M., Miłowska K., **Hemocompatibility of Carbosilane Dendrimers as a Therapeutic siRNA Delivery System across Blood−Brain Barrier.** ACS Appl. Mater. Interfaces 2026, 18, 11671−11686 https://doi.org/10.1021/acsami.5c12952

Punkty MNiSW$_{2024}$: 200

IF$_{2024}$: 8,2 (2-letni); 8,5 (5-letni)

Manuskrypty prac doświadczalnych przesłane do czasopisma:

(IV) Zawadzki S., Okła E., Ortega López P., de la Mata F.J., Ionov M., Jansons J., Skrastiņa D., Kreišmane M., Bryszewska M., Miłowska K. **Multilevel Assessment of Carbosilane Dendrimer–siRNA Nanoplatform: Cellular Compatibility, Blood–Brain Barrier Model Integrity, and Murine Model Biodistribution.** 2026, wysłany do czasopisma ACS Appl. Mater. Interfaces.

(V) Zawadzki S., Okła E., Michlewska S., Bednarek R., Jansons J., Skrastiņa D., Kreišmane M., Piļipenko V., Jansone B., Ortega López P., de la Mata F.J., Ionov M., Bryszewska M., Miłowska K. **Tiered Evaluation of Carbosilane–siRNA Nanoplatform from Single-Cell Biocompatibility to Blood-Brain Barrier Model Dynamics, and Murine Alzheimer Model Behavior Assessment.** 2026, wysłany do czasopisma ACS Appl. Mater. Interfaces.

Łączny IF opublikowanych prac wchodzących w skład rozprawy doktorskiej: 17,1

(480 pkt MNiSW).

IV. Wprowadzenie

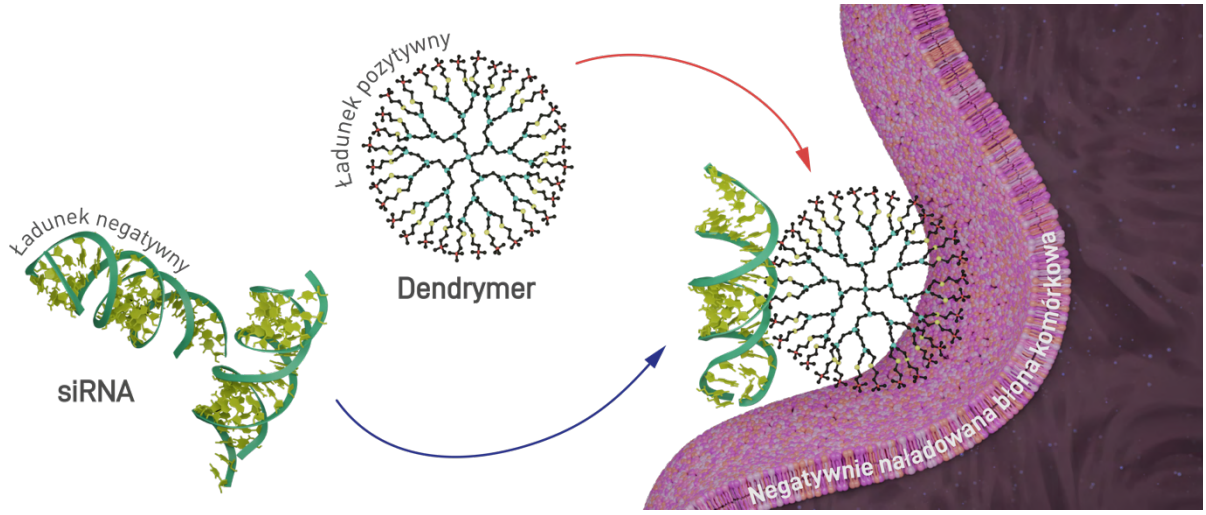
Współczesna neurofarmakoterapia wyraźnie zmienia kierunek przechodząc od leczenia jedynie objawów w stronę terapii wpływających na przebieg choroby (disease-modifying therapies, DMT). Podejście to, ukierunkowane na molekularnych mechanizmach powstawania i rozwoju choroby neurodegeneracujnej, znajduje już odzwierciedlenie w praktyce klinicznej. W schorzeniach rdzenia kręgowego oraz osi rdzeniowo-opuszkowej jak np. 5q-rdzeniowy zanik mięśni (SMA) i SOD1-zależne stwardnienie zanikowe boczne (ALS), wdrożono terapie oparte na oligonukleotydach antysensownych, małocząsteczkowych modulatorach splicingu oraz inżynierii genowej.[1,2] Większe wyzwania wiążą się natomiast z projektowaniem strategii DMT dla chorób, w których proces patologiczny obejmuje struktury mózgowe. W tej grupie jedyną szerzej wdrożoną klinicznie formą terapii DMT pozostają przeciwciała monoklonalne stosowane w chorobie Alzheimera (AD), podczas gdy w chorobie Parkinsona (PD) i Huntingtona (HD) analogiczne rozwiązania nadal pozostają na etapie badań klinicznych.[3–5] W przypadku AD ograniczenia strategii DMT wynikają w dużej mierze z faktu, że obecnie stosowane przeciwciała monoklonalne są podawane ogólnoustrojowo, a ich przenikanie przez barierę krew–mózg (BBB) pozostaje istotnie ograniczone i przestrzennie niejednorodne. W konsekwencji uzyskanie efektu biologicznego wymaga długotrwałego podawania wysokich dawek terapeutycznych. Pomimo udokumentowanej redukcji obciążenia amyloidem i mierzalnego spowolnienia progresji klinicznej u pacjentów we wczesnym stadium choroby, rzeczywista korzyść terapeutyczna pozostaje umiarkowana.[6,7] Ograniczona penetracja do mózgu rzutuje przy tym nie tylko na skuteczność, lecz także na bezpieczeństwo terapii. Interakcja przeciwciał z amyloidem zlokalizowanym w ścianie naczyń wiąże się z ryzykiem wystąpienia zaburzeń, obejmujących obrzęk oraz zmiany krwotoczne, w tym mikrowylewy.[3]

W tym kontekście coraz większe znaczenie zyskują strategie etiotropowe, które nie skupiają się na usuwaniu późnych skutków choroby, lecz na regulowaniu wcześniejszych mechanizmów prowadzących do jej rozwoju. W odróżnieniu od przeciwciał monoklonalnych, które oddziałują głównie na pozakomórkowe patologiczne formy amyloidu β, terapie oparte na oligonukleotydach umożliwiają selektywną regulację ekspresji czynników uczestniczących w patogenezie neurodegeneracji. Mechanizm ten opiera się na zjawisku interferencji RNA (RNAi), w którym dwuniciowy siRNA po wniknięciu do komórki zostaje włączony do kompleksu RISC, a następnie kieruje sekwencyjnie swoistą degradacją komplementarnego mRNA. W efekcie dochodzi do posttranskrypcyjnego wyciszenia ekspresji

genu docelowego i wtórnego obniżenia poziomu kodowanego przez niego białka. Z perspektywy terapeutycznej RNAi pozwala precyzyjnie wpływać na molekularne czynniki choroby, zwłaszcza wtedy, gdy celem jest wybiórcze oddziaływanie na warianty genetyczne bezpośrednio związane z jej rozwojem.[8]

Jednym z obiecujących kierunków zastosowania tej strategii w chorobie Alzheimera jest ukierunkowanie terapii na konkretne, dobrze scharakteryzowane czynniki genetyczne ryzyka. Szczególne miejsce zajmuje tu izoforma APOE4 jako najsilniejszy powszechny czynnik ryzyka późno rozpoczynającej się postaci AD, powiązany zarówno z zaburzeniem integralności BBB, jak i z upośledzeniem homeostazy amyloidu β.[9–12] W tym świetle siRNA stanowi obiecujące narzędzie terapeutyczne, ponieważ umożliwia selektywne wyciszanie ekspresji genów bezpośrednio zaangażowanych w procesy patogenetyczne. Uzasadnienie wyboru APOE4 jako celu terapeutycznego oraz omówienie zastosowania tej strategii w terapii AD zostały przedstawione w pracy **(V)**.

Praktyczne zastosowanie terapeutycznych kwasów nukleinowych wymaga jednak przezwyciężenia szeregu barier fizjologicznych. Wykorzystanie nieskompleksowanych oligonukleotydów pozostaje w dużej mierze nieskuteczne z powodu ich niskiej stabilności, podatności na degradację enzymatyczną, szybkiego klirensu oraz braku zdolności do przenikania przez błony biologiczne.[8,13] Z tego powodu opracowanie zaawansowanych nośników staje się warunkiem koniecznym dla zastosowania tego rodzaju terapii. Skuteczny nośnik przeznaczony do dostarczania siRNA musi chronić transportowaną substancję leczniczą przed degradacją, destabilizacją i przedwczesną eliminacją. Powinien również zachowywać stabilność koloidalną w środowisku biologicznym oraz ograniczać nieswoiste interakcje z komponentami krwi i tkanek. Dodatkowo powinien minimalizować immunogenność i cytotoksyczność, wspierać transport przez bariery biologiczne oraz zwiększać efektywność internalizacji komórkowej (Ryc. 1). Kluczowa jest także jego zdolność do umożliwienia uwolnienia siRNA z endosomów i dostarczenia go do przedziału subkomórkowego właściwego dla mechanizmu interferencji RNA.

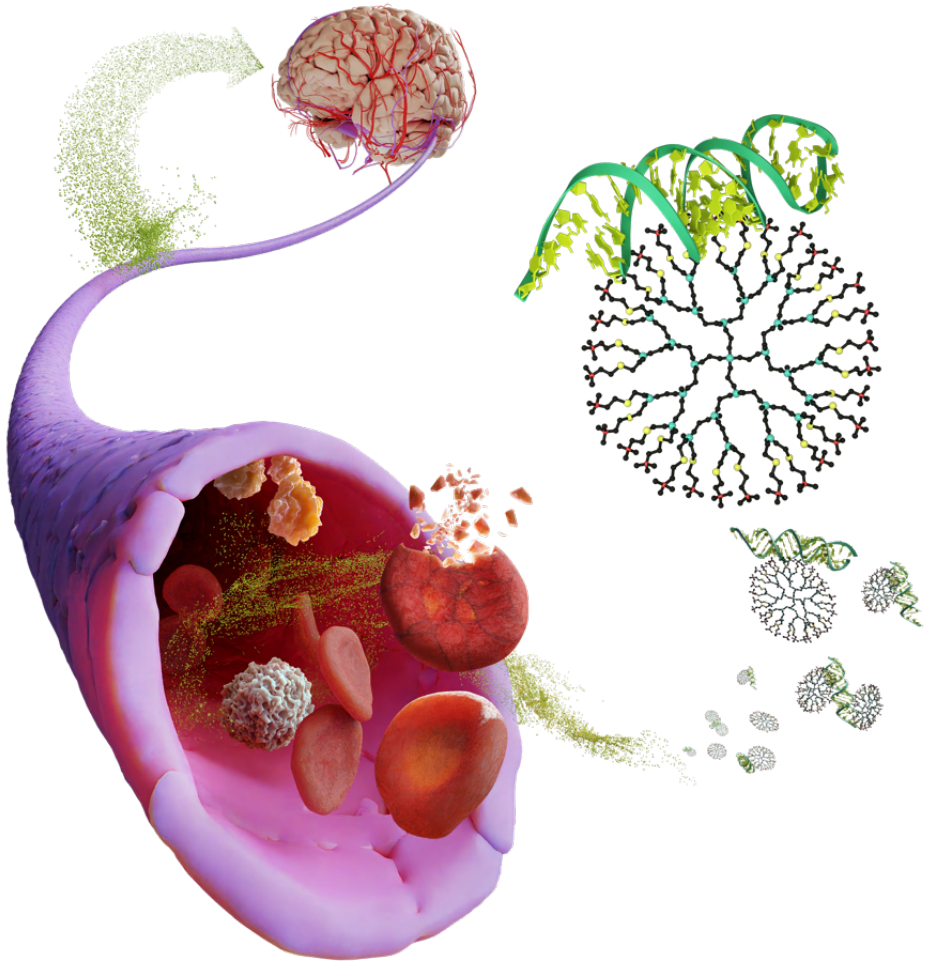


Rycina 1. Schemat formowania dendrypleksów poprzez kompleksację kationowych dendrymerów z ujemnie naładowanymi cząsteczkami siRNA oraz ich adsorpcji na ujemnie naładowanej powierzchni błony komórkowej.

Wśród licznych rodzajów nanonośników dendrymery zajmują szczególnie istotne miejsce ze względu na dobrze zdefiniowaną strukturę cząsteczki i wysoki stopień monodyspersyjności. Ich precyzyjnie zaprojektowana, wielogałęziowa budowa umożliwia kontrolowane modyfikowanie parametrów fizykochemicznych, które bezpośrednio wpływają na profil farmakokinetyczny układu oraz na rodzaj oddziaływań z restrykcyjnymi barierami biologicznymi. Dzięki zdolności do efektywnego kompleksowania kwasów nukleinowych oraz możliwości precyzyjnego kształtowania właściwości powierzchniowych i biologicznego profilu układu, dendrymery stanowią szczególnie obiecujące platformy nośnikowe dla tych cząsteczek.[14,15] Wykorzystując te właściwości, opracowano preparaty dendrymerowe, które wykazały zdolność do pokonywania głównych barier fizjologicznych, w tym skóry, błony śluzowej dróg oddechowych, nabłonka jamy ustnej i jelit, powierzchni oka, bariery łożyskowej oraz bariery krew-mózg.[16–21]

Organizacja przestrzenna i właściwości fizykochemiczne nanocząstki określają jej kluczowe parametry, takie jak stabilność i efektywność jego kompleksowania z siRNA. Parametry te wpływają także na charakter oddziaływania układu z otoczeniem fizjologicznym. Po wprowadzeniu do krążenia ogólnoustrojowego powierzchnia nanocząstki zostaje „opłaszczona” przez składniki osocza, co prowadzi do utworzenia korony biomolekularnej i w konsekwencji nadania jej nowych właściwości biologicznych. Ta wtórnie ukształtowana warstwa powierzchniowa w dużym stopniu wpływa na właściwości farmakokinetyczne nanocząstki. Określa m.in. czas jej krążenia we krwi, sposób rozpoznawania przez układ

odpornościowy, efektywność internalizacji komórkowej, biodystybucję oraz zdolność do selektywnego pokonywania barier biologicznych. Proces formowania korony biomolekularnej bezpośrednio wpływa na hemokompatybilność nanosystemu, stanowiąc jeden z kluczowych warunków bezpieczeństwa i skuteczności nośników podawanych parenteralnie (Ryc. 2).[22–24] Interakcje nanocząstek z erytrocytami mogą prowadzić do hemolizy, deformacji błony, zmian lepkości i zaburzeń mikrokrążenia. Z kolei oddziaływania z płytkami krwi mogą modulować trombogenność i nasilać odpowiedź immunologiczną, natomiast kontakt z leukocytami może sprzyjać aktywacji układu odpornościowego, fagocytozie, sekrecji cytokin i akumulacji w narządach układu fagocytarnego.



Rycina 2. Ilustracja obrazuje dendrypleksy po iniekcji dożylnej i ich interakcje z elementami morfotycznymi krwi. Procesy te mogą indukować skutki uboczne, w tym hemolizę, powstawania zakrzepów oraz aktywację układu odpornościowego.

Biodystrybucja nanosystemu wynika z jego właściwości fizykochemicznych, zmian zachodzących na jego powierzchni po kontakcie z osoczem oraz z procesów odpowiedzialnych za jego usuwanie z organizmu. Te czynniki wspólnie określają, jaka część podanej dawki jest w stanie dotrzeć do mikrokrążenia mózgowego. Skuteczność przenikania nośnika do ośrodkowego układu nerwowego (CNS) zależy od jego oddziaływania z barierą krew-mózg, która stanowi wysoce selektywną i dynamiczna granicę pomiędzy krążeniem ogólnoustrojowym a miąższem nerwowym. Jej właściwości wynikają nie tylko z obecności połączeń ścisłych ograniczających transport parakomórkowy i niskiej intensywności nieswoistej transcytozy, lecz także z ściśle regulowanych mechanizmów transportu transkomórkowego. Obejmują one bierną dyfuzję wybranych cząsteczek lipofilnych, transport nośnikowy, transcytozę receptorową oraz aktywny effluks ksenobiotyków.[25–27] BBB nie jest przy tym strukturą jednorodną, lecz segmentowo zróżnicowaną, której skład komórkowy, ekspresja transporterów i przepuszczalność zmieniają się wzdłuż osi tętniczkowo-kapilarno-żylnej. Wpływa to nie tylko na możliwość przedostania się terapeutyku do CNS, lecz również na sposób jego dystrybucji w obrębie tkanki mózgowej.[28–30] Z perspektywy projektowania terapii oznacza to, że skuteczne dostarczanie substancji leczniczej do mózgu zależy zarówno od zdolności przekroczenia samej bariery, jak i od uwzględnienia architektonicznej i funkcjonalnej złożoności mikrokrążenia mózgowego. W konsekwencji BBB należy traktować nie jako bierną przeszkodę, lecz jako kluczowy element, który współkształtuje farmakokinetykę leku, jego dostępność w tkance mózgowej oraz realne możliwości wdrożenia terapii ukierunkowanych na ośrodkowy układ nerwowy.

V. Założenia i cel pracy

Skuteczne leczenie chorób neurodegeneracyjnych, takich jak choroba Alzheimera, wciąż stanowi poważne wyzwanie. Mimo postępu w opracowywaniu terapii modyfikujących przebieg choroby ich skuteczność pozostaje ograniczona, a uzyskanie terapeutycznego stężenia leków w ośrodkowym układzie nerwowym po podaniu ogólnoustrojowym jest w znacznym stopniu zależne od ich interakcji z barierą krew–mózg. siRNA ukierunkowany na APOE4 stanowi racjonalne narzędzie modulacji ekspresji genu związanego zarówno z ryzykiem choroby, jak i z dysfunkcją neuro-naczyniową. Jego zastosowanie ograniczają jednak niska trwałość wolnego oligonukleotydu w środowisku biologicznym, szybki klirens oraz trudności w osiągnięciu skutecznej ekspozycji w ośrodkowym układzie nerwowym.

Zastosowanie terapeutycznego siRNA wymaga nośnika zdolnego do tworzenia stabilnych kompleksów z oligonukleotydem, który ogranicza nieswoiste interakcje z komponentami krwi i tkanek, minimalizuje immunogenność oraz cytotoksyczność. Ponadto wspiera transport przez bariery biologiczne, zwiększa efektywność wychwytu komórkowego i dostarcza ładunek terapeutyczny do przedziału subkomórkowego właściwego dla mechanizmu interferencji RNA.

Cel główny

Głównym celem pracy była ocena właściwości fizykochemicznych, biofizycznych, biokompatybilności oraz funkcjonalności nanosystemu dendrymer–siRNA w modelach o narastającej złożoności biologicznej ukierunkowanej na zastosowanie w terapii chorób neurodegeneracyjnych ośrodkowego układu nerwowego.

Cele szczegółowe

1. Charakterystyka fizykochemiczna panelu kationowych dendrymerów karbokrzemowych i ich kompleksów z siRNA oraz wyłonienie nośnika o najkorzystniejszym profilu do dalszych badań.
2. Analiza oddziaływań wybranego nośnika z reprezentatywnymi białkami osocza i złożonym środowiskiem osocza oraz określenie hemokompatybilności, obejmujące parametry hemoreologiczne, immunologiczne i krzepnięcia.

3. Ocena wpływu dendrymeru i jego dendrypleksu na komórki jednostki neuronaczyniowej oraz analiza integralności i przepuszczalności modelu bariery krew–mózg.

4. Określenie profilu biodystrybucji oraz weryfikacja skuteczności terapeutycznej dendrypleksu siRNA w zakresie przywracania wybranych parametrów sprawności neurobehawioralnej w modelu mysim.

Hipoteza badawcza:

Stabilny kompleks PEGylowanego dendrymeru karbokrzemowego z terapeutycznym siRNA umożliwia dostarczanie oligonukleotydu do komórek przy zachowaniu hemokompatybilności i biokompatybilności w modelu bariery krew-mózg *in vitro* oraz pozwalają na wydłużenie ekspozycji układowej i osiągnięcie poprawy wybranych parametrów behawioralnych *in vivo*.

VI. Materiały

Dendrymery karbokrzemowe

W badaniach wykorzystano dwa typy PEGylowanych dendrymerów karbokrzemowych zsyntetyzowanych w Katedrze Chemii Organicznej i Nieorganicznej Uniwersytetu w Alcalá w Madrycie (Hiszpania), różniących się rodzajem rdzenia, generacją oraz zakresem modyfikacji powierzchniowych. Struktury badanych dendrymerów przedstawiono na Rycinie 3.

1. Dendrymer o rdzeniu krzemowym zawierający na powierzchni trzeciorzędowe grupy aminowe oraz pojedynczy łańcuch glikolu polietylenowego (PEG) o masie cząsteczkowej 6000 Da.

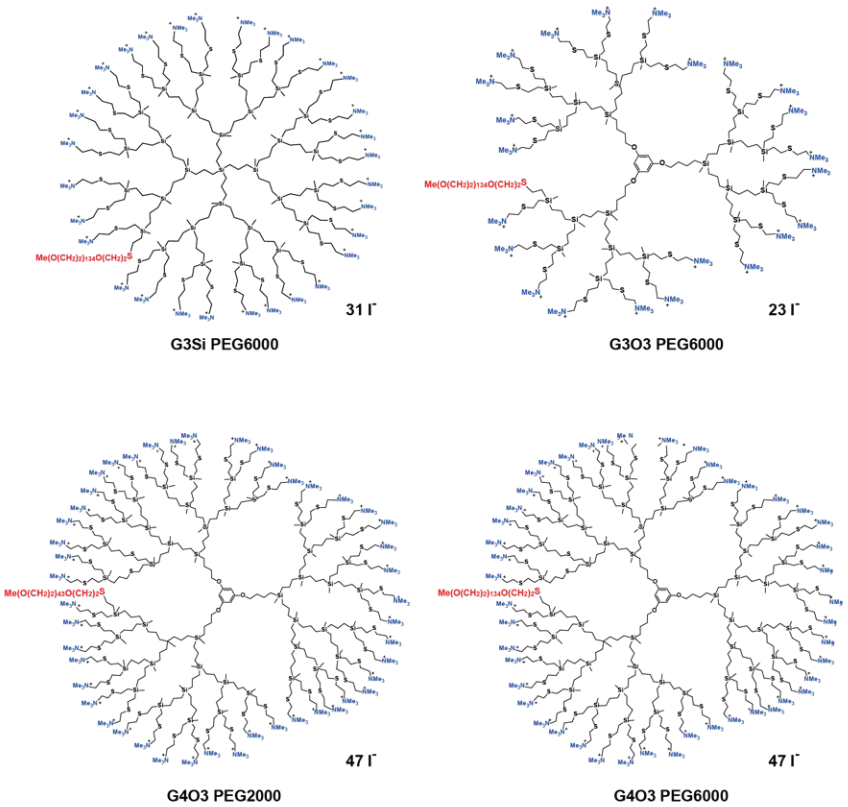
   G3Si(PEG6000)$(NMe^{3+})_{31}$

2. Dendrymery o rdzeniu floroglucynolowym z trzeciorzędowymi grupami aminowymi na powierzchni i jednym łańcuchem glikolu polietylenowego (PEG) o masie cząsteczkowej 2000 lub 6000 Da.

   G3O3(PEG6000)$(NMe^{3+})_{23}$

   G4O3(PEG2000)$(NMe^{3+})_{47}$

   G4O3(PEG6000)$(NMe^{3+})_{47}$



Rycina 3. Wzory stukturalne badanych dendrymerów karbokrzemowych.

siRNA (Dharmacon Inc., Lafayette, CO, USA)

W badaniach wykorzystano dwuniciowy mały interferujący RNA (siRNA) ukierunkowany przeciwko sekwencji genu apolipoproteiny E4 (APOE4), stanowiący właściwy ładunek terapeutyczny dla badanych nanosystemów dendrymerowych. Oligonukleotyd stosowano w postaci nieznakowanej oraz zależnie od rodzaju doświadczenia, w wariantach znakowanych izotiocyjanianem fluorosceiny (FITC) lub Cyjaniną-5 (Cy-5).

- siRNA

  nić sensowna: 5’-GAUUACCUGCGCUGGGUGCUU-3’
  nić antysenesowna: 5’-PGCACCCAGCGCAGGUAAUCUU-3’

- siRNA-FITC

  nić sensowna: 5’-FITC-GAUUACCUGCGCUGGGUGCUU-3’
  nić antysenesowna: 5’-PGCACCCAGCGCAGGUAAUCUU-3’

- siRNA-Cy-5

  nić sensowna: 5’-Cy-5-GAUUACCUGCGCUGGGUGCUU-3’
  nić antysenesowna: 5’-PGCACCCAGCGCAGGUAAUCUU-3’

Linie komórkowe

Do badań *in vitro* wykorzystano trzy ludzkie linie komórkowe istotne z punktu widzenia biologii bariery krew–mózg.

- Komórki śródbłonka mikronaczyń mózgowych wyizolowanych z kory mózgowej HBEC-5i (ATCC, Manassas, VA, USA)
- Astrocyty ludzkie HA (ScienCell Research Laboratories, Carlsbad, CA, USA)
- Ludzkie perycyty naczyń włosowatych mózgu HBVP (ScienCell Research Laboratories, Carlsbad, CA, USA)

Komórkowe składniki krwi oraz krew pełna

W badaniach wykorzystano komórkowe składniki krwi obwodowej pochodzące od zdrowych dawców, obejmujące erytrocyty oraz komórki jednojądrzaste krwi obwodowej (PBMC), które izolowano z kożuchów leukocytarno-płytkowych zakupionych w Regionalnym Centrum Krwiodawstwa i Krwiolecznictwa w Łodzi.

Do wybranych analiz wykorzystywano krew pełną pobraną od zdrowych ochotników płci męskiej w wieku 20–30 lat, u których nie stwierdzono istotnych schorzeń; materiał pobierano po całonocnym poście. Wszystkie procedury prowadzono zgodnie z obowiązującymi zasadami etycznymi dotyczącymi badań z udziałem materiału biologicznego pochodzenia ludzkiego. Badanie to przeprowadzono zgodnie z zasadami etycznymi określonymi w Deklaracji Helsińskiej, a protokół badania został zatwierdzony przez Instytucjonalną Komisję Etyczną przy Instytucie Onkologii św. Elżbiety w Bratysławie (nr zatwierdzenia 03-2020/EK OSA, podpisany 4 marca 2020 r.).

Białka

W badaniach wykorzystano dwa reprezentatywne białka surowicy ludzkiej, dobrane ze względu na ich znaczenie fizjologiczne oraz odmienny profil oddziaływań z cząsteczkami egzogennymi: albuminę surowicy ludzkiej (HSA) (Sigma Aldrich, St. Louis, MO, USA) oraz transferynę surowicy ludzkiej (Tf) (Biorbyt Ltd, Cambridge, UK).

Zwierzęta

W badaniach wykorzystano samice myszy C57BL/6 (Charles River, Niemcy) oraz samice mysiego modelu typu knock-in APOE4 (B6(SJL)-*Apoe*$^{tm1.1(APOE*4)Adiuj}$/J; The Jackson Laboratory, USA). Zwierzęta utrzymywano grupowo (5–8 osobników w klatce) w warunkach kontrolowanych, w temperaturze 22°C, przy 12-godzinnym cyklu światło/ciemność, z nieograniczonym dostępem do karmy i wody. Przed rozpoczęciem doświadczeń myszy aklimatyzowano przez 7 dni oraz regularnie monitorowano pod względem pobierania pokarmu i wody, masy ciała, stanu skóry i sierści oraz zmian w miejscu iniekcji.

Wszystkie procedury przeprowadzano zgodnie z Europejską konwencją o ochronie zwierząt kręgowych wykorzystywanych do celów doświadczalnych i innych celów naukowych (Strasburg, 1986) oraz po uzyskaniu zgody Komisji Etycznej Łotewskiej Służby Żywności i Weterynarii (nr 142/2023). Zabiegi inwazyjne wykonywano w znieczuleniu ogólnym, a po zakończeniu eksperymentów zwierzęta poddawano humanitarnej eutanazji po uprzednim głębokim znieczuleniu. Wszystkie procedury wykonywał przeszkolony personel.

VII. Metody

Synteza dendrymerów karbokrzemowych – część badań wykonano podczas stażu w Katedrze Chemii Organicznej i Nieorganicznej Uniwersytetu w Alcalá de Henares (Hiszpania).

- Synteza prekursorów dendrymerów opartych na rdzeniu floroglucynolowym lub krzemowym oraz ich heterofunkcjonalizacja z użyciem łańcucha PEG i grup aminowych.
- Spektroskopia protonowego rezonansu magnetycznego (^{1}H-NMR) została wykorzystana do potwierdzenia kolejnych etapów syntezy i funkcjonalizacji dendrymerów.

Charakterystyka fizykochemiczna i biofizyczna

- Dynamiczne rozpraszanie światła (DLS) zostało zastosowane do wyznaczania średnicy hydrodynamicznej dendrymerów i dendrypleksów oraz oceny ich dyspersyjności w roztworze.
- Pomiar potencjału zeta został przeprowadzony w celu określenia ładunku powierzchniowego dendrymerów i ich kompleksów z siRNA oraz wyznaczenia punktu wysycenia kompleksu.
- Transmisyjna mikroskopia elektronowa (TEM) została wykorzystana do oceny morfologii, kształtu i rozmiaru wolnych dendrymerów oraz dendrypleksów.
- Mikroskopia sił atomowych (AFM) została zastosowana do obrazowania morfologii siRNA, dendrymerów oraz ich kompleksów.
- Polazryzacja fluorescencji (FP) została wykorzystana do monitorowania zmian uporządkowania i ruchliwości siRNA znakowanego fluoresceiną podczas stopniowej kompleksacji z badanymi dendrymerami oraz do oceny trwałości dendrypleksów w czasie.
- Spektroskopia dichroizmu kołowego siRNA (CD) została zastosowana do oceny zmian struktury oligonukleotydu po kontakcie z rosnącymi stężeniami dendrymerów.
- Elektroforeza agarozowa z barwnikiem GelRed została wykorzystana do wyznaczenia punktu wysycenia kompleksu na podstawie zaniku sygnału wolnego oligonukleotydu w żelu.

Analizy oddziaływań z białkami osocza oraz złożonym środowiskiem osocza

- Technika wygaszania fluorescencji tryptofanu w białkach została zastosowana do oceny oddziaływań dendrymeru z albuminą surowicy ludzkiej i transferyną na podstawie zmian intensywności ich autofluorescencji.
- Spektroskopia dichroizmu kołowego (CD) została przeprowadzona w celu oceny zmian struktury drugorzędowej albuminy i transferyny w obecności dendrymeru, a udział poszczególnych elementów strukturalnych określono metodą dekonwolucji CDNN.
- Izotermiczna kalorymetria miareczkowa (ITC) zostało wykorzystane do wyznaczenia stechiometrii, stałej wiązania oraz funkcji termodynamicznych oddziaływania dendrymer–albumina w roztworze.
- Mikroskopia sił atomowych (AFM) została wykorzystana do oceny przestrzennego rozmieszczenia i morfologii albuminy, osocza i ich koniugatów z dendrymerem.
- Transmisyjna mikroskopia elektronowa (TEM) została zastosowana do oceny przestrzennego rozmieszczenia i zmian morfologicznych albuminy, osocza i ich koniugatów z dendrymerem.

Ocena hemokompatybilności – część badań wykonano podczas stażu w Katedrze Fizyki Jądrowej i Biofizyki, Uniwersytetu Komeńskiego w Bratysławie (Słowacja).

- Hemolizę erytrocytów po ekspozycji na dendrymer oraz dendrypleks oznaczano spektrofotometrycznie, zarówno w warunkach bez, jak i w obecności osocza.
- Test redukcji resazuryny (Alamar Blue) został zastosowany do oceny aktywności mitochondrialno-metabolicznej oraz żywotności komórek jednojądrzastych krwi obwodowej (PBMC) po inkubacji z dendrymerem lub dendrypleksem na podstawie fluorescencyjnego odczytu redukcji barwnika.
- Wieloparametrowy test immunologiczny oparty na systemie Luminex MAGPIX został zastosowany do ilościowego oznaczania interferonu α2 (IFNα2), interleukiny 6 (IL-6), interleukiny 8 (IL-8), interleukiny 10 (IL-10), podjednostki p40 interleukiny 12 (IL-12p40) i czynnika martwicy nowotworów α (TNFα) w supernatantach hodowli PBMC po ekspozycji na badane związki, zarówno w środowisku o niskiej oraz wysokiej zawartości osocza
- Reometria rotacyjna pełnej krwi została zastosowana do oceny właściwości hemoreologicznych na podstawie pomiaru lepkości w szerokim zakresie szybkości ścinania.

- Pomiar anizotropii fluorescencji sond DPH i TMA-DPH został zastosowany do oceny wpływu badanych związków na płynność błon erytrocytarnych.
- Oznaczanie parametrów morfologii krwi z użyciem analizatora COULTER DxH 800 zostało przeprowadzone w celu ilościowej oceny zmian hematologicznych po ekspozycji na badane związki.
- Oznaczanie parametrów hemostatycznych z wykorzystaniem analizatora ACL Top 500 CTS zostało zastosowane do oceny zmian w układzie krzepnięcia po kontakcie krwi z badanymi związkami.

Profilowanie biokompatybilności komórkowej

- Test redukcji MTT został wykorzystany do oceny aktywności mitochondrialno-metabolicznej oraz żywotności komórek po inkubacji z dendrymerem lub dendrypleksem na podstawie spektrofotometrycznego odczytu redukcji barwnika.
- Oznaczanie reaktywnych form tlenu (ROS) z użyciem sondy H_2DCF-DA zostało wykorzystane do ilościowej oceny stresu oksydacyjnego indukowanego przez badane związki w komórkach.
- Oznaczanie potencjału błony mitochondrialnej ($\Delta\Psi m$) z wykorzystaniem sondy fluorescencyjnej JC-1 zostało zastosowane do oceny zaburzeń funkcji mitochondrialnej po ekspozycji na dendrymer lub jego dendrypleks.
- Szybki test halo (Fast Halo Assay, FHA) został przeprowadzony w celu oceny uszkodzeń DNA analizowanych na poziomie pojedynczej komórki z wykorzystaniem mikroskopii fluorescencyjnej i półautomatycznej analizy obrazów.
- Mikroskopia konfokalna znakowanych fluorescencyjnie: siRNA, dendrymerów i dendrypleksów została wykorzystana do oceny internalizacji i subkomórkowej lokalizacji badanych związków.

Analiza integralności oraz funkcjonalności modelu bariery krew–mózg

- Monitorowanie impedancji w czasie rzeczywistym za pomocą systemu xCELLigence RTCA eSight zostało zastosowane do oceny odpowiedzi modelu BBB na ekspozycję na nośnik lub dendrypleks.
- Mikroskopia fluorescencyjna żywych komórek z użyciem barwnika jądrowego eLive Red została wykorzystana do równoległej oceny konfluencji jądrowej i zmian morfologicznych w modelu BBB monitorowanym w czasie rzeczywistym.
- Pomiar oporu elektrycznego (TEER) w dwuprzedziałowym systemie opartym na insertach membranowych został wykorzystany do oceny przewodnictwa jonowego i integralności modelu BBB po ekspozycji na badane związki.
- Test przepuszczalności parakomórkowej z wykorzystaniem fluorescencyjnie znakowanego dekstranu został zastosowany do ilościowej oceny transportu makrocząsteczek przez model BBB po ekspozycji na badane związki w dwuprzedziałowym układzie opartym na insertach membranowych, na podstawie pomiaru intensywności fluorescencji.

Charakterystyka biodystybucji i efektów behawioralnych w modelu mysim – badania wykonane w Łotewskim Centrum Badań i Studiów Biomedycznych (Latvian Biomedical Research and Study Centre) w Rydze (Łotwa).

- Fluorescencyjne obrazowanie *in vivo* (IVIS) zostało wykorzystane do nieinwazyjnej, oceny ustrojowej biodystybucji i utrzymywania się fluorescencyjnie znakowanego siRNA w modelu mysim po wielokrotnym dożylnym podaniu dendrypleksu lub nieskompleksowanego siRNA.
- Fluorescencyjne obrazowanie narządów *ex vivo* metodą IVIS zostało zastosowane do oceny dystrybucji fluorescencyjnie znakowanego siRNA w wątrobie, śledzionie, nerkach, sercu, płucach i mózgu po wielokrotnym dożylnym podaniu dendrypleksu lub nieskompleksowanego siRNA.
- Test labiryntu wodnego Morrisa (MWM) został wykorzystany do oceny zmian behawioralnych, obejmujących uczenie przestrzenne i pamięć referencyjną, w mysim modelu choroby Alzheimera oraz grupie kontrolnej po wielokrotnym dożylnym podaniu dendrypleksu lub nieskompleksowanego siRNA.

VIII. Omówienie prac wchodzących w skład rozprawy doktorskiej

Cykl pięciu prac składających się na niniejszą rozprawę doktorską został opracowany jako spójny ciąg badań, mający na celu ocenę właściwości, bezpieczeństwa i funkcjonalności nanosystemu dendrymer–siRNA. Kolejne prace realizują założenia inteligentnej strategii testowania (ITS/IATA), opartej na iteracyjnym redukowaniu niepewności badawczej poprzez dobór modeli o rosnącym stopniu złożoności oraz wnioskowanie oparte na łącznej ocenie dowodów (*weight of evidence)*. Podejście to uwzględnia złożoność interakcji nanomateriału począwszy od charakterystyki jego parametrów fizykochemicznych, poprzez analizę korony biomolekularnej i ocenę hemokompatybilności oraz odpowiedzi komórkowej, następnie przechodząc do oceny integralności i przepuszczalności modelowej bariery krew-mózg (BBB), aż po weryfikację w modelu *in vivo*. Tak zdefiniowana sekwencja walidacji hipotez została bezpośrednio włączona do wytycznych toksykologicznych ISO oraz OECD, podkreślając znaczenie wielopoziomowej preselekcji oraz komplementarnego doboru punktów końcowych.

Punkt wyjścia cyklu badań stanowiła synteza i charakterystyka fizykochemiczna czterech kationowych dendrymerów karbokrzemowych o zróżnicowanej strukturze **(praca I)**. Panel obejmował cztery niedostępne komercyjnie dendrymery karbokrzemowe o dodatnim ładunku powierzchniowym, różniące się typem rdzenia, generacją oraz długością łańcucha polietylenoglikolowego (PEG). Zastosowanie technik biofizycznych pozwoliło na wykazanie bezpośredniej zależności między budową chemiczną dendrymerów a ich stabilnością i właściwościami powierzchniowymi.

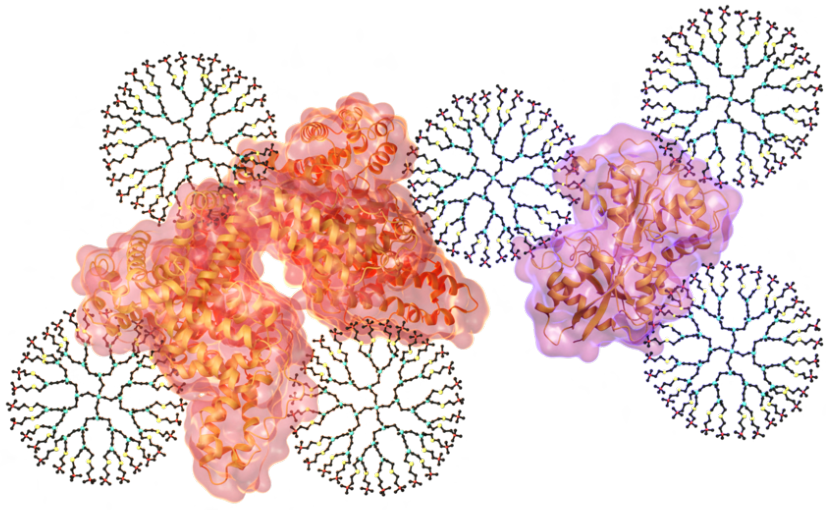
Charakterystykę fizykochemiczną przeprowadzono zarówno dla nośników w formie wolnej, jak i po utworzeniu kompleksów z siRNA (dendrypleksów). Metoda dynamicznego rozpraszania światła (DLS) posłużyła do wyznaczenia średnicy hydrodynamicznej obejmującej nanocząstkę wraz z otoczką solwatacyjną i łańcuchem PEG. Z kolei pomiary potencjału zeta pozwoliły określić potencjał elektrostatyczny na płaszczyźnie poślizgu cząsteczki co determinuje siłę oddziaływań kationowego nośnika z anionowymi fosforanami siRNA. Morfologię wybranego układu zweryfikowano za pomocą transmisyjnej mikroskopii elektronowej (TEM) oraz mikroskopii sił atomowych (AFM), dostarczając informacji o rozkładzie wielkości i organizacji przestrzennej. Proces kompleksowania opisano wielometodowo, traktując go jako kluczowy element warunkujący funkcjonalność nanosystemu. Analiza procesu kompleksowania pozwoliła na szczegółową charakterystykę mechanizmu oddziaływania dendrymer-siRNA, ocenę wpływu dendrymerów na strukturę

przestrzenną oligonukleotydu oraz morfologię wybranego układu. Analiza polaryzacji fluorescencji umożliwiła określenie stabilności kompleksów w czasie i ocenę powinowactwa wiązania siRNA poprzez monitorowanie stopnia zahamowania rotacji wyznakowanego oligonukleotydu w roztworze. Dichroizm kołowy (CD) dostarczył wglądu w zmiany konformacji przestrzennej siRNA na skutek oddziaływania z dendrymerem. Proces kompleksacji monitorowano także za pomocą elektroforezy żelowej, która pozwoliła na wizualizację wygaszania fluorescencji siRNA wskutek tworzenia dendrypleksów i zahamowania migracji w żelu agarozowym. Na podstawie wyników tych analiz określono punkt optymalnego wysycenia kompleksu siRNA wykorzystując segmentową analizę regresji. Równolegle przeprowadzona przesiewowa ocena cytotoksyczności dendrymerów z wykorzystaniem testu MTT, umożliwiającego pomiar mitochondrialnej aktywności oksydacyjnej, w komórkach śródbłonka naczyniowego mózgu (linia HBEC-5i) dostarczyła danych dotyczących biokompatybilności badanych nośników, co pozwoliło na wyłonienie kandydata o najkorzystniejszym profilu bezpieczeństwa.

Analiza danych biofizycznych i biologicznych pozwoliła wybrać dendrymer G3Si PEG6000 jako kandydat do dalszych etapów badań, ze względu na najsilniejsze powinowactwo do siRNA, najmniejszą średnicą hydrodynamiczną powstających dendrypleksów oraz najbardziej korzystny, z punktu widzenia bezpieczeństwa komórkowego, profil cytotoksyczności. Wybór nośnika o optymalnych parametrach wyjściowych w połączeniu z precyzyjnym określeniem stosunku kompleksacji siRNA z dendrymerem (1:2,5) wykorzystywanego w kolejnych etapach eksperymentalnych, stanowi kluczowy fundament dalszych badań umożliwiając wdrażanie modeli o wyższym stopniu złożoności biologicznej.

Drugi etap badań poświęcono analizie tożsamości biologicznej wybranego nośnika, rozumianej jako zespół właściwości fizykochemicznych ujawniających się dopiero w kontakcie z krwią. Po wprowadzeniu do krążenia ogólnoustrojowego dendrymer natychmiast oddziałuje z białkami osocza, lipidami oraz cukrami, co prowadzi do adsorpcji tych biomolekuł na jego powierzchni i powstania korony biomolekularnej. Powstająca w ten sposób warstwa między nanomateriałem a środowiskiem biologicznym współdecyduje zarówno o biodystrybucji, jak i o hemokompatybilności układu. Celem tego etapu było przejście od charakterystyki fizykochemicznej nośnika do oceny jego zachowania w kontakcie z osoczem oraz wpływu tych interakcji na jego aktywność biologiczną. Wyniki tych analiz przedstawiono w pracach **(II)** i **(III)**.

W pierwszej części tego etapu **(praca II)** skoncentrowano się na oddziaływaniach dendrymeru G3Si PEG6000 z reprezentatywnymi białkami osocza (transferryną i albuminą surowicy ludzkiej) oraz złożonym środowiskiem osocza (Ryc. 4). Analiza wygaszania fluorescencji wykazała wyższe powinowactwo badanego dendrymeru do transferryny niż do albuminy. Jednocześnie pomiary dichroizmu kołowego (CD) wykazały, że reorganizacja struktury drugorzędowej jest silniejsza w przypadku albuminy. Złożony, wieloetapowy charakter zmian konformacyjnych obu białek wskazuje na udział wielu domen wiążących oraz dynamiczny charakter formowania się oddziaływań dendrymer–białko. W toku dalszych eksperymentów albuminę przyjęto jako kluczowy model, ze względu na silne interakcje z dendrymerem prowadzące do istotnych modyfikacji jej struktury drugorzędowej. Wyniki izotermicznej kalorymetrii miareczkowej (ITC) potwierdziły, że oddziaływanie albumina–G3Si-PEG6000 zachodzi z udziałem wielu cząsteczek dendrymeru przypadających na jedną cząsteczkę HSA, a profil termodynamiczny procesu wskazuje dominujący udział entropii. Dane te, skorelowane z obrazowaniem za pomocą mikroskopii sił atomowych (AFM) oraz transmisyjnej mikroskopii elektronowej (TEM), sugerują, że zmiany w strukturze drugo- i trzeciorzędowej indukowane przez dendrymer mogą inicjować proces nukleacji, które sprzyjają nieprawidłowemu fałdowaniu białek, oligomeryzacji i tworzeniu protofibryli.



Rycina 4. Ilustracja oddziaływań białkowo-dendrymerowych z udziałem albuminy (fiolet) i transferryny (pomarańcz).

Należy jednak zaznaczyć, że efekt działania dendrymerów *in vivo* jest wypadkową pomiędzy ich zdolnością do koncentracji białek a potencjałem do ich sekwestracji i stabilizacji. W warunkach fizjologicznych proces ten jest modulowany przez charakter przepływu krwi (laminarny oraz turbulentny), dynamiczną przebudowę korony na drodze konkurencyjnej adsorpcji (efekt Vromana) oraz mechanizmy klirensu systemowego. W konsekwencji badanie hemokompatybilności nanosystemu G3Si PEG6000 ujęto jako kompleksową ocenę interakcji zarówno wolnego dendrymeru, jak i dendrypleksu, rozróżniając efekty wynikające z bezpośredniego kontaktu powierzchni nośnika z komponentami krwi od efektów wynikających z oddziaływania za pośrednictwem korony biomolekularnej. Przyjęcie tak sformułowanego protokołu badawczego zapewnia holistyczny wgląd w profil bezpieczeństwa nośnika, obejmujący zarówno bezpośrednie interakcje z elementami morfotycznymi, jak i wpływ na parametry hemoreologiczne, kaskadę krzepnięcia oraz odpowiedź immunologiczną.

Weryfikacja hemolityczna wykazała, że nieskompleksowany dendrymer indukuje hemolizę erytrocytów, jednak kompleksacja dendrymeru z siRNA oraz formowanie korony biomolekularnej skutecznie ograniczają bezpośrednie uszkodzenia erytrocytów. Oznacza to, że w warunkach zbliżonych do fizjologicznych kationowe grupy dendrymeru są słabiej eksponowane. Zmiany hemoreologiczne w krwi pełnej wywołane przez dendrypleks miały umiarkowany charakter i ujawniały się przede wszystkim przy niskich szybkościach ścinania. Analiza anizotropii fluorescencji sond DPH i TMA-DPH wykazała, że badany nanosystem zwiększa płynność błon erytrocytów. Pozwoliło to sformułować hipotezę, że obserwowany wzrost lepkości wynika z nasilenia sił adhezji między komórkami, a nie z usztywnienia błon erytrocytów. Wyniki uzyskane testem Alamar Blue nie wykazały istotnego spadku żywotności jednojądrzastych komórek krwi obwodowej (PBMC) po 24 i 48 godzinach ekspozycji, co wskazuje, że nanosystem nie zaburza ich funkcji i może być dobrze tolerowany przez komórki układu odpornościowego.

Analiza wpływu nanosystemu na profil sekrecji cytokin oraz chemokin przez PBMC przy użyciu multipleksowej analizy metodą cytometrii przepływowej na mikrokulkach wykazało obecność subtelnych, a zarazem zależnych od obecności osocza, zmian w poziomach interleukiny 6 (IL-6), interleukiny 8 (IL-8) oraz czynnika martwicy nowotworów α (TNFα). Zmiany te pozostawały jednak poniżej progów istotności klinicznej. Analizy hematologiczne wykorzystujące wiele zintegrowanych technik wskazują, że badane nanowektory nie wpływają negatywnie na parametry związane z czerwonymi krwinkami, białymi krwinkami ani płytkami

krwi. Co istotne, większość wskaźników krzepnięcia utrzymała się w zakresie wartości fizjologicznych. Wyjątek stanowiło zależne od stężenia, wydłużenie czasu częściowej tromboplastyny po aktywacji (aPTT). Zjawisko to sugeruje niewielki wpływ badanych substancji na wewnętrzną kaskadę krzepnięcia przy jednoczesnym zachowaniu prawidłowych wartości czasu protrombinowego (PT) i trombinowego (TT).

Uzyskany zestaw wyników pozwolił zakwalifikować dendrypleks G3Si PEG6000 jako układ o profilu hemokompatybilności umożliwiającym jego dalszą ocenę przedkliniczną, przy jednoczesnym wskazaniu obszarów wrażliwych wymagających dalszego monitorowania. Etap ten stanowi wstępną walidację translacyjną, ponieważ minimalizuje ryzyko, że efekty obserwowane w kolejnych modelach będą wynikiem niespecyficznych zaburzeń wywołanych interakcją z elementami krwi, a nie konsekwencją mechanizmów właściwych dla oddziaływania nanosystemu z modelami o wyższej złożoności biologicznej. W konsekwencji kolejne etapy badań objęły modele o rosnącym stopniu złożoności, rozpoczynając od profilowania metabolicznego i mechanistycznego w komórkach jednostki neuronaczyniowej, następnie przechodząc do oceny integralności i przepuszczalności modelu BBB, a ostatecznie weryfikując uzyskane obserwacje w modelu zwierzęcym.

W pierwszej części kolejnego etapu badań, przedstawionego w pracach **(IV)** oraz **(V)**, skoncentrowano się na profilowaniu komórkowym. Ocenę cytotoksyczności metabolicznej dendrymeru oraz jego dendrypleksu przeprowadzono testem MTT w trzech liniach tworzących jednostkę neuronaczyniową, czyli komórkach śródbłonka, perycytach i astrocytach. Badania te pozwoliły na precyzyjne zidentyfikowanie perycytów jako najbardziej wrażliwej populacji, podczas gdy astrocyty wykazały najwyższą tolerancję metaboliczną na badany nanosystem. Mechanistyczny wgląd w procesy uszkodzeń komórkowych uzyskano poprzez ilościowe oznaczanie reaktywnych form tlenu (ROS) oraz pomiary potencjału błony mitochondrialnej ($\Delta\Psi m$). Wykazano, że depolaryzacja mitochondriów zachodzi już przy stężeniach subcytotoksycznych, stanowiąc wczesny marker stresu komórkowego poprzedzający inicjację śmierci komórki.

Równolegle przeprowadzona ocena genotoksyczności testem Fast Halo Assay (FHA), poprzez pomiar pęknięć nici DNA, wykazała, że kompleksacja dendrymeru z siRNA redukuje jego genotoksyczny efekt. Dzieje się tak pomimo tego, że zarówno nieskomplekowany dendrymer oraz dendrypleks indukują porównywalny poziom reaktywnych form tlenu. Sugeruje to, że pęknięcia DNA są w większym stopniu związane z mechanizmami niezależnymi od ogólnej produkcji ROS, prawdopodobnie wynikającymi z bezpośrednich

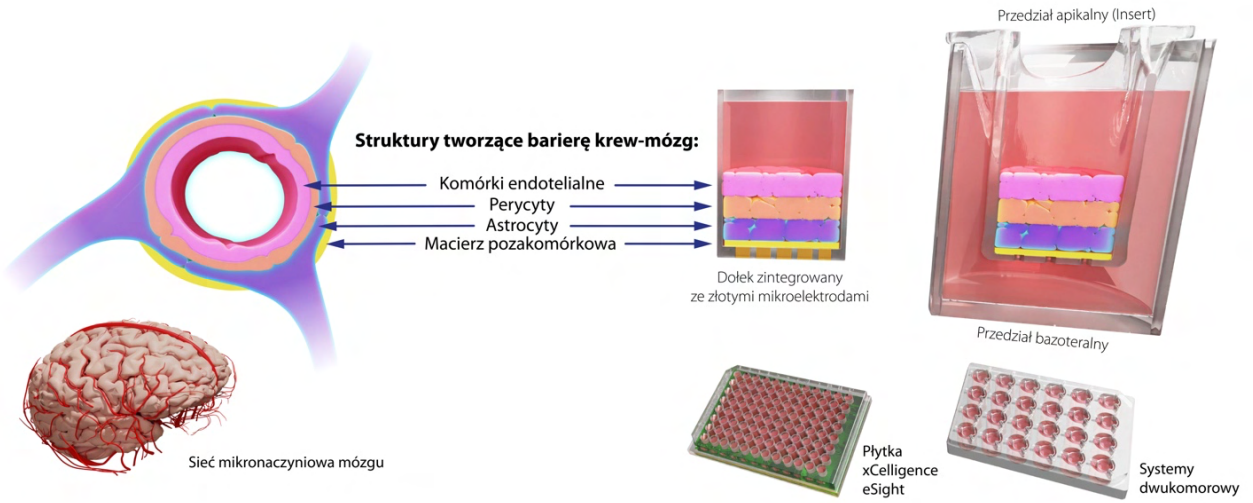
interakcji nośnika z materiałem genetycznym, które ulegają osłabieniu po związaniu siRNA. Jednocześnie, należy podkreślić, że test FHA może rejestrować również pęknięcia wtórne towarzyszące procesom apoptotycznym, a pomiary ROS są zależne od czasu i miejsca powstawania reaktywnych form tlenu.

Skuteczność dostarczania siRNA potwierdzono metodą mikroskopii konfokalnej, która wykazała wydajną internalizację dendrypleksów oraz ich selektywną akumulację w obrębie cytoplazmy. Z perspektywy mechanizmu interferencji RNA, akumulacja siRNA w przedziale pozajądrowym stanowi kluczowy warunek skutecznego wyciszania ekspresji genów docelowych. Równocześnie obrazowanie wykazało, że nieskompleksowany dendrymer był zlokalizowany w rejonie jądra komórkowego. W kontekście wcześniejszych wyników dotyczących genotoksyczności można ostrożnie zasugerować spójny kierunek interpretacji: obecność wolnego nośnika w pobliżu struktur jądrowych może zwiększać prawdopodobieństwo nieswoistych interakcji z materiałem genetycznym lub procesami jądrowymi, co potencjalnie sprzyja nasilaniu sygnału pęknięć nici DNA obserwowanego w teście FHA. Z kolei cytoplazmatyczna dystrybucja dendrypleksów, połączona ze spadkiem sygnału genotoksycznego po kompleksacji z siRNA, wspiera tezę, że formulacja z siRNA nie tylko umożliwia dostarczenie siRNA do właściwego przedziału komórkowego, ale też ogranicza ekspozycję jądra komórkowego i tym samym może redukować ryzyko indukowania uszkodzeń DNA.

Druga część tego etapu walidacji dotyczyła oceny integralności i przepuszczalności trójkulturowego modelu bariery krew-mózg, odzwierciedlającego kontekst jednostki neuronaczyniowej (NVU). Wykorzystany układ oparto na bezpośrednim, warstwowym kontakcie, replikującym fizjologiczne proporcje komórek śródbłonka, perycytów oraz astrocytów, co pozwoliło na odtworzenie orientacji ściany naczyń włosowatych oraz ich wsparcia abluminalnego. Tak zaprojektowane mikrośrodowisko umożliwia nie tylko zachowanie niezbędnej sygnalizacji międzykomórkowej, ale stanowi również istotny punkt odniesienia dla oceny zmian przepuszczalności bariery wywołanych przez badane związki. Wykorzystując monitorowanie impedancji w czasie rzeczywistym (xCELLigence eSight system) wskazano, że wysokie dawki nieskompleksowanego dendrymeru powodują nieodwracalną utratę adhezji, co interpretowano jako obraz zgodny z utrwalonym uszkodzeniem modelu bariery i utratą adhezji oraz żywotności komórek, a nie przejściowym zaburzeniem. Jednocześnie w niższych, subcytotoksycznych stężeniach zaobserwowano dwufazową odpowiedź bariery, w której dendrypleks indukował przejściowy

spadek, a następnie wzrost indeksu komórkowego (CI), odzwierciedlającego adhezję, proliferację i konfluencję. Uzupełnieniem powyższej interpretacji było monitorowanie integralności modelu w czasie rzeczywistym przy użyciu barwnika jądrowego eLive Red. Zastosowanie techniki obrazowania przyżyciowego pozwoliło na dynamiczną ocenę stopnia konfluencji oraz weryfikację ciągłości modelu bariery komórkowej w trakcie trwania eksperymentu. Najwyższe stężenie wolnego dendrymeru spowodowało wyraźny spadek impedancji, któremu towarzyszył równoległy spadek konfluencji. Obrazowanie mikroskopowe ujawniło ponadto odrywanie się komórek od podłoża w postaci dużych arkuszy. Taki charakter odpowiedzi komórkowej dostarcza szczególnie ważnych informacji mechanistycznych, ponieważ wskazuje na zachowanie kohezji komórka-komórka podczas odrywania. Sugeruje to, że „słabym ogniwem" mogą być nie połączenia międzykomórkowe, ale adhezje komórka-macierz.

Analiza integralności bariery z wykorzystaniem parametru TEER wykazała niemonotoniczny profil odpowiedzi zależny od stężenia i kompleksacji z siRNA. Wyniki te sugerują, że w całym zakresie stężeń odpowiedź komórek obejmuje fazę początkowego osłabienia integralności bariery, po której następuje uruchomienie mechanizmów adaptacyjnych. Brak długofalowego obniżenia wartości oporu elektrycznego TEER we wszystkich badanych układach pozostaje w wyraźnym kontraście do nieodwracalnej destabilizacji bariery komórkowej zarejestrowanej w pomiarach impedancji prowadzonych przy najwyższych stężeniach nanosystemu. W dwuprzedziałowym modelu opartym na insertach membranowych dominowały procesy o charakterze przejściowym lub mechanizmy adaptacyjne, prowadzące wtórnie do przywrócenia ciągłości bariery. Różnice w wynikach uzyskiwanych w obu systemach badawczych należy interpretować przez pryzmat odmiennych parametrów ekspozycji badanych związków i akumulacji metabolitów w czasie. W modelu dwuprzedziałowym zachowany jest swobodny przepływ badanych substancji pomiędzy przedziałem apikalnym a bazolateralnym, podczas gdy w statycznym układzie jednoprzestrzennym przedłużona inkubacja sprzyja generowaniu stresu metabolicznego, wynikającego z wyczerpania zasobów odżywczych oraz progresywnej akumulacji cytotoksycznych metabolitów (Ryc. 5). Istotnym aspektem niniejszego etapu badań była ocena przepuszczalności parakomórkowej dekstranu o masie 40 kDa, która wykazała rozbieżność między oporem jonowym a dyfuzją makromolekularną w 72. godzinie po aplikacji nanosystemu. Ta rozbieżność stanowi przesłankę do wnioskowania o selektywnej i odwracalnej modulacji architektury połączeń ścisłych, prowadzącej do przejściowej modyfikacji szlaku parakomórkowego w odpowiedzi na interakcję z nanonośnikiem.



Rycina 5. Schemat struktury naczynia włosowatego mózgu i przygotowanych modeli bariery krew-mózg w dołkach płytki systemu xCelligence eSight oraz na insertach systemu dwukomorowego.

Kluczowym elementem weryfikacji postawionych hipotez badawczych było przeniesienie analiz na poziom organizmalny, co zrealizowano poprzez zastosowanie modelu mysiego. Badania biodystrybucji *in vivo* z wykorzystaniem systemu IVIS wykazały, że podanie siRNA w formie dendrypleksu istotnie wydłuża okres jego obecności w układzie krążenia, co w ujęciu probabilistycznym zwiększa szansę ekspozycji mikrokrążenia mózgowego na terapeutyk i stwarza warunki do potencjalnego oddziaływania z barierą krew-mózg. Jednocześnie analiza *ex vivo* narządów potwierdziła dominującą kumulację w nerkach i wątrobie, co pozostaje zgodne z szeroko opisywanym sposobem dystrybucji oligonukleotydów i nanonośników. Wysoka intensywność sygnału w nerkach może odzwierciedlać procesy filtracji kłębuszkowej oraz potencjalną dysocjację kompleksów w mikrośrodowisku kanalikowym, prowadzącą do eliminacji frakcji niezwiązanej. Z kolei znacząca akumulacja w wątrobie jest zgodna z mechanizmami wychwytu przez układ siateczkowo-śródbłonkowy (RES) oraz procesami sekwestracji charakterystycznymi dla narządów o wysokiej aktywności fagocytarnej wobec struktur makromolekularnych.

Istotnym elementem interpretacji danych na tym etapie jest uwzględnienie ograniczeń metod optycznych stosowanych w obrębie ośrodkowego układu nerwowego (CNS). Niski lub trudny do jednoznacznego uchwycenia sygnał fluorescencyjny w obrębie mózgu nie może być traktowany jako dowód braku dostarczania terapeutyku, ponieważ intensywność sygnału jest silnie zależna od progu detekcji, tłumienia przez tkanki oraz właściwości znacznika w złożonym, heterogennym mikrośrodowisku CNS **(praca IV)**.

Przedstawiony profil biodystrybucji wskazuje na poprawę parametrów farmakokinetycznych oraz zmianę dystrybucji tkankowej terapeutyku. Wyniki te wymagają jednak ostatecznego potwierdzenia za pomocą metod o wysokiej czułości analitycznej, umożliwiających bezpośredni pomiar stężenia siRNA w ośrodkowym układzie nerwowym, co pozwoli na definitywną ocenę skuteczności transportu przez barierę krew-mózg.

Dopełnieniem badań *in vivo* było przejście od charakterystyki biodystrybucji do weryfikacji funkcjonalnej w mysim modelu choroby Alzheimera. W transgenicznym mysim modelu obciążonym ryzykiem rozwoju choroby Alzheimera zastosowano protokół oceny uczenia przestrzennego i pamięci, co umożliwiło ewaluację wpływu długofalowej, wielokrotnej ekspozycji dendrypleksów na mierzalne parametry behawioralne. Odnotowana poprawa wskaźników kognitywnych, przy jednoczesnym braku analogicznej odpowiedzi w grupie kontrolnej otrzymującej wolne siRNA, stanowi silny argument potwierdzający tezę, iż to kompleksacja siRNA z dendrymerem determinuje efektywność biologiczną ładunku w warunkach systemowych. Należy zaznaczyć, iż uzyskane wyniki behawioralne powinny być interpretowane z zachowaniem należytej ostrożności jako dowód słuszności koncepcji, a nie wyczerpujące wyjaśnienie mechanizmu działania **(praca V)**.

W strukturze niniejszej dysertacji finałowy etap badań w modelu mysim pełni zatem dwojaką funkcję: po pierwsze potwierdza, że opracowany dendrypleks efektywnie modyfikuje profil farmakokinetyczny i biodystrybucyjny siRNA; po drugie zaś wprowadza funkcjonalny punkt końcowy, stanowiący uzasadnienie dla przyszłych badań nakierowanych na precyzyjne skorelowanie obecności siRNA w tkance docelowej z poziomem wyciszenia ekspresji genu oraz obserwowanym efektem fenotypowym.

IX. Perspektywy przyszłych badań

Przedstawiony cykl badawczy, choć stanowi zamkniętą i spójną całość, która potwierdza potencjał dendrymerów karbokrzemowych jako nośników siRNA w terapii skierowanej przeciwko chorobie Alzheimera, otwiera jednocześnie szereg nowych kierunków badawczych. Wykazana skuteczność nanosystemu *in vivo* oraz poznane mechanizmy jego interakcji z barierą krew-mózg stanowią podstawę do rozszerzenia badań w trzech głównych obszarach: molekularnym, technologicznym oraz toksykologicznym.

Najważniejszym kierunkiem dalszych badań jest wyjaśnienie zależności między obserwowanym efektem behawioralnym a molekularnym działaniem terapeutyku. Przyszłe analizy powinny skoncentrować się na ilościowym oznaczaniu stężeń siRNA przy uwzględnieniu struktury BBB i kompartmentalizacji ośrodkowego układu nerwowego. Wymaga to zastosowania technik o wysokiej czułości analitycznej, takich jak chromatografia cieczowa ze spektrometrią mas (LC-MS/MS) lub kropelkowy cyfrowy PCR (ddPCR). Równoległe badanie stopnia wyciszenia genu docelowego na poziomie mRNA oraz weryfikacja zmian w ekspresji białka (Western Blot, ELISA) pozwolą na lepsze zdefiniowanie zależności między ekspozycją, a odpowiedzią biologiczną w ujęciu farmakokinetyczno-farmakodynamicznym (PK/PD). Takie podejście umożliwi precyzyjne określenie zakresu skutecznego i bezpiecznego działania terapeutyku oraz optymalizację schematów dawkowania w oparciu o dynamikę wyciszenia ekspresji genu docelowego. Istotnym uzupełnieniem powyższych analiz powinno być również rozszerzenie oceny behawioralnej o komplementarne próby oceniające pamięć rozpoznawczą, pamięć roboczą i wpływ czynników pozapoznawczych, takie jak test rozpoznawania nowych obiektów (NOR), labirynt Y i test otwartego pola (OFT).

Choć dotychczasowe badania wykazały zdolność badanego nanoukładu do modyfikacji przepuszczalności modelowej bariery, dokładny szlak transportu i internalizacji nanosystemu wymaga pogłębionej charakterystyki. Wskazane jest przy tym uzupełnienie obrazowania mikroskopowego o ilościową analizę cytometryczną, co pozwoli na statystyczną weryfikację kinetyki poboru w szerszej populacji komórek. Przyszłe analizy powinny obejmować mapowanie szlaków internalizacji z wykorzystaniem specyficznych inhibitorów endocytozy (np. chloropromazyny dla szlaku zależnego od klatryny czy filipiny dla szlaku zależnego od kaweoliny). Ponadto, kluczowe znaczenie ma precyzyjne rozróżnienie między transportem transcelularnym a parakomórkowym. W tym celu niezbędne jest wdrożenie

wysokorozdzielczej mikroskopii konfokalnej z wykorzystaniem immunofluorescencyjnego znakowania kluczowych białek połączeń ścisłych takich jak zonula occludens-1 (ZO-1), klaudyna-5 oraz okludyna. Pozwoli to na przestrzenną wizualizację i bezpośrednie potwierdzenie, czy obserwowane w pomiarach TEER przejściowe zaburzenie bariery wiąże się z odwracalną reorganizacją i rozszczelnieniem kompleksów białkowych szlaku międzykomórkowego.

Mając na uwadze wykazane różnice w odpowiedzi modeli BBB między wykorzystywanymi układami statycznymi, wprowadzenie czynnika mechanicznego w postaci przepływu medium pozwoli na jeszcze wierniejsze odtworzenie fizjologicznej odpowiedzi badanej bariery modelowej oraz dynamiki formowania się korony biomolekularnej w warunkach krążenia w mikrokapilarach mózgowych. Modele te mogłyby zostać opracowane w oparciu o indukowane pluripotencjalne komórki macierzyste (iPSC), co pozwoliłoby na uzyskanie ludzkich, standaryzowanych i powtarzalnych komponentów jednostki neuronaczyniowej, w tym komórek śródbłonka o fenotypie BBB, perycytów i astrocytów wyprowadzonych z jednego tła genetycznego.

Zidentyfikowane w toku oceny hemokompatybilności zależne od stężenia wydłużenie czasu częściowej tromboplastyny po aktywacji (aPTT) wyznacza istotny obszar dla przyszłej ewaluacji toksykologicznej. Zrozumienie wpływu dendrypleksów na układ hemostazy wymaga przejścia od podstawowych testów przesiewowych do pogłębionej analizy mechanistycznej. Konieczne jest zbadanie wpływu nośnika na poszczególne zymogeny szlaku wewnątrzpochodnego kaskady krzepnięcia (w szczególności czynniki VIII, IX, XI i XII) oraz wykorzystanie testu generacji trombiny (TGA) w celu oceny globalnego potencjału pro- lub antykoagulacyjnego. Dodatkowo, analiza powinna zostać rozszerzona o badania agregacji i aktywacji płytek krwi (np. ekspresja P-selektyny metodą cytometrii przepływowej), co pozwoli lepiej scharakteryzować potencjalne ryzyko powikłań zatorowo-zakrzepowych lub skaz krwotocznych przy przedłużonej ekspozycji systemowej *in vivo*.

Włączenie powyższych zagadnień do przyszłych protokołów badawczych nie tylko umożliwi pełniejsze zrozumienie mechanizmów biofizycznych badanych dendrypleksów, ale również znacząco podniesie wartość translacyjną proponowanego nanosystemu lub wpłynie na rozwinięcie alternatywnego układu na podstawie wyciągniętych wniosków. Przejście od fundamentalnej analizy fizykochemicznej do zaawansowanej biologii systemowej i terapii skojarzonej stanowi niezbędny krok na drodze do ewentualnych badań klinicznych w obszarze nowoczesnych neuroterapii.

X. Podsumowanie i wnioski

1. Spośród analizowanych kationowych dendrymerów karbokrzemowych najbardziej korzystnym profilem właściwości fizykochemicznych i bezpieczeństwa charakteryzował się PEGylowany dendrymer G3Si PEG6000, który wyłoniono do dalszych etapów oceny jako nośnik terapeutycznego siRNA.
2. Wykazano, że biologiczne zachowanie badanego nośnika jest w istotnym stopniu uwarunkowane jego interakcjami z białkami osocza. Jednocześnie uzyskane wyniki wskazują, że zjawisko to wymaga ostrożnej interpretacji, ponieważ wiąże się także ze zmianami konformacyjnymi badanych białek.
3. W modelach komórkowych jednostki neuronaczyniowej oraz w modelu bariery krew-mózg *in vitro* dendrypleks cechował się szerszym zakresem tolerowanych stężeń niż wolny nośnik i nie powodował trwałego pogorszenia integralności bariery, chociaż obserwowano przejściowe zaburzenia wybranych parametrów przepuszczalności i utrzymujące się cechy stresu mitochondrialnego.
4. Dendrypleks wykazywał korzystniejszy profil hemokompatybilności i biokompatybilności niż wolny nośnik, jednakże poprawa profilu bezpieczeństwa nie oznacza pełnej obojętności biologicznej badanego nanosystemu, ponieważ zaobserwowano stres mitochondrialny, przejściowe zaburzenia przepuszczalności bariery oraz zmiany hemoreologiczne i koagulologiczne.
5. W badaniach *in vivo* wykazano, że kompleksacja siRNA z dendrymerem wydłuża okres jego obecności w układzie krążenia względem wolnego siRNA oraz częściową poprawę wybranych parametrów neurobehawioralnych w modelu mysim.

W świetle uzyskanych wyników cel główny pracy został zrealizowany, natomiast hipotezę badawczą można uznać za potwierdzoną częściowo: przede wszystkim w zakresie otrzymania funkcjonalnego nanosystemu o korzystniejszym profilu bezpieczeństwa po kompleksacji z siRNA oraz wydłużonej ekspozycji układowej, przy zachowaniu ostrożności w odniesieniu do wniosków o skuteczności terapeutycznej w ośrodkowym układzie nerwowym.

Wniosek:

Dendrymer karbokrzemowy G3Si PEG6000 stanowi wysoce obiecujący nośnik do dostarczania terapeutycznego siRNA do ośrodkowego układu nerwowego.

XI. Streszczenie

Terapie oparte na siRNA stanowią obiecującą strategię w leczeniu choroby Alzheimera, jednak ich zastosowanie kliniczne jest ograniczone przez niekorzystny profil farmakokinetyczny oraz selektywność bariery krew-mózg. W ramach niniejszej pracy opracowano nanonośnik siRNA oparty o dendrymer karbokrzemowy, który poddano walidacji z wykorzystaniem hierarchicznej strategii badawczej. Miała ona na celu powiązanie właściwości fizykochemicznych nośnika z jego aktywnością biologiczną przy szczególnym uwzględnieniu ograniczeń wynikających z właściwości bariery krew-mózg.

Charakterystyka biofizyczna i ocena cytotoksyczności pozwoliły wskazać dendrymer G3Si PEG6000 jako optymalny nośnik spośród czterech badanych dendrymerów. Badania interakcji z białkami wykazały szybkie tworzenie się korony białkowej, kształtowanej przez wielowartościowe oddziaływania o entropowym charakterze, którym towarzyszyły zmiany konformacyjne białek osocza. Analiza hemokompatybilności wykazała, że utworzenie kompleksu z siRNA istotnie ograniczało hemolizę oraz poprawiało ogólną zgodność nanosystemu z krwią.

W neuro-naczyniowych modelach komórkowych dendrypleks zwiększał akumulację siRNA w cytoplazmie oraz wykazywał niższą cytotoksyczność w porównaniu z wolnym nośnikiem. W trójkulturowym modelu bariery krew-mózg, odzwierciedlającym środowisko jednostki neuro-naczyniowej, wpływ na integralność bariery zależał od skompleksowania i stężenia, jednak zmiany te miały na ogół charakter przejściowy, a nie trwale destabilizujący. W badaniach *in vivo* dendrypleks wydłużył ogólnoustrojową ekspozycję na siRNA oraz poprawił wyniki uczenia się i pamięci przestrzennej mysiego modelu choroby Alzheimera, podczas gdy wolne siRNA nie wykazało analogicznego efektu.

Uzyskane wyniki wskazują, że dendrypleksy G3Si PEG6000 stanowią wysoce obiecujący nanosystem do dostarczania terapeutycznego RNA do ośrodkowego układu nerwowego. W ujęciu translacyjnym wyniki te stanowią solidny fundament do dalszej optymalizacji terapii ukierunkowanych na chorobę Alzheimera i innych schorzeniach neurodegeneracyjnych.

XII. Abstract

siRNA-based approaches represent a plausible disease-modifying strategy for Alzheimer's disease, but their therapeutic use is restricted by the unfavorable pharmacokinetic profile of naked oligonucleotides and the restrictive properties of the blood–brain barrier. A carbosilane dendrimer–siRNA nanosystem was developed and validated through a hierarchical testing strategy designed to connect synthetic identity with biological performance under blood–brain barrier constraints.

Biophysical and cytotoxicity profiling identified G3Si PEG6000 as the most suitable carrier among four candidate dendrimers. Protein interaction studies demonstrated rapid formation of a biologically relevant corona, with multivalent, predominantly entropy-driven binding accompanied by conformational rearrangements of plasma proteins. Hemocompatibility analyses showed that siRNA complexation markedly reduced hemolysis and improved overall blood tolerance.

In neurovascular cell systems, the dendriplex enhanced intracellular siRNA localization in the cytoplasmic compartment and attenuated damage-associated responses relative to the non-complexed carrier. In tri-culture blood–brain barrier models, barrier effects were formulation- and dose-dependent but generally transient rather than permanently disruptive. *In vivo*, the dendriplex prolonged systemic exposure of siRNA and improved a sensitive spatial learning and memory measure in APOE4 knock-in mice, whereas free siRNA showed no analogous benefit.

These results support G3Si PEG6000 dendriplexes as a suitable platform for further CNS-targeted RNA interference research. Within this translational framework, the present work provides a rigorous basis for further optimization of dendrimer-based siRNA delivery systems for Alzheimer's disease and related CNS indications.

XIII. Literatura

(1) De Waele, L.; Servais, L. Treatment Strategies for Patients with Spinal Muscular Atrophy. *Expert Review of Neurotherapeutics* **2025**, *25* (3), 259–261. https://doi.org/10.1080/14737175.2024.2439486.

(2) Hamad, A. A.; Alkhawaldeh, I. M.; Nashwan, A. J.; Meshref, M.; Imam, Y. Tofersen for SOD1 Amyotrophic Lateral Sclerosis: A Systematic Review and Meta-Analysis. *Neurol Sci* **2025**, *46* (5), 1977–1985. https://doi.org/10.1007/s10072-025-07994-2.

(3) Rafii, M. S.; Aisen, P. S. Amyloid-Lowering Immunotherapies for Alzheimer Disease: Current Status and Future Directions. *Nat Rev Neurol* **2025**, *21* (9), 490–498. https://doi.org/10.1038/s41582-025-01123-5.

(4) Sampaio, C. Huntington Disease – Update on Ongoing Therapeutic Developments and a Look toward the Future. *Parkinsonism & Related Disorders* **2024**, *122*, 106049. https://doi.org/10.1016/j.parkreldis.2024.106049.

(5) Wu, K.-M.; Zhang, Y.; Wang, T.-T.; Wu, J.-Y.; Huang, Y.-Y.; Yuan, P.; Yu, J.-T. Advancing Disease-Modifying Therapies for Parkinson's Disease: Current Strategies and Future Directions. *The Innovation* **2025**, 101112. https://doi.org/10.1016/j.xinn.2025.101112.

(6) Sevigny, J.; Chiao, P.; Bussière, T.; Weinreb, P. H.; Williams, L.; Maier, M.; Dunstan, R.; Salloway, S.; Chen, T.; Ling, Y.; O'Gorman, J.; Qian, F.; Arastu, M.; Li, M.; Chollate, S.; Brennan, M. S.; Quintero-Monzon, O.; Scannevin, R. H.; Arnold, H. M.; Engber, T.; Rhodes, K.; Ferrero, J.; Hang, Y.; Mikulskis, A.; Grimm, J.; Hock, C.; Nitsch, R. M.; Sandrock, A. The Antibody Aducanumab Reduces Aβ Plaques in Alzheimer's Disease. *Nature* **2016**, *537* (7618), 50–56. https://doi.org/10.1038/nature19323.

(7) Pardridge, W. M. Alzheimer's Disease: Future Drug Development and the Blood-Brain Barrier. *Expert Opinion on Investigational Drugs* **2019**, *28* (7), 569–572. https://doi.org/10.1080/13543784.2019.1627325.

(8) Paunovska, K.; Loughrey, D.; Dahlman, J. E. Drug Delivery Systems for RNA Therapeutics. *Nat Rev Genet* **2022**, *23* (5), 265–280. https://doi.org/10.1038/s41576-021-00439-4.

(9) Halliday, M. R.; Rege, S. V.; Ma, Q.; Zhao, Z.; Miller, C. A.; Winkler, E. A.; Zlokovic, B. V. Accelerated Pericyte Degeneration and Blood–Brain Barrier Breakdown in Apolipoprotein E4 Carriers with Alzheimer's Disease. *J Cereb Blood Flow Metab* **2016**, *36* (1), 216–227. https://doi.org/10.1038/jcbfm.2015.44.

(10) Montagne, A.; Nation, D. A.; Sagare, A. P.; Barisano, G.; Sweeney, M. D.; Chakhoyan, A.; Pachicano, M.; Joe, E.; Nelson, A. R.; D'Orazio, L. M.; Buennagel, D. P.; Harrington, M. G.; Benzinger, T. L. S.; Fagan, A. M.; Ringman, J. M.; Schneider, L. S.; Morris, J. C.; Reiman, E. M.; Caselli, R. J.; Chui, H. C.; Tcw, J.; Chen, Y.; Pa, J.; Conti, P. S.; Law, M.; Toga, A. W.; Zlokovic, B. V. APOE4 Leads to Blood–Brain Barrier Dysfunction Predicting Cognitive Decline. *Nature* **2020**, *581* (7806), 71–76. https://doi.org/10.1038/s41586-020-2247-3.

(11) Montagne, A.; Nikolakopoulou, A. M.; Huuskonen, M. T.; Sagare, A. P.; Lawson, E. J.; Lazic, D.; Rege, S. V.; Grond, A.; Zuniga, E.; Barnes, S. R.; Prince, J.; Sagare, M.; Hsu, C.-J.; LaDu, M. J.; Jacobs, R. E.; Zlokovic, B. V. APOE4 Accelerates Advanced-Stage Vascular and Neurodegenerative Disorder in Old Alzheimer's Mice via Cyclophilin A Independently of Amyloid-β. *Nat Aging* **2021**, *1* (6), 506–520. https://doi.org/10.1038/s43587-021-00073-z.

(12) Deane, R.; Sagare, A.; Hamm, K.; Parisi, M.; Lane, S.; Finn, M. B.; Holtzman, D. M.; Zlokovic, B. V. apoE Isoform–Specific Disruption of Amyloid β Peptide Clearance from Mouse Brain. *J. Clin. Invest.* **2008**, *118* (12), 4002–4013. https://doi.org/10.1172/JCI36663.
(13) Choi, G.-W.; Kim, J. H.; Kang, D. W.; Cho, H.-Y. A Journey into siRNA Therapeutics Development: A Focus on Pharmacokinetics and Pharmacodynamics. *European Journal of Pharmaceutical Sciences* **2025**, *205*, 106981. https://doi.org/10.1016/j.ejps.2024.106981.
(14) Abbasi, E.; Aval, S. F.; Akbarzadeh, A.; Milani, M.; Nasrabadi, H. T.; Joo, S. W.; Hanifehpour, Y.; Nejati-Koshki, K.; Pashaei-Asl, R. Dendrimers: Synthesis, Applications, and Properties. *Nanoscale Res Lett* **2014**, *9* (1), 247. https://doi.org/10.1186/1556-276X-9-247.
(15) Martinho, N.; Florindo, H.; Silva, L.; Brocchini, S.; Zloh, M.; Barata, T. Molecular Modeling to Study Dendrimers for Biomedical Applications. *Molecules* **2014**, *19* (12), 20424–20467. https://doi.org/10.3390/molecules191220424.
(16) Kuhn, E.; Srinageshwar, B.; Story, D. T.; Swanson, D.; Sharma, A.; Dunbar, G. L.; Rossignol, J. Delivery of PAMAM Dendrimers and Dendriplexes across Natural Barriers (Blood–Brain Barrier and Placental Barrier) in Healthy Pregnant Mice. *Discover Nano* **2024**, *19* (1), 148. https://doi.org/10.1186/s11671-024-04105-6.
(17) Goldberg, D. S.; Vijayalakshmi, N.; Swaan, P. W.; Ghandehari, H. G3.5 PAMAM Dendrimers Enhance Transepithelial Transport of SN38 While Minimizing Gastrointestinal Toxicity. *Journal of Controlled Release* **2011**, *150* (3), 318–325. https://doi.org/10.1016/j.jconrel.2010.11.022.
(18) Oliveira, J. M.; Salgado, A. J.; Sousa, N.; Mano, J. F.; Reis, R. L. Dendrimers and Derivatives as a Potential Therapeutic Tool in Regenerative Medicine Strategies—A Review. *Progress in Polymer Science* **2010**, *35* (9), 1163–1194. https://doi.org/10.1016/j.progpolymsci.2010.04.006.
(19) D'Emanuele, A.; Jevprasesphant, R.; Penny, J.; Attwood, D. The Use of a Dendrimer-Propranolol Prodrug to Bypass Efflux Transporters and Enhance Oral Bioavailability. *Journal of Controlled Release* **2004**, *95* (3), 447–453. https://doi.org/10.1016/j.jconrel.2003.12.006.
(20) Mehta, P.; Kadam, S.; Pawar, A.; Bothiraja, C. Dendrimers for Pulmonary Delivery: Current Perspectives and Future Challenges. *New J. Chem.* **2019**, *43* (22), 8396–8409. https://doi.org/10.1039/C9NJ01591D.
(21) Manikkath, J.; Hegde, A. R.; Kalthur, G.; Parekh, H. S.; Mutalik, S. Influence of Peptide Dendrimers and Sonophoresis on the Transdermal Delivery of Ketoprofen. *International Journal of Pharmaceutics* **2017**, *521* (1–2), 110–119. https://doi.org/10.1016/j.ijpharm.2017.02.002.
(22) Monopoli, M. P.; Åberg, C.; Salvati, A.; Dawson, K. A. Biomolecular Coronas Provide the Biological Identity of Nanosized Materials. *Nature Nanotech* **2012**, *7* (12), 779–786. https://doi.org/10.1038/nnano.2012.207.
(23) Pearson, R. M.; Juettner, V. V.; Hong, S. Biomolecular Corona on Nanoparticles: A Survey of Recent Literature and Its Implications in Targeted Drug Delivery. *Front. Chem.* **2014**, *2*. https://doi.org/10.3389/fchem.2014.00108.
(24) Ghosh, G.; Panicker, L. Protein–Nanoparticle Interactions and a New Insight. *Soft Matter* **2021**, *17* (14), 3855–3875. https://doi.org/10.1039/D0SM02050H.
(25) Abbott, N. J.; Patabendige, A. A. K.; Dolman, D. E. M.; Yusof, S. R.; Begley, D. J. Structure and Function of the Blood–Brain Barrier. *Neurobiology of Disease* **2010**, *37* (1), 13–25. https://doi.org/10.1016/j.nbd.2009.07.030.

(26) Pardridge, W. M. BLOOD-BRAIN BARRIER DRUG TARGETING: THE FUTURE OF BRAIN DRUG DEVELOPMENT. *Molecular Interventions* **2003**, *3* (2), 90–105. https://doi.org/10.1124/mi.3.2.90.
(27) Sweeney, M. D.; Zhao, Z.; Montagne, A.; Nelson, A. R.; Zlokovic, B. V. Blood-Brain Barrier: From Physiology to Disease and Back. *Physiological Reviews* **2019**, *99* (1), 21–78. https://doi.org/10.1152/physrev.00050.2017.
(28) Bonkowski, D.; Katyshev, V.; Balabanov, R. D.; Borisov, A.; Dore-Duffy, P. The CNS Microvascular Pericyte: Pericyte-Astrocyte Crosstalk in the Regulation of Tissue Survival. *Fluids Barriers CNS* **2011**, *8* (1), 8. https://doi.org/10.1186/2045-8118-8-8.
(29) Vanlandewijck, M.; He, L.; Mäe, M. A.; Andrae, J.; Ando, K.; Del Gaudio, F.; Nahar, K.; Lebouvier, T.; Laviña, B.; Gouveia, L.; Sun, Y.; Raschperger, E.; Räsänen, M.; Zarb, Y.; Mochizuki, N.; Keller, A.; Lendahl, U.; Betsholtz, C. A Molecular Atlas of Cell Types and Zonation in the Brain Vasculature. *Nature* **2018**, *554* (7693), 475–480. https://doi.org/10.1038/nature25739.
(30) Schaeffer, S.; Iadecola, C. Revisiting the Neurovascular Unit. *Nat Neurosci* **2021**, *24* (9), 1198–1209. https://doi.org/10.1038/s41593-021-00904-7.

XIV. Aktywność naukowa i organizacyjna

Prace wchodzące w skład rozprawy doktorskiej:

1. **Zawadzki S.**, Martín-Serrano Á., Okła E., Kędzierska M., Garcia-Gallego S., López P.O., de la Mata F.J., Michlewska S., Makowski T., Ionov M., Pędziwiatr-Werbicka E., Bryszewska M., Miłowska K., **Synthesis and biophysical evaluation of carbosilane dendrimers as therapeutic siRNA carriers.** Sci. Rep. 2024, 14, 1615. https://doi.org/10.1038/s41598-024-51238-w
2. **Zawadzki S.**, Okła E., Michlewska S., Makowski T., Buczkowski A., O. López P., de la Mata F.J., Ionov M., Bryszewska M., Miłowska K., **Structural and conformational rearrangements of human serum albumin, transferrin, and blood plasma induced by carbosilane dendrimer therapeutic delivery system.** Sci. Rep. 2025, 15, 39650. https://doi.org/10.1038/s41598-025-23355-7
3. **Zawadzki S.**, Suty S., Okła E., Ortega López P., de la Mata F.J., Waczulikova I., Ionov M., Bryszewska M., Miłowska K., **Hemocompatibility of Carbosilane Dendrimers as a Therapeutic siRNA Delivery System across Blood−Brain Barrier.** ACS Appl. Mater. Interfaces 2026, 18, 11671−11686 https://doi.org/10.1021/acsami.5c12952

Manuskrypty prac doświadczalnych przesłane do czasopisma:

4. **Zawadzki S.**, Okła E., Ortega López P., de la Mata F.J., Ionov M., Jansons J., Skrastiņa D., Kreišmane M., Bryszewska M., Miłowska K. **Multilevel Assessment of Carbosilane Dendrimer–siRNA Nanoplatform: Cellular Compatibility, Blood–Brain Barrier Model Integrity, and Murine Model Biodistribution.** 2026, wysłany do czasopisma ACS Appl. Mater. Interfaces.
5. **Zawadzki S.**, Okła E., Michlewska S., Bednarek R., Jansons J., Skrastiņa D., Kreišmane M., Piļipenko V., Jansone B., Ortega López P., de la Mata F.J., Ionov M., Bryszewska M., Miłowska K. **Tiered Evaluation of Carbosilane–siRNA Nanoplatform from Single-Cell Biocompatibility to Blood-Brain Barrier Model Dynamics, and Murine Alzheimer Model Behavior Assessment.** 2026, wysłany do czasopisma ACS Appl. Mater. Interfaces.

Wykaz pozostałych prac:

1. Juszczak K., Kubicka A., Kitel R., Dzido G., Łabieniec-Watała M., **Zawadzki S.**, Marczak A., Walczak K., Matczak K., Tomczyk M. D. **Hexokinase 2 Inhibition and Biological Effects of BNBZ and Its Derivatives: The Influence of the Number and Arrangement of Hydroxyl Groups** Int. J. Mol. Sci; 2022, 23, 2616, doi: 10.3390/ijms23052616.
2. Okła E., Michlewska S., Buczkowski A., **Zawadzki S.**, Miłowska K., Sánchez-Nieves J., Gómez R., de la Mata F. J., Bryszewska M., Błasiak J., Ionov M. **Pegylated gold nanoparticles interact with lipid bilayer and human serum albumin and transferrin.** Sci. Rep.; 2024, 14, 24408, doi: 10.1038/s41598-024-74898-0
3. Okła E., Hołota M., Michlewska S., **Zawadzki S.**, Miłowska K., Sánchez-Nieves J., Gómez R., de la Mata F. J., Bryszewska M., Ionov M. **Crossing Barriers: PEGylated Gold Nanoparticles as Promising Delivery Vehicles for siRNA Delivery in Alzheimer's Disease.** Biomedicines; 2025, 13, 2108, doi: 10.3390/biomedicines13092108

Łączny IF wszystkich opublikowanych prac: 31,8 (860 ptk. MNiSW)

Komunikaty zjazdowe międzynarodowe:

1. **S. Zawadzki**, K. Miłowska, *Influence of Dendrimers and Their Complexes with siRNA on Cells*, XVIII Congress of the Polish Biophysical Society (PTBF), 6 – 9.09.2022, Warszawa, Polska
2. **S. Zawadzki**, K. Miłowska, *Physicochemical Properties of Dendrimers and siRNA Complexes*, XVIII Congress of the Polish Biophysical Society (PTBF), 6 – 9.09.2022, Warszawa, Polska
3. **S. Zawadzki**, K. Miłowska, *Dendrimers as Gene Delivery System*, IEEE 12th International Conference "Nanomaterials: Applications & Properties", 11 – 16.09.2022, Kraków, Poland
4. **S. Zawadzki**, K. Miłowska, *Effect of Dendrimer-Based Gene Delivery System on Cells*, 12th International Congress of Societas Humboldtiana Polonorum, 30.06 – 2.07.2023, Łódz, Polska
5. **S. Zawadzki**, K. Miłowska, *Dendrimer-Mediated Delivery of Therapeutics Across the Blood Brain Barrier*, EMBO-Neuro 2023 - Cell Biology of the nervous system, 8 – 11.05.2023, Heraklion, Grecja
6. **S. Zawadzki**, K. Miłowska, *Nanotechnology in Neurodegenerative Disease Treatment: Delivery of Therapeutics Across the Blood-Brain Barrier*, Imaging life: the future, 17 – 19.10.2023, Montpellier, France
7. K. Miłowska, **S. Zawadzki**, *Enhancing Therapeutic Delivery to The Brain: Dendrimer-Mediated Transport and Its Effect on Oxidative Stress in Neurodegenerative Diseases*, The 25th International Conference on Redox Medicine, 21 – 23.06.2023, Paryż, Francja
8. E. Okła, S. Michlewska, M. Hołota, **S. Zawadzki**, M. Bryszewska, M. Ionov, *Gold Nanoparticles as a Delivery System of Therapeutic siRNA into Human Brain Endothelial Cells: In Vitro Studies*, 47th FEBS Congress 2023, 8 – 12.07.2023, Tours, Francja
9. **S. Zawadzki**, Š. Sutý, I. Waczulikowá, K. Miłowska, *Hemocompatibility of G3Si PEG6000 Dendrimer and Its Dendriplex: Effects on Erythrocytes and Hemorheology*, Biogene Amines and Related Biologically Active Compounds: XIXth Conference of the Polish Histamine Research Society, 24 – 26.10.2024, Łódz, Polska

10. **S. Zawadzki**, Š. Sutý, I. Waczulikowá, K. Miłowska, *Impact of Carbosilane Dendrimers and Their Complexes with siRNA Directed Against Alzheimer's Disease on In Vitro Blood–Brain Barrier Model and Blood Flow*, 48th FEBS Congress – Mining biochemistry for human health and well-being, 29.06 – 3.07.2024, Mediolan, Włochy
11. K. Krawczyk, **S. Zawadzki**, A. Macieja, S. Michlewska, M.Tynecka, J. Wieczfińska, M. Kowalewicz-Kulbat, *The halophilic archaea, Halorhabdus rudnickae, positively enhance the barrier integrity of the human epithelial cell line Calu-3*, World Immune Regulation Meeting XIX, 12-15.03.2025, Davos, Szwajcaria

Komunikaty zjazdowe krajowe:

1. A. Gabryanczyk, A. Churska, K. Matczak, **S. Zawadzki**, *Ocena Stresu Oksydacyjnego Generowanego w Komórkach HMEC-1 Poddanych Działaniu Liposomalnych Form Cytostatyków – Analiza Zmian Całkowitego Potencjału Antykosydacyjnych Metodą Spektrofotemtryczną z TPTZ*, IV Studencka Konferencja Biologii Medycznej BioFuzje, 24 – 26.05.2019, Warszawa, Polska
2. A. Churska, A. Gabryanczyk, K. Matczak, **S. Zawadzki**, *Rola Zależności Pomiędzy Autofagią i Apoptozą w Komórkach Ludzkiego Raka Piersi*, V Ogólnopolska Konferencja Doktorantów Nauk o Życiu BioOpen, 30 – 31.05.2019, Łódź, Polska
3. A. Gabryanczyk, A. Churska, K. Matczak, **S. Zawadzki**, *Ocena Stresu Oksydacyjnego Generowanego w Komórkach Śródbłonka Mikrowaskularnego HMEC-1 Poddanych Działaniu Liposomalnych Form Cytostatyków – Wyniki Analizy RFT i RFA*, V Ogólnopolska Konferencja Doktorantów Nauk o Życiu BioOpen, 30 – 31.05.2019, Łódź, Polska
4. **S. Zawadzki**, K. Matczak, *Potencjalne Nowe Inhibitory Heksokinazy II*, XII Sesja Magistrantów i Doktorantów Łódzkiego Środowiska Chemików, 17.06.2021, Łódź, Polska
5. **S. Zawadzki**, K. Miłowska, *Zastosowanie Dendrymerów Jako Nośników Związków Biologicznie Czynnych*, VIII Ogólnopolskie Sympozjum Biomedyczne ESKULAP, 4.12.2021, online
6. **S. Zawadzki**, M. Kędzierska, K. Miłowska, *Wpływ Dendrymerów G3Si oraz Ich Kompleksów z siRNA na Komórki Śródbłonka Bariery Krew-Mózg i Erytrocyty Ludzkie,* VII Ogólnopolska Konferencja Doktorantów Nauk o Życiu BioOpen, 7 – 8.04.2022, online

7. **S. Zawadzki**, K. Miłowska, *Badanie Oddziaływań Dendrymerów Karbokrzemowych z siRNA: Kompleksowe Podejście z Wykorzystaniem Metod Fizykochemicznych*, VIII Ogólnopolska Konferencja Doktorantów Nauk o Życiu, 13 – 14.04.2022, online
8. K. Krawczyk, **S. Zawadzki**, A. Macieja, S. Michlewska, M.Tynecka, J. Wieczfińska, M. Kowalewicz-Kulbat, *Archeony halofilne, Halorhabdus rudnickae, wzmacniają integralność bariery nabłonkowej w modelu linii komórkowej Calu-3*, Alergia Astma Immunologia Kliniczna, 5 – 7.06.2025, Łódź, Polska

Projekty badawcze

1. Prowadzenie badań w ramach projektu M-ERA NET 2 pt.: „*Transfer nanocząsteczek przez barierę śródbłonkową*” o akronimie NanoTENDO (UMO-2018/30/Z/NZ1/00911)
2. Prowadzenie badań w ramach stażu naukowego NAWA współpraca Polska–Słowacja pt.: „*Dendrymery fosforowe jako potencjalne czynniki wspomagające proces gojenia ran*” (nr BPN/BSK/2021/1/00053/U/00001)

Staże naukowe

1. Staż naukowy w Zakładzie Chemii Organicznej i Nieorganicznej, Wydział Farmacji Uniwersytetu w Alcalá de Henares, Hiszpania. Wyjazd w ramach międzynarodowego projektu M-ERA.NET 2019-2023 „*Nanoparticle transfer through endothelial barrier*" UMO- 2018/30/Z/NZ1/00911 finansowanego przez Narodowe Centrum Nauki oraz europejski program Horizon 2020 (14.02 – 14.03.2022 r.).
2. Staż naukowy w Katedrze Fizyki Jądrowej i Biofizyki, Wydział Matematyki i Fizyki Uniwersytet Komeńskiego w Bratysławie, Słowacja. Wyjazd w ramach programu wymiany bilateralnej między Rzeczpospolitą Polską a Republiką Słowacką, „*Dendrymery fosforowe jako potencjalne czynniki wspomagające proces gojenia ran*” Nr.: BPN/BSK/2021/1/00053/U/00001 finansowanego przez Narodową Agencję Wymiany Akademickiej (20.9 – 02.10.22).
3. Staż naukowy w Katedrze Fizyki Jądrowej i Biofizyki, Wydział Matematyki i Fizyki Uniwersytet Komeńskiego w Bratysławie, Słowacja. Wyjazd w ramach programu wymiany bilateralnej między Rzeczpospolitą Polską a Republiką Słowacką, „*Dendrymery fosforowe jako potencjalne czynniki wspomagające proces gojenia ran*” Nr.: BPN/BSK/2021/1/00053/U/00001 finansowanego przez Narodową Agencję Wymiany Akademickiej (23.11 – 3.12.23).

Szkolenia, warsztaty i kursy

1. Szkolenie Narodowe Centrum Nauki, „*Szkolenie dla wnioskodawców*” 19.11.2021
2. Warsztaty European Molecular Biology Organization (EMBO), “*Cell biology of the nervous system: Long-term resilience and vulnerability*” 8 – 11.05.2023
3. Kurs Twinalt, „*Course on in silico methods in the safety assessment of chemicals*” 21 – 22.06.2023
4. Kurs Centrum Medyczne Kształcenia Podyplomowego w Warszawie, „*Immunocytochemia*” 11 – 13.12.2024

Uzyskane stypendia wyjazdowe:

1. Stypendium wyjazdowe PROM 2023 – NAWA „Międzynarodowa wymiana stypendialna doktorantów i kadry akademickiej” w warsztatach „*Cell biology of the nervous system: Long-term resilience and vulnerability*", 8 – 11.05.2023, Heraklion, Grecja
2. Stypendium wyjazdowe Federation of European Biochemical Societies „48th FEBS Congress – Bursaries”. Stypendium na sfinansowanie udziału w konferencji 48th FEBS Congress, 29.06 – 03.07.2024, Mediolan, Włochy

Działalność organizacyjna i promocyjna

1. Warsztaty dla uczestników Dziecięcej Akademii Młodych Twórców, 12.01.2022
2. Warsztaty dla uczniów Szkoły Podstawowej nr 199 w Łodzi w ramach Festiwalu Nauki i Techniki, 13.05.2022
3. Wywiad dla portalu Biotechnologia.pl, 26.04.2022
4. Prowadzenie zajęć w ramach Instytutu Kreatywnej Biologii, 18.11.2022; 24.02.2023; 21.04.2023; 16.06.2023
5. Prowadzenie zajęć w ramach Nocy Biologów, 13.01.2023
6. Prowadzenie zajęć w ramach Nocy Biologów, 10.01.2025
7. Prowadzenie zajęć w ramach Instytutu Kreatywnej Biologii, 17.01; 07.02; 14.03.2025
8. Zaangażowanie w opiekę nad magistrantami – zaznajomienie studentów z technikami hodowli komórkowych i nadzór nad pracą.

9. Opieka merytoryczna i organizacyjna nad gośćmi Katedry Biofizyki Ogólnej odwiedzającymi jednostkę w ramach współprac i staży naukowych (mgr Oscar Barrios-Gumiel oraz mgr Samuel Takvor Mena z Uniwersytetu w Alcalá de Henares, Hiszpania, 2022; mgr Patrick Mydla, Juraj Jacko z Comenius University w Bratysławie, Słowacja, 2022; dr Šimon Sutý, prof. Iveta Waczulikowá, dr Katarina Čechová z Comenius University w Bratysławie, Słowacja, 2023).
10. Zaangażowanie w prace organizacyjne w Katedrze Biofizyki Ogólnej – zamówienie serwisu do aparatury badawczej i realizacja zamówień odczynników laboratoryjnych.
11. Organizacja demonstracji aparatury badawczej – organizacja i koordynacja demonstracji urządzeń LiteScope™ AFM-in-SEM, xCELLigence RTCA eSight, MAGPIX® System oraz FIDA 1, oferowanych przez firmy Omixys Sp. z o.o., BioTech a.s., Accela s.r.o., Technolutions Sp. z o.o. oraz Merck Life Science Sp. z o.o., obejmujący przygotowanie organizacyjne wydarzenia, przygotowanie infrastruktury badawczej, kontakt z przedstawicielami producentów, koordynację harmonogramu prezentacji oraz wsparcie merytoryczne uczestników w zakresie możliwości wdrożenia aparatury do prac badawczych prowadzonych w Katedrze Biofizyki Ogólnej Uniwersytetu Łódzkiego.
12. Nawiązywanie współpracy i organizacja badań między jednostkami badawczymi – zainicjowanie oraz koordynacja współpracy z Zakładem Cytobiologii i Proteomiki Wydziału Nauk o Zdrowiu Uniwersytetu Medycznego w Łodzi; Uniwersyteckim Laboratorium Naukowym CoreLab Uniwersytetu Medycznego w Łodzi; Centrum Badań Molekularnych i Makromolekularnych (CBMiM) Polskiej Akademii Nauk obejmującej realizację wspólnych badań, organizację spotkań oraz realizację publikacji naukowych.

XV. Prace wchodzące w skład rozprawy doktorskiej

scientific reports

Check for updates

OPEN

Synthesis and biophysical evaluation of carbosilane dendrimers as therapeutic siRNA carriers

Serafin Zawadzki[1,2]✉, Ángela Martín-Serrano[3], Elżbieta Okła[1], Marta Kędzierska[1], Sandra Garcia-Gallego[3,4,5], Paula O. López[3,4,5], Francisco J. de la Mata[3,4,5], Sylwia Michlewska[6], Tomasz Makowski[7], Maksim Ionov[1,8], Elżbieta Pędziwiatr-Werbicka[1], Maria Bryszewska[1] & Katarzyna Miłowska[1]

Gene therapy presents an innovative approach to the treatment of previously incurable diseases. The advancement of research in the field of nanotechnology has the potential to overcome the current limitations and challenges of conventional therapy methods, and therefore to unlocking the full potential of dendrimers for use in the gene therapy of neurodegenerative disorders. The blood–brain barrier (BBB) poses a significant challenge when delivering therapeutic agents to the central nervous system. In this study, we investigated the biophysical properties of dendrimers and their complexes with siRNA directed against the apolipoprotein E (APOE) gene to identify an appropriate nanocarrier capable of safely delivering the cargo across the BBB. Our study yielded valuable insights into the complexation process, stability over time, the mechanisms of interaction, the influence of dendrimers on the oligonucleotide's spatial structure, and the potential cytotoxic effects on human cerebral microvascular endothelium cells. Based on our findings, we identified that the dendrimer G3Si PEG6000 was an optimal candidate for further research, potentially serving as a nanocarrier capable of safely delivering therapeutic agents across the BBB for the treatment of neurodegenerative disorders.

It was nearly a century ago when the British bacteriologist Griffith described the process of bacterial transformation and almost 5 decades later, Friedmann and Roblin- the precursors of modern genomics technology, hypothesized the idea of delivering an exogenous gene copy for the treatment of genetically inherited diseases[1,2]. Today, gene therapy provides curative alternatives for disorders that were previously untreatable. Most modern, conventional therapies target proteins with the aim of symptomatic relief, but do not address underlying pathologies. Employing nucleic acids may modify cell gene expression obtaining therapeutic effects for the treatment of many diseases such as cancers, cardiovascular disorders, infectious diseases, ocular, inflammatory diseases and neurological pathologies[3].

Gene therapy was originally defined to be the use of DNA in the treatment of various illnesses[4]. As science and technology progresses, more strategies have emerged which now allow cDNA, rDNA, mRNA, ASO, miRNA, siRNA and restriction enzymes to be used as potential medicinal agents[5]. The strategies utilizing these listed medical agents may be divided generally into: gene correction (replacement or repair of a malfunctioning gene), augmentation (introduction of a functional version of a mutant), inactivation (silencing the expression of an

[1]Department of General Biophysics, Faculty of Biology and Environmental Protection, University of Lodz, 141/143 Pomorska St., 90-236 Lodz, Poland. [2]BioMedChem Doctoral School of the University of Lodz and Lodz Institutes of the Polish Academy of Sciences, 21/23 Matejki St., 90-237 Lodz, Poland. [3]Department of Organic and Inorganic Chemistry, IQAR, University of Alcalá, 28805 Madrid, Spain. [4]Networking Research Center on Bioengineering, Biomaterials and Nanomedicine (CIBER-BBN), 28029 Madrid, Spain. [5]Ramón y Cajal Health Research Institute (IRYCIS), 28034 Madrid, Spain. [6]Laboratory of Microscopic Imaging and Specialized Biological Techniques, Faculty of Biology and Environmental Protection, University of Lodz, Banacha 12/16, 90-237 Lodz, Poland. [7]Centre of Molecular and Macromolecular Studies, Polish Academy of Sciences, Sienkiewicza 112, 90-363 Lodz, Poland. [8]Faculty of Medicine, Collegium Medicum, Mazovian Academy in Plock, 2 Dabrowskiego Sq, 09-402 Plock, Poland. ✉email: serafin.zawadzki@edu.uni.lodz.pl

abnormal gene) and suicide gene therapy (implementation of a gene to a cancer cell that expresses an enzyme that can convert pro-drugs into cytotoxic agents)[6].

To achieve the desired therapeutic result an extraordinary engineering challenge must be solved. Since naked nucleic acid implementations are largely inefficient for their limited resilience to enzymatic activity, intrinsic stability, and inability to penetrate lipid bilayers, it is necessary to design an effective delivery vector[7]. Attaining successful gene functionality requires the vector to transport and unload the delivered therapeutics into target cells efficiently while not causing side effects. It must prevent cargo degradation and clearance, evade immune detection and prevent nonspecific interactions. Moreover, the vectors must have large-scale production and commercialization properties. The intended effect can be achieved by both viral vectors and non-viral vectors. Selecting the appropriate vector depends on the duration of expression of the transported material, its size, as well as the intended destination[8]. Both viral and non-viral vectors have been used in clinical trials and have unique benefits. Although viruses have evolved to cross multiple anatomical barriers and efficiently transfer their genomes to mammalian cells, their utilization in gene therapy is also associated with several drawbacks. Viral vectors exhibit intrinsic disadvantages, such as high immunogenicity, that led to the inflammatory reactions that caused the first gene therapy-related fatality due to treatment with an adenovirus vector[9]. Another significant detrimental effect concerning the usage of viral vectors is their potential carcinogenetic effect, low specificity, low packaging capacity and high production cost[8,10].

These limitations have prompted researchers to look for new strategies for effective and safe transgene carriers. There is little to no doubt that non-viral vectors offer a significantly safer approach, including the decreased ability to undergo insertional mutagenesis, a lower pathogenicity and immunogenicity[11,12]. Additionally, they provide a variety of possible benefits, such as the ease of production, lower cost, higher stability and fewer restrictions on vector size[12]. However, initially, non-viral nanocarriers appeared to be less effective than viral approaches, but with subsequent developments they have increased their gene delivery efficiency.

Possible gene nanocarriers include many types of nanoparticles such as inorganic or metal nanoparticles, quantum dots, liposomes, micelles and dendrimers. Among these nanosystems, dendrimers have emerged as promising synthetic vectors since their first application as transfection agents[13]. Carbosilane dendrimers achieve good gene transfection efficiency in vitro, reaching values as high as the lentiviruses[14]. Several factors set dendrimers apart from other polymers, dendrimers being radially symmetrical nanoparticles with well-defined, homogeneous and monodisperse structures. Unlike stochastic polymers, dendrimers are produced methodically step-by-step. Their synthesis process controls their architecture and therefore their properties, such as shape, size, charge and solubility. Dendrimers consist of a symmetrical core from which radiating monomer units grow, forming branches known as "dendrons". The repeated branching cycle is called a generation. Dendrimers are composed of inner and outer shells with many functional groups responsible for their high solubility and reactivity. This design by encapsulation, complexation or conjugation, allows dendrimers to carry different agents such as drug molecules, genetic material, targeting agents and dyes. Combining dendrimers with drugs or nucleic acids can improve treatment outcomes by increasing the solubility of the therapeutics, modifying pharmacokinetics and improving bioavailability. These features permit the delivery and application of medical agents that otherwise would not have a chance to be utilized[15,16].

The dendrimer–nucleic acid complexes are called dendriplexes and are formed by electrostatic interactions. The interaction highly depends on the protonation of the dendrimer cationic groups. The strong interaction between the highly charged groups of the dendrimer and the gene causes wrapping of the DNA around the dendrimer, resulting in nucleosome-like structures[17].

Positively charged dendriplexes increase enzymatic resistance and enhance cellular uptake, thereby increasing their transport into cells. Formation of colloidally stable, positively charged dendriplexes occurs when an excess of dendrimer exists in its non-complexed form. The ratio of nucleic acid to the nanoparticle is a crucial parameter in the formation of the complex. The free dendrimers also play a role in the internalization of the dendriplexes. Free dendrimers can significantly affect transfection efficiency and toxicity as the free polymer causes transient pore formation in the cell membrane, increasing permeability but also leading to cytotoxic side effects by disrupting the cellular membrane via nanohole formation, membrane thinning and erosion[18–20].

Given their adjustable characteristics impacting pharmacokinetics, bioavailability, immunogenicity, toxicity, and transfection efficiency, dendrimers emerge as promising agents for gene delivery. Despite these promising features, a significant knowledge gap exists regarding the impact of dendrimer exposure in delivering biologically active compounds to the brain. In light of this, it becomes imperative to systematically design and investigate dendrimer nanocarriers delivering therapeutics across the most formidable barrier in the human body—the blood–brain barrier (BBB). Our study's objective is to evaluate the biophysical properties of dendrimers and their complexes with siRNA for the selection of a plausible candidate for the siRNA nanocarrier through the model of the blood–brain barrier. For this purpose, we assessed whether 4 carbosilane dendrimers could form complexes with siRNA directed against the apolipoprotein E (APOE) gene. The results of our investigation provided valuable insights into the complexation process, stability, the mechanisms of interaction, the influence of tested dendrimers on the oligonucleotide's spatial structure and possible cytotoxic effects.

siRNA directed against the APOE4 gene was selected for this study as the literature data indicates APOE4 as a factor in many disorders observed in Alzheimer's disease, including disturbance of insulin signalling pathways in the brain, abnormal distribution of cholesterol and fatty acids, reduction of the integrity of the BBB and a decrease in glucose uptake by the brain[21].

Material and methods

Dendrimers

The 2 types carbosilane dendrimers were synthesized in the Department of Organic and Inorganic Chemistry, University of Alcalá, Madrid, Spain:

1. Dendrimer with a silicon atom core, surface tertiary ammonium groups and polyethylene glycol (PEG) (one; 6000) -G3Si
2. Dendrimers with phloroglucinol core, surface tertiary ammonium groups (third or fourth generation) and PEG (one; 2000 or 6000)—G3O3 and G4O3.

Dendrimers are presented in Fig. 1 and Table 1.

The choice of carbosilane as the dendrimer skeleton for our investigation stems from its distinctive attributes, characterized by low polarity and the high energy inherent in the C–Si bond. This structural framework confers heightened hydrophobicity relative to alternative dendrimer systems. The functionalization process applied to these dendrimers is executed in a statistically controlled manner, strategically introducing a singular polyethylene glycol (PEG) chain per dendritic molecule. This deliberate modification serves a dual purpose in our design strategy. Firstly, the inclusion of PEG chains is intended to mitigate potential toxicity associated with cationic charge derived from quaternary amines functioning as exterior terminal groups, enhancing the overall

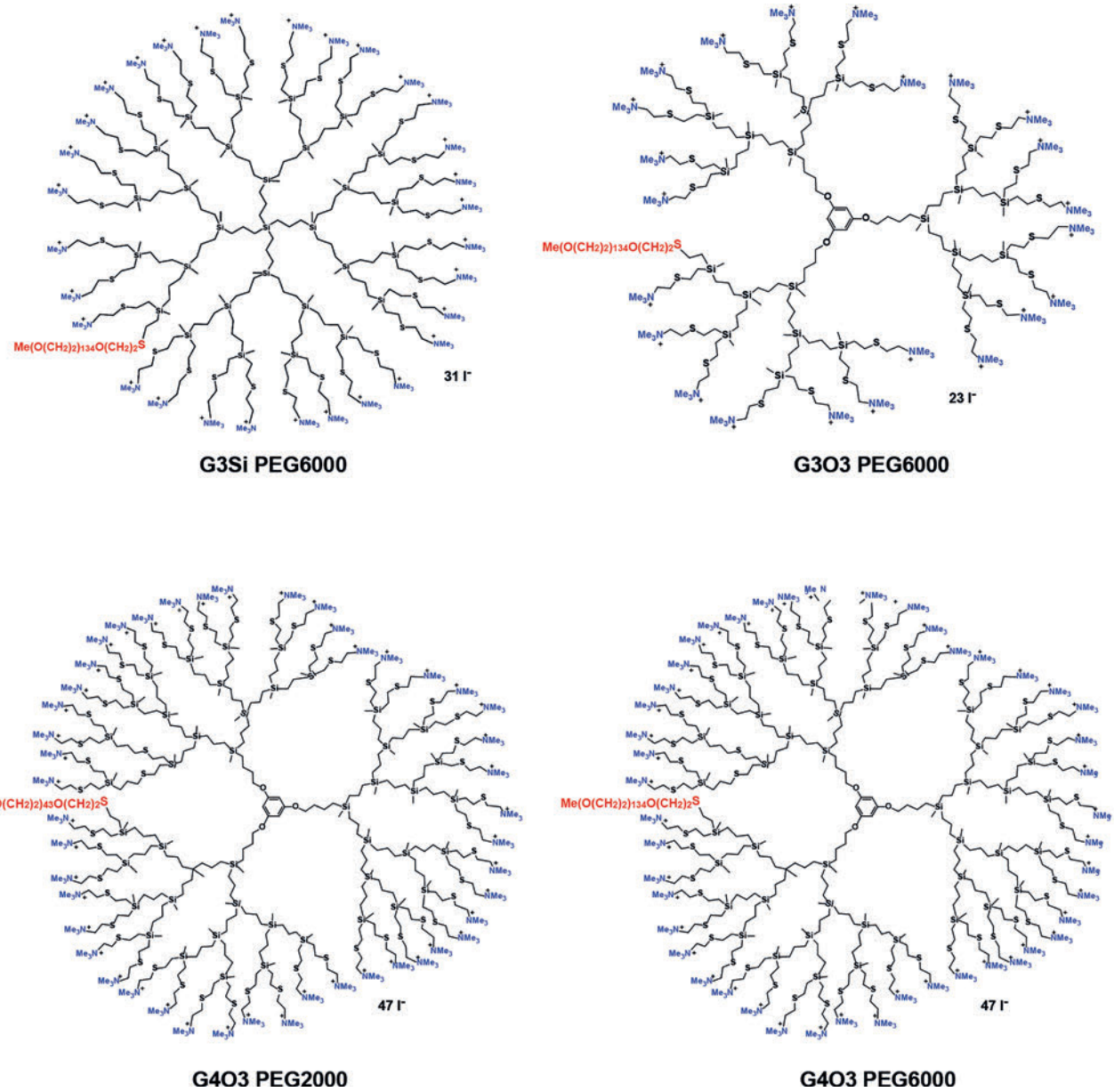


Figure 1. Structures of studied dendrimers.

Dendrimer	Abbreviation	Chemical formula	MW (g/mol)
G3Si(PEG6000)$(NMe_3^+)_{31}$	G3Si PEG6000	$C_{601}H_{1324}I_{30}N_{31}O_{135}S_{32}Si_{29}$	16,794.81
G3O3(PEG6000)$(NMe_3^+)_{23}$	G3O3 PEG6000	$C_{527}H_{1136}I_{23}N_{23}O_{138}S_{24}Si_{21}$	14,285.12
G4O3(PEG2000)$(NMe_3^+)_{47}$	G4O3 PEG2000	$C_{609}H_{1393}I_{47}N_{47}O_{47}S_{50}Si_{44}$	18,932.37
G4O3(PEG6000)$(NMe_3^+)_{47}$	G4O3 PEG6000	$C_{790}H_{1755}I_{47}N_{47}O_{138}S_{50}Si_{44}$	22,927.17

Table 1. Chemical formula and molecular mass of the dendrimers.

biocompatibility of the delivery system. Secondly, the modulation of the dendrimer's surface with PEG chains is anticipated to exert a nuanced influence on the strength of its electrostatic interactions with biomolecules such as serum proteins and prolong retention time in the circulatory system.

G_nYV_m
Precursor dendrimers with vinyl groups at the periphery and with a silicon (G_nSiV_m) or phloroglucinol ($G_nO_3V_m$) core were synthesized as previously described in the literature[22,23].

$G_nY(SPEG)(SNMe_2HCl)_{m-1}$
Corresponding precursor dendrimer G_nYV_m (0.01 mmol), corresponding thiolated PEG (0.01 mmol) and 2,2-dimethoxy-2-phenylacetophenone (DMPA) (0.001 mmol) were dissolved in a 1:2 THF–methanol as solvent. After purging with argon for deoxygenation, the reaction mixture was irradiated for 1 h. After PEG incorporation, the rest of vinyl groups on the precursor dendrimers were functionalised as follows. 2-(dimethylamino) ethanethiol hydrochloride (0.00525·m-1 mmol) and DMPA (0.001 mmol) were added, the solution was purged with argon and irradiated for 1 h. This step was performed twice. The absence of vinyl groups after hydrothiolation was confirmed by ^{1}H-NMR.

$G_nY(SPEG)(SNMe_2)_{m-1}$
Na_2CO_3 (0.01·m^{-1} mmol) was added to the reaction mixture containing corresponding $G_nY(SPEG)(SNMe_2HCl)_{m-1}$ dendrimer .The mixture was left to react overnight at room temperature. After complete neutralization was confirmed by ^{1}H-NMR, the solvents were eliminated by rotaevaporation. Then THF was added and the solution was filtered to remove formed salts and DMPA.

$G_nY(SPEG)(SNMe_3I)_{m-1}$
Quaternization was performed by adding MeI (0.012·m mmol) to $G_nY(SPEG)(SNMe_2)_{m-1}$ solution in THF and left to react overnight at room temperature. Solvent and the excess of MeI were evaporated under reduced pressure. The final quaternized compounds were dissolved in water and purified by dialysis to remove excess of free thiol.

siRNA
The following non-fluorescent or FITC-labelled siRNA was used in the present study (Dharmacon Inc, Lafayette, CO, USA):

Sense: 5′-GAUUACCUGCGCUGGGUGCUU.
Antisense: 5′-P GCACCCAGCGCAGGUAAUCUU.

Other reagents
The HBEC-5i cell line derived from human cerebral microvascular endothelium (ATCC® CRL3245™) was purchased from American Type Culture Collection ATCC® (Manassas, VA, USA). DMEM-F12 (Dulbecco's Modified Eagle Medium-F12) medium supplemented with stable Glutamine and 15 mM Hepes, along with Fetal bovine serum (FBS), were obtained from Biowest, Nuaillé, France. Sigma-Aldrich (Saint Louis, MO, USA) supplied Phosphate buffered saline (PBS) tablets, 1% Penicillin–Streptomycin, Endothelial cell growth supplement (ECGS) sourced from bovine neural tissue, and trypsin. Avantor (Radnor, PA, USA) supplied Dimethyl sulfoxide (DMSO) and 3-(4,5-2-yl)-2-5-diphenyl tetrazolium bromide (MTT). Maximus, (Łódź, Poland) provided Agarose, while Biotium, Inc. (Fremont, CA, USA) supplied GelRed stain. Other basic chemical reagents (sodium dihydrogen phosphate, disodium hydrogen phosphate) were obtained from the local supplier, Chempur (Piekary Śląskie, Poland). These chemicals were of analytical grade, and solutions were prepared using water purified using the Mili-Q system.

Hydrodynamic diameter and zeta potential
The hydrodynamic diameter and zeta potential of the dendrimers and their complexes with siRNA were measured using Zetasizer Nano ZS, Malvern Instruments (UK). The dendrimers and dendriplexes were prepared in distilled water at room temperature. Increasing concentrations of the dendrimer in the range of 0.5–20 µM were added to siRNA at 0.5 µM and the zeta potential was measured. Each sample was measured 5 times in 7 runs. Zeta potential was calculated using the Helmholtz-Smoluchowski equation in Malvern software. The hydrodynamic diameter of the particles and their complexes were measured using dynamic light scattering (DLS), and

the same concentrations of the siRNA and dendrimers as in the zeta potential measurement. Single samples were measured 5 times in 3 runs. Values with PDI > 0.5 were dismissed.

Transmission electron microscopy (TEM)

The morphological structure, shape and size of the G3Si PEG6000 dendrimer was evaluated using a JEOL-1010 (Japan) transmission electron microscope at 100 000 × magnification. The dendriplex was created by combining siRNA with the dendrimer in PBS at room temperature. The dendriplex was prepared in a molar ratio of 2.5:1 (the optimal dendrimer/siRNA ratio), with a concentration of siRNA of 25 μM. After 20 min. incubation, 15 μl of the dendriplex or non-complexed dendrimer was placed for 10 min. on a 200-mesh copper grid with a carbon-coated surface. A saturated solution of uranyl acetate 2% (m/v) was used to stain both samples for 20 min. To enhance legibility, images have been sharpened.

Atomic force microscopy (AFM)

The morphology studies of siRNA and dendrimers were conducted on droplets deposited on mica (Grade V-1 Muscovite) by atomic force microscopy (AFM). Measurements were carried out using the Flex Axiom Nanosurf apparatus with a C3000 controller (NanosurfAG, Liestal, Switzerland). The experiments were performed in the dynamic force mode (taping mode) and phase imaging mode. The analysis was performed using probes (HI'RES-C14/CR-AU μmasch) with a typical curve radius < 1 nm, a spring constant of 5 N/m and a resonance frequency of 160 kHz. The images were recorded with a resolution of 512 × 512 data points. Image analysis was carried out using Scanning Probe Image Processor Software (SPIP) by Image Metrology, Hørsholm, Denmark.

Fluorescence polarization and time stability

This technique is based on the changes of fluorescence polarization of fluorescein labeled siRNA, after adding a dendrimer. The tested dendrimers were subsequently titrated to the siRNA-FITC solutions (1 μM, in 10 mM phosphate buffer) in order to achieve dendrimer/siRNA molar ratios ranging from 1:1 to 20:1. The dendrimer/siRNA mixtures were incubated at room temperature for 20 min. to ensure the formation of complexes, and then fluorescence polarization was measured on a Perkin-Elmer LS-55 spectrofluorometer in 1-cm path length quartz cuvettes. The excitation and emission wavelengths were 485 and 520 nm, with the excitation and emission slit widths being set to 7 and 5 nm, respectively. The cuvette holder was temperature controlled (25 °C).

Fluorescence polarization technique was also used to analyze the stability of the dendriplexes (dendrimer/siRNA in optimal saturation) in time. Measurements were taken immediately following a 20-min. pre-incubation period, as well as at 1, 5, 15 and 30-min. and subsequently at 1, 1.5, 2, 3, and 4-h later.

Circular dichroism (CD)

Circular dichroism (CD) of siRNA (1 μM) titrated with increasing concentrations (0.5–10 μM) of dendrimers was measured with a Jasco J-815 CD spectrometer (Jasco International Co., Ltd., Tokyo, Japan) in 5-mm path length quartz cuvettes at 25 °C, with a wavelength step of 1 nm, a response time of 4 s and a scan rate of 50 nm/min. CD spectra for siRNA alone and in presence of dendrimers was measured between 200 and 320 nm. All samples were prepared in 10 mM phosphate buffer. Pure phosphate buffer was used also as a baseline.

Gel electrophoresis

Electrophoresis in agarose gel was performed for the dendrimer/siRNA complexes. Dendrimers (0.5–10 μM) were mixed with siRNA (1 μM) in 10 mM Na-phosphate buffer, pH 7.4. and incubated at room temperature for 20 min. In the negative control, the non-complexed dendrimer was used at the maximum concentration tested. Meanwhile, in the positive control the siRNA was used without any dendrimer. Electrophoresis was run in a 3% agarose gel with GelRed stain (0.05 μg/ml) at 35 mA, 90 V for 45 min. The obtained electropherograms were analyzed using a ChemiDoc-It^2 Imager (UVP, Cambridge, UK).

Cell line

In vitro experiments were conducted with a HBEC-5i cell line (Human Brain Endothelial Cells). The cells were cultured on flasks covered with 1% gelatin in DMEM-F12 medium enriched with 1% Penicillin–Streptomycin, 10% FBS and 40 μg/ml ECGS under standard conditions (37 °C, 5% CO2).

Cytotoxicity of dendrimers

HBEC-5i cells were seeded into 96-well plates at 1×10^4 cells/well. Dendrimers were added to cells in increasing concentrations between 0.1 and 50 μM and incubated for 24 h (37 °C, 5% CO_2). After incubation, cells were washed in PBS and incubated with 0.5 mg/mL of MTT at 37 °C for 3 h. Then the MTT was discarded carefully, and DMSO was added to solubilize the formazan crystals[24]. Finally, the absorbance was measured for each well at a wavelength of 570 nm using a Bio-Tek Synergy HT Microplate Reader (Bio-Tek Instruments, Winooski, VT, USA). All experiments were performed in 6 repetitions. Cell viability was calculated as the percent ratio of absorbance of the samples to the reference control, according to the formula:

$$\%\ \text{viability} = (\text{As}/\text{Ac}) \times 100\%$$

where As—absorbance of cells treated with dendrimer, Ac—absorbance of control cells (untreated).

Statistical analysis

The results are presented as mean values ± standard deviation (SD). Segmental regression analysis was used to determine the ratio of the tested dendrimers to siRNA at which optimal saturation of the complex occurs.

Results

Dendrimer synthesis

To carry out this work, we prepared 4 carbosilane pegylated cationic dendrimers to study the influence of dendritic core size as well as a number of cationic groups and pegylation, for biomedical purposes (Fig. 2).

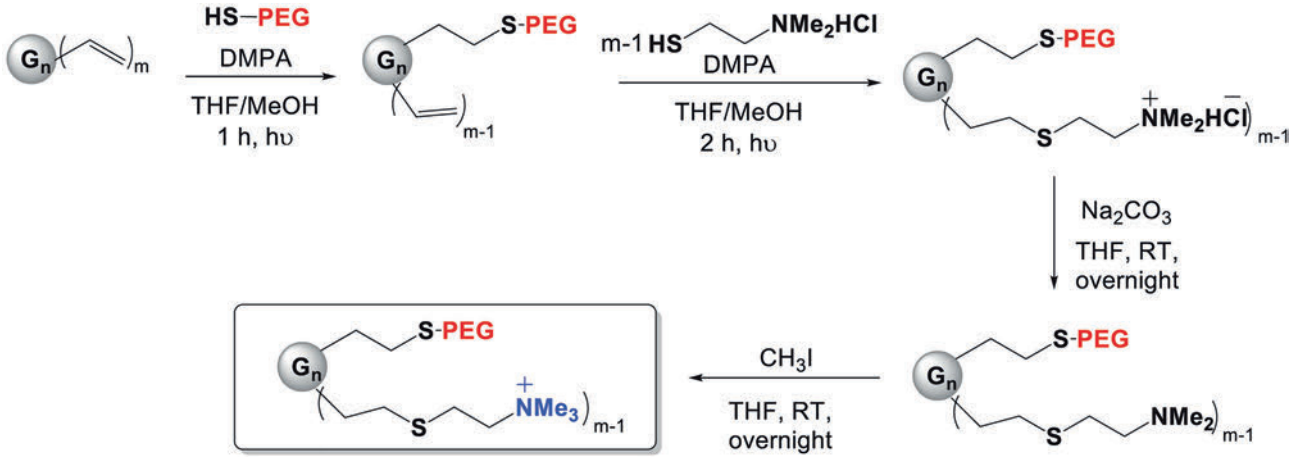


Figure 2. Synthesis of cationic pegylated dendrimers. "n" refers to dendrimer generation, "m" refers to number of peripheral functions. The thiolene addition reaction was employed to functionalize vinyl-terminated carbosilane dendrimers with alkene groups at the periphery. Commercial SH-PEG$_x$ (x = 2000 or 6000) was used to decorate one branch, while 2-(Dimethylamino)ethanethiol hydrochloride was added to the remaining branches in the presence of DMPA as the photoinitiator. Neutralization with Na_2CO_3 and subsequent quaternization with MeI resulted in the synthesis of hetero-functionalized cationic pegylated carbosilane dendrimers with 23, 31, or 47 positive charges.

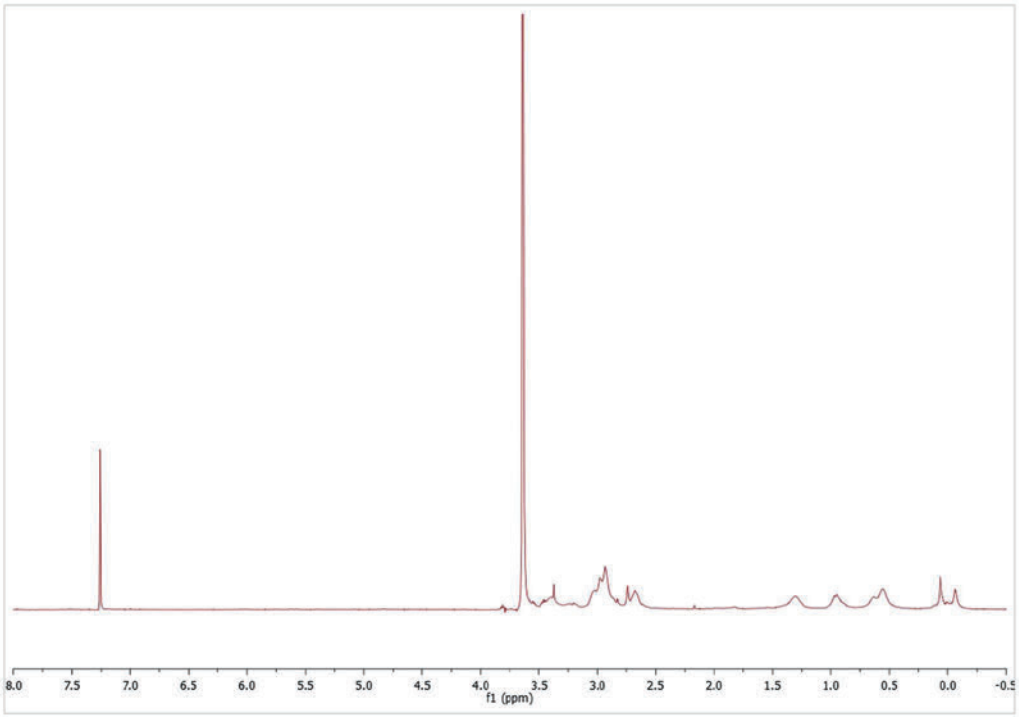


Figure 3. ^{1}H-NMR ($CDCl_3$) of intermediate compound $G_3Si(SPEG6000)(SNMe_2HCl)_{31}$. The signal at 3.60 ppm corresponds to PEG and NMe_2.HCl, which are overlapped.

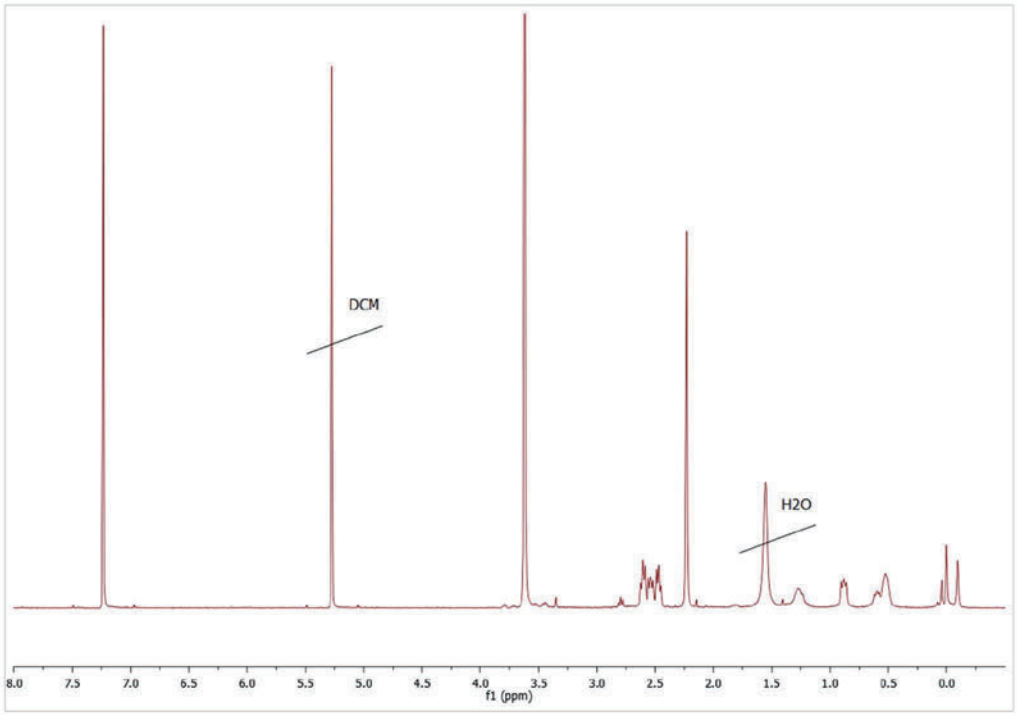


Figure 4. ^{1}H-NMR ($CDCl_3$) of intermediate compound $G_3Si(SPEG6000)(SNMe_2)_{31}$. The signal at 3.60 ppm corresponds to PEG and the signal at 2.25 ppm corresponds to NMe_2.

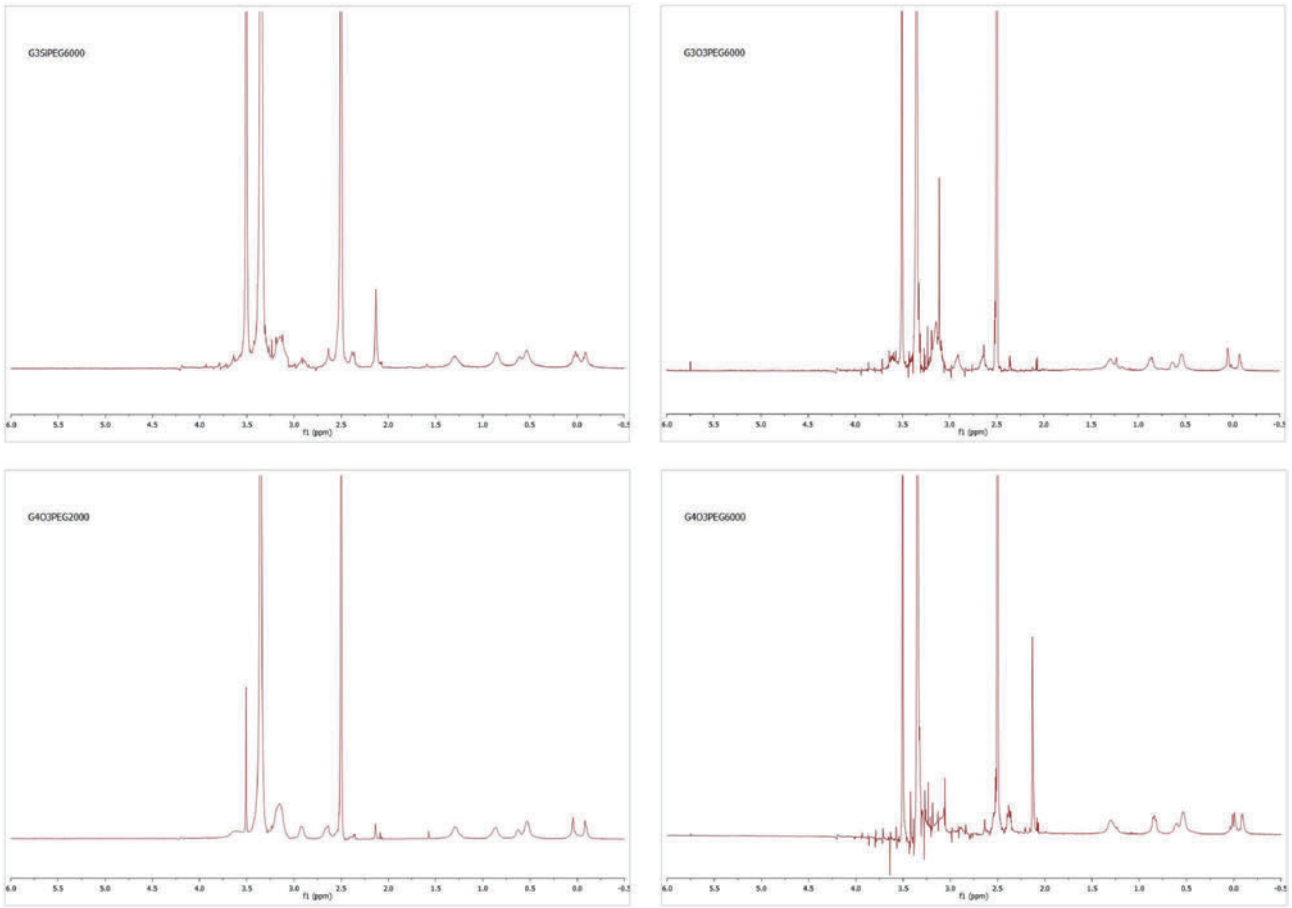


Figure 5. ^{1}H-NMR (DMSO) of the final compounds. The signal at 3.40 ppm corresponds to PEG and NMe_3, which are overlapped.

Heterofunctionalization with 2 types of commercial thiols, followed by neutralization and quaternization created $G_nY(SPEG)(SNMe_3I)_{m-1}$ dendrimers bearing PEG2000 or PEG6000 and 23 (G3O3), 31 (G3Si) or 47 (G4O3) positive charges (Fig. 6A). These compounds were perfectly soluble in water.

Transformation of the vinyl precursor dendrimers into pegylated cationic analogues was followed by ^{1}H-NMR. After PEG incorporation, a singlet appeared around 3.50 ppm, and vinyl representative signals at 6.15 ppm, 6.00 ppm and 5.71 ppm disappeared after the thiolene reaction with 2-(dimethylamino)ethanethiol hydrochloride was completed (Fig. 3). A representative singlet signal in $G_nY(SPEG)(SNMe_2)_{m-1}$ compounds at 2.25 ppm, which corresponded to neutralized peripheral dimethylamino groups disappearing by the time the reaction was completed (Fig. 4). Furthermore, methyl groups bound to the quaternary nitrogen atom appeared as a singlet around 3.40 ppm in $G_nY(SPEG)(SNMe_3I)_{m-1}$ compounds, overlapping with the PEG signal (Fig. 5). Detailed NMR spectra peak characterization can be found in supplementary Information.

Zeta potential, size and morphological structure

The zeta potential and hydrodynamic diameter data for the tested dendrimers are presented in Table 2. The results indicate that all the dendrimers possess a positively charged surface in line with their chemical structures. Dendrimers G3O3 PEG6000 and G4O3 PEG6000 displayed the highest zeta potential, while the lowest values were observed for G3Si PEG6000 and G4O3 PEG2000.

The hydrodynamic diameter, which incorporated both the core size of the nanoparticle and the surface molecules or polymers on the dendrimers, was determined via DLS particle size measurements. Based on these measurements, the dendrimer G4O3 PEG2000 displayed the largest hydrodynamic diameter, while G3Si PEG6000 exhibited the smallest.

Introducing the tested dendrimers to the siRNA led to a considerable increase in the zeta potential of siRNA (Fig. 6A). The G4O3 PEG2000/siRNA complex showed the highest zeta potential among all the studied dendriplexes. Notably, the continuous addition of dendrimer molecules to the siRNA complex reached a plateau, indicating a saturation point and suggesting that this is the optimal quantity of dendrimer molecules bound to the siRNA molecule.

The hydrodynamic size of the dendrimer/siRNA complexes, as determined by DLS, remained consistent regardless of dendrimer generation or concentration (Fig. 6B). The observed size range of the complexes was 100–330 nm. Increasing the dendrimer concentration has a negligible effect on the size of the complexes.

The morphological structure and size of the formed dendrimer/siRNA complex were explored using transmission electron microscopy (TEM) (Fig. 7). As a representative example, only the G3Si PEG6000 dendrimer was studied in detail. It was observed that the non-complexed dendrimer formed aggregates, while complexation

Dendrimer	Z-potential (mV)	Z-size (nm)
G3Si PEG6000	20.23 ± 3.00	115.68 ± 57.10
G3O3 PEG6000	35.75 ± 2.60	261.26 ± 114.64
G4O3 PEG2000	25.83 ± 3.84	319.83 ± 108.23
G4O3 PEG6000	34.50 ± 2.86	248.22 ± 92.98

Table 2. Zeta potential and hydrodynamic diameter of uncomplexed dendrimers (without siRNA). The data given from 3 repetitions as mean and standard deviation.

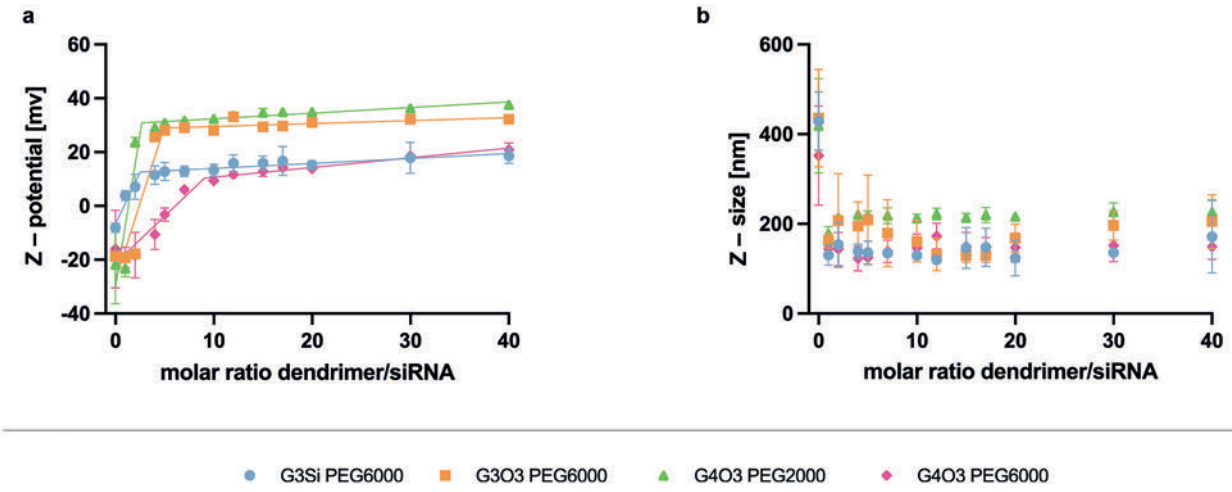


Figure 6. Zeta potential (**a**) and hydrodynamic diameter (**b**) of the dendrimer/siRNA complexes. The concentration of siRNA = 0.5 µM. The results are shown for 5 repetitions as mean and standard deviation.

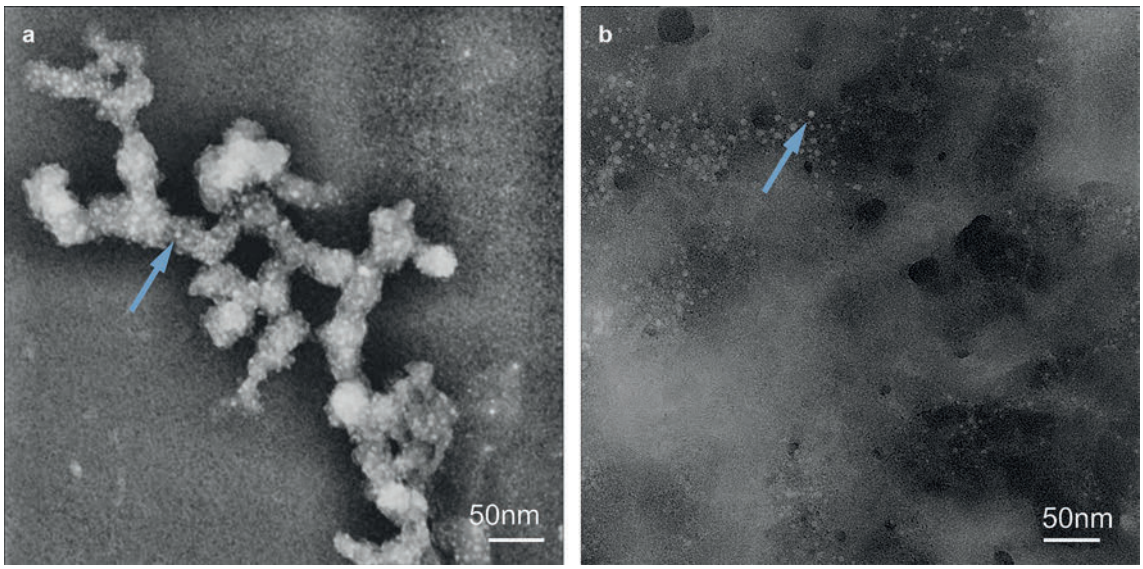


Figure 7. Transmission electron microscope images of the G3Si PEG6000 dendrimer (**a**) and G3Si PEG6000/siRNA dendriplex in a molar ratio of 2.5:1 (the optimal dendrimer/siRNA ratio) (**b**). The arrows point at instances of dendrimers as representative examples within the samples. A magnification of 100 000 × was used to analyze the complexes.

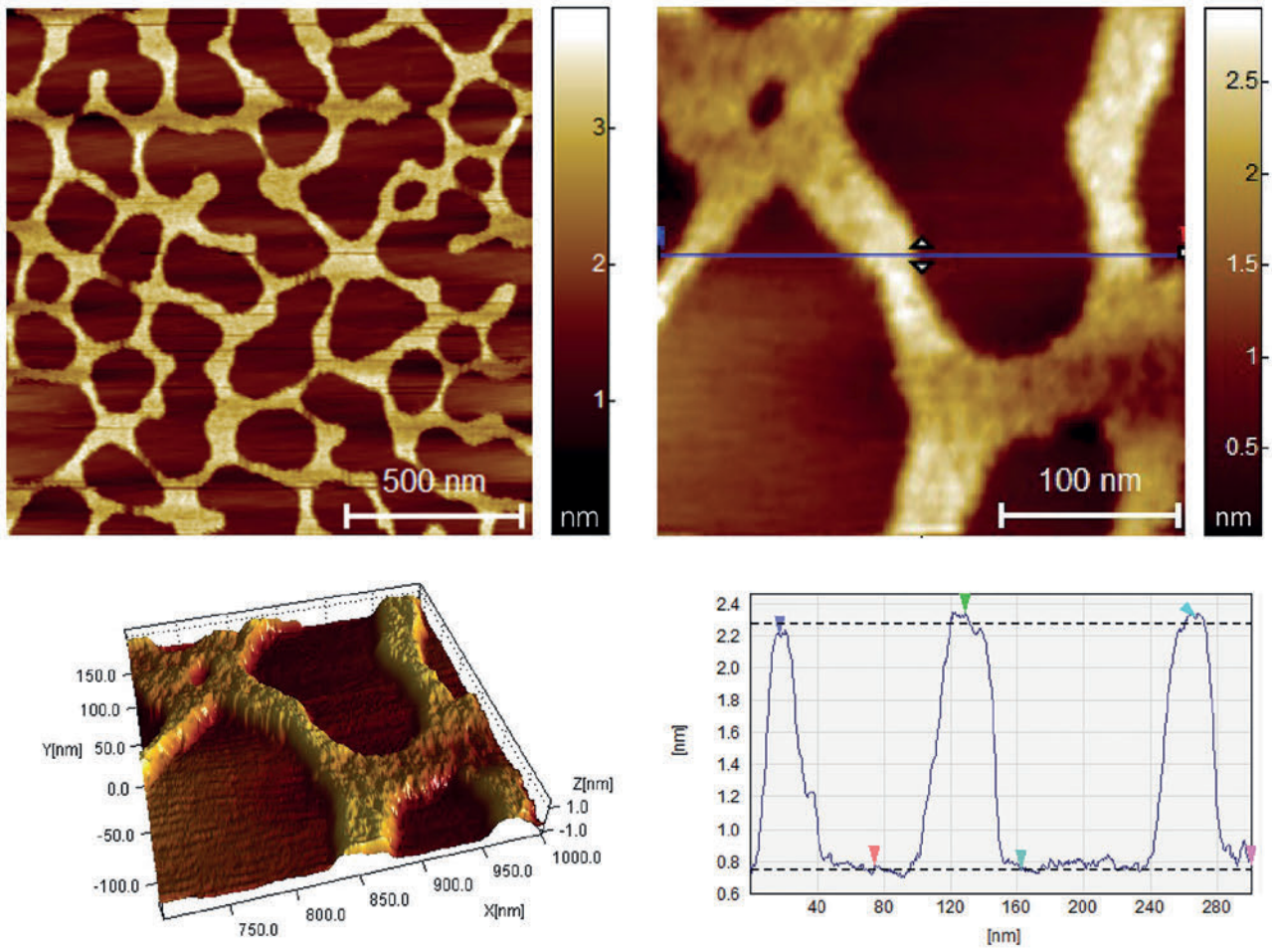


Figure 8. AFM images of siRNA and 3D visualization of its structure.

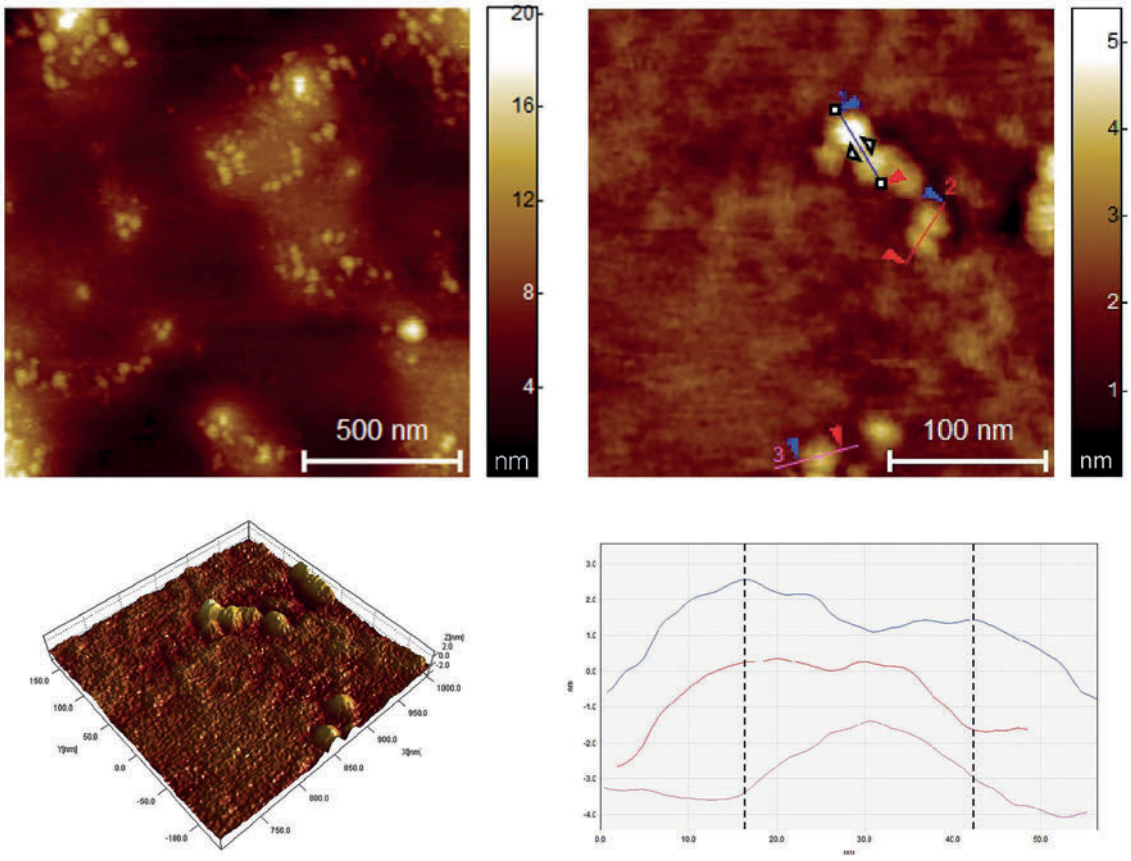


Figure 9. AFM images of G3Si PEG6000 dendrimer and 3D visualization of its structure.

with siRNA led to the dispersion of the dendrimer. Analysis of the transmission electron microscopy images revealed that the dendrimer G3Si PEG6000 had a spherical shape with a size of approximately 5.78 ± 1.19 nm.

The morphological features and dimensional properties of the siRNA, the uncomplexed dendrimer and dendrimer/siRNA complex, were thoroughly examined using AFM. The AFM images of siRNA revealed distinctive arrangement patterns of siRNA molecules (Fig. 8). The structures exhibited a uniform height profile of approximately 0.77 nm, indicative of a well-organized arrangement consisting of 2 layers of siRNA molecules stacked on each other[25]. These measurements were reproducible across multiple analyses, affirming the reliability and consistency of the stacked siRNA conformation on the mica surface.

The height images provided detailed information regarding the dendrimers' size distribution and spatial arrangement. The G3Si PEG6000 dendrimer exhibited an average diameter of approximately 22.5 nm. The size difference compared to the images of TEM is due to the interaction with the substrate, as well as flattening resulting from the in Tap- ping Mode (AFM) observation (Fig. 9).

In order to assess the characteristics of the G3Si PEG6000/siRNA dendriplex, both height and phase images were acquired (Fig. 10). Our results demonstrated that the G3Si PEG6000/siRNA dendriplex exhibited an average diameter of approximately 14 nm.

Fluorescence polarization

The fluorescence polarization of the evaluated dendrimers was analyzed and the results are presented in Fig. 11. The formation of dendrimer/siRNA complexes contributed to the reduction of the movement of siRNA molecules in suspension, which is observed as an increase in siRNA-FITC fluorescence polarization. During the addition of subsequent portions of tested dendrimers to siRNA-FITC solution, an increase in fluorescence polarization was observed until reaching the plateau phase which indicated the formation of the complexes.

Time stability

Measurement of the fluorescence polarization of the formed complexes dendrimer/siRNA-FITC at different times also allowed for the evaluation of their stability. The formed complexes (dendrimer/siRNA-FITC molar ratio calculated by fluorescence polarization measurement) were incubated and the fluorescence polarization was measured for 4 h. The obtained results (Fig. 12) showed that the fluorescence polarization of dendriplexes did not change significantly when increasing incubation time, proving that the formed complexes were stable over a 4 h period.

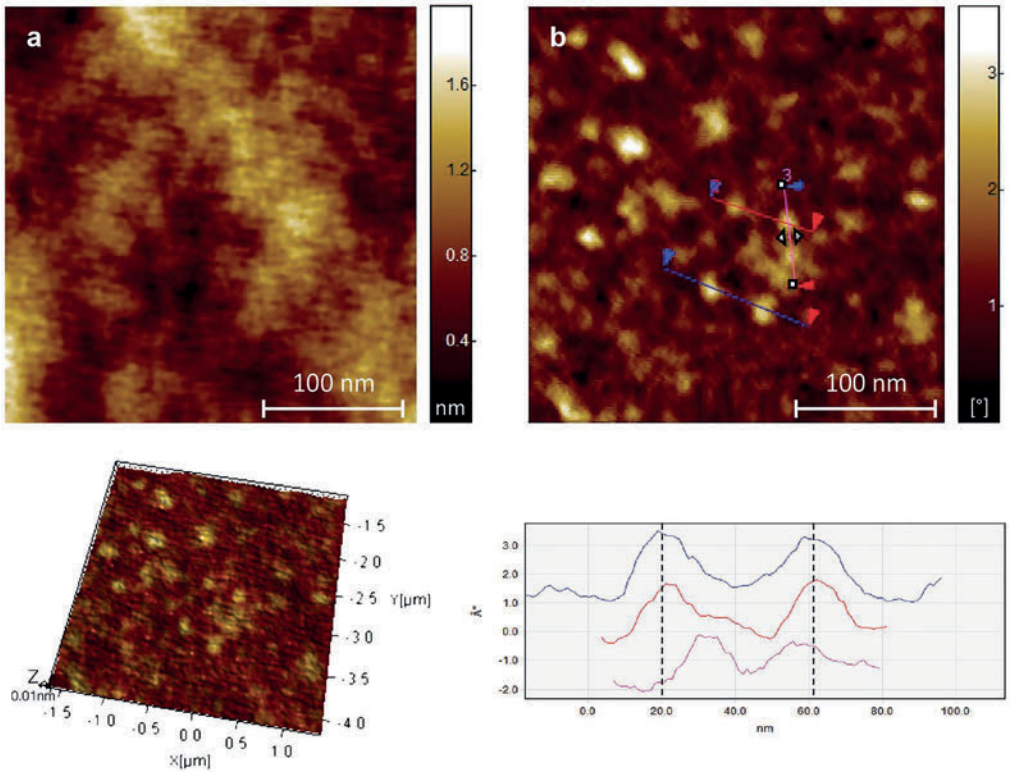


Figure 10. AFM height image (**a**) and phase image (**b**) of G3Si PEG6000/siRNA dendriplex in a molar ratio of 2.5:1 (the optimal dendrimer/siRNA ratio) and 3D visualization of its structure.

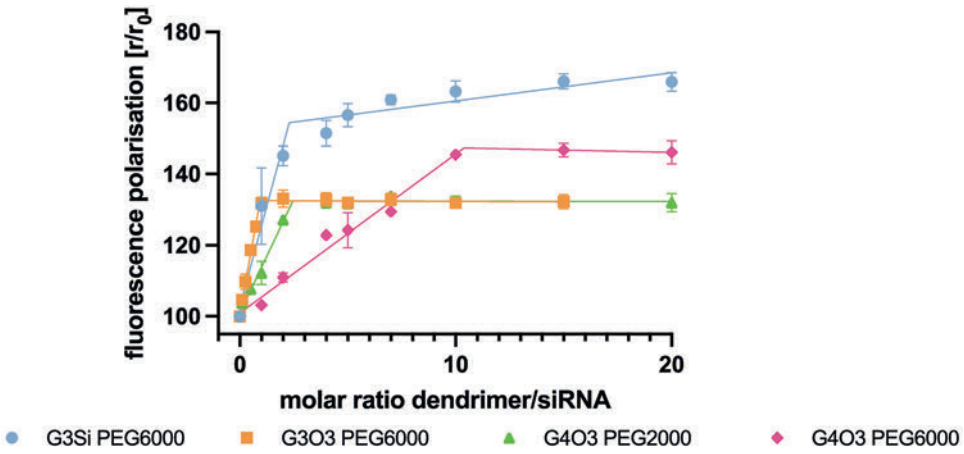


Figure 11. Changes in siRNA-FITC (1 µM) fluorescence polarization upon titration of the studied dendrimers. The excitation and emission wavelengths were 485 and 520 nm, accordingly. The results are shown for 3 repetitions as mean and standard deviation.

Circular dichroism

After normalization of ellipticity of the native siRNA spectra (the highest peak at 260 nm) at around 5 deg × cm^2 × $dmol^{-1}$, it was found that all tested dendrimers could bind to siRNA, changing the conformation (Fig. 13). The G3Si PEG6000, G3O3 PEG600 and G4O3 PEG6000 dendrimers caused a concentration-dependent increase in signal intensity for both the negative peak (205–215 nm) and the positive peak (260–270 nm) in the siRNA CD spectra. In contrast, increasing the concentration of G4O3 PEG2000 caused the flattening of both the negative and positive peaks. The spectral analysis revealed that the G4O3 PEG2000 induced a notable red-shift throughout the entire spectra.

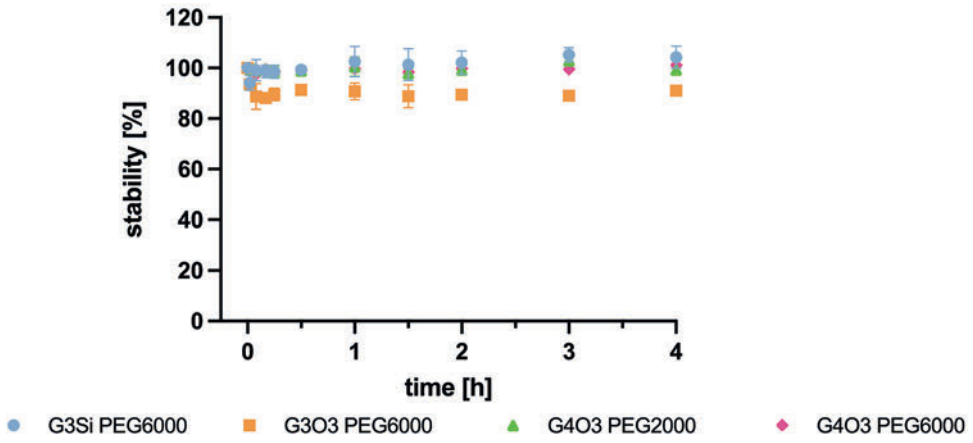


Figure 12. The time dependence of dendriplex fluorescence polarization, expressed as a percentage of control (siRNA-FITC without dendrimers). The results are shown for 3 repetitions as mean and standard deviation.

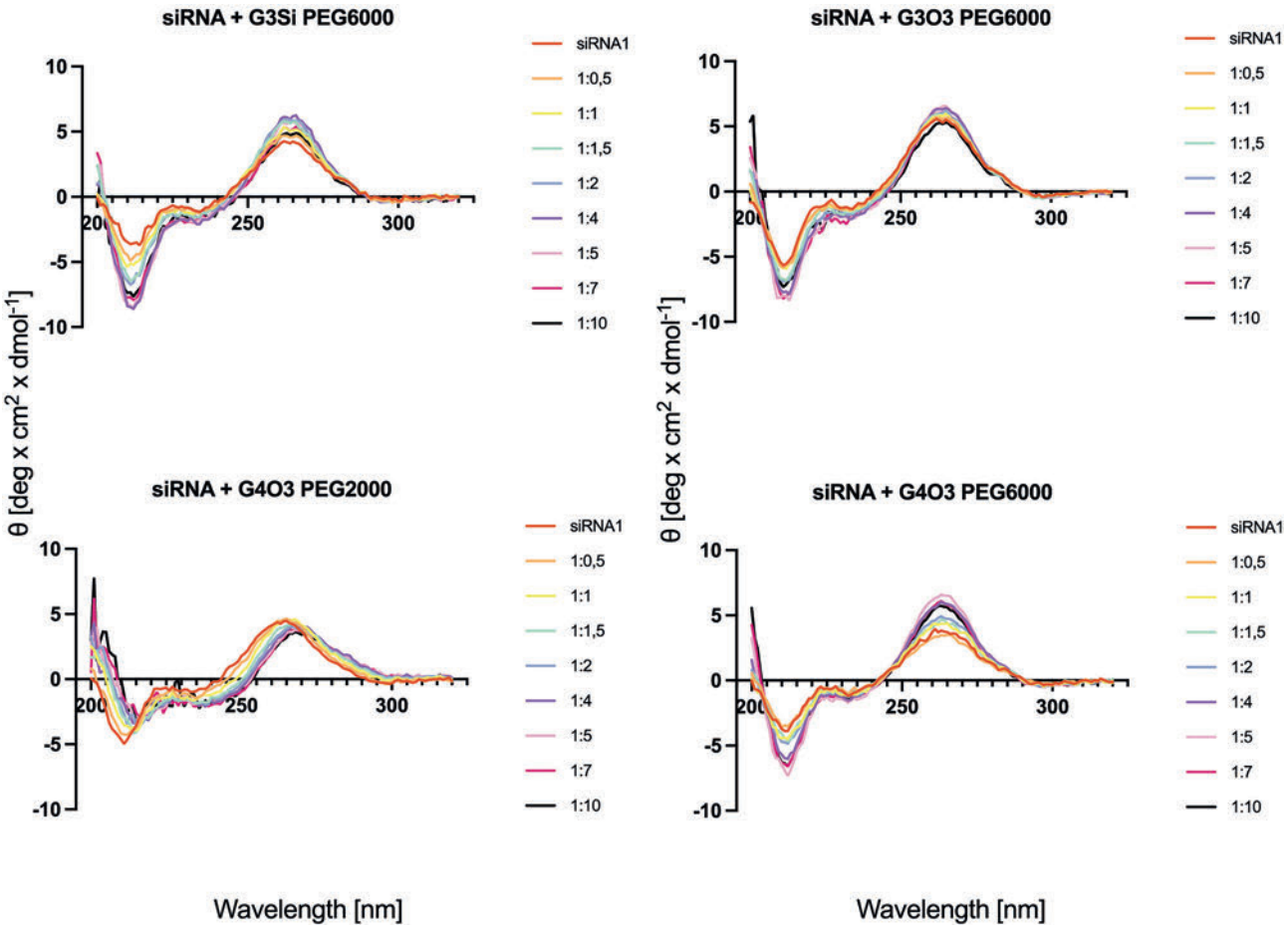


Figure 13. CD spectra for siRNA (C = 1 μM) in the presence of the studied dendrimers (C = 0.5–10 μM). The results are shown for 3 repetitions.

The results indicate that the siRNA samples that were combined with the dendrimers G4O3 PEG6000 and G3Si PEG6000, respectively, exhibited the most substantial difference in ellipticity compared to other samples (Fig. 14).

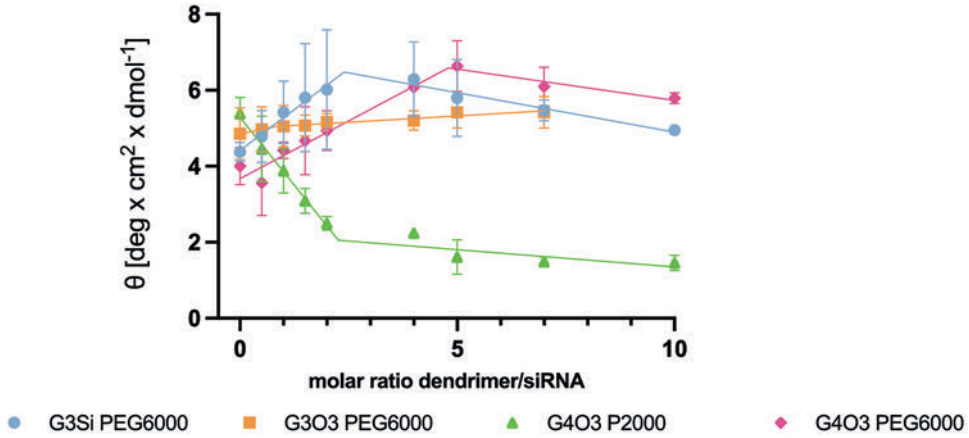


Figure 14. Changes in mean residue ellipticity of siRNA at λ equal to the dendrimers' maximum peak (260–270 nm). The results are shown for 3 repetitions as mean and standard deviation.

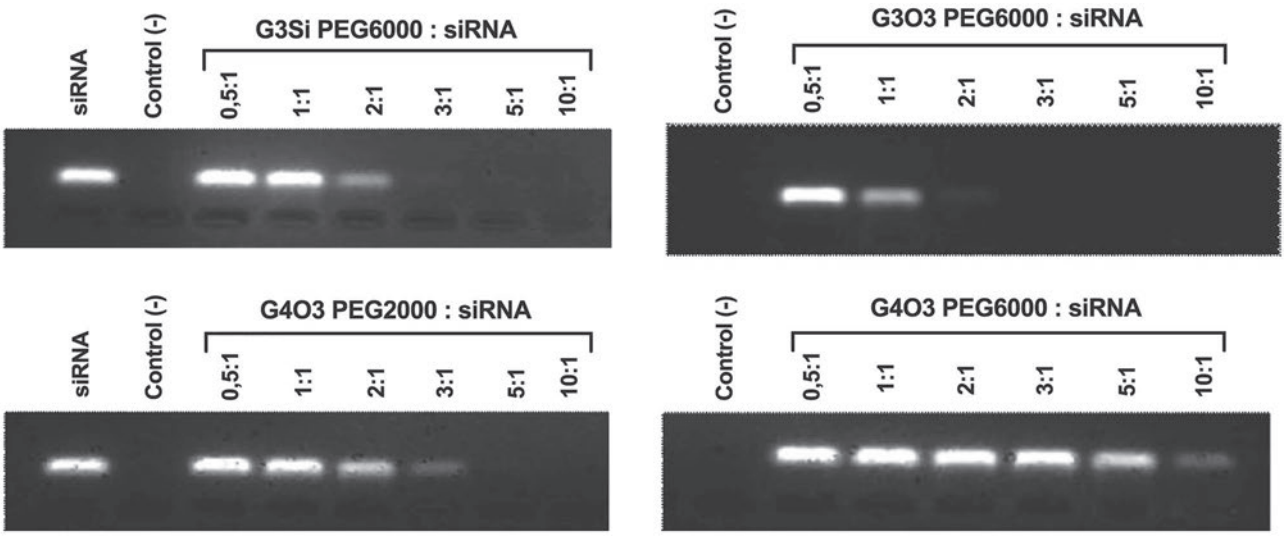


Figure 15. Analysis of dendrimer/siRNA complexes in different ratios in 3% agarose gel with GelRed. Complexes were prepared in 10 mmol/l PBS.

Gel electrophoresis

The visualization of siRNA electropherograms enabled the analysis of the dendrimer-siRNA complex formation. Gel electrophoresis results revealed that all dendrimers interacted with siRNA, leading to the quenching of the fluorescence signal. As the dendrimers formed complexes with siRNA, the amount of uncomplexed siRNA decreased until it was fully saturated and the fluorescence was completely extinguished. The data obtained suggested that out of the tested dendrimers, the G4O3 PEG6000 dendrimer formed complexes with siRNA that were optimally saturated in the highest molar ratio, while the G3O3 PEG6000 dendrimer exhibited the lowest molar ratio at which the complex with siRNA is optimally saturated (Fig. 15). The results obtained from all the biophysical assays describing the optimal saturation of the complexes are summarized in Table 3.

Cytotoxicity

An MTT assay was conducted to evaluate the cytotoxicity of studied dendrimers on cerebral microvascular endothelial cells (HBEC-5i). This assay measured mitochondrial oxidative activity of the HBEC-5i cells after incubation with dendrimers for 24 h. The findings of this study (Fig. 16) indicate that all dendrimers exhibited significant toxicity on HBEC-5i cell line at higher concentrations (> 25 μM). Among the tested dendrimers, G3Si PEG6000 exhibited the lowest IC50 (7.84 μM), with the dendrimers G4O3 PEG2000 and G3Si PEG6000 exhibiting the lowest IC20 (2.97 and 2.34 μM, respectively). G4O3 PEG6000 showed the highest toxicity at IC50 (1.27 μM) and IC20 (0.38 μM).

Dendrimer	Zeta potential	Fluorescence polarization	Circular dichroism	Gel electrophoresis*
G3Si PEG6000	2.52	2.29	2.40	Over 2
G3O3 PEG6000	4.93	0.94	0.82	Over 1
G4O3 PEG2000	2.67	2.46	2.27	Over 2
G4O3 PEG6000	9.03	10.39	4.80	Over 10

Table 3. The data collected from the conducted biophysical assays (excluding the gel electrophoresis) describing the optimal saturation of the complexes, were subjected to an analysis using segmented regression. This analytical approach allowed for the identification of a change in slope, resulting in the identification of a sharp transition point. This rapid transition signified the ratio of the tested dendrimers to siRNA at which optimal saturation of the complex occurred. The table shows the molar ratio of the tested dendrimers to 1 mol of studied siRNA. *Visual examination was used to evaluate the electropherograms obtained from the gel electrophoresis.

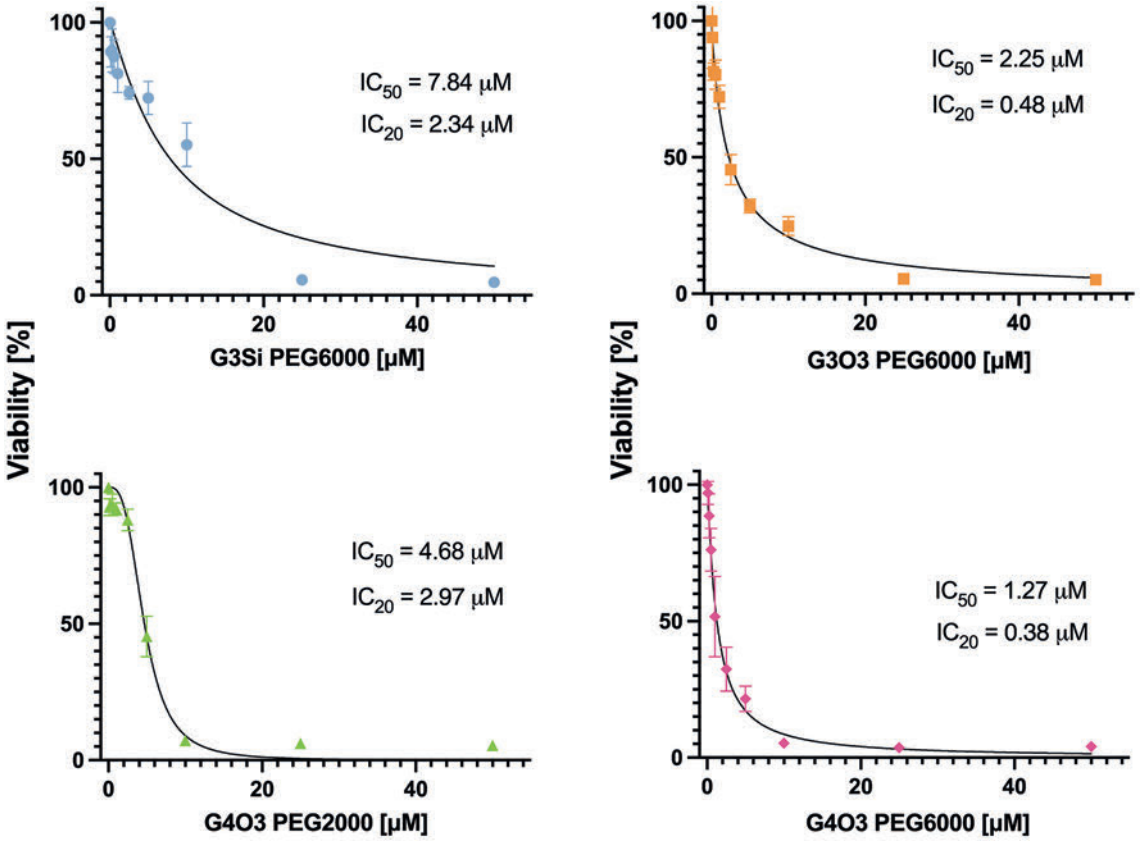


Figure 16. IC50 and IC20 values of HBEC-5i cells treated with dendrimers showed in MTT assay, after 24 h incubation. The results are shown for 6 repetitions as mean and standard deviation. The results are shown for 6 repetitions as mean and standard deviation.

Discussion

Since the discovery of the "cascade molecule" in 1978 and the first complete dendrimer family that was synthesized from generation 1 to 7 in 1985, nanoparticle development has led to the creation of various dendrimer structures with diverse applications in fields such as light harvesting and energy transfer, nanoscale catalysis, chemical sensors, unimolecular micelles, enzyme mimics, encapsulation of guest molecules, molecular recognition, diagnostic agents and gene and drug delivery[26–28]. Due to their unique structural features, dendrimers have received considerable attention for use as potential nucleic acid carriers[18,29–31]. Carbosilane dendrimers were found to be a stable and effective delivery system with high transfection efficiency by Weber et al.[28,32] Advancing research in this area has the potential to overcome the current limitations and challenges of today's therapy methods and unlock the full potential of dendrimers for the treatment of neurodegenerative disorders and other diseases. It is crucial to continue the development and characterization of these extraordinary tools for gene therapy applications.

The BBB is the most restrictive barrier within the body and prevents entry into the brain for most small molecules and nearly all macromolecular therapeutics developed for central nervous system (CNS) pathologies[33]. Highly astute scientific research must be pursued to achieve an applicable gene silencing directed against neurodegenerative disorders. The BBB presents obstacles to siRNA delivery to the CNS due to tight junctions preventing passive diffusion, low pinocytosis reducing active transport, and high metabolic activity leading to potential enzymatic degradation[34]. These features collectively impede the effective entry of therapeutic siRNA molecules into the brain. In addressing these challenges, our study delves into the intricate aspects of siRNA delivery. To address these challenges, we analyzed the biophysical characteristics of 4 dendrimers and their complexes with siRNA to identify a suitable candidate for a siRNA nanocarrier capable of transferring cargo safely across the BBB model. The findings of our study offer valuable insights into the process of complexation, stability in time, mechanisms of interaction, the influence of the tested dendrimers on the spatial structure of the oligonucleotide and the potential cytotoxic effects of the dendrimers on the human cerebral microvascular endothelium cells in the context of the challenges posed by crossing the BBB.

The size and surface charge of nano-delivery systems significantly impacts pharmacokinetics, absorption, tissue distribution and intracellular clearance. Therefore, careful consideration must be given to the selection of the appropriate size of carrier for the intended application. The BBB, which is characterized by tight intercellular junctions and zonula occludens between closely connected capillary endothelial cells, presents a formidable obstacle due to the non-fenestrated nature of brain capillaries[35,36]. Consequently, there is low probability of paracellular transport for nanoparticles compared to the transcytotic transport through cellular vesicles. However, it has been established that nanoparticles are able to exploit both the para-cellular and transcellular pathways[37]. Changes in the vasculature during neurodegenerative disorders, such as endothelial degeneration, can impact the normal diffusion of solutes across brain extracellular spaces, reducing the expression of tight and adherens junctions at the BBB, and ultimately affecting the delivery of therapeutic agents[38]. Although sole particle size cannot predict cellular absorption mechanisms, there is evidence that particles within certain size ranges utilize specific uptake pathways.

In our studies, dynamic light scattering (DLS), transmission electron microscopy (TEM) and atomic force microscopy (AFM) were used in the analysis of the size and shape of the dendrimers and dendriplexes. The particle size measurement obtained from DLS is referred to as a "hydrodynamic diameter", as it accounts for the core size of the nanoparticle and also for any polymers or molecules on the surface of the dendrimers. Consequently, DLS measurements exhibited larger mean diameters than those obtained by TEM and AFM due to factors such as particle aggregation, solvation shell, and PEG polymer[39].

The AFM studies of the G3Si PEG6000 dendrimer showed a uniform particle size distribution. However, the size obtained from the AFM measurements differed from the results obtained from TEM. This difference may be attributed to the fact that the deposition of the dendrimer was performed on a strongly hydrophobic surface (mica). The dendrimer surface possesses highly charged ions exhibiting hydrophilic properties. On contact with hydrophobic air and solvent evaporation (water), significant deformation occurs, causing the dendrimer to assume a disk-like shape (Fig. 9). When we formed the G3Si PEG6000/siRNA dendriplex, the situation changed. Since the measurement is performed in a buffer system consisting of water and the siRNA dendrimer, we observed that after water evaporation the formed complex is likely located within the matrix, possibly the buffer and excess siRNA. The average size of the complex was approximately 14 nm. In this case, the complex size, more precisely its diameter, is determined by the attached siRNA. The reason for the complex being smaller than the non-complexed dendrimer can be attributed to the reduced impact of the environment (air) on the complex confined inside the matrix (Fig. 10).

TEM imaging of the non-complexed dendrimer showed that the G3Si PEG6000 dendrimer is approximately the same size and shape as haemoglobin, suggesting that its size is favourable for cellular uptake through the clathrin-independent endocytotic pathway. Particles in the submicron size range, such as the analyzed dendriplexes, have been found to use uptake pathways such as caveolae-mediated, clathrin-mediated endocytosis or macropinocytosis[17,36,40]. Multiple studies have demonstrated that the smaller nanocarriers exhibit a greater capacity to cross the BBB with an accelerated rate, and result in enhanced tissue penetration and deeper transport of their cargo[41,42]. As a consequence, small-sized dendrimers may have a greater ability to penetrate the BBB and achieve wider distribution throughout the tissue. The acquired data indicated that dendrimer G3Si PEG6000 possessed the smallest hydrodynamic diameter while also forming one of the smallest dendriplexes amongst those examined. It is also noteworthy that the smallest size of the G4O3 PEG6000 dendrimer compared to its less PEGylated counterpart (G4O3 PEG2000) may be attributed to greater hydrophobic interactions and increased polymer flexibility in highly PEGylated dendrimers. Additionally, high ionic strength modifies the observed zeta potential of the 2 dendrimers, as well as the PEG conformation and as result, affects complexation with nucleic acids[39,43–45].

The positive surface charge of dendrimers and dendriplexes is a critical factor in determining their binding with other oppositely charged particles. It governs the stability of the complex, affects the interaction with the cell membrane and, ultimately, its transfection efficiency. However, a high positive surface charge may also result in membrane disruption via nano-hole formation, membrane thinning and erosion[46,47]. The charge of a nanoparticle's surface is expressed as the zeta potential, which is the electrostatic potential at the interface between the nanoparticles' diffuse layer of ions, called the shear plane, and the surrounding liquid. Among the tested dendrimers, the G3O3 PEG6000 and G4O3 PEG6000 exhibited the highest zeta potential. As anticipated, the dendrimers with the highest zeta potential exhibited the highest cytotoxicity. However, complexation with nucleic acid mitigates, to some extent, the cytotoxic effects of the dendrimer. Further studies are required to obtain a comprehensive picture of the cytotoxic effects of the studied carriers[47]. The positive surface charge of the dendrimers interacted with negatively charged phosphate molecules on the siRNA. As the electrostatic interactions are the predominant factor driving the complexation, the zeta potential enables the determination of the

appropriate dendrimer concentration required for optimal complex saturation. The saturation point is achieved when the continuous addition of the dendrimer reaches a plateau indicating the optimal quantity of dendrimer molecules bound to the siRNA molecule. It was observed that dendrimer G4O3 PEG6000, despite having high zeta potential, creates saturated complexes with siRNA in relatively high concentrations. It is hypothesized that this may be due to high repulsion between the dendrimers[39].

Various physicochemical methods were employed to investigate the efficacy of dendrimers in binding siRNAs and determining their optimal properties for forming a saturated complex. Among these methods was fluorescence polarization. Fluorescently labelled siRNA in solution at 20–37 °C has a flexible structure, but upon complexation, its rotation is hindered, fluorescence intensity lowered and polarization increased. The higher the polarization value, the stronger the siRNA is bound to a dendrimer[48]. Dendrimer G3Si PEG6000 reached the highest fluorescence polarization values. Thus, we conclude that the siRNA had the strongest affinity to this dendrimer. This was also confirmed by the fact that the dendrimer G3Si PEG6000 creates one of the smallest dendriplexes amongst all those tested. This may be due to the fact that the strong affinity of the siRNA to the dendrimer could result in tighter wrapping of the nucleic acid around the dendrimer molecules[17]. It is noteworthy that both G4O3 PEG6000 and G3Si PEG6000 dendrimers create dendriplexes of comparable size. Even though the dendriplex created with the G3Si PEG6000 dendrimer has a lower zeta potential than the dendriplex with G4O3 PEG6000 dendrimer, the former has higher fluorescence polarization. The G3Si PEG6000 dendrimer may induce a more significant effect on siRNA conformation while possessing a lower surface charge, most likely due to the geometry of peripheral cations and their availability for interaction with the siRNA. Fluorescence polarization was also employed to assess the time stability of the tested dendrimers. Notably, all the tested dendrimers displayed consistent fluorescence polarization values and no statistically significant changes were observed over the designated time period. This suggests that the dendrimers remained stable throughout the entire duration of the experiment. This consistent behaviour of the dendrimers over time further supports their potential.

Circular Dichroism (CD) was employed to investigate the impact of dendrimers on the 3-dimensional configuration of the siRNA. This technique is well-suited for studying nucleic acids due to the chiral nature resulting from the helical arrangement of nucleotides and the intrinsic asymmetry of nucleosides. Specifically, nucleic acids absorb left and right circularly polarized light unequally, leading to differential light absorption and conversion into elliptically polarized light. This conversion yields an ellipse with a characteristic angle, θ, whose tangent is equivalent to the ratio of the minor to major axes of the ellipse. The manifestation of ellipticity is commonly referred to as circular dichroism[49–51]. The absorption characteristic for nucleic acids is determined by a complex interplay of individual nucleotide absorption and their interactions. Therefore, the excitation coefficient of a nucleic acid at any given wavelength depends on its sequence and conformation[50]. The studied siRNA CD spectra exhibited a minimum near 210 nm, a maximum near 260 nm, and small negative CD values between 290 and 300 nm, indicating a right-handed A-form structure. However, the conformation of nucleic acids is dynamic and it changes upon exposure to dendrimers. The G3Si PEG6000, G3O3 PEG6000 and G4O3 PEG6000 dendrimers caused an increase in the ellipticity of the siRNA. Conversely, the G4O3 PEG2000 dendrimer decreased the ellipticity of the oligonucleotide. To investigate the interplay between dendrimers and nucleic acids further, it was necessary to consider the specific alterations occurring within the siRNA structure that influenced changes in spatial configuration and the resulting CD spectrum. Circular dichroism of nucleic acids is determined by the geometric relationship between coupled electronic transition dipoles on adjacent nucleotides and the distance between bases, with the stacking arrangement of the bases exerting a predominant influence on the overall CD signature. Based on these considerations, it can be inferred that the observed increase in siRNA ellipticity induced by the dendrimers was associated with hyperchromicity and manifested as an increase in absorption. Accordingly, the decrease of ellipticity caused by dendrimer G4O3 PEG2000 was related to hypochromicity and suggested the siRNA adopted a less compact arrangement with the dendrimer[49,50,52]. It is noteworthy that a red shift of the siRNA spectra was observed upon titration of dendrimer G4O2 PEG2000. This observation provided further evidence of conformational changes occurring in the oligonucleotide during complexation with the dendrimer[51,52]. The greatest difference in ellipticity was observed in the siRNA samples combined with dendrimer G4O3 PEG6000 and G3Si PEG6000, respectively. These findings suggested that these dendrimers exerted the most pronounced influence on the conformation of siRNA. The outcomes of this investigation aligned with those obtained via the fluorescence polarization assay. The analysis of CD spectra also exhibited a sufficient signal intensity, facilitating the identification of an optimal concentration of dendrimer required for complex saturation.

The formation of dendriplexes was investigated using a gel electrophoresis assay, resulting in the acquisition of presented electropherograms. As nucleic acid oligomers are polyanions at neutral pH, they migrated toward the positive electrode in the electrophoretic gels. Non-complexed siRNA traversing through the porous agarose gel stained with GelRed-stained created a fluorescent band. The formation of the studied dendrimer-siRNA complexes led to a reduction in fluorescence intensity, which we attributed to the hindrance of dye-siRNA interactions. As a result, the gradual decrease of band fluorescence was observed, with an increase of dendrimer concentration until a state of saturation was reached and led to complete fluorescence quenching. The results obtained from the gel electrophoresis and all other biophysical assays discussed are summarized in Table 2. The results are consistent with the results obtained by other methods.

To be utilized effectively, dendrimers must exhibit low toxicity and non-immunogenicity, as well as biocompatibility and biodegradability. These attributes are vital for ensuring safe and effective use in the development of various biomedical and pharmaceutical products. Cytotoxic properties of the tested dendrimers were assessed using a colourimetric assay measuring formazan, proportional to the number of viable cells with active mitochondrial dehydrogenases. Dendrimer G4O3 PEG6000 was found to have the highest cytotoxic properties among the dendrimers examined. G3Si PEG6000 and G4O3 PEG2000 dendrimers had the least cytotoxic effects on cells. Although G3Si PEG6000 and G4O3 PEG2000 exhibited comparable IC20 values, the cytotoxicity of G4O3 PEG2000 increased rapidly, resulting in a substantially reduced IC50 value. This finding raised concerns about

the safety of G4O3 PEG2000 at higher concentrations or prolonged exposure. G3Si PEG6000 was a preferable option in terms of safety compared to G4O3 PEG2000, as it manifested a higher IC50 value and did not exhibit the rapid increase in cytotoxicity at higher concentrations. These results demonstrate the considerable variance in cytotoxicity among various dendrimers. The findings underscored the potential of G3Si PEG6000 as the superior nanocarrier for biomedical applications, both regarding safety while simultaneously revealing markedly elevated cytotoxic properties of the G4O3 PEG6000. It was found that dendrimers exhibiting the highest cytotoxicity also demonstrated the greatest zeta potential. This observation provided further evidence of the critical role played by the zeta potential in determining the biocompatibility and safety of dendrimers. It is essential to highlight that the amount of cationic quaternary ammonium groups ($R\text{-}NMe_3^+$) did not strictly correlate with zeta potential and cytotoxicity, as dendrimer G3Si PEG6000 did not have the least amount of cationic surface groups but exhibited the lowest zeta potential and cytotoxic properties. This confirms the significant impact of dendrimer composition and their structural characteristics.

The investigation conducted by Jiménez et al. used the 2G-NN16 carbosilane dendrimer for siRNA delivery to the brain, with similar cationic moieties as those presented in the current research. The findings of this study revealed that the tested dendrimers effectively transported siRNA to human normal astrocytes, resulting in gene silencing without inducing cytotoxicity at tested concentrations[53]. Dendrimers G3Si PEG600 and G4O3 PEG2000 did not possess cytotoxic properties, (viability lower than 80%), in concentrations of the 2G-NN16 dendrimer tested in the aforementioned study. It is important to highlight that the studies were performed on different cell lines. The same dendrimer, 2G-NN16, was utilized by Posadas et al. in a study demonstrating its transfection of siRNA into primary rat cortical neuronal cells. The study revealed that the 2G-NN16 dendrimer did not have significant cytotoxicity in all concentrations tested (up to 5 μM)[14]. The investigation by Serramía and colleagues, which employed carbosilane second-generation phloroglucinol-core dendrimers bearing $R\text{-}NMe_3^+$ moieties, also demonstrated the successful delivery of siRNA to normal human astrocytes. Notably, the study highlighted the transfection efficiency of these dendrimers in an in vivo mice model, thereby showing their potential for therapeutic interventions in various neurological disorders[54]. Another very interesting use of carbosilane dendrimers was performed by Białkowska et al. for the purpose of pro-apoptotic siRNA delivery to cancer cells. The cytotoxicity of 2 second generation dendrimers with tertiary or quaternary ammonium groups was tested with MCF-7 cells. Interestingly, the dendrimer with the tertiary ammonium groups appeared more cytotoxic. In their investigation, the team found that dendrimers created a saturated complex with siRNA at a dendrimer/siRNA ratio of 20:1. The resulting complexes exhibited higher levels of cytotoxicity compared to the uncomplexed dendrimers[55]. The studies described above emphasize the critical role of the dendrimer-to-siRNA ratio when developing dendrimer-based delivery systems for therapeutic use. These findings highlight the importance of carefully considering the optimal ratio of dendrimer to siRNA to achieve maximum efficacy while minimizing toxicity. Collectively, these studies demonstrate the vast potential of carbosilane dendrimers for versatile and efficient platforms for siRNA delivery and in other therapeutic applications. However, further research is necessary to optimize their design and ensure their safety and efficacy in clinical settings. These studies provide a strong foundation for future research in the field of dendrimer-based drug delivery and pave the way for the development of new and innovative therapeutic interventions.

Conclusion

The present study involved the biophysical characterization of 4 carbosilane dendrimers and their dendriplexes with siRNA. Our findings provide insights into the complexation process, interaction mechanisms and influences of the dendrimers on the spatial structure of the oligonucleotide as well as the cytotoxic effect of the studied dendrimers on human brain endothelial cells. It was shown that the G4O3 PEG6000 dendrimer forms saturated complexes with siRNA at the least favourable dendrimer/siRNA ratio. It exhibited the highest cytotoxic activity among the tested compounds, rendering it unsuitable for further research. In contrast, the G3O3 PEG6000 dendrimer displayed a saturation point of the complex with the studied siRNA in a molar ratio of about 1/1, suggesting potential as an siRNA carrier. However, due to its high cytotoxicity and poor binding affinity with siRNA, it is not an ideal candidate despite the capacity to transport a greater amount of siRNA. The G3Si PEG6000 and G4O3 PEG2000 dendrimers exhibited optimal levels of dendriplex saturation in a similar molar ratio. The G4O3 PEG2000 dendrimer generates the largest dendriplexes of all the tested dendrimers. Moreover, this dendrimer displays a lower binding affinity towards siRNA and a higher cytotoxicity when compared to the G3Si PEG6000 dendrimer.

This research, therefore, suggests that the G3Si PEG6000 dendrimer is the optimal candidate for further study, as it exhibits the lowest cytotoxicity, the highest affinity for siRNA, exerts a pronounced influence on the conformation of siRNA, displays the smallest hydrodynamic diameter of a non-complexed dendrimer and has the smallest dendriplexes, all the while maintaining a good dendrimer concentration necessary for complex saturation.

While our research has provided valuable insights into the characteristics and potential of the G3Si PEG6000 dendrimers as a siRNA nanocarrier, further studies are crucial to fully understand its potential for biomedical application. Overall, the results of our study suggest a promising direction for further research, and we anticipate that continued efforts in this field will lead to significant advancements in siRNA delivery and disease treatment.

Data availability

The datasets generated during and/or analysed during the current study are available from the corresponding author on reasonable request. Correspondence and should be addressed to S.Z.

Received: 13 November 2023; Accepted: 2 January 2024
Published online: 18 January 2024

References

1. Griffith, F. The significance of pneumococcal types. *J. Hyg.* **27**, 113–159 (1928).
2. Friedmann, T. & Roblin, R. Gene therapy for human genetic disease?. *Science* **175**, 949–955 (1972).
3. Ginn, S. L., Amaya, A. K., Alexander, I. E., Edelstein, M. & Abedi, M. R. Gene therapy clinical trials worldwide to 2017: An update. *J. Gene Med.* **20**, e3015 (2018).
4. Wirth, T., Parker, N. & Ylä-Herttuala, S. History of gene therapy. *Gene* **525**, 162–169 (2013).
5. Kim, B., Park, J. & Sailor, M. J. Rekindling RNAi therapy: Materials design requirements for in vivo siRNA delivery. *Adv. Mater.* **31**, 1903637 (2019).
6. Xu, H., Li, Z. & Si, J. Nanocarriers in gene therapy: A review. *J. Biomed. Nanotechnol.* **10**, 3483–3507 (2014).
7. Hudry, E. & Vandenberghe, L. H. Therapeutic AAV gene transfer to the nervous system: A clinical reality. *Neuron* **101**, 839–862 (2019).
8. Ramamoorth, M. Non viral vectors in gene therapy—An overview. *JCDR* https://doi.org/10.7860/JCDR/2015/10443.5394 (2015).
9. Hollon, T. Researchers and regulators reflect on first gene therapy death. *Nat. Med.* **6**, 6–6 (2000).
10. Waehler, R., Russell, S. J. & Curiel, D. T. Engineering targeted viral vectors for gene therapy. *Nat. Rev. Genet.* **8**, 573–587 (2007).
11. Woods, N.-B. Lentiviral vector transduction of NOD/SCID repopulating cells results in multiple vector integrations per transduced cell: Risk of insertional mutagenesis. *Blood* **101**, 1284–1289 (2003).
12. Nayerossadat, N., Ali, P. & Maedeh, T. Viral and nonviral delivery systems for gene delivery. *Adv. Biomed. Res.* **1**, 27 (2012).
13. Haensler, J. & Szoka, F. C. Polyamidoamine cascade polymers mediate efficient transfection of cells in culture. *Bioconjugate Chem.* **4**, 372–379 (1993).
14. Posadas, I. *et al.* Highly efficient transfection of rat cortical neurons using carbosilane dendrimers unveils a neuroprotective role for HIF-1α in early chemical hypoxia-mediated neurotoxicity. *Pharm. Res.* **26**, 1181–1191 (2009).
15. Abbasi, E. *et al.* Dendrimers: Synthesis, applications, and properties. *Nanoscale Res. Lett.* **9**, 247 (2014).
16. Svenson, S. & Tomalia, D. A. Dendrimers in biomedical applications—Reflections on the field. *Adv. Drug Deliv. Rev.* **57**, 2106–2129 (2005).
17. Peng, S.-F. *et al.* Effects of the nanostructure of dendrimer/DNA complexes on their endocytosis and gene expression. *Biomaterials* **31**, 5660–5670 (2010).
18. Santander-Ortega, M. J., Lozano, M. V., Uchegbu, I. F. & Schätzlein, A. G. 6—Dendrimers for gene therapy. In *Polymers and Nanomaterials for Gene Therapy* (ed. Narain, R.) 113–146 (Woodhead Publishing, 2016). https://doi.org/10.1016/B978-0-08-100520-0.00006-0.
19. Hong, S. *et al.* Interaction of poly(amidoamine) dendrimers with supported lipid bilayers and cells: Hole formation and the relation to transport. *Bioconjugate Chem.* **15**, 774–782 (2004).
20. Leroueil, P. R. *et al.* Wide varieties of cationic nanoparticles induce defects in supported lipid bilayers. *Nano Lett.* **8**, 420–424 (2008).
21. Brandon, J. A., Farmer, B. C., Williams, H. C. & Johnson, L. A. APOE and Alzheimer's disease: Neuroimaging of metabolic and cerebrovascular dysfunction. *Front. Aging Neurosci.* **10**, 180 (2018).
22. Strašák, T. *et al.* Carbosilane metallodendrimers with titanocene dichloride end groups. *Organometallics* **31**, 6779–6786 (2012).
23. Sánchez-Nieves, J., Ortega, P., Muñoz-Fernández, M. A., Gomez, R. & Mata, F. Synthesis of carbosilane dendrons and dendrimers derived from 1,3,5-trihydroxybenzene. *Tetrahedron* **66**, 9203–9213 (2010).
24. Mosmann, T. Rapid colorimetric assay for cellular growth and survival: Application to proliferation and cytotoxicity assays. *J. Immunol. Methods* **65**, 55–63 (1983).
25. Zhang, C. *et al.* siRNA-containing liposomes modified with polyarginine effectively silence the targeted gene. *J. Control. Release* **112**, 229–239 (2006).
26. Buhleier, E., Wehner, W. & Vögtle, F. Cascade'- and 'nonskid-chain-like' syntheses of molecular cavity topologies. *Synthesis* **1978**, 155–158 (2002).
27. Tomalia, D. A. *et al.* A new class of polymers: starburst-dendritic macromolecules. *Polym. J.* **17**, 117–132 (1985).
28. Bermejo, J. F. *et al.* Water-Soluble Carbosilane Dendrimers: Synthesis Biocompatibility and Complexation with Oligonucleotides; Evaluation for Medical Applications. *Chem. Eur. J.* **13**, 483–495 (2007).
29. Dufès, C., Uchegbu, I. F. & Schätzlein, A. G. Dendrimers in gene delivery. *Adv. Drug Deliv. Rev.* **57**, 2177–2202 (2005).
30. Boas, U. & Heegaard, P. M. H. Dendrimers in drug research. *Chem. Soc. Rev.* **33**, 43 (2004).
31. Biswas, S. & Torchilin, V. Dendrimers for siRNA Delivery. *Pharmaceuticals* **6**, 161–183 (2013).
32. Weber, N. *et al.* Characterization of carbosilane dendrimers as effective carriers of siRNA to HIV-infected lymphocytes. *J. Control Release* **132**, 55–64 (2008).
33. Pardridge, W. M. The blood-brain barrier: Bottleneck in brain drug development. *NeuroRx* **2**, 3–14 (2005).
34. Kimura, S. & Harashima, H. Current status and challenges associated with CNS-targeted gene delivery across the BBB. *Pharmaceutics* **12**, 1216 (2020).
35. Shilo, M. *et al.* The effect of nanoparticle size on the probability to cross the blood-brain barrier: An in-vitro endothelial cell model. *J Nanobiotechnology* **13**, 19 (2015).
36. Danaei, M. *et al.* Impact of particle size and polydispersity index on the clinical applications of lipidic nanocarrier systems. *Pharmaceutics* **10**, 57 (2018).
37. Hersh, D. S. *et al.* Evolving Drug delivery strategies to overcome the blood brain barrier. *Curr. Pharm. Des.* **22**, 1177–1193 (2016).
38. Sweeney, M. D., Sagare, A. P. & Zlokovic, B. V. Blood–brain barrier breakdown in Alzheimer disease and other neurodegenerative disorders. *Nat. Rev. Neurol.* **14**, 133–150 (2018).
39. Rabanel, J.-M., Hildgen, P. & Banquy, X. Assessment of PEG on polymeric particles surface, a key step in drug carrier translation. *J. Control. Release* **185**, 71–87 (2014).
40. Conner, S. D. & Schmid, S. L. Regulated portals of entry into the cell. *Nature* **422**, 37–44 (2003).
41. Hanada, S. *et al.* Cell-based in vitro blood-brain barrier model can rapidly evaluate nanoparticles' brain permeability in association with particle size and surface modification. *Int. J. Mol. Sci.* **15**, 1812–1825 (2014).
42. Gao, K. & Jiang, X. Influence of particle size on transport of methotrexate across blood brain barrier by polysorbate 80-coated polybutylcyanoacrylate nanoparticles. *Int. J. Pharm.* **310**, 213–219 (2006).
43. Hashemi, M. *et al.* PEGylation of polypropylenimine dendrimer with alkylcarboxylate chain linkage to improve DNA delivery and cytotoxicity. *Appl. Biochem. Biotechnol.* **177**, 1–17 (2015).
44. Martinho, N. *et al.* Molecular modeling to study dendrimers for biomedical applications. *Molecules* **19**, 20424–20467 (2014).
45. Andrian, T., Pujals, S. & Albertazzi, L. Quantifying the effect of PEG architecture on nanoparticle ligand availability using DNA-PAINT. *Nanoscale Adv.* **3**, 6876–6881 (2021).
46. Yang, J., Zhang, Q., Chang, H. & Cheng, Y. Surface-engineered dendrimers in gene delivery. *Chem. Rev.* **115**, 5274–5300 (2015).
47. Kesharwani, P. *et al.* PAMAM dendrimers as promising nanocarriers for RNAi therapeutics. *Mater Today* **18**, 565–572 (2015).
48. Shcharbin, D., Pedziwiatr, E. & Bryszewska, M. How to study dendriplexes I: Characterization. *J. Control. Release* **135**, 186–197 (2009).

49. Ranjbar, B. & Gill, P. Circular dichroism techniques: Biomolecular and nanostructural analyses—A review. *Chem. Biol. Drug Des.* **74**, 101–120 (2009).
50. Bloomfield, V., Crothers, D. & Tinoco, I. *Nucleic Acids: Structures, Properties, and Function* (University Science Books, 2000).
51. Fasman, G. D. *Circular Dichroism and the Conformational Analysis of Biomolecules* (Springer, 1996). https://doi.org/10.1007/978-1-4757-2508-7.
52. Chang, P. K. C., Prestidge, C. A. & Bremmell, K. E. Interfacial analysis of siRNA complexes with poly-ethylenimine (PEI) or PAMAM dendrimers in gene delivery. *Colloids Surf. B Biointerfaces* **158**, 370–378 (2017).
53. Jiménez, J. L. *et al.* Carbosilane dendrimers to transfect human astrocytes with small interfering RNA targeting human immunodeficiency virus. *BioDrugs* **24**, 331–343 (2010).
54. Serramía, M. J. *et al.* In vivo delivery of siRNA to the brain by carbosilane dendrimer. *J. Control. Release* **200**, 60–70 (2015).
55. Białkowska, K. *et al.* Interaction of cationic carbosilane dendrimers and their siRNA complexes with MCF-7 cells. *Int. J. Mol. Sci.* **22**, 7097 (2021).

Acknowledgements

This work was supported by Grant 2018/30/Z/NZ1/00911 of the Project "NanoTENDO" financed by the National Science Centre, under the M-ERA.NET 2, which has received funding from the European Union's Horizon 2020 research. This research was also funded by Grants from PID2020-112924RB-I00 (MINECO) and CIBER-BBN from ISCIII with assistance from the European Regional Development Fund.

Author contributions

Conceptualization, M.B., K.M. and S.Z.; methodology, M.B., K.M., M.I., E.P-W., E.O. and S.Z.; validation, S.Z.; formal analysis, S.Z. and K.M.; investigation, S.Z., E.O., M.K., Á.M-S., S.M. and T.M.; resources, M.B., S.G-G., P.O.L. and F.J.d.l.M.; data curation, K.M.; writing—original draft preparation, S.Z.; writing—review and editing, K.M. M.B., M.I., E.P-W., S.G-G., P.O.L., F.J.d.l.M. and S.Z.; visualisation, S.Z.; supervision, K.M.; project administration, M.B., K.M.; funding acquisition, M.B.

Competing interests

The authors declare no competing interests.

Additional information

Supplementary Information The online version contains supplementary material available at https://doi.org/10.1038/s41598-024-51238-w.

Correspondence and requests for materials should be addressed to S.Z.

Reprints and permissions information is available at www.nature.com/reprints.

Publisher's note Springer Nature remains neutral with regard to jurisdictional claims in published maps and institutional affiliations.

Open Access This article is licensed under a Creative Commons Attribution 4.0 International License, which permits use, sharing, adaptation, distribution and reproduction in any medium or format, as long as you give appropriate credit to the original author(s) and the source, provide a link to the Creative Commons licence, and indicate if changes were made. The images or other third party material in this article are included in the article's Creative Commons licence, unless indicated otherwise in a credit line to the material. If material is not included in the article's Creative Commons licence and your intended use is not permitted by statutory regulation or exceeds the permitted use, you will need to obtain permission directly from the copyright holder. To view a copy of this licence, visit http://creativecommons.org/licenses/by/4.0/.

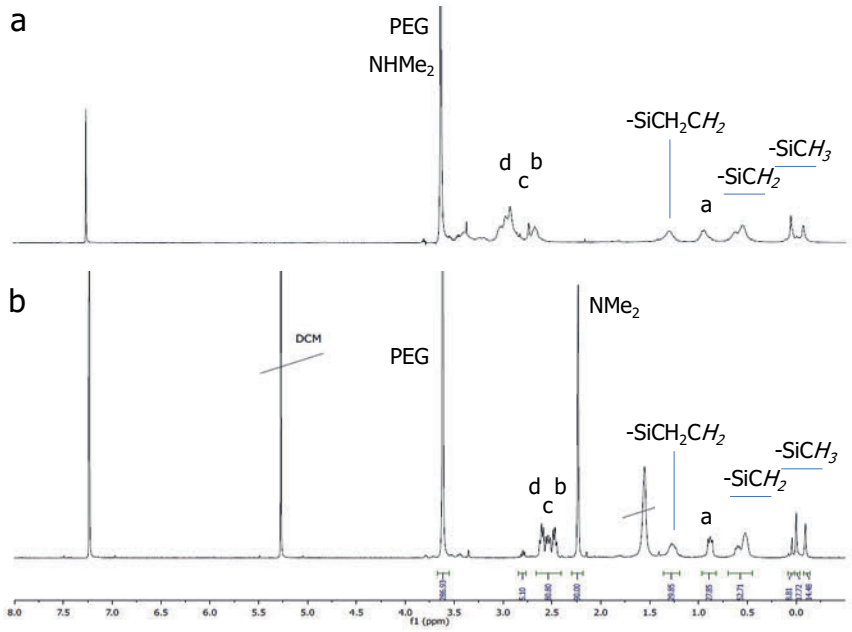
© The Author(s) 2024

Supplementary information for:

Synthesis and Biophysical Evaluation of Carbosilane Dendrimers as Therapeutic siRNA Carriers

Serafin Zawadzki [1,2], Ángela Martín-Serrano [3], Elżbieta Okła [1], Marta Kędzierska [1], Sandra Garcia-Gallego [3,4,5], Paula O. López [3,4,5], Francisco J. de la Mata [3,4,5], Sylwia Michlewska [6], Tomasz Makowski [7], Maksim Ionov [1,8], Elżbieta Pędziwiatr-Werbicka [1], Maria Bryszewska [1] and Katarzyna Miłowska [1]

1. Department of General Biophysics, Faculty of Biology and Environmental Protection, University of Lodz, 141/143 Pomorska St., 90-236 Lodz, Poland; 2. BioMedChem Doctoral School of the University of Lodz and Lodz Institutes of the Polish Academy of Sciences, 21/23 Matejki St., 90-237 Lodz, Poland; 3. University of Alcalá, Department of Organic and Inorganic Chemistry, IQAR, 28805 Madrid, Spain; 4. Networking Research Center on Bioengineering, Biomaterials and Nanomedicine (CIBER-BBN), 28029 Madrid, Spain; 5. Ramón y Cajal Health Research Institute (IRYCIS), 28034 Madrid, Spain; 6. Laboratory of Microscopic Imaging and Specialized Biological Techniques, Faculty of Biology and Environmental Protection, University of Lodz, Banacha 12/16, 90-237 Lodz, Poland; 7. Centre of Molecular and Macromolecular Studies, Polish Academy of Sciences, Sienkiewicza 112, 90-363 Lodz, Poland; 8. Mazovian Academy in Plock, Collegium Medicum, Faculty of Medicine, 2 Dabrowskiego Sq, 09-402 Plock, Poland



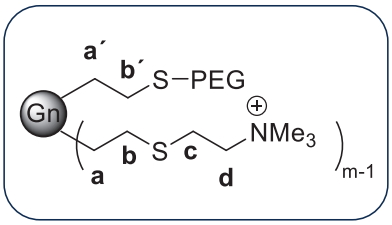


Figure S1. a) ^{1}H-NMR ($CDCl_3$) of intermediate compound $G_3Si(SPEG6000)(SNMe_2HCl)_{31}$. The signal at 3,60 ppm corresponds to PEG and NMe_2·HCl, which are overlapped. **b)** ^{1}H-NMR ($CDCl_3$) of intermediate compound $G_3Si(SPEG6000)(SNMe_2)_{31}$. The signal at 3,60 ppm corresponds to PEG and the signal at 2,25 ppm corresponds to NMe_2

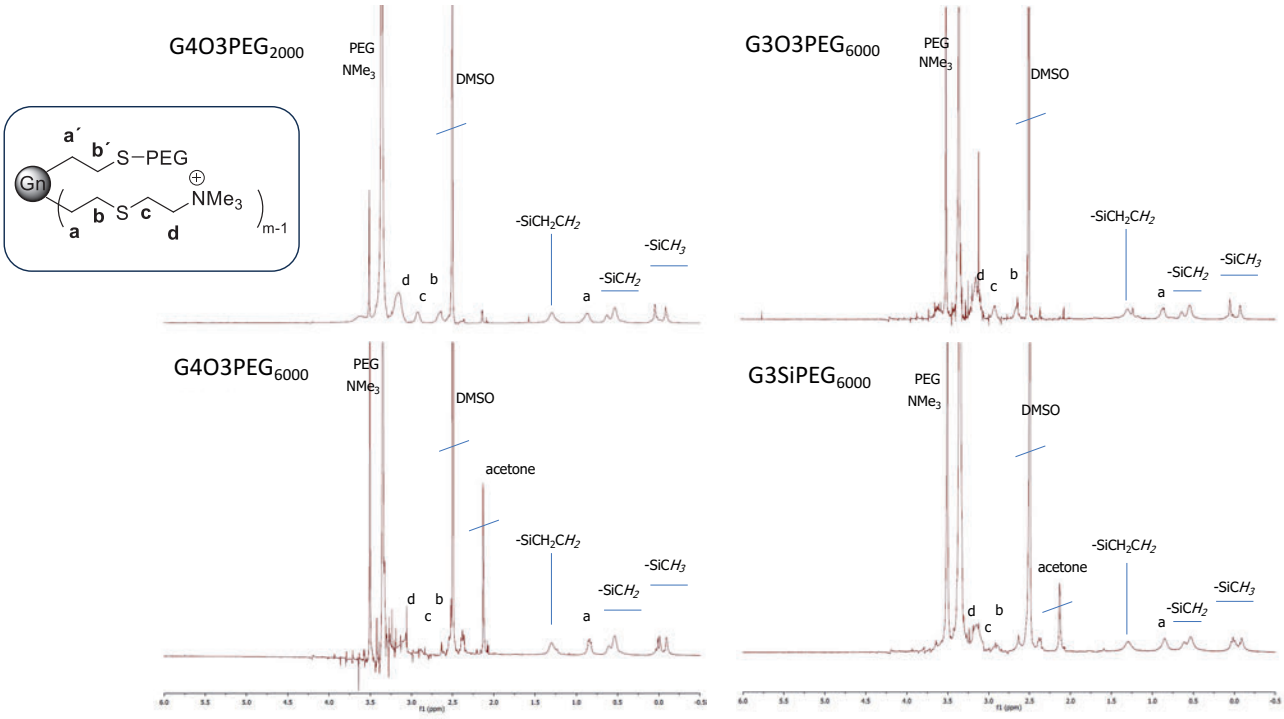


Figure S2. ^{1}H-NMR (DMSO) of the final compounds. The signal at 3.40 ppm corresponds to PEG and NMe_3, which are overlapped.

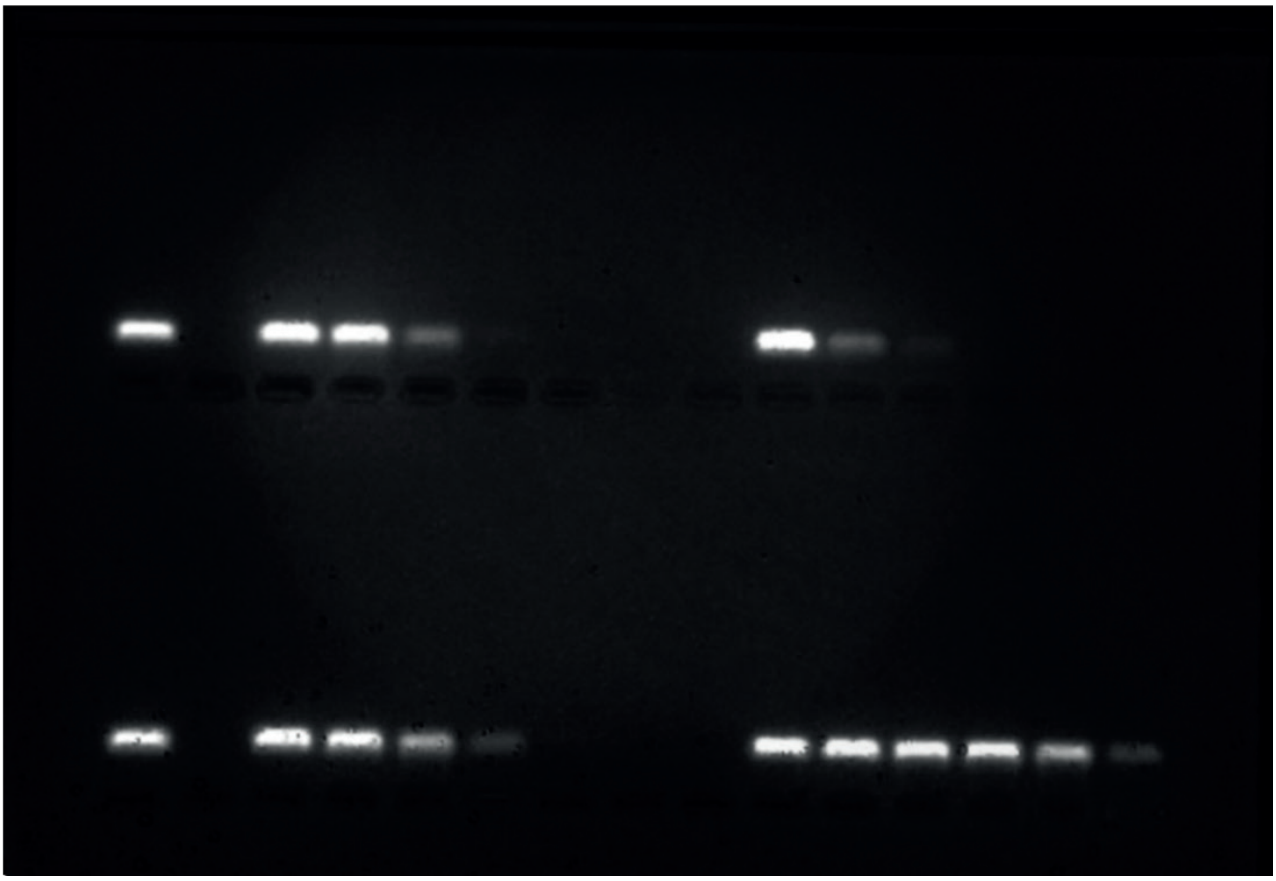


Figure S3. Original image corresponding to the Figure 15 in the main manuscript. Analysis of dendrimer/siRNA complexes in different ratios in 3% agarose gel with GelRed. Complexes were prepared in 10 mmol/l PBS.

scientific reports

Check for updates

OPEN

Structural and conformational rearrangements of human serum albumin, transferrin, and blood plasma induced by carbosilane dendrimer therapeutic delivery system

Serafin Zawadzki[1,2]✉, Elżbieta Okła[1], Sylwia Michlewska[3], Tomasz Makowski[4], Adam Buczkowski[5], Paula O. López[6,7], Francisco J. de la Mata[6,7,8], Maksim Ionov[1,9], Maria Bryszewska[1] & Katarzyna Miłowska[1]✉

Upon intravenous administration, nanoparticles quickly become enveloped by plasma proteins, lipids, and sugars, forming a biomolecular corona that redefines their biological identity and directs systemic distribution. In this study, we examine a third-generation, positively charged, PEGylated carbosilane dendrimer engineered for the delivery of therapeutic siRNA across the blood-brain barrier. Employing a comprehensive array of analytical techniques—including fluorescence quenching assays, circular dichroism spectroscopy, isothermal titration calorimetry, atomic force microscopy, and transmission electron microscopy—we characterize the dendrimer's binding kinetics and thermodynamics, and its impact on structure of human serum albumin, transferrin and complex environment of plasma. Our findings reveal that the dendrimer induces distinct conformational rearrangements at both tertiary and secondary levels, with thermodynamic analyses indicating that the interactions are predominantly driven by favorable entropy changes and multivalent binding. Furthermore, the dendrimer appears to promote a reorganization of plasma components, potentially leading to aggregation and misfolding reminiscent of fibril formation. Collectively, these findings provide critical insights into the more profound understanding of nanoparticle-protein interactions affecting the biodistribution and hemocompatibility of nanovectors and lay a foundation for further research aimed at safer and more effective therapeutic applications.

Keywords Protein corona, Carbosilane dendrimer, Plasma protein interactions, Hemocompatibility

Abbreviations

AFM	Atomic force microscopy
APOE4	Apolipoprotein E4

[1]Department of General Biophysics, Faculty of Biology and Environmental Protection, University of Lodz, 141/143 Pomorska St., Lodz 90-236, Poland. [2]Bio-Med-Chem Doctoral School of the University of Lodz and Lodz Institutes of the Polish Academy of Sciences, University of Lodz, Matejki 21/23, Lodz 90-237, Poland. [3]Laboratory of Microscopic Imaging and Specialized Biological Techniques, Faculty of Biology and Environmental Protection, University of Lodz, Banacha12/16, Lodz 90-237, Poland. [4]Centre of Molecular and Macromolecular Studies, Polish Academy of Sciences, Sienkiewicza 112, Lodz 90-363, Poland. [5]Division of Biophysical Chemistry, Department of Physical Chemistry, Faculty of Chemistry, University of Lodz, Pomorska 163/165, Lodz 90-236, Poland. [6]Department of Organic and Inorganic Chemistry, IQAR, University of Alcalá, Madrid 28805, Spain. [7]Networking Research Center on Bioengineering, Biomaterials and Nanomedicine (CIBER-BBN), Madrid 28029, Spain. [8]Ramón y Cajal Health Research Institute (IRYCIS), Madrid 28034, Spain. [9]Faculty of Medicine, Collegium Medicum, Mazovian Academy in Plock, 2 Dabrowskiego Sq, Plock 09-402, Poland. ✉email: serafin.zawadzki@edu.uni.lodz.pl; katarzyna.milowska@biol.uni.lodz.pl

BBB	Blood-brain barrier
CD	Circular dichroism
CNS	Central nervous system
HSA	Human serum albumin
ITC	Isothermal calorimetric titration
MPS	Mononuclear phagocyte system
PEG	Polyethylene glycol
Phe	Phenylalanine TEM
Trp	Tryptophan
Tf	Human transferrin
Tyr	Tyrosine

A wealth of work has been published providing extensive insight into the evaluation and potential applications of dendrimer-based nanosystems in treating brain diseases[1–8]. Our research investigated a third-generation, positively charged, PEGylated carbosilane dendrimer and its complex with siRNA targeted against the apolipoprotein E4 (APOE4) gene, a major genetic risk factor for Alzheimer's disease[9]. Recognizing that the hemocompatibility of intravenously administered nanoparticles is critical to their therapeutic efficacy and safety, our study examined explicitly the dendrimer's interactions within plasma. Accordingly, in this manuscript we focus exclusively on dendrimer–plasma interactions. Upon injection into the bloodstream, nanoparticles rapidly encounter plasma proteins, lipids, and sugars, which immediately cover their surface, forming a "biomolecular corona". This process leads to the development of a new "biological identity" for the nanoparticles. The nanoparticle's size, shape, and surface chemistry, which is collectively termed "synthetic identity", directly influences the formation of a biomolecular layer on the nanoparticle surface. Both the nanoparticle's synthetic identity and its acquired biological identity dictate the nanoparticle fate *in vitro* and, ultimately, in systemic responses[10,11]. The inherent complexity and variability of biomolecular layers conjugated with a nanovector arise from the diverse interactions and functions of macromolecules within the physiological environment. Proteins play a critical role in shaping the biomolecular corona. The Plasma Proteome Database has annotated a total of 7614 plasma protein products derived from 3778 unique genes, highlighting the plasma proteome as one of the most complex and diverse among body fluids[12]. Initially, proteins abundant in serum bind to the nanoparticle surface, forming a transient "soft corona" that is later replaced by less abundant but higher affinity proteins, resulting in the formation of the "hard corona". This competitive adsorption phenomenon is known as the Vroman effect[13]. The formed protein corona is a highly dynamic 3D assembly of proteins that are bound to each other[14]. Comprehensive data analysis across multiple studies has identified a distinct set of proteins, termed the "adsorbome", exhibiting a high affinity for nanomaterials. The analysis suggests that a typical plasma protein corona comprises approximately 2–6 high-abundance proteins and a larger pool of low-abundance proteins[15]. The adsorbed proteins' composition and conformation can significantly influence the fate and impact nanoparticles' biological functionality by either enhancing or hindering it. Nanoparticles can disrupt native protein conformation by inducing partial unfolding, misfolding, aberrant secondary structures, oxidative damage, or complete denaturation. These alterations not only trigger an immunogenic response but also compromise critical protein-protein interactions, cellular signaling, and DNA transcription processes[16]. Nanoparticles can induce conformational changes in proteins that lead to fibril formation associated with neurodegenerative diseases such as Parkinson's, Alzheimer's, and Creutzfeld-Jacob disease. Fibrillation occurs when partially or fully unfolded proteins aggregate into β-sheet-rich structures, which subsequently elongate and organize into large, insoluble amyloid fibrils. Linse et al. demonstrated that nanoparticles—including copolymers, cerium oxide particles, carbon nanotubes, and quantum dots—accelerated the fibrillation of β2-microglobulin by concentrating proteins on their surfaces, thereby facilitating oligomer formation[17]. In contrast, gold nanoparticles have been found to inhibit this fibrillation process, highlighting their potential as therapeutic agents for these conditions[18,19]. The altering of adsorbed proteins' structural and functional properties may result in immune cells' recognition and uptake. Specifically, such interactions could induce abnormal unfolding that leads to the formation of novel "cryptic" conformational epitopes or destabilize native protein structures to reveal previously hidden continuous epitopes[20]. Recognition by the immune system may also be caused by direct opsonization, such as the adsorption of immunoglobulins, coagulation proteins, and complement proteins. These reduce the circulation time of nanoparticles by enhancing recognition by the macrophage receptors and clearance by the mononuclear phagocyte system (MPS), consequently leading to inflammation, nanoparticle accumulation in organs, and even immune system impairment. Conversely, adsorbed dysopsonins, including most apolipoproteins, decrease nanoparticle clearance, extending their circulation time and prolonging their *in vivo* persistence, ultimately enhancing their efficacy.

Among the various plasma proteins typically found in the protein corona, apolipoproteins significantly influence the ability of the nanoparticles to cross biological barriers. Specifically, the presence of Apo B and Apo E has been shown to enhance the uptake of liposomes by hepatocytes, and Apo A-I, Apo E, and Apo B-100 significantly improve the transport of nanoparticles into the central nervous system[21–23]. The variation in systemic biodistribution arises from cell-type-specific receptor expression profiles, which may cause enhanced internalization depending on the protein corona composition. At the same time, the protein corona can hinder internalization by creating a protein layer between the nanoparticle and the cell membrane. This steric hindrance reduces the nanoparticle's ability to interact with cell surface receptors and impedes internalization. The exact mechanism mitigates the nanovector's cytotoxic effects on vessel walls and blood components, such as eryptosis[24,25]. Furthermore, the protein corona can modulate nanoparticle-thrombocyte interactions influencing thrombogenicity[26,27].

To counteract these adverse effects—building on the success of attaching polyethylene glycol (PEG) chains to therapeutic proteins for improved systemic delivery— PEGylation of nanoparticles has become a widely adopted strategy for enhancing efficiency and safety. PEG is often favored due to its well-documented biocompatibility, long history of safe use in humans, and classification as Generally Regarded as Safe (GRAS) by the Food and Drug Administration (FDA). By forming a hydrated steric barrier around the nanoparticle, PEG effectively reduces protein adsorption, minimizes nanoparticle aggregation, and limits opsonization and phagocytosis, thereby enhancing therapeutic efficacy. Consequently, PEGylated nanovectors exhibit prolonged systemic circulation, reduced immunogenicity, and improved stability in various biological environments. PEGylation mitigates hemolysis and facilitates nanoparticle penetration through challenging biological barriers, such as the BBB. Although PEG reduces non-specific protein adsorption, studies have shown that PEGylated surfaces still acquire a protein corona. Notably, all these effects depend highly on PEG architecture factors such as chain length and surface density[28–31].

A comprehensive understanding of nanocarrier–blood protein interactions is essential for optimizing nanoparticle-based delivery systems. Our objective was to develop a nanovector that evades immune recognition, prolongs systemic circulation, and efficiently transports siRNA across the blood-brain barrier, thereby offering a promising therapeutic strategy for Alzheimer's disease[9]. This study assesses protein interactions with the third-generation carbosilane dendrimer G3Si PEG6000, specifically evaluating its interactions with human serum albumin, transferrin, and whole plasma. By elucidating the mechanistic aspects of protein corona formation, we establish a foundation for future assessments of its impact on blood morphotic elements, hemocompatibility, and therapeutic efficacy.

Materials and methods

Dendrimer

Dendrimer with a silicon atom core, surface tertiary ammonium groups, and single polyethylene glycol (PEG) (6000) – G3Si PEG6000 with chemical formula $C_{601}H_{1324}I_{30}N_{31}O_{135}S_{32}Si_{29}$ and molar weight 16794.81 g/mol is presented in Fig. 1. The studied dendrimer was diluted in a phosphate buffer solution of 7.4 pH. The synthesis and biophysical characterization of the dendrimer, along with its complex with siRNA, was described in previous work[32].

Other reagents

Human serum albumin (HSA) was obtained from Sigma-Aldrich (St. Louis, MO, USA), while human transferrin (Tf) was sourced from Biorbyt Ltd. (Cambridge, UK). Additional chemical reagents, including sodium dihydrogen phosphate and disodium hydrogen phosphate, were sourced from Chempur (Piekary Śląskie, Poland). All reagents were of analytical grade, and solutions were prepared using Milli-Q purified water to ensure high purity and reproducibility.

Fluorescence quenching of HSA and Tf

Tryptophan fluorescence quenching of HSA and Tf (1 μM) was studied by titrating increasing concentrations of dendrimer G3Si PEG6000 (4–20 μM). Measurements were conducted at 25 °C in 1-cm quartz cuvettes using a Perkin-Elmer LS-55 spectrofluorimeter (Perkin-Elmer, Waltham, MA, USA). The excitation and emission

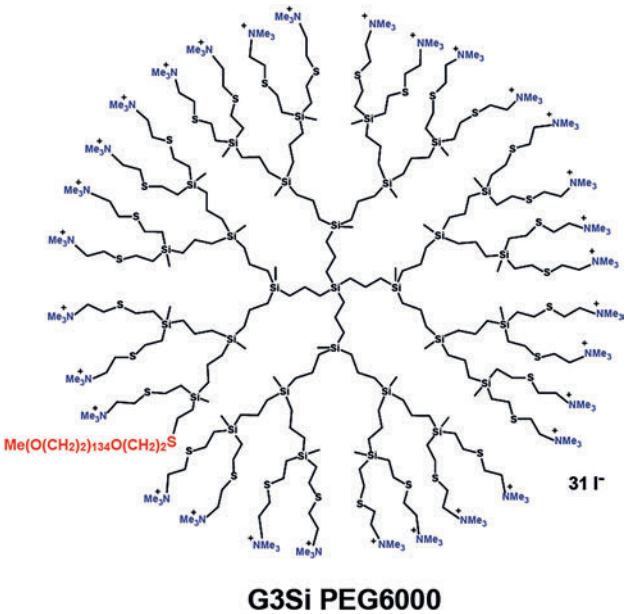


Fig. 1. Structure of studied dendrimer G3Si PEG6000.

wavelengths were at 305 and 445 nm, with the excitation and emission slit widths being set to 2.5 and 9 nm, respectively. The experiment was performed in 3 repetitions.

Circular dichroism of HSA and Tf

Circular dichroism (CD) measurements were performed to examine HSA and Tf (0.5 μM) in the presence of the stepwise increasing concentration (0.5–20 μM) of the G3Si PEG6000 dendrimer, without isolating complexes. The experiments were conducted using a Jasco J-815 CD spectrometer (Jasco International Co., Ltd., Tokyo, Japan) with 5-mm path length quartz cuvettes at a constant temperature of 25 °C. CD spectra of the proteins alone and in the presence of the dendrimer were measured between 195 and 260 nm. Thus, the resulting signals of the proteins in the presence of the dendrimer represents ensemble averages of free protein, free dendrimer, and complexed species. The percentage of the protein secondary structure content in the presence of the G3Si PEG6000 dendrimer was calculated using CDNN circular dichroism spectroscopy deconvolution software version 2.1 (Applied Photophysics Ltd., Surrey, United Kingdom). All samples were prepared in a 10 mM phosphate buffer, and the same buffer was used as the baseline for the measurements. The experiment was performed in 3 repetitions.

Isothermal calorimetric titration of HSA

An isothermal calorimetric titration (ITC) (LV Affinity ITC with gold cells, TA Instruments) was performed in order to measure the thermodynamics of interactions between HSA and the G3Si PEG6000 carbosilane dendrimer in aqueous 10 mM phosphorous buffer solution pH 7.4. HSA solution (182 μl; 10 μM; in cell) was titrated by adding 31 of 5 μl doses of a 0.2 mM dendrimer solution (from the syringe). Pre-isolation of complexes was not used. The time interval between successive injections was 300 s. Measurements of the thermal effects of the titration were carried out at 25 °C with a stirring rate of 125 RPM in an auto-equilibrate mode. During the titration, the molar ratio of dendrimer to HSA, increased from 1.1/1 to 27/1. The thermal effects of diluting the dendrimer solution (in the syringe) in 10 mM phosphorous buffer solution pH 7.4 (in the cell) were determined independently, maintaining the same calorimeter parameters as for the proper titrations. The thermal effects of the direct interaction of HSA with dendrimer were calculated by subtracting the effects of dendrimer dilution from the corresponding thermal effects of the protein solution's titration with the dendrimer solution. The determined binding isotherms describing the thermal effects of the direct interaction of HSA with studied dendrimers as a function of the titrated solution composition were analyzed in NanoAnalyze software by non-linear multiparameter regression using the independent-site model to calculate the stoichiometric parameter, equilibrium binding constant and the standard thermodynamic functions describing the process of receptor macromolecule (protein) binding with molecules of studied dendrimers: enthalpy, entropy and Gibbs free energy.

Atomic force microscopy of HSA and plasma

The morphology of HSA, plasma, and their conjugates with the G3Si PEG6000 dendrimer was analyzed using atomic force microscopy (AFM) on droplets deposited onto mica (Grade V-1 Muscovite). Whole-blood donations from $n = 3$ healthy donors were collected by the Regional Centre for Blood Donation and Haemotherapy in Lodz into CPD (citrate–phosphate–dextrose) anticoagulant blood-bag systems. All experiments used individual-donor plasma (no pooling was applied). Human plasma was separated from blood by centrifuging it at 4200 rpm for 15 min. Conjugates were prepared by mixing HSA or plasma with the dendrimer in PBS and incubated at room temperature for 20 min. AFM measurements were conducted using a Flex Axiom Nanosurf apparatus equipped with a C3000 controller (Nanosurf AG, Liestal, Switzerland). The experiments employed dynamic force mode (tapping mode) and phase imaging to capture detailed surface characteristics. The analysis was performed using HI'RES-C14/CR-AU μmasch probes with a typical tip radius of < 1 nm, a spring constant of 5 N/m, and a resonance frequency of 160 kHz. The resulting images were recorded at a resolution of 512 × 512 data points. Image processing and analysis were conducted using the Scanning Probe Image Processor (SPIP) software (Image Metrology, Hørsholm, Denmark).

Transmission electron microscopy of HSA and plasma

The morphological characteristics and spatial distribution of HSA, plasma, and their conjugates with the G3Si PEG6000 dendrimer were analyzed using a JEOL-1010 transmission electron microscope (Japan) at 100,000× magnification. Whole-blood donations from $n = 3$ healthy donors were collected by the Regional Centre for Blood Donation and Haemotherapy in Lodz into CPD (citrate–phosphate–dextrose) anticoagulant blood-bag systems. All experiments used individual-donor plasma (no pooling was applied). Human plasma was separated from blood by centrifuging it at 4200 rpm for 15 min. The conjugates were formed by mixing HSA or plasma with the dendrimer in PBS at room temperature for 20 min. A molar ratio of 1:9 HSA to dendrimer was employed, representing the optimal saturation ratio determined through ITC analysis, with the dendrimer concentration set at 36 μM. For plasma samples, the same dendrimer concentration was added to a 55% plasma solution to prepare 100 μL solution. 15 μL of either the conjugate or the unbound protein was applied to a 200-mesh copper grid coated with carbon and allowed to adhere for 10 min. Both samples were stained with a 2% (w/v) uranyl acetate solution for 20 min to enhance contrast. To enhance legibility, images have been sharpened.

Results and discussion

Despite extensive efforts to minimize the protein adsorption on nanoparticle surfaces, complete elimination of this phenomenon remains unattainable. The inevitable formation of a protein corona has profound implications for nanoparticle behavior, influencing their biological fate, stability, and therapeutic efficacy. This realization has redirected many research efforts toward understanding the relationship between nanocarrier surface

properties and nanoparticle-protein interactions. We employed a comprehensive suite of analytical techniques, including fluorescence quenching, circular dichroism, isothermal titration calorimetry, transmission electron microscopy, and atomic force microscopy, to discover the interactions between the G3Si PEG6000 dendrimer and plasma proteins. Human serum albumin (HSA) and Transferrin (Tf) are often selected as model proteins due to their critical roles in blood plasma and their relevance in the physiological processes affecting recognition by the immune system, cell internalization, toxicity, drug stability, half-life, biodistribution and BBB permeability[21,23,33–37]. This approach allowed direct comparisons with other nanovectors studied by different research teams and contributed to a broader and more standardized framework for evaluating nanoparticle behavior in biological systems. We extended our investigation to include interactions with plasma proteins to assess the studied dendrimer behavior in complex, physiologically relevant environments.

Fluorescence quenching of HSA and Tf

We employed fluorescence quenching assay as it is a very sensitive method for providing a basis for quantitative measurements, giving insight into measuring drugs, drug carriers or xenobiotics, and protein interactions on a molecular level. The intrinsic fluorescence of proteins primarily arises from aromatic amino acid residues—tryptophan (Trp), tyrosine (Tyr), and phenylalanine (Phe). Changes in the emission spectrum of Trp resulting in fluorescence quenching often indicate alterations in protein conformation, excited state reactions, energy transfer, the formation of ground state complexes, and collision quenching[38]. From a structural perspective, HSA is composed of a single amino acid chain that folds into three homologous α-helical domains labeled I, II, and III. Each domain contains ten helices, which are further divided into two subdomains: a six-helix subdomain (A) and a four-helix subdomain (B). The first four helices in both subdomains form similar anti-parallel α-helix bundles. A single tryptophan residue is located in subdomain IIA. As anticipated, gradually adding the dendrimer to the HSA protein solution led to a decrease in tryptophan fluorescence intensity (Fig. 2). In the same manner, the red shift of the fluorescence spectra was observed.

Building upon our findings with HSA, our investigation was extended to explore the interactions between the dendrimer and Tf. This analysis allowed us to compare and contrast the dendrimer's behavior with different protein targets, providing a more comprehensive understanding of its potential biological interactions. Tf is a bilobal protein, with each lobe composed of two domains consisting of a series of α-helical subdomains arranged around a central β-sheet scaffold. Tf contains eight tryptophan residues, three located in the N-lobe and five in the C-lobe[39]. A sequence of initial rapid quenching, recovery and gradual diminution of fluorescence was observed. These observations suggest a complex, multi-step interaction between the dendrimer and tested proteins, potentially involving multiple binding sites. The initial rapid quenching followed by fluorescence recovery may indicate conformational changes in the protein structure or rearrangement of the protein-dendrimer complex. The subsequent slow diminution in fluorescence intensity likely represents a more gradual process of dendrimer-protein association or further structural modifications. The persistent red shift in the fluorescence spectra corroborates the hypothesis of alterations in the local environment of the tryptophan residue, potentially due to dynamic changes in protein conformation or dendrimer binding.

Fluorescence quenching can be categorized into two distinct mechanisms: static and dynamic. Dynamic quenching (collisional quenching) arises from the collisions between these molecules when the fluorophore returns to its ground state without emitting a photon, thus decreasing fluorescence intensity. Static quenching occurs in the ground state when the quencher binds to the fluorophore, forming a non-fluorescent complex that effectively reduces the overall fluorescence. The type of quenching can be speculated based on the Stern–Volmer plots. The classical Stern-Volmer equation describes the decrease in fluorescence intensity as a function of the concentration of a collisional quencher:

$$F_0/F = 1 + k_q \tau_0 [Q]$$

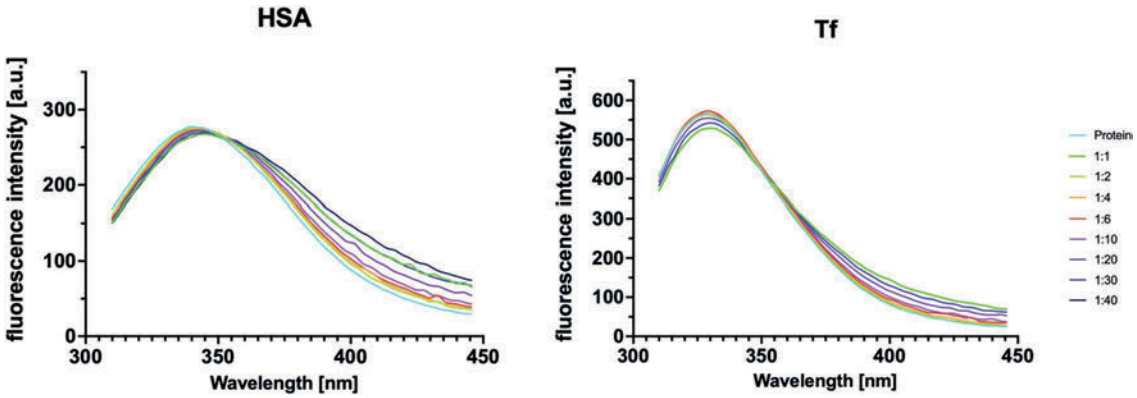


Fig. 2. Fluorescence emission spectra of human serum albumin and transferrin in the presence of increasing concentrations of the G3Si PEG6000 dendrimer at a wavelength ranging from 310 to 445 nm.

Protein	$K_{sv}\ \left[M^{-1}\right]$	$K_q\ \left[M^{-1}s^{-1}\right]$	$K_b\ \left[M^{-1}\right]$
HSA	8.3×10^2	1.5×10^{11}	3.3×10^2
Tf	1.8×10^3	5.9×10^{11}	9.6×10^2

Table 1. Protein-dendrimer interaction parameters were determined from fluorescence quenching data.

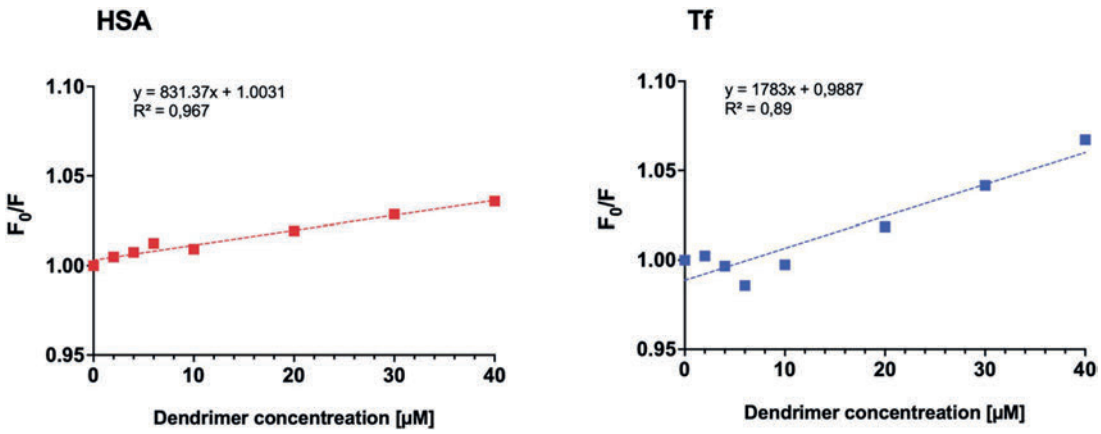


Fig. 3. Stern–Volmer plots of the human serum albumin and transferrin fluorescence quenching in the presence of increasing concentrations of the G3Si PEG6000 dendrimer.

In this equation, F_0 and F represent the fluorescence intensities in the absence and presence of the quencher, respectively. The term k_q denotes the bimolecular quenching constant, while τ_0 is the lifetime of the fluorophore in the absence of a quencher. The concentration of the quencher is indicated by $[Q]$. The Stern-Volmer quenching constant, K_{sv}, is defined as the multiplication of k_q and τ_0. It has been widely reported that the maximum bimolecular quenching rate constant for various quenchers interacting with biopolymers is approximately 2.0 $\times$ 10^{10} M^{-1} s^{-1}, serving as a reference threshold for diffusion-controlled quenching processes[40,41]. Given that in our experiment, the k_q values for the quenching of both studied proteins by the G3Si PEG6000 dendrimer exceed 2.0 $\times$ 10^{10} M^{-1} s^{-1}, it can be inferred that, within the tested concentration range, the observed fluorescence quenching predominantly occurs via a static mechanism. While dendrimer–HSA interactions are likely governed by a linear quenching process, dendrimer–Tf interactions involve an additional variable. Tf contains eight Trp residues, each having potentially distinct microenvironments and varying degrees of accessibility to the quencher, resulting in a more complex fluorescence quenching behavior. The Stern–Volmer plot for the Tf–G3Si PEG6000 deviates from linearity toward the x-axis up to 1:10 molar ratio, also decreasing the square of the correlation coefficient (R^2). This non-linearity likely arises from conformational changes in the tertiary structure of Tf, leading to differential accessibility of fluorophores to the quencher[38].

To determine the binding constant K_b, the experimental data were fitted to the following equation:

$$\log\left(F_0/_F\right) = logK_b + nlog\,[Q]$$

where n is the number of binding sites. As presented in Table 1, the K_{sv} for the Tf-G3Si PEG6000 conjugate is approximately twofold higher than that for the HSA: G3Si PEG6000 conjugate, yielding a markedly steeper Stern–Volmer plot (Fig. 3). Consequently, this indicates that energy transfer occurs substantially more efficiently between Tf and the G3Si PEG6000 dendrimer compared to the interaction with HSA. Furthermore, the K_b for the Tf-G3Si PEG6000 is nearly three times greater than that for the HSA conjugate, which suggests a markedly higher binding affinity between Tf and the G3Si PEG6000 dendrimer (Table 1). A comparative analysis of the k_q and the K_{sv} for the tested dendrimer-HSA interaction reveals distinctive characteristics relative to other compounds documented in the literature. The k_q value of β-Carboline silver compounds, which exhibit potential for crossing the BBB, indicates the quenching mechanism to be static with the k_q value reaching up to 5.37 $\times$ 10^{13} M^{-1} s^{-1}[42]. Similarly, studies on α-Cembrenediol, known for its neuroprotective effects, show the k_q value reaching up to 1.49 $\times$ 10^{11} M^{-1} s^{-1}, indicative of the static quenching mechanism of HSA[43]. Another well-characterized group of compounds includes the first-generation polyphenolic carbosilane dendrimers, which exhibit quenching rate constants of up to 1.27 $\times$ 10^{11} M^{-1} s^{-1}, also suggesting quenching the HSA fluorescence via the static mechanism[44]. A study of tyrosine-modified polyethyleneimines designed for siRNA delivery exhibited k_q values in the range from 4.6 $\times$ 10^{12} to 1.5 $\times$ 10^{14} M^{-1} s^{-1} for the different polymers studied, indicating also the static quenching mechanism of HSA[45]. These findings highlight how different physicochemical properties influence protein interactions. Compounds with similar structures or

applications, such as polyphenolic carbosilane dendrimers, β-carboline silver complexes, and tyrosine-modified polyethyleneimines, exhibit strong and potentially biologically relevant interactions with serum albumins. Like the studied G3Si PEG6000 dendrimer, these compounds demonstrate high binding affinities and predominantly static quenching mechanisms, suggesting their potential to influence protein conformation and function in biological environments.

Circular dichroism of HSA and Tf

Circular dichroism (CD) is a spectroscopic technique based on the differential absorption of left- and right-handed circularly polarized light by chiral molecules. CD measurements of proteins affected by nanovectors in the far-ultraviolet regions are primarily influenced by the $n\rightarrow\pi^*$ and $\pi\rightarrow\pi^*$ electrons energy transition of their amide groups. These transitions are sensitive to the geometry changes of the polypeptide backbone, resulting in spectral changes that provide insight into alterations in the secondary structure.

CD fluorescence spectra revealed that both HSA and Tf undergo conformational changes upon interaction with the G3Si PEG6000 dendrimer (Fig. 4). The CD spectra of HSA in the absence of the studied dendrimer due to the $\pi\rightarrow\pi^*$ transition show a single positive ellipticity at 193 nm and a negative band at 208 nm. The second negative band at 222 nm is due to the $n\rightarrow\pi^*$ characteristic for the α-helix rich protein. The observed spectra flattening indicative of loss of α-helical content were most pronounced after the initial addition of the dendrimer in the 1:1 ratio of HSA to dendrimer and continued to evolve, with a less pronounce shift occurring at the 1:15 ratio of HSA to dendrimer. This pattern was further confirmed by deconvolution analysis, which provided estimates of the secondary structure composition for each CD spectrum (Fig. 5). The α-helical content of HSA decreased by approximately 13% at a 1:1 HSA-to-dendrimer ratio, with a further reduction of about 6.2% at the 1:15 ratios of HSA to dendrimer. The structural changes in HSA were more pronounced than those observed for Tf. The Tf spectra in the absence of the studied dendrimer due to the $n\rightarrow\pi^*$ transition show a single positive ellipticity at 195 nm and a negative band at 215 nm, indicating protein with a high β-sheet secondary structure content. The first significant change in the Tf structure occurred at a 1:2 Tf- dendrimer ratio, leading to a 3.7% reduction in α-helical content. A second major structural shift was observed at a 1:20 ratio, where a slight increase in α-helical content was accompanied by a decrease in anti-parallel content.

The findings suggest a multi-step interaction mechanism for the formation of the G3Si PEG6000–protein conjugate. A multi-step conformation shift typically suggests the presence of multiple domains affected. We hypothesize that initially, the dendrimer associates with the protein, partially unfolding it, and upon the increase of the dendrimer concentration, the conjugate transitions into a highly misfolded state. This integrated perspective allows for further comparisons across different nanovectors and research studies, advancing the understanding of nanoparticle behavior and protein interaction mechanisms. The conjugation of the protein with the polyphenolic carbosilane dendrimers at 1:10 molar ratio reduces the α-helical content up to 53.40%[44]. The effect of the β-Carboline silver compounds on the HSA structure shown similar conformational shift reaching 35.63% of HSA α-helical structure at the molar ratio of 1:5000 HSA to tested compounds[42]. Similarly, the dendrimer G3Si PEG6000, pegylated gold nanoparticles intended for nucleic acid delivery across the BBB markedly reduce the α-helical content of HSA, while Tf shows only minor changes in secondary structure[46].

Isothermal calorimetric titration of HSA

To determine the reaction thermodynamics and kinetics of protein–dendrimer interactions, isothermal titration calorimetry (ITC) was employed. In this and consecutive experiments, HSA was chosen as a complexation partner as its interactions with the studied dendrimer are strong and profoundly affect protein secondary structure compared to dendrimer-Tf interactions. After injections of the G3Si PEG6000 dendrimer solution into a calorimetric cell containing the HSA solution, the heat is measured by determining the power required to maintain a constant temperature with respect to a reference solution of dendrimer titrated into a buffer. The reaction heats tend to zero as the titration progresses, and the binding sites become saturated. The heat rate as a function of time is presented in Fig. 6. The heat rates of both titrations were integrated into thermal effects (Fig. 7).

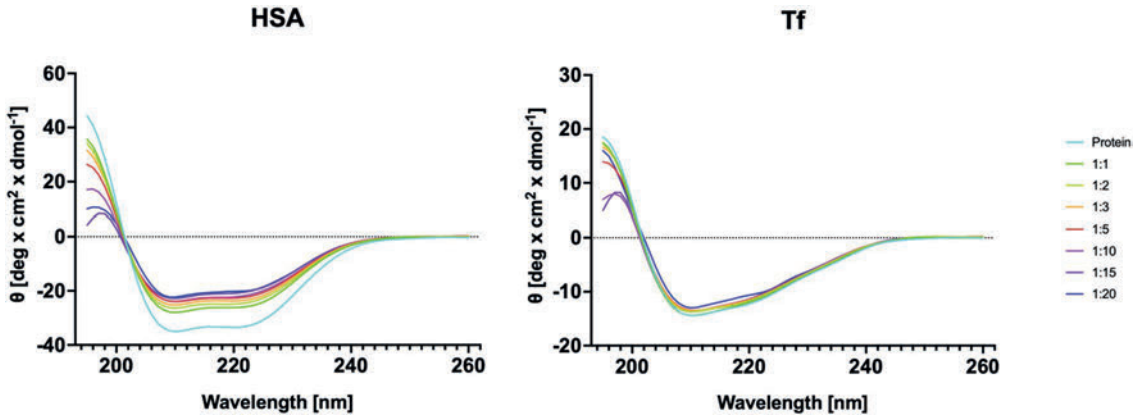


Fig. 4. Circular Dichroism spectra of human serum albumin and transferrin following the addition of dendrimer G3Si PEG6000 at a wavelength ranging from 195 to 260 nm.

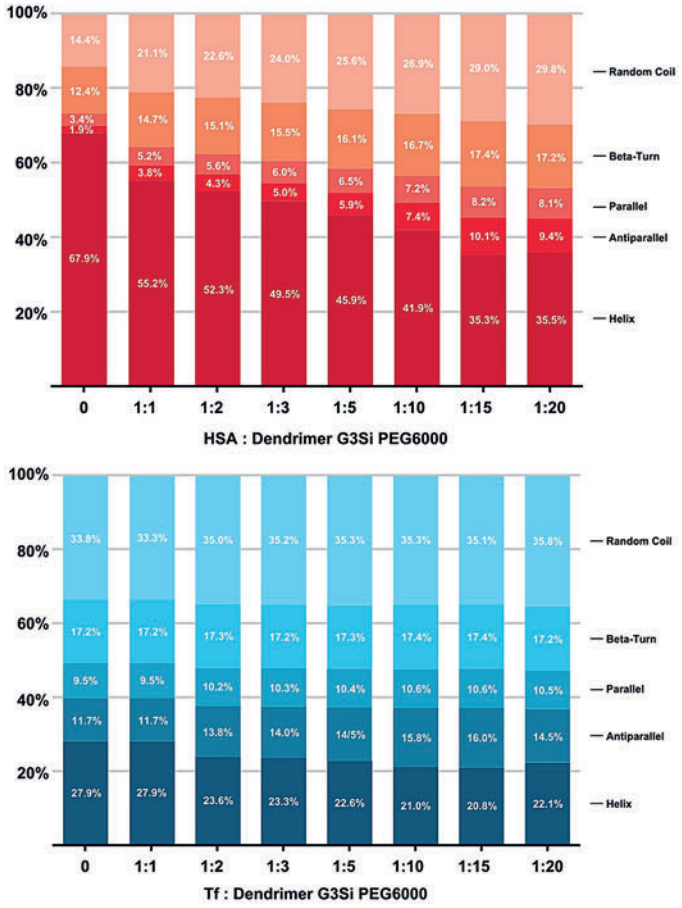


Fig. 5. Alterations in the secondary structure of human serum albumin (red) and transferrin (blue) upon interaction with dendrimer G3Si PEG6000. The analysis highlights changes in specific structural elements, such as α-helices, β-sheets, parallel, anti-parallel arrangement, and random coils, potentially indicating conformational rearrangements induced by dendrimer binding.

The enthalpy of the HSA interaction with the studied dendrimer (Fig. 8), corrected by the dendrimer dilution effects, were analyzed in the NanoAnalyze software by non-linear multiparameter regression using the identical-site model. The stoichiometric parameters, the binding constant, and thermodynamic functions are summarized in Table 2. The stoichiometric parameter indicates a multivalent interaction where each HSA molecule can bind 9 ± 3 dendrimer molecules. This is in reasonable agreement with the CD spectral shifts, which indicate that a single HSA molecule undergoes a major secondary structure conformation change, at least at the 1:15 HSA: dendrimer molar ratio. The determined binding constant (logK = 4.47 > 3) reflects the high affinity between the dendrimer and each HSA active site. Thermodynamically, the process is driven by a highly favorable entropy change ($T\Delta\ S$ = 36 kJ mol^{-1}), which indicates a significant disorder introduced into the system, likely due to several contributions comprising the changes of protein structure caused by its interactions with dendrimer and the changes in dendrimer macromolecule structure including the changes in PEG6000 substituent itself as well as the release of water molecules or ions during dendrimer binding with the HSA active sites. This positive entropy change overcomes the unfavorable positive enthalpy of binding ($\Delta\ H$ = 11 kJ mol^{-1}), which suggests that the direct interactions between the HSA and dendrimer are weakly endothermic, likely due to desolvation or conformational adjustments. The overall Gibbs free energy change ($\Delta\ G$ = −26 kJ mol^{-1}) confirms that the binding is thermodynamically spontaneous, with entropy as the driving force.

Atomic force microscopy of HSA and plasma

Atomic force microscopy (AFM) imaging was employed to investigate the morphology of HSA-dendrimer conjugates. HSA, in the absence of dendrimer conjugation, exhibits a monodisperse, uniform globular morphology indicative of its intrinsic structural stability (Fig. 9). The mica substrate was essentially not visible, indicating near-continuous coverage by HSA. This made it impossible to determine absolute feature height (no exposed baseline); only lateral dimensions were gauged from cross-sections. Consequently, the ~ 50 nm "diameter" observed for HSA alone should be interpreted as clusters of albumins on tightly packed monolayers inflated by the tip-sample convolution rather than single proteins. Upon interaction with the G3Si PEG6000 dendrimer, significant structural alterations are observed, marked by the emergence of elongated aggregates. This suggests that the dendrimer disrupts the native state of HSA, facilitating protein aggregation and secondary

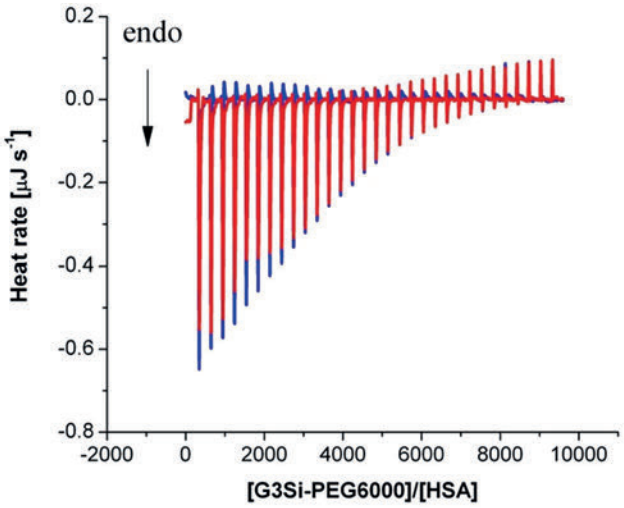


Fig. 6. Curves of thermal power as a function of time during titration of 10 μM HSA solution with 0.2 mM G3Si PEG6000 dendrimer solution (red peaks) and dilution of 0.2 mM dendrimer solution into buffer without HSA (blue peaks). All titrations were carried out at 25 °C in aqueous 10 mM phosphorous buffer solution pH 7.4. Downward peaks describe endothermic heat effects.

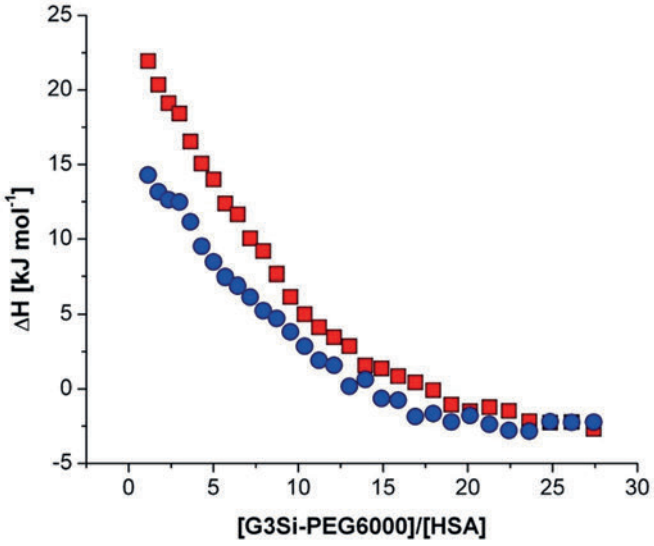


Fig. 7. Integrated thermal effects of the ITC titration of 10 μM HSA solution with 0.2 mM G3Si PEG6000 dendrimer solution (red squares) and corresponding effects of dilution of dendrimer (blue circles) in aqueous 10 mM phosphorous buffer solution pH = 7.4 at 25 °C as a function of the dendrimer to HSA mole ratio.

and tertiary structural rearrangements. Globular proteins, including HSA, can undergo conformational changes upon external perturbation, which leads to partial unfolding and subsequent aggregation into fibrillar structures[47]. The conformational rearrangement of HSA, affected by interactions with G3Si PEG6000, appear as linear or curvilinear assemblies of multiple globules and resembles semiflexible albumin fibrils observed in multiple studies[48,49]. The dendrimer-induced aggregates exhibit lateral widths on the order of ~ 50 nm (similar to the HSA-alone). Individual aggregates were analyzed, yielding heights ranging from approximately 5.5 nm up to 9.8 nm. We emphasize that the height values are much more accurate indicators of aggregate thickness than lateral size, since the vertical measurement is less prone to tip broadening or edge convolution. Nonetheless, the appearance of ~ 8 nm high, ~ 50 nm wide, elongated clusters in the HSA conjugated with dendrimer sample is a robust, reproducible finding. Dendrimer addition clearly produces a new morphology: linear aggregates that were absent in HSA alone. The observed aggregates likely result from intermolecular interactions that promote β-sheet formation, a hallmark of protein misfolding and aggregation. These changes align with findings from the CD spectroscopy, which also reveals rearrangement in its secondary structure.

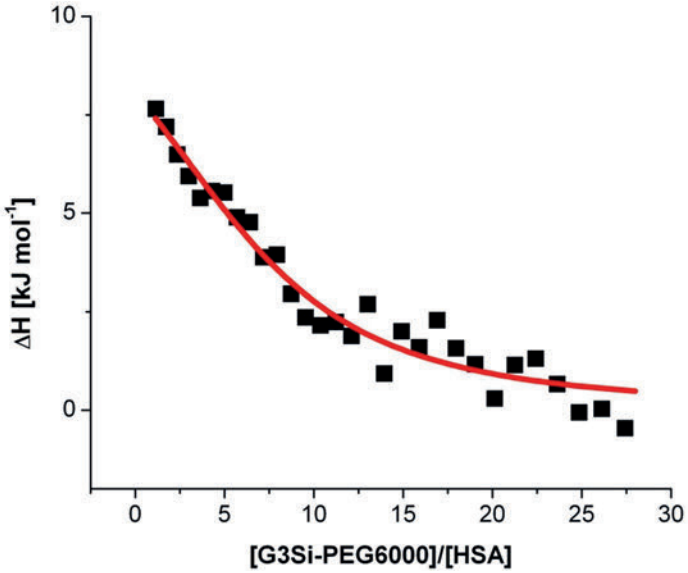


Fig. 8. Thermal effects of direct interactions (per mole of injectant) between HSA and G3Si PEG6000 dendrimer as a function of the dendrimer to HSA mole ratio in aqueous 10 mM phosphorous buffer solution pH 7.4 at 25 °C the ITC curve of HSA binding interaction with studied dendrimer was described with the identical-site model (solid lines).

Dendrimer	n	$logK$	ΔH (kJ mol^{-1})	$T\Delta S$ (kJ mol^{-1})	ΔG (kJ mol^{-1})
G3Si PEG6000	9 ± 3	4.47	11	36	−26

Table 2. Calorimetrically determined stoichiometric parameter n, binding constant K (M^{-1}), and standard thermodynamic functions of HSA interaction with G3Si PEG6000dendrimer in 10 mM phosphorous buffer solution pH 7.4 at 25 °C.

Nanovectors *in vivo* encounter a protein-rich environment where their interactions can have dual effects on protein aggregation. On the one hand, the dendrimers may act as scaffolds or catalysts, locally concentrating proteins and enhancing aggregation processes such as fibril nucleation and elongation. On the other hand, when the protein concentration is high, the dendrimer surface becomes saturated with proteins that competitively bind to it. This competitive binding can block the active sites necessary for further protein-protein interactions, thereby inhibiting fibril formation[50]. Consequently, dendrimers' net effect *in vivo* depends on the balance between their ability to concentrate proteins versus the potential to sequester and stabilize them, which can influence both the extent and the nature of aggregation observed in biological systems. It is also important to denote that a multitude of factors like blood flow, axial margination, protein corona composition, etc., could potentially alter the interactions.

Utilizing an *in vitro* approach, the AFM phase images reveal multiple areas with notable morphological changes, where the plasma structure transitions from predominantly globular forms to more elongated aggregate structures similar to the changes observed upon the addition of dendrimer G3Si PEG6000 to HSA (Fig. 10). Upon close inspection, the elongated aggregate arrangements are composed of smaller, rod-like units. Each globular node along these chains had an apparent lateral size of ~ 23 nm on average, significantly smaller than the ~ 60 nm globules seen in plasma without introduction of the studied dendrimer. This suggests that the dendrimer may reorganize the native plasma protein into finer units. This change suggests that by altering protein secondary and tertiary structures, the dendrimer may start a nucleation process by locally increasing protein concentration or inducing conformational changes that favor protein misfolding, oligomerization, and protofibril formation. Height images demonstrate an enhanced regularity of plasma dispersion across the entire surface of the sample compared to the more irregular protein distribution prior to the dendrimer addition. This improved dispersion could indicate the stabilization or reorganization of plasma components facilitated by interactions with the dendrimer. The improved dispersion implies that the dendrimer might simultaneously limit uncontrolled aggregate growth, potentially by reorganization of plasma components.

Transmission electron microscopy of HSA and plasma

Transmission electron microscopy (TEM) provided complementary insights into the structural changes induced by the interaction of dendrimer G3Si PEG6000 with HSA and plasma (Fig. 11). Free albumin exhibited an

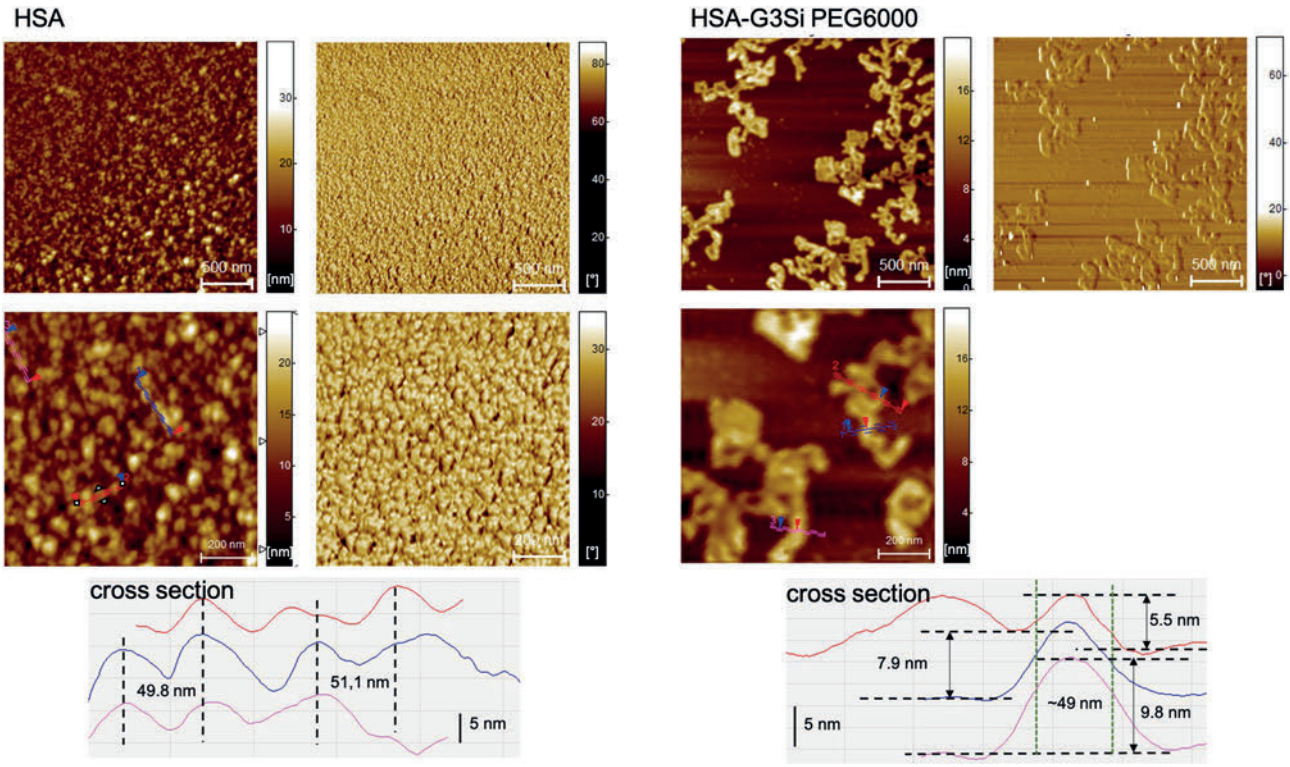


Fig. 9. AFM height and phase images of HSA (left panel) and its conjugates with the dendrimer G3Si PEG6000 (right panel). Corresponding cross-section line profiles (taken along the colored guide lines) are shown beneath each image.

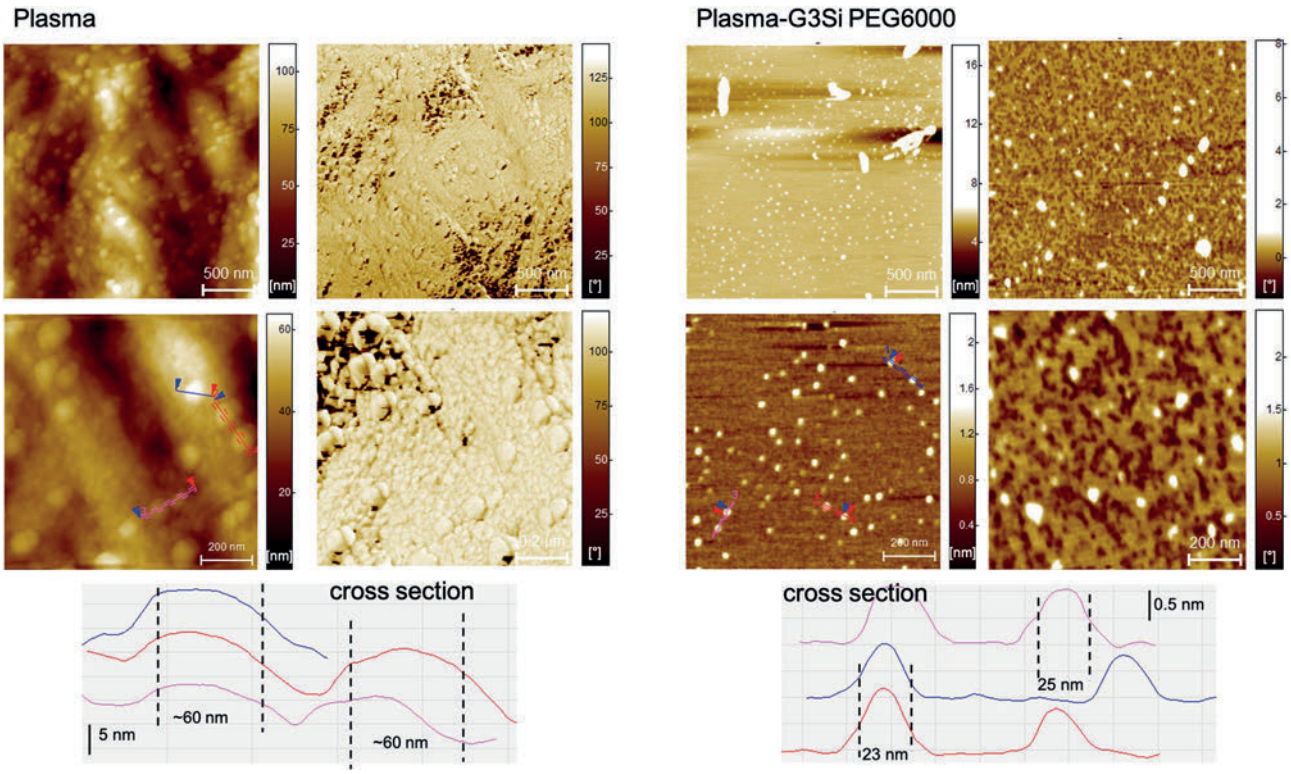


Fig. 10. AFM height and phase images of plasma (left panel) and its conjugates with the dendrimer G3Si PEG6000 (right panel). Corresponding cross-section line profiles (taken along the colored guide lines) are shown beneath each image.

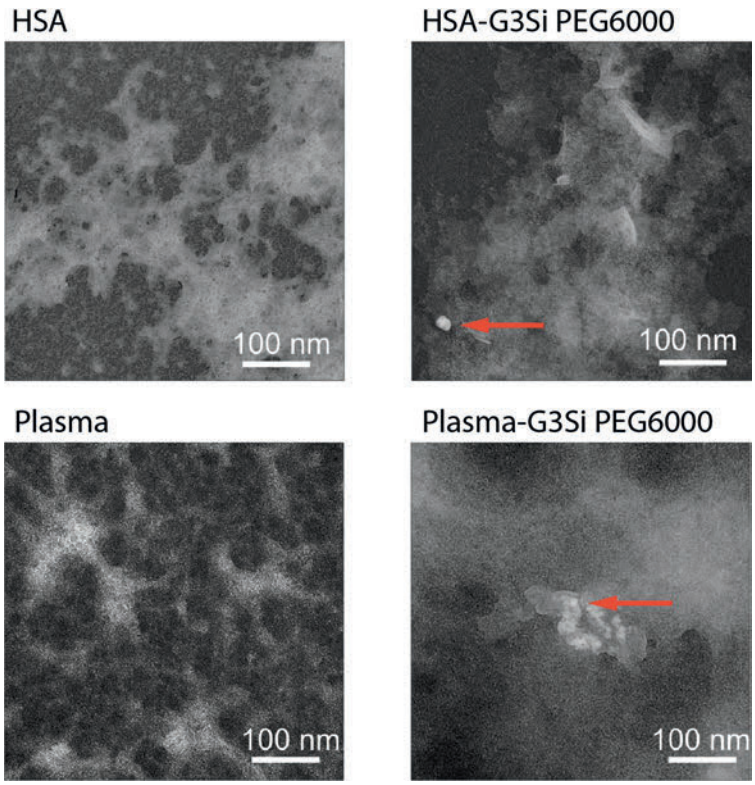


Fig. 11. Transmission electron microscope images HSA (top left), HSA in the presence of the dendrimer G3Si PEG6000 in 9:1 molar ratio (top right), plasma (bottom left), and the G3Si PEG6000 dendrimer in plasma environment (bottom right). A magnification of 100 000 × was used to analyze the samples. Arrows point at partial aggregation into denser protein assemblies. TEM micrographs of the not conjugated dendrimer G3Si PEG6000 are available in our prior work[32].

amorphous aggregate morphology. The differences in HSA images observed in AFM and TEM can be attributed to the distinct principles and preparation requirements of these techniques. As a morphological reference, representative TEM micrographs of the not conjugated dendrimer G3Si PEG6000 acquired under the same negative-stain conditions are available in our prior work[32]. Upon dendrimer addition, the structures became slightly more compact, suggesting that the dendrimer interacts with HSA, which induces partial aggregation into denser protein assemblies. In plasma, which inherently exhibited more complex and intertwined structures compared to HSA alone, the introduction of the dendrimer led to a more dispersed protein arrangement, resembling the patterns observed in AFM images, with localized interactions between the dendrimer and plasma proteins visible. AFM and TEM morphology report cannot, on their own, confirm protein fibrillation; orthogonal assays are required for that determination.

Conclusions

A key reason for the longstanding interest in nanovector–protein interactions is the pursuit of effective and safe therapeutic delivery. Unraveling the underlying mechanisms is fundamental to achieving controlled biodistribution and fully realizing the potential of nanomedicine. Our studies reveal that G3Si PEG6000 dendrimers interact with model proteins in distinct ways. Fluorescence quenching data indicate that the dendrimer binds Tf with higher affinity than HSA, suggesting that dendrimer binding induces more pronounced tertiary conformational changes in Tf. In contrast, circular dichroism analyses reveal that the G3Si PEG6000 dendrimer binding with the model proteins induces a more pronounced effect on the HSA secondary structure. The interactions of the dendrimer with both of the proteins show distinct, multi-step conformational modifications of these proteins, implicating the involvement of multiple binding domains. Isothermal titration calorimetry studies also confirm that the HSA–G3Si PEG6000 dendrimer interaction is characterized by multivalent binding and is driven by a favorable entropy change. Together with AFM and TEM imaging, these findings suggest that at high concentrations, the G3Si PEG6000 dendrimer can alter the protein's secondary and tertiary structures, potentially reorganizing plasma components and initiating nucleation processes that render the proteins more susceptible to misfolding. Though inherently complex, the interaction profile of G3Si PEG6000 dendrimers mirrors key characteristics observed in referenced and well-established nanocarrier systems. The study highlights the intrinsic and multifaceted nature of protein–nanovector interactions and reinforces the suitability of this platform for continued investigation in drug delivery and precision medicine. A multitude of physiological processes, including blood flow, corona remodeling through competitive adsorption, and systemic clearance pathways, are likely to influence these interactions. Therefore, extrapolating from these *in vitro* results

to *in vivo* behavior should be done with caution. These dendrimer-induced, concentration-dependent alterations must be further assessed within a broader biological context, where the vast and dynamic network of molecular interactions in the circulatory system dictates a spectrum of potential outcomes. Future studies of the G3Si PEG6000 dendrimer will extend these insights by including morphotic elements to further describe the impact of dendrimer–protein interactions on the dendrimer's therapeutic delivery and safety.

Data availability

The datasets generated during and/or analysed during the current study are available from the corresponding authors on reasonable request. Correspondence and should be addressed to S.Z or K.M.

Received: 22 August 2025; Accepted: 6 October 2025
Published online: 12 November 2025

References

1. Florendo, M. et al. Use of polyamidoamine dendrimers in brain diseases. *Molecules* **23**, 2238 (2018).
2. Santos, S. D. et al. PAMAM dendrimers: blood-brain barrier transport and neuronal uptake after focal brain ischemia. *J. Controlled Release*. **291**, 65–79 (2018).
3. Somani, S. & Dufès, C. Applications of dendrimers for brain delivery and cancer therapy. *Nanomed. (Lond)*. **9**, 2403–2414 (2014).
4. Dwivedi, N. et al. Dendrimer-mediated approaches for the treatment of brain tumor. *J. Biomater. Sci. Polym. Ed.* **27**, 557–580 (2016).
5. Jiang, Y. et al. PEGylated polyamidoamine dendrimer conjugated with tumor homing peptide as a potential targeted delivery system for glioma. *Colloids Surf., B*. **147**, 242–249 (2016).
6. Zhang, F. et al. Generation-6 hydroxyl PAMAM dendrimers improve CNS penetration from intravenous administration in a large animal brain injury model. *J. Controlled Release*. **249**, 173–182 (2017).
7. Nance, E. et al. Nanoscale effects in dendrimer-mediated targeting of neuroinflammation. *Biomaterials* **101**, 96–107 (2016).
8. Yellepeddi, V. K. et al. Pediatric oral formulation of dendrimer-N-acetyl-l-cysteine conjugates for the treatment of neuroinflammation. *Int. J. Pharm.* **545**, 113–116 (2018).
9. Raulin, A. C. et al. ApoE in alzheimer's disease: pathophysiology and therapeutic strategies. *Mol. Neurodegeneration*. **17**, 72 (2022).
10. Nel, A. E. et al. Understanding biophysicochemical interactions at the nano–bio interface. *Nat. Mater.* **8**, 543–557 (2009).
11. Lima, T., Bernfur, K., Vilanova, M. & Cedervall, T. Understanding the lipid and protein Corona formation on different sized polymeric nanoparticles. *Sci. Rep.* **10**, 1129 (2020).
12. Muthusamy, B. et al. Plasma proteome database as a resource for proteomics research. *Proteomics* **5**, 3531–3536 (2005).
13. Vroman, L. & Adams, A. L. Findings with the recording ellipsometer suggesting rapid exchange of specific plasma proteins at liquid/solid interfaces. *Surf. Sci.* **16**, 438–446 (1969).
14. Zhang, Y., Wu, J. L. Y., Lazarovits, J. & Chan, W. C. W. An analysis of the binding function and structural organization of the protein Corona. *J. Am. Chem. Soc.* **142**, 8827–8836 (2020).
15. Walkey, C. D. & Chan, W. C. W. Understanding and controlling the interaction of nanomaterials with proteins in a physiological environment. *Chem. Soc. Rev.* **41**, 2780–2799 (2012).
16. Turci, F. et al. *An Integrated Approach to the Study of the Interaction Between Proteins and Nanoparticles* (2010).
17. Linse, S. et al. *Nucleation of Protein Fibrillation by Nanoparticles*.
18. Rocha, S. et al. Influence of fluorinated and hydrogenated nanoparticles on the structure and fibrillogenesis of amyloid beta-peptide. *Biophys. Chem.* **137**, 35–42 (2008).
19. Yokoyama, K. & Welchons, D. R. The conjugation of amyloid beta protein on the gold colloidal nanoparticles' surfaces. *Nanotechnology* **18**, 105101 (2007).
20. Deng, Z. J., Liang, M., Monteiro, M., Toth, I. & Minchin, R. F. Nanoparticle-induced unfolding of fibrinogen promotes Mac-1 receptor activation and inflammation. *Nat. Nanotech.* **6**, 39–44 (2011).
21. Berrecoso, G., Crecente-Campo, J. & Alonso, M. J. Unveiling the pitfalls of the protein Corona of polymeric drug nanocarriers. *Drug Deliv Transl Res.* **10**, 730–750 (2020).
22. Rahman, M., Laurent, S., Tawil, N., Yahia, L. & Mahmoudi, M. *Protein-Nanoparticle Interactions*, vol. 15, 45–63 (Springer, 2013).
23. Breznica, P., Koliqi, R. & Daka, A. A review of the current understanding of nanoparticles protein corona composition. *Med. Pharm. Rep.* https://doi.org/10.15386/mpr-1756 (2020).
24. Francia, V. et al. Corona composition can affect the mechanisms cells use to internalize nanoparticles. *ACS Nano*. **13**, 11107–11121 (2019).
25. Yin, H. et al. Reducing the cytotoxicity of ZnO nanoparticles by a pre-formed protein Corona in a supplemented cell culture medium. *RSC Adv.* **5**, 73963–73973 (2015).
26. De Paoli, S. H. et al. The effect of protein Corona composition on the interaction of carbon nanotubes with human blood platelets. *Biomaterials* **35**, 6182–6194 (2014).
27. Yang, J. Y. et al. Surface functionalization-specific binding of coagulation factors by zinc oxide nanoparticles delays coagulation time and reduces thrombin generation potential in vitro. *PLoS ONE*. **12**, e0181634 (2017).
28. Suk, J. S., Xu, Q., Kim, N., Hanes, J. & Ensign, L. M. PEGylation as a strategy for improving nanoparticle-based drug and gene delivery. *Adv. Drug Deliv. Rev.* **99**, 28–51 (2016).
29. Wang, R. L. C., Kreuzer, H. J. & Grunze, M. Molecular conformation and solvation of Oligo(ethylene glycol)-Terminated Self-Assembled monolayers and their resistance to protein adsorption. *J. Phys. Chem. B*. **101**, 9767–9773 (1997).
30. Grenier, P., Viana, I. M. D. O., Lima, E. M. & Bertrand, N. Anti-polyethylene glycol antibodies alter the protein Corona deposited on nanoparticles and the physiological pathways regulating their fate in vivo. *J. Controlled Release*. **287**, 121–131 (2018).
31. Gref, R. et al. Stealth' Corona-core nanoparticles surface modified by polyethylene glycol (PEG): influences of the Corona (PEG chain length and surface density) and of the core composition on phagocytic uptake and plasma protein adsorption. *Colloids Surf., B*. **18**, 301–313 (2000).
32. Zawadzki, S. et al. Synthesis and biophysical evaluation of carbosilane dendrimers as therapeutic SiRNA carriers. *Sci. Rep.* **14**, 1615 (2024).
33. Jiang, X. et al. Quantitative analysis of the protein Corona on fept nanoparticles formed by transferrin binding. *J. R. Soc. Interface* **7** (2010).
34. Saha, K., Moyano, D. F. & Rotello, V. M. Protein Coronas suppress the hemolytic activity of hydrophilic and hydrophobic nanoparticles. *Mater. Horiz.* **1**, 102–105 (2014).
35. Martinez, D. S. T. et al. Monitoring the hemolytic effect of mesoporous silica nanoparticles after human blood protein Corona formation. *Eur. J. Inorg. Chem.* **2015**, 4595–4602 (2015).
36. Kratz, F. Albumin as a drug carrier: design of prodrugs, drug conjugates and nanoparticles. *J. Controlled Release*. **132**, 171–183 (2008).
37. Fanali, G. et al. Human serum albumin: from bench to bedside. *Mol. Aspects Med.* **33**, 209–290 (2012).

38. Lakowicz, J. R. *Principles of Fluorescence Spectroscopy* (Springer, 2010).
39. Li, C., Zhou, L. & Yin, X. Pathophysiological aspects of transferrin-A potential nano-based drug delivery signaling molecule in therapeutic target for varied diseases. *Front. Pharmacol.* **15**, 1342181 (2024).
40. Zhang, G., Que, Q., Pan, J. & Guo, J. Study of the interaction between Icariin and human serum albumin by fluorescence spectroscopy. *J. Mol. Struct.* **881**, 132–138 (2008).
41. Ray, A., Koley Seth, B., Pal, U. & Basu, S. Nickel(II)-Schiff base complex recognizing domain II of bovine and human serum albumin: spectroscopic and Docking studies. *Spectrochim. Acta Part A Mol. Biomol. Spectrosc.* **92**, 164–174 (2012).
42. Alsalme, A. et al. β -Carboline silver compound binding studies with human serum albumin: A comprehensive multispectroscopic analysis and molecular modeling study. *Bioinorg. Chem. Appl.* **2018**, 1–11 (2018).
43. Su, X. K. et al. Interaction of α-cembrenediol with human serum albumin based on spectroscopic and computational analyses. *J. Spectrosc.* **2024**, 9923310 (2024).
44. Grodzicka, M. et al. A new class of polyphenolic carbosilane dendrimers binds human serum albumin in a structure-dependent fashion. *Sci. Rep.* **14**, 5946 (2024).
45. Kubczak, M. et al. The effect of novel tyrosine-modified polyethyleneimines on human albumin structure – Thermodynamic and spectroscopic study. *Colloids Surf., B.* **227**, 113359 (2023).
46. Okła, E. et al. Pegylated gold nanoparticles interact with lipid bilayer and human serum albumin and transferrin. *Sci. Rep.* **14**, 24408 (2024).
47. Chiti, F., Dobson, C. M., Protein & Misfolding Functional Amyloid, and human disease. *Annu. Rev. Biochem.* **75**, 333–366 (2006).
48. Usov, I., Adamcik, J. & Mezzenga, R. Polymorphism in bovine serum albumin fibrils: morphology and statistical analysis. *Faraday Discuss.* **166**, 151 (2013).
49. Usov, I., Adamcik, J. & Mezzenga, R. Polymorphism complexity and handedness inversion in serum albumin amyloid fibrils. *ACS Nano.* **7**, 10465–10474 (2013).
50. Khan, R., Ahmad, E., Zaman, M., Qadeer, A. & Rabbani, G. Nanoparticles in relation to peptide and protein aggregation. *IJN* **899**. https://doi.org/10.2147/IJN.S54171 (2014).

Acknowledgements

This work was supported by grant 2018/30/Z/NZ1/00911 of the Project "NanoTENDO" financed by the National Science Centre, under the M-ERA.NET 2, which has received funding from the European Union's Horizon 2020 research. This research was also funded by grants from PID2020-112924RB-I00 (MINECO) and CIBER-BBN from ISCIII with assistance from the European Regional Development Fund.

Author contributions

Serafin Zawadzki: Conceptualization, Methodology, Validation, Formal analysis, Investigation, Writing—Original Draft, Writing—Review & Editing, Visualization; Elżbieta Okła: Investigation; Sylwia Michlewska: Investigation; Tomasz Makowski: Investigation; Adam Buczkowski: Investigation; Paula O. López: Resources; Francisco J. de la Mata: Resources; Maksim Ionov: Methodology, Writing—Review & Editing; Maria Bryszewska: Conceptualization, Methodology, Resources, Writing—Review & Editing, Project administration, Funding acquisition; Katarzyna Miłowska: Conceptualization, Methodology, Formal analysis, Data Curation, Writing—Review & Editing, Supervision, Project administration.

Funding

This work was supported by grant 2018/30/Z/NZ1/00911 of the Project "NanoTENDO" financed by the National Science Centre, under the M-ERA.NET 2, which has received funding from the European Union's Horizon 2020 research. This research was also funded by grants from PID2020-112924RB-I00 (MINECO) and CIBER-BBN from ISCIII with assistance from the European Regional Development Fund.

Declarations

Competing interests

The authors declare no competing interests.

Additional information

Correspondence and requests for materials should be addressed to S.Z. or K.M.

Reprints and permissions information is available at www.nature.com/reprints.

Publisher's note Springer Nature remains neutral with regard to jurisdictional claims in published maps and institutional affiliations.

Open Access This article is licensed under a Creative Commons Attribution 4.0 International License, which permits use, sharing, adaptation, distribution and reproduction in any medium or format, as long as you give appropriate credit to the original author(s) and the source, provide a link to the Creative Commons licence, and indicate if changes were made. The images or other third party material in this article are included in the article's Creative Commons licence, unless indicated otherwise in a credit line to the material. If material is not included in the article's Creative Commons licence and your intended use is not permitted by statutory regulation or exceeds the permitted use, you will need to obtain permission directly from the copyright holder. To view a copy of this licence, visit http://creativecommons.org/licenses/by/4.0/.

© The Author(s) 2025

ACS APPLIED MATERIALS & INTERFACES

www.acsami.org

Research Article

Hemocompatibility of Carbosilane Dendrimers as a Therapeutic siRNA Delivery System across Blood–Brain Barrier

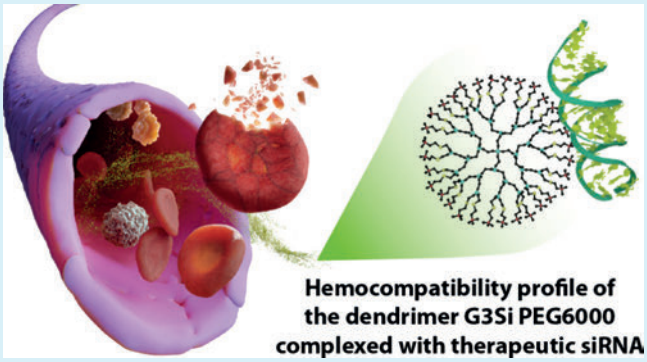
Serafin Zawadzki,* Simon Suty, Elżbieta Okła, Paula Ortega López, F. Javier de la Mata, Iveta Waczulikova, Maksim Ionov, Maria Bryszewska, and Katarzyna Miłowska*

Cite This: *ACS Appl. Mater. Interfaces* 2026, 18, 11671–11686

Read Online

ACCESS | Metrics & More | Article Recommendations

ABSTRACT: The development of nanocarriers offers a promising strategy for the delivery of therapeutics to the central nervous system. However, the clinical translation of nanosystems hinges on their interactions with blood components, which not only dictate their biodistribution and therapeutic efficacy but also may pose potential risks to hemostasis. In this study, we assess the hemocompatibility of a novel, third-generation PEGylated carbosilane dendrimer (G3Si PEG6000) and its dendriplex designed for siRNA delivery across the blood-brain barrier pertinent to Alzheimer's disease. Utilizing a comprehensive array of advanced analytical techniques, we assess cellular responses, cytokine expression, hemorheological properties, hematological parameters, and coagulation dynamics within a physiologically relevant environment. Our findings demonstrate that the investigated nanosystem elicits changes in blood rheology, immune recognition, and the intrinsic coagulation cascade, yet these effects remain below thresholds associated with clinically significant adverse outcomes. Hemolysis was ∼8-fold lower for dendriplexes than the dendrimer in PBS at the highest concentration (accordingly 3.5 ± 0.14% vs 27.46 ± 4.66%, 24 h), in 55% plasma, both formulations were nonhemolytic across all concentrations. Whole blood viscosity increased by up to ∼11% (dendrimer) and ∼16% (dendriplex) relative to the control. At 10 μM, the dendrimer approximately doubled the aPTT, whereas the corresponding dendriplex increased the aPTT by ∼30% of the control. Importantly, neither adverse effects on red blood cell and platelet indices nor toxicological responses in white blood cells were observed under the tested conditions. These findings not only support the translational potential of the studied nanosystem for therapy but also emphasize the critical role of the therapeutic cargo and the formation of a biomolecular corona in shaping the nanocarrier's biological identity and its subsequent interactions within the bloodstream. The results provide a compelling scientific basis for advancing this platform in further investigations.



KEYWORDS: *carbosilane dendrimer, nanoparticles, siRNA, drug delivery system, hemocompatibility, immunocompatibility*

INTRODUCTION

The blood–brain barrier (BBB) presents a significant challenge to the treatment of neurological disorders. This is due to the restrictive nature of the BBB, which impedes the delivery of therapeutics to the central nervous system (CNS). Nanotechnology offers a promising solution by employing nanovectors to cross the BBB and deliver therapeutic agents to the target site. The success of nanocarriers is heavily dependent on their biocompatibility. Hemocompatibility is particularly crucial given that many therapeutic strategies involve parenteral administration, which bypasses the gastrointestinal tract and often results in direct exposure of the bloodstream to administered substances. This approach offers the advantage of systemic delivery, circumventing first-pass metabolism and potentially enhancing therapeutic effects. However, the blood environment is highly complex, and the interactions of nanoparticles with blood components can significantly influence the fate and efficacy of the nanovector particles (further nanovectors) as well as constitute risks to hematological balance. Therefore, blood-contacting nanomaterials must be tested for adverse interactions with the blood components. In order to assess the hemocompatibility of nanoparticles, it is imperative to recognize their possible impact on the properties and functions of individual blood components within a highly interactive environment where all

Received: July 2, 2025
Revised: January 14, 2026
Accepted: January 22, 2026
Published: February 10, 2026



ACS Publications © 2026 American Chemical Society

elements are in constant communication. Figure 1 illustrates nanovectors crossing the BBB, emphasizing their interactions with blood components.



Figure 1. Illustration depicts nanovectors (in green) after intravenous injection, interacting with blood components such as red blood cells, blood platelets, and immune cells potentially, leading to adverse effects like hemolysis, clot formation, and immune response.

Erythrocytes, the most common blood cells, perform vital functions beyond oxygen and carbon dioxide transport, including roles in hemostasis, thrombosis, and the regulation of blood viscosity. Their distinctive rheological properties contribute to the non-Newtonian behavior of blood, influencing its flow dynamics and overall circulatory function.[1,2] The interactions of nanoparticles with erythrocytes can disrupt the delicate physiological balance, leading to a cascade of intertwined and mutually reinforcing adverse events, including hemolysis, erythrocyte deformation, aggregation, and an increased risk of thrombosis. Nanoparticle-induced hemolysis, while reducing erythrocyte numbers and potentially leading to life-threatening anemia, also causes the release of hemoglobin, which can contribute to endothelial dysfunction and thrombus formation through nitric oxide sequestration.[3−6] Nanoparticle-induced hemotoxicity can significantly alter the blood rheology. Hemolysis can often lead to a decrease in blood viscosity, which in turn increases the risk of bleeding, especially in patients with fever. Conversely, nanoparticle-mediated erythrocyte deformation, often leading to an increased RBC membrane rigidity, can elevate blood viscosity. This increased viscosity contributes to a range of hematological and neurological disorders by promoting microvessel occlusion, altering blood flow patterns, and facilitating platelet activation, ultimately increasing thrombotic potential.[7,8] Furthermore, nanoparticles can induce phosphatidylserine exposure on erythrocyte membranes, creating a procoagulant surface that promotes platelet adhesion and increases the risk of thrombosis, thereby influencing coagulation.[9−14]

Blood platelets are the second most abundant cell type in the blood. Formerly regarded solely as regulators of hemostasis, platelets are now vastly acknowledged for their involvement in various crucial functions, including vascular inflammation, combating infections, innate immunity, regulating tumor growth, and promoting angiogenesis.[15,16] This expanded understanding necessitates careful consideration of platelet interactions with nanovectors, as their encounters can trigger unintended activation of signaling pathways, potentially leading to consequences beyond blood clot formation. Notably, the negatively charged sialic acid residues present on the platelet surface exhibit a strong affinity for cationic nanoparticles, which can induce platelet aggregation via cross-bridge formation.[17] A critical consequence of nanoparticle-induced platelet activation is the release of pro-inflammatory mediators, including β-thromboglobulin, and the translocation of the membrane protein P-selectin, subsequently triggering leukocyte recruitment, which can further amplify the inflammatory response.[18−20]

Leukocytes are essential components of the immune system that orchestrate complex recognition and response mechanisms, leading to the neutralization or elimination of foreign entities. Depending on their biological and synthetic identity, nanoparticles may be perceived as foreign, self-conscious, or evade immune recognition entirely. If recognized as foreign, nanoparticles can trigger a defensive immune reaction, leading to their engulfment by macrophages, neutrophils, dendritic cells, or monocytes.[21] The mononuclear phagocytic system (MPS) and reticuloendothelial system (RES) contribute to the accumulation of nanoparticles in off-target organs such as the liver, spleen, and lungs.[22] Due to their role in clearing foreign particles from the bloodstream, which often results in the high accumulation of nanoparticles inside immune cells, leukocytes are particularly susceptible to nanoparticle toxicity. Nanoparticles can interfere with chemotaxis, cytokine secretion, oxidative bursts, and phagocytosis. Additionally, they may induce more severe adverse effects, such as morphological changes, DNA damage, and apoptosis, leading to immune system pathologies.[23]

Given the critical role of hemocompatibility in the successful application of nanocarriers, it is essential to thoroughly evaluate their effect on blood physiology. By providing a holistic understanding of their interactions with blood components, we can identify potential adverse effects and optimize their design for improved biocompatibility and therapeutic efficacy. In our previous work, we have synthesized, characterized, and chosen a single dendrimer best fit for delivering therapeutic agents across the blood-brain barrier.[24] However, for every nanovector, its potential for clinical translation is contingent on its hemocompatibility profile in the range of effective doses. The current broad-based study aims to assess the hemocompatibility of the third-generation, positively charged, PEGylated carbosilane dendrimer and its complex with siRNA targeting the apolipoprotein E 4 (APOE4) gene.[25] This gene-targeting nanosystem is a potential therapeutic target for Alzheimer's disease, and understanding the hemocompatibility of this system is crucial for its development as a therapeutic approach. The findings of our analysis encompassed valuable insights, including erythrocyte interactions, immune cell responses, hemorheology, and multiple hematological and coagulation parameters. These effects were examined across three distinct experimental conditions: in the absence of plasma, with plasma present,

https://doi.org/10.1021/acsami.5c12952
ACS Appl. Mater. Interfaces 2026, 18, 11671−11686

and with whole blood. This approach allowed us to assess how plasma and blood components influence the studied nanovector system's interactions with blood morphotic elements, providing a comprehensive view of its biological activity. To contextualize the present hemocompatibility analyses, we captured G3Si PEG6000 nanosystem with biomolecular corona binding signatures and morphology under conditions approximating the intended plasma milieu.[26] The findings contribute significantly to a more profound understanding of the safety and efficacy of the nanocarriers studied for potential clinical applications and guide future research efforts toward more in-depth investigation of specific areas of concern.

MATERIALS AND METHODS

Dendrimer

Dendrimer with a silicon atom core, surface tertiary ammonium groups, and single polyethylene glycol (PEG) (6000)-G3Si PEG6000 with chemical formula $C_{601}H_{1324}I_{30}N_{31}O_{135}S_{32}Si_{29}$, and a molar weight of 16,794.81 g/mol is presented in Figure 2. The studied dendrimer

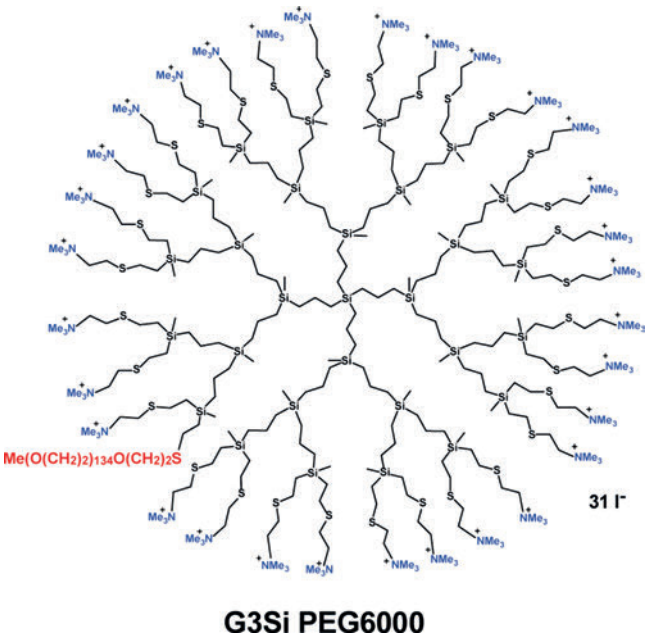


Figure 2. Structure of the studied dendrimer G3Si PEG6000.

was diluted in a phosphate buffer solution of 7.4 pH. The synthesis and biophysical characterization of the dendrimer, along with its complex with siRNA, were described in previous work.[24]

siRNA

The following siRNA was used in the present study (Dharmacon Inc., Lafayette, CO, USA): Sense: 5′-GAUUACCUGCGCUGGGUG-CUU; Antisense: 5′-PGCACCCAGCGCAGGUAAUCUU.

Other Reagents

Fetal bovine serum (FBS), RPMI-1640 medium, and resazurin were obtained from Biowest, Nuaillé, France. Sigma-Aldrich (Saint Louis, MO, USA) supplied Histopaque-1077, MILLIPLEX Human Cytokine Panel, phosphate-buffered saline (PBS) tablets, DPH (1,6-diphenyl-1,3,5-hexatriene), TMA-DPH (N,N,N-trimethyl-4-(6-phenyl-1,3,5-hexa-triene-1-yl), and 1% penicillin-streptomycin. Other chemical reagents, including sodium dihydrogen phosphate and disodium hydrogen phosphate, were obtained from Chempur (Piekary Śląskie, Poland). These chemicals were of analytical grade, and solutions were prepared using water purified with the Mili-Q system.

Dendriplex Formation

Our prior research provides insights into the dendrimer/siRNA complexation process. We characterized Dendrimer G3Si PEG6000 and determined its optimal dendriplex saturation at a molar ratio of dendrimer to siRNA of 2.5:1.[24] In this research, we chose dendrimer G3Si PEG6000 concentrations ranging from 0.1 to 10 μM and 0.04 to 4 μM for the siRNA in dendriplex. The dendrimer/siRNA complexes were incubated in PBS at room temperature for 20 min to ensure the formation of complexes.

Hemolysis

Blood donations from healthy donors were collected by the Regional Centre for Blood Donation and Hemotherapy in Lodz into CPD (citrate−phosphate−dextrose) anticoagulant blood-bag systems. All experiments used individual-donor plasma (no pooling was applied). Erythrocytes were separated from blood plasma and white blood cells (WBCs) and washed three times with PBS by centrifugation at 3000 rpm, 10 min, at 4 °C. Erythrocytes were used immediately after isolation. To evaluate the effects of G3Si PEG6000 and its dendriplexes on erythrocytes, the studied compounds were added to red blood cells (RBCs, 2% hematocrit) and incubated at 37 °C for either 3 or 24 h, followed by centrifugation at 3000 rpm for 10 min. Hemolysis was assessed by measuring the hemoglobin content in the supernatant at a wavelength of 540 nm by using a multiwell plate reader (BioTek PowerWave HT, BioTek Instruments, Inc., Winooski, VT, USA). The percentage of hemolysis was calculated using eq 1:

$$\% \text{ Hemolysis} = \frac{A_s}{A_c} \times 100\% \quad (1)$$

where A_s is the absorbance of cells treated with dendrimer or dendriplex, and A_c is the absorbance of erythrocytes in water (100% of hemolysis). The experiment was performed in 3 repetitions.

Hemolysis Assay in the Presence of Plasma Proteins

Human plasma was separated from blood by centrifuging at 4200 rpm for 15 min. All experiments used individual-donor plasma (no pooling was applied). The dendrimer and dendriplex were preincubated in a 55% plasma solution (v/v) in PBS at 37 °C and time of 1 h as it is often considered sufficient for corona formation equilibrium.[27] Following this preincubation, the samples were mixed with isolated RBC and plasma to create 2% hematocrit and 55% plasma solution (v/v) in PBS and were further incubated for 3 or 24 h. The same procedure was used to assess hemolysis in the presence of plasma, as described earlier. The experiment was performed in 3 repetitions.

PBMC Cytotoxicity

PBMCs were isolated using Histopaque from the buffy coat of 3 healthy blood donors obtained from the Regional Centre for Blood Donation and Hemotherapy in Lodz into CPD (citrate−phosphate−diastereose) anticoagulant blood-bag systems. All experiments used individual-donor plasma (no pooling was applied). After isolation, the cells were resuspended in RPMI-1640 medium supplemented with 10% FBS (heat-inactivated), 1% penicillin, and streptomycin. The cells were seeded on 96-well black plates in a density of 1×10^4 cells/well (37 °C, 5% CO_2). To evaluate the effects of G3Si PEG6000 and its dendriplex on PBMC, they were incubated for 24 and 48 h. After incubation, a resazurin solution in PBS was added for 2 h, obtaining a final concentration of 0.125 mg/mL per well. Fluorescence measurements were read at wavelengths of λ_{ex} = 530 nm and λ_{em} = 590 nm using a multiwell plate reader (BioTek PowerWave HT, BioTek Instruments, Inc., Winooski, VT, USA). The cell viability percentage was calculated using eq 2:

$$\% \text{ Viability} = \frac{A_s}{A_c} \times 100\% \quad (2)$$

where A_s is the absorbance of cells treated with dendrimer or dendriplex, and A_c is the absorbance of control cells (untreated). The experiment was performed in 4 repetitions.

https://doi.org/10.1021/acsami.5c12952
ACS Appl. Mater. Interfaces 2026, 18, 11671−11686

PBMC Cytokine and Chemokine Expression Pattern

To evaluate secretion of cytokines and chemokines by PBMCs in response to dendrimer G3Si PEG6000 and its dendriplex, PBMCs were isolated, seeded as described earlier, and incubated with the tested compounds at 37 °C and 5% CO_2. After 48 h incubation, cell culture supernatants were collected and analyzed using the Luminex MAGPIX analyzer (Luminex, Austin, Texas, United States) to assess IFNα 2, IL-6, IL-8, IL-10, IL-12p40, and TNFα levels. All procedures were strictly followed according to the manufacturer's protocols. The studies were carried out at the Research Laboratory CoreLab of the Medical University of Lodz. The experiment was performed in 7 repetitions.

PBMC Cytokine Expression in the Presence of Plasma Proteins

Human plasma was separated from blood by centrifuging it at 4200 rpm for 15 min. All experiments used individual-donor plasma (no pooling was applied). Dendriplexes and the not complexed dendrimer were preincubated in a 55% plasma solution (v/v) in PBS for 1 h at 37 °C. Following this preincubation, the samples were mixed with isolated PBMCs and 55% plasma solution (v/v) in RPMI-1640 and were further incubated for 48 h. The same procedure was used to assess PBMC cytokine expression in the presence of plasma, as described earlier. The experiment was performed in 6 repetitions.

Hemorheology

Blood samples were collected from three healthy male volunteers (aged 20−30 years) with no known severe health conditions following an overnight fast. Males were selected for this study due to their physiologically higher baseline hematocrit than females, making them more susceptible to the adverse effects of elevated blood viscosity. This study was conducted in accordance with the ethical principles set forth in the Declaration of Helsinki, and the study protocol was approved by the Institutional Ethics Committee at the St. Elizabeth Cancer Institute in Bratislava (approval no. 03-2020/EK ÓSA, signed on March 4, 2020). To maintain physiological conditions, blood samples were immediately placed in a water bath maintained at a constant temperature of 37 °C using a thermostatic controller (Polystat Control CC1, Huber, Berching, Germany). Gentle manual agitation of the tubes every 10 min prevented sedimentation. Rheological properties were subsequently analyzed by using a modular compact rheometer (MCR 102, Anton Paar, Graz, Austria) equipped with a double-gap measuring system (DG 26.7/Ti). All measurements were conducted at 37 °C, maintained by the rheometer's integrated Peltier temperature control system. Viscosity measurements were performed over a shear rate range of 1−1000 s^{-1}, with the duration of each measurement point determined automatically by the instrument to ensure the acquisition of stable viscosity values.

Erythrocyte Membrane Fluidity

To evaluate the impact of G3Si PEG6000 and its dendriplex on erythrocyte membrane fluidity and their ability to interact with both hydrophobic and hydrophilic regions of the erythrocyte lipid bilayer, fluorescence anisotropy measurements were performed using two probes: DPH (1,6-diphenylhexatriene) and its hydrophilic derivative TMA-DPH (1-(4-Trimethylammoniophenyl)-6-phenyl-1,3,5-hexatriene p-toluenesulfonate). The experiments were conducted utilizing 0.05% erythrocyte solution in PBS at 37 °C in 1 cm path-length quartz cuvettes using a PerkinElmer LS-55 spectrofluorometer (PerkinElmer, Waltham, MA, USA). The excitation and emission wavelengths were set to 348 and 358 nm for DPH and 426 and 428 nm for TMA-DPH, respectively. The experiment was performed in 6 repetitions.

Hematological and Coagulation Blood Parameters

Blood was obtained from 3 volunteers as described in the rheology section. The samples were collected in two separate tubes: with K2EDTA for hematological analysis and with sodium citrate for coagulation analysis. For hematological analysis, blood samples in K2EDTA tubes were incubated at room temperature, protected from light, for 3 h before analysis using a COULTER DxH 800 automatic hematology analyzer (Beckman Coulter Inc., Brea, CA, USA). Coagulation parameters were immediately assessed using an ACL Top 500 CTS automatic hemostasis analyzer (Instrumentation Laboratory, Bedford, MA, USA). This methodology enabled the simultaneous quantitative assessment of hematological parameters using a combination of multiple techniques. Impedance analysis, based on Coulter's principle, measured and sized cells by detecting changes in electrical resistance as they traversed a small aperture. Radiofrequency analysis provided insights into the internal conductivity of cells, offering information about cellular density and granularity through the application of a high-frequency electromagnetic field. Flow cytometric light scatter was employed to detect light scattered by cells at various angles, yielding data on the cell size (forward scatter) and internal complexity or granularity (side scatter). Additionally, spectrophotometry was used to determine hemoglobin levels by measuring the absorbance of specific wavelengths of light, while supravital staining allowed the examination of living cells stained with dyes that penetrated their membranes without causing cell death.

Statistical Analyses

Statistical analyses and data visualization were performed using Prism version 10.4.2 (GraphPad Software, Boston, MA, USA). The Shapiro−Wilk test was used to assess the normality of data distributions. Depending on experimental design, either one-way or multiple-way ANOVA was applied to assess differences in group means. Where ANOVA indicated statistically significant main effects, appropriate post hoc multiple comparison tests were selected based on the structure of the comparisons: Tukey's test was used for evaluating all pairwise group differences, Dunnett's test for comparisons of multiple treatments against a single control group, and Sidák's test for a limited set of planned comparisons. In case of non-normally distributed data or ordinal outcomes the simple effects were assessed using nonparametric Kruskal−Wallis test followed by Dunn's multiple comparisons test. All tests were two-tailed and performed at a significance level $\alpha = 0.05$. In our graphical representations, significance is denoted by asterisks: one asterisk (*) indicates a p-value < 0.05, two asterisks (**) represent a p-value < 0.01, and three asterisks (***) denote a p-value < 0.001.

RESULTS AND DISCUSSION

The earliest experiments leading to recognition of the importance of hemocompatibility had their rudimentary beginnings in the 19th century. Hewson observed that stationary blood exhibited different clotting behavior within a living vein segment compared to an open bowl.[28] Later, Virchow showed that in addition to the blood-material interface, other factors like blood composition and flow influence measurable blood clotting.[29] The foundation for modern testing methods was established in the 1970s and 80s through a series of seminars and consensus conferences.[30,31] This groundwork led regulatory bodies like the USA Food and Drug Administration (FDA) and the European Medicines Agency (EMA) to establish official guidelines. These guidelines recommend specific assays that manufacturers must perform to ensure the safety of blood-exposed foreign materials. Further solidifying these practices, the ISO 10993-4 standard (issued in 2002 and updated in 2009 by the International Organization for Standardization, the American National Standards Institute, and the Association for the Advancement of Medical Instrumentation) provides a guideline for hemocompatibility testing.[32] Standardized in vitro tests, while invaluable for ensuring comparability and regulatory alignment, often fail to address nanoparticles' nuanced behaviors. To bridge this gap, tailored approaches that thoroughly investigate nanoparticle-specific properties and their interactions with biological systems must complement existing standards, ensuring that

https://doi.org/10.1021/acsami.5c12952
ACS Appl. Mater. Interfaces 2026, 18, 11671−11686

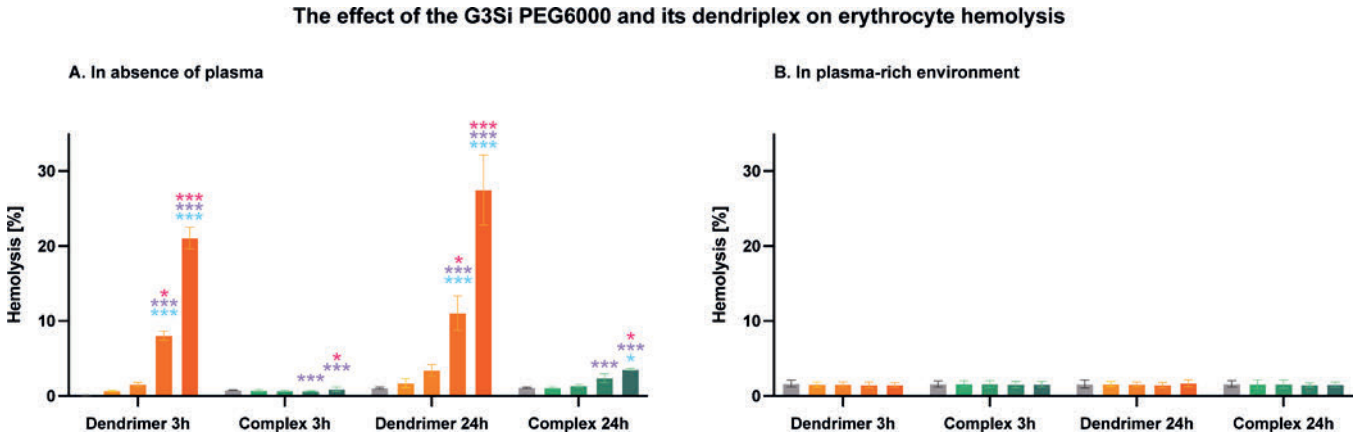


Figure 3. Hemolysis of erythrocytes treated with dendrimer G3Si PEG6000 and its dendriplex following 3 and 24 h incubation in PBS (A) and 55% plasma in PBS (B). A red asterisk denotes statistically significant effects attributed to incubation time; a violet asterisk indicates significant differences due to dendrimer-siRNA complexation; and a blue asterisk marks significant differences relative to the negative control.

results remain comparable and facilitate regulatory evaluation while capturing the complexities of nanoparticle behavior. Such a balanced strategy enables the reliable assessment of safety and efficacy, paving the way for successfully integrating nanoparticle-based medical products into clinical and commercial use.[33,34]

Hemolysis

Hemolytic properties are typically the primary parameters assessed when evaluating the hemocompatibility of nanovectors. In this study, we assessed the hemolytic properties by spectroscopic measurement of hemoglobin released from erythrocytes after 3 and 24 h treatment with G3Si PEG6000 dendrimer and its dendriplex (Figure 3). The most pronounced and statistically significant hemolytic effect was observed for 2.5 and 10 μM concentrations of the noncomplexed dendrimer, with the effect increasing over the duration of incubation. After 24 h, the 10 μM dendrimer concentration induced hemolysis equivalent to 27.46%, indicating the loss of integrity of the erythrocyte membrane or rupture accompanied by a leakage of hemoglobin. The complexation of the nanovector with siRNA significantly reduced hemoglobin release, demonstrating markedly lower hemotoxicity. The complexation of counter-anions of siRNA effectively neutralizes a fraction of the accessible amine charge, and PEGylation provides additional spatial repulsion and establishes a steric/hydration barrier, fundamentally altering the physicochemical properties of the cationic nanosystem.[35−37] This reduction in effective positive surface charge lessens electrostatic docking between the nanoparticle and anionic cell membranes, such as those of erythrocytes, thereby the interfacial charge masking limits membrane perturbation and mitigates disruption of bilayer integrity, nanoscopic poration with ensuing hemolysis.[38] The highest tested dendriplex concentration exhibited 3.5% hemolysis after the 24 h incubation period. This reduction of hemotoxicity can be attributed to the lower positive charge of dendriplexes compared to noncomplexed dendrimers. Since the surface of RBCs is negatively charged, the diminished electrostatic attraction between dendriplexes and the cell membrane minimizes disruption and subsequent hemoglobin leakage.

While the assay provides valuable insights into cell type-specific responses, its current design does not reflect in vivo comparative toxicity endpoints. Many studies have explored the hemolytic properties of nanoparticles, but few have considered the influence of the biomolecular corona. The formation of a biomolecular corona on the nanoparticle surface is a critical factor that can mitigate hemolytic activity by masking the nanoparticle's synthetic identity properties and altering its interactions with biological systems.[39,40] Consistent with this view, our companion study on the same G3Si PEG6000 platform shows that the dendrimer engages albumin and transferrin through multivalent, entropy-favored binding with secondary/tertiary conformational modifications indicative of rapid corona establishment that passivates the interface and thus may attenuate direct RBC membrane disruption.[26] To quantify the hemolysis suppression effect, the tested nanoformulations were preincubated with 55% plasma in PBS for 1 h prior to their addition to RBCs in a 55% plasma solution. This approach showed that while uncoated dendrimer G3Si PEG6000 had a significant hemolytic effect on RBC, the formation of a biomolecular corona interface on the particle surface protected the cells from being damaged. In PBS, G3Si PEG6000 induced 27.46 $\pm$ 4.66% hemolysis, while the dendriplex induced 3.50 $\pm$ 0.14%. In 55% plasma, reduced hemolysis for both formulations was reached at the level of the negative control (background), corresponding to relative reductions of ~100%. These findings align with other studies investigating the effects of plasma protein layer on the nanoparticle surface on RBC hemolysis, which similarly reported reduced hemolytic activity.[41−44] Upon plasma exposure, macromolecules rapidly assemble into a corona on cationic surfaces that masks cationic/hydrophobic motifs, lowers the effective surface potential, and establishes a hydrated steric layer. This interfacial remodeling shifts contacts from direct electrostatic engagement with the anionic, sialic-acid-rich RBC glycocalyx to protein-mediated interactions, thereby attenuating membrane perturbation, hemolysis, and eryptosis.[45−47] Although some highly hydrophobic or strongly cationic nanoparticles can retain hemolytic activity after plasma exposure, the tested nanosystem, even in the siRNA-free form, did not exhibit such residual activity under 55% plasma conditions. This suggests that the presence of a biomolecular corona on the positively charged surface of the dendrimer G3Si PEG6000 can significantly diminish the hemolytic potential of these nanostructures. However, many nanovectors can still significantly impact erythrocyte function, even with limited direct hemolytic activity. These effects can manifest as

https://doi.org/10.1021/acsami.5c12952
ACS Appl. Mater. Interfaces 2026, 18, 11671−11686

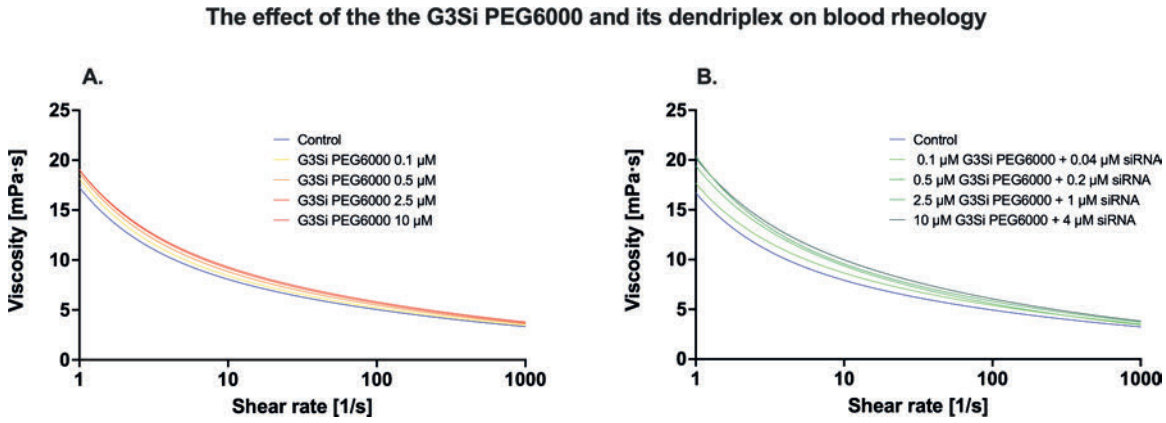


Figure 4. Changes of whole blood viscosity for different shear rate parameters following the addition of dendrimer G3Si PEG6000 (A) and its dendriplex (B). The Herschel-Bulkley model for non-Newtonian fluids was fit to the data.

erythrocyte aggregation or morphological deformation, both of which can disrupt hemorheology and impair blood flow, potentially leading to vascular complications.[23]

Hemorheology

Hemorheology examines the influence of blood flow dynamics on hemostasis, primarily with particular attention paid to the interplay between shear rates and blood viscosity. Erythrocytes, due to their unique properties, are the primary contributors to blood viscosity and the non-Newtonian behavior of blood.[48] Under low shear rates, the slow movement of blood, macromolecules dispersed in the plasma (such as fibrinogen), and the discoid shape of erythrocytes collectively promote erythrocytes to aggregate into stacked face-to-face "rouleaux" structures. As the diameter of vessels decreases and the shear rate increases, RBC aggregates gradually separate, causing a substantial viscosity drop of ∼10 s^{-1}. Furthermore, a subsequent 4-fold viscosity decrease occurs due to a morphological transition in RBC.[49,50] Erythrocyte physiological reversible aggregation plays a significant role in influencing the distribution of cellular components within the bloodstream. Moving mostly near the blood vessel center, erythrocytes force platelets and other particles toward the periphery. This process, known as axial margination, depends on blood viscosity and erythrocyte aggregation and influences the distribution of platelets, leukocytes, and other elements like nanovectors within the vasculature.[51−53] All events taking place in flowing blood generate shear forces that influence blood behavior. Typical shear rates in vivo are approximately 20−200 s^{-1} for veins, 300−800 s^{-1} for large arteries, 500−1600 s^{-1} for arterioles, and 800−10,000 s^{-1} for atherosclerotic stenosed arteries.[54] Increasing concentrations of the dendrimer and its dendriplex led to a notable increase in blood viscosity, particularly at lower shear rates. This effect is highly comparable between dendriplexes and noncomplexed dendrimers. In our in vitro study, at a shear rate of 1 s^{-1}, the viscosity of a blood sample without the addition of tested compounds was equal to 16.48 ± 1.74 mPa s. After introducing the highest concentration of dendrimer G3Si PEG6000, the viscosity increased to 18.57 ± 2.17 mPa s, while with the addition of the highest concentration of dendriplex, it rose to 19.30 ± 1.56 mPa s. In higher shear rates, the effect is less visible. As shown in Figure 4, the viscosity of the samples decreases with increasing shear rates (decreasing vessel diameter), a phenomenon known as the Fåhræus−Lindqvist effect caused by the formation of a few-micron-thick cell-free layer adjacent to the vessel walls.[55,56] Increased viscosity can reduce cardiac output and elevate peripheral resistance, leading to higher blood pressure and placing additional mechanical strain on the cardiovascular system. This can exacerbate conditions such as poor circulation, heart failure, and hematological and neurological disorders while significantly raising the risk of ischemic stroke.[51,52,57−59] In our study, the increase in blood viscosity observed after the addition of the tested compounds within the concentration range does not reach levels likely to cause cardiovascular complications linked to hemorheology.[60]

Nanoparticles can have diverse effects on blood rheology depending on their size, shape, surface properties, and concentration. For example, amphiphilic phosphorene dendrons increase blood viscosity in a concentration-dependent manner, most likely mainly due to electrostatic interactions with cell membranes.[61] Conversely, diesel exhaust particles, an environmental nanoparticle, can alter blood flow properties by damaging erythrocyte cell membranes, potentially reducing blood viscosity.[7] This highlights the importance of considering nanoparticle-driven effects on hemorheology. As there are three main factors that can influence blood viscosity, namely, hematocrit, erythrocyte aggregation, and erythrocyte deformation, there are two most probable potential mechanisms that may lead to the increase of blood viscosity observed in our study. The tested dendrimer-based therapeutic system attached to the surface of erythrocytes may increase the value of the adhesion force acting between them or may cause the stiffening of the RBC membrane.

Erythrocyte Membrane Fluidity

Nanovectors can significantly influence membrane fluidity by interacting with the RBC membranes' lipid bilayer and structural proteins. These interactions may alter erythrocytes' deformability and biconcave shape, which is critical for their role in maintaining proper blood viscosity and efficient microcirculation perfusion. Disruption of the double-lipid membrane or transmembrane protein organization by nanoparticles could hinder the integrity of membrane architecture, affecting their functions and lifespan and potentially leading to eryptosis.[62] The influence of the G3Si PEG6000 dendrimer on erythrocyte membrane fluidity was assessed by fluorescence spectroscopy. The measurement of fluorescent anisotropy of TMA-DPH and DPH, respectively, reflects membrane fluidity of the hydrophilic surface and hydrophobic membrane core of the lipid bimolecular layer. Exposure to the G3Si PEG6000

https://doi.org/10.1021/acsami.5c12952
ACS Appl. Mater. Interfaces 2026, 18, 11671−11686

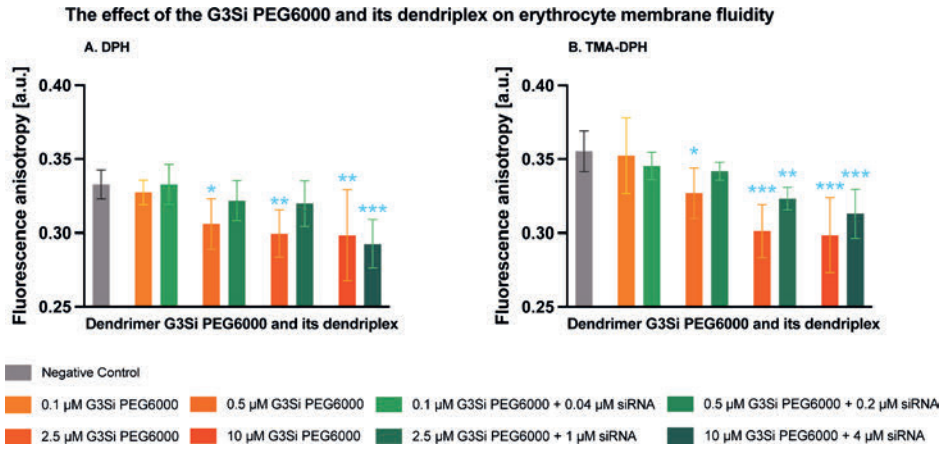


Figure 5. Fluorescence alterations of DPH (A) and TMA-DPH (B) probes indicate changes in membrane fluidity upon interaction with dendrimer G3Si PEG6000 and its dendriplex. A blue asterisk marks significant differences relative to the negative control.

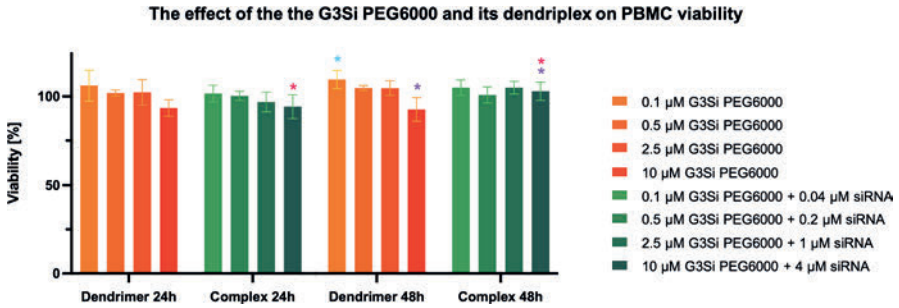


Figure 6. Viability of PBMCs treated with dendrimer G3Si PEG6000 and its dendriplex following 24 and 48 h incubation. A red asterisk denotes statistically significant effects attributed to incubation time, a violet asterisk indicates significant differences due to dendrimer-siRNA complexation, and a blue asterisk marks significant differences relative to the untreated cells (100%).

dendrimer and its dendriplex resulted in decreased membrane rigidity (Figure 5), with a slightly greater effect observed in the hydrophilic regions compared to the hydrophobic core. This increased interaction with the hydrophilic membrane surface is likely due to the highly charged ionic nature of G3Si PEG6000 dendrimers, which exhibit hydrophilic properties that facilitate interactions with polar regions of the lipid bilayer.[63] However, these same hydrophilic characteristics present a challenge for membrane penetration, as the dendrimers must overcome the substantial energy barrier imposed by the hydrophobic core of the lipid bilayer.[64] This effect is more pronounced with the studied dendrimer than with its dendriplex, as the dendrimer alters membrane fluidity at a lower concentration compared to the dendriplex, underscoring the effect of dendrimer-siRNA interactions in modulating membrane fluidity. This observation aligns with hemotoxicity studies, which similarly highlight how the complexation of the dendrimer with siRNA modulates its interaction with biological membranes, reducing its impact on cellular integrity. While the lipid bilayer is highly adaptable and expandable, its ability to stretch is inherently limited, failing under tension beyond just a few percent deformation, highlighting its sensitivity to such interactions.[64] The interaction of the studied dendrimer-based therapeutic system with isolated RBCs results in an increase in membrane fluidity rather than rigidity. Based on this observation, we conclude that the observed increase in blood viscosity after the addition of the dendrimer and its dendriplex, as seen in the hemorheological study conducted on whole blood, is more likely attributed to an increase in the adhesion forces between the RBC. A decrease in deformability, by contrast, would typically lead to a viscosity increase; however, this study indicates an increase in erythrocyte deformability, supporting the hypothesis of enhanced RBC adhesion as the primary mechanism.[65]

PBMC Cytotoxicity

Peripheral blood mononuclear cells (PBMCs) comprise lymphocytes (T cells, B cells, and NK cells), monocytes, and dendritic cells.[66] PBMC cell viability was evaluated using the AlamarBlue assay, which measures the metabolic activity of PBMCs upon exposure to test compounds (Figure 6). This assay relies on the reduction of resazurin, a fully oxidized, blue, and nonfluorescent dye, into resorufin, a pink and fluorescent compound, through cellular redox reactions. Mitochondrial oxidoreductases mediate the reduction process, reflecting mitochondrial function and providing insights into cellular viability and proliferation.[67,68] The assay results demonstrate no statistically significant cytotoxic effects following 24 and 48 h incubation with either the dendrimer or its dendriplex at any tested concentration when compared to the negative control. At the highest tested dendriplex concentration (10 μM), a statistically significant difference was observed between the 24 and 48 h time points, indicating a time-dependent normalization of cell viability. This temporal effect was not observed for the noncomplexed dendrimer, and a statistically significant difference between the dendrimer and dendriplex at the highest concentration suggests that complexation with siRNA may modulate the biological response. Notably, the only statistically significant difference relative to the negative control

https://doi.org/10.1021/acsami.5c12952
ACS Appl. Mater. Interfaces 2026, 18, 11671−11686

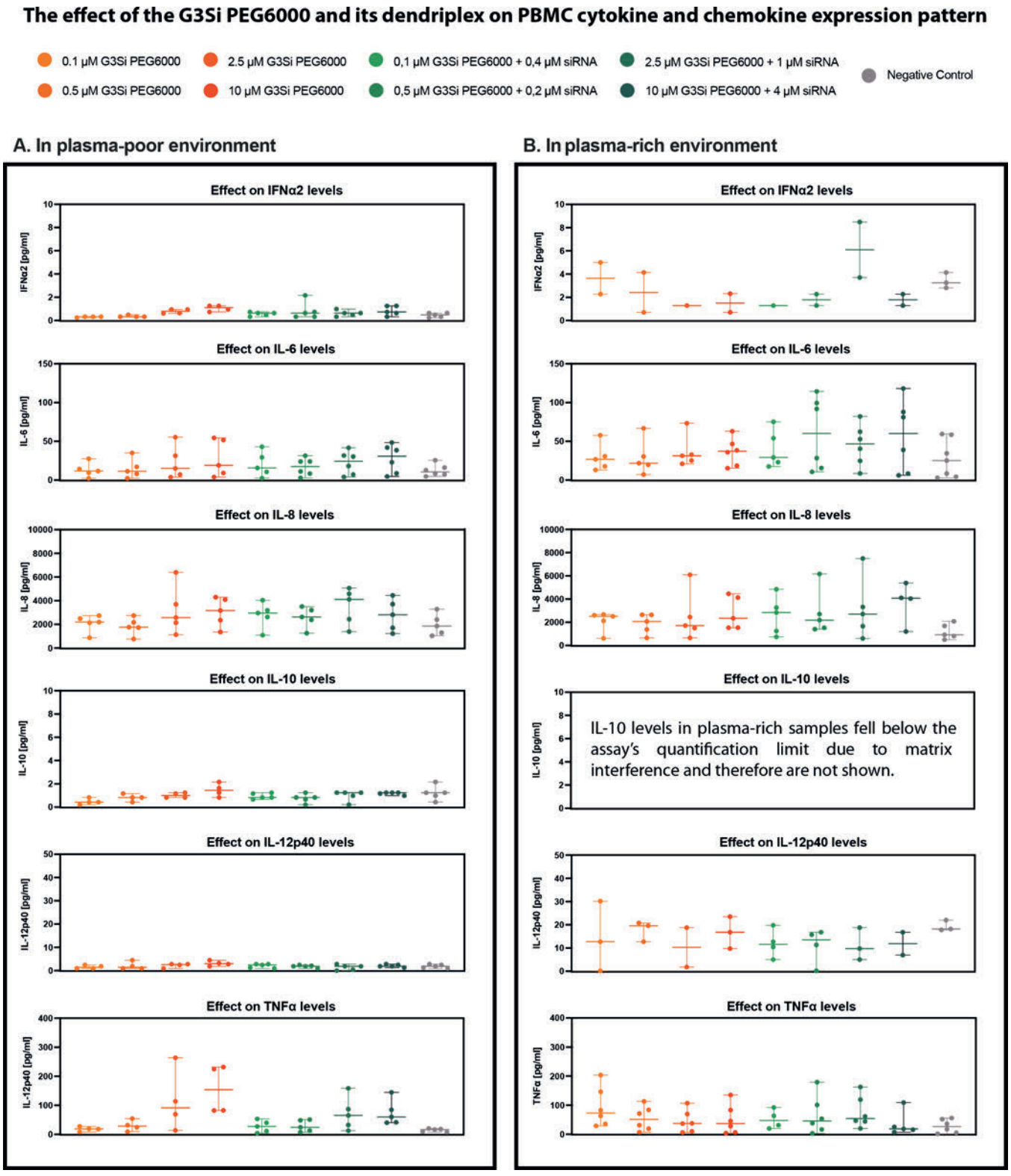


Figure 7. Effects of the G3Si PEG6000 dendrimer and its dendriplexes on cytokine and chemokine expression patterns. Panel A presents the effects of the nanosystem in the plasma-poor environment, whereas panel B illustrates the corresponding responses in the plasma-rich environment.

was an increase in PBMC viability, indicative of a proliferative response, following 48 h incubation with the lowest concentration of the noncomplexed dendrimer. Multiple nanoparticles have the capacity to induce the proliferation or death of PBMCs. These dual effects arise from complex interactions between the nanoparticles and cellular pathways.[69]

The minimal effect on PBMC viability is very beneficial, as it suggests the preservation of physiological immune functions without disrupting cellular processes. This property positions dendrimer G3Si PEG6000 as a promising candidate for biomedical applications, as it does not compromise the immune system by inducing cytotoxic effects, thereby

https://doi.org/10.1021/acsami.5c12952
ACS Appl. Mater. Interfaces 2026, 18, 11671−11686

preserving immunological homeostasis. While the absence of cytotoxicity toward PBMCs is an encouraging factor, comprehensive characterization of the immunological footprint of this nanosystem under physiologically relevant conditions is crucial for predicting systemic tolerance.

PBMC Cytokine and Chemokine Expression Pattern

Nanoparticles can be recognized by antibodies and cellular receptors, thereby eliciting an immune response, inducing the release of cytokines and chemokines that regulate inflammation, drive immune cell recruitment, and influence cellular differentiation and activation. Biomolecular coronas can promote nanoparticle recognition by activating pattern recognition receptors (PRRs). PRRs may inadvertently cross-react with misfolded proteins or surface modifications that structurally mimic pathogen-associated molecular patterns (PAMPs) and damage-associated molecular patterns (DAMPs), resulting in activation of the immune response.[70] While the biomolecular corona can induce both pro-inflammatory and anti-inflammatory signaling pathways, it can redefine a nanoparticle's biological identity by masking synthetic surface features of possibly mitigating recognition by phagocytic cells and reducing the clearance rate from the bloodstream.[71−73] Recent work reinforces that the formation of a plasma protein corona can markedly suppress nanoparticle-induced hemolysis and has spurred "corona-engineering" approaches by preloading nanoparticles with dysopsonins-rich layers such as clusterin or ApoA-I to stabilize cationic carriers and improve hemocompatibility.[74] In light of the context-dependent cytokine modulation, we implemented a dual-environment experimental framework in both plasma-rich and plasma-poor environments. Evaluating both conditions in parallel, we ensure that the impact of adsorbed plasma proteins on the dendrimer surface identity and subsequent immune signaling is fully captured. Moreover, to more accurately recapitulate in vivo immunobiology, we extended our analysis beyond isolated cell types to include mixed cultures. This heterogeneous cellular milieu preserves critical paracrine interactions and cell−cell cross-talk, thereby revealing emergent cytokine networks and regulatory feedback loops that are inherently undetectable in single-cell assays. Collectively, this holistic strategy affords a deeper understanding of how the plasma milieu and native cellular complexity converge to dictate dendrimer-mediated immunomodulation.[75,76] The selection of cytokines and chemokines was based on the interrelated roles, allowing observation of the influence that the studied dendrimer has on the inflammatory (IL-8, IL-12p40, TNFα), anti-inflammatory (IL-10), and pleiotropic (IFNα2, IL-6) immune signaling molecules (Figure 7).

Our results suggest that introducing the nanoparticles into a plasma-rich environment led to a more heterogeneous and thus variable immune cell response, reflected by the cytokine and chemokine expression profiles. This variability of dendrimer G3Si PEG6000 is the most pronounced on IFNα2, IL-6, and IL-12p40 expression in plasma-rich environments, likely reflecting how the complex, dynamic, and heterogeneous protein corona modulates immune cell activation. In plasma-rich samples, IL-10 concentrations consistently fell below the lowest quantifiable concentration for the MAGPIX Luminex assay and were therefore excluded. The high protein content of plasma amplifies background noise, leading to substantial matrix interference that disproportionately diminishes the assay sensitivity for low-abundance analytes such as IL-10. In plasma-poor environments, the biomolecular corona is less complex, leading to a more consistent cellular activation pattern, if any. Our results indicate that under plasma-poor and plasma-rich environments, the G3Si PEG6000 dendrimer and its dendriplex induce IL-6 expression by PBMCs. In the plasma-poor environment, the highest tested dendrimer concentration mediated the release of IL-6 with a median reaching 19 pg/mL, while incubation with the highest tested dendriplex concentration resulted in a median equal to 30.76 pg/mL, representing accordingly a 1.80-fold and 2.9-fold increase compared to the negative control (10.54 pg/mL). In the plasma-rich environment, the median of IL-6 expression level reached 37.07 pg/mL for cells incubated with the highest tested dendrimer concentration and 60.06 pg/mL for samples incubated with the highest tested dendriplex concentration, representing accordingly a 0.6-fold and 2.4-fold increase compared to the negative control (25.17 pg/mL). Although these trends suggest an upregulation of IL-6 expression with higher concentrations of dendriplex, the differences did not achieve statistical significance. These observations, together with findings from several other studies, reinforce the concept that the siRNA cargo is not merely a passive therapeutic payload but plays a role in defining nanoparticle properties and modulating the resultant immune response.[77] Moreover, our results suggest that the expression of IL-8 is modulated by both the dendrimer and its dendriplex in a manner that is dependent on the plasma environment. Under plasma-poor conditions, incubation of PBMCs with the highest concentration of the dendrimer G3Si PEG6000 resulted in the median of IL-8 expression level reaching 2855.59 pg/mL, corresponding to a 5.3-fold increase relative to the negative control, while the dendriplex further elevated the IL-8 median level to 3688.9 pg/mL, corresponding to a 6.9-fold increase compared to the negative control value. Conversely, in the plasma-rich environment, the dynamics shift occurs: the highest concentration of the studied dendrimer affected an IL-8 expression of median equal to 3171.46 pg/mL, representing a 1.7-fold increase over the control, while the incubation with the dendriplex led to a slightly lower level of 2814.09 pg/mL, representing a 1.5-fold increase relative to the negative control. In parallel to the trends observed for IL-8, the results suggest concentration-dependent effects of the tested nanosystem on TNFα expression in the plasma-poor environment, with the highest tested dendrimer concentration median reaching a 9.3-fold increase compared to the negative control value. In plasma-rich environments, however, the formation of a biomolecular corona masks the features of synthetic identity bioactive sites of the studied dendrimer, thereby reducing the dendrimer's capacity to modulate TNFα level compared to the effects of the studied nanosystem in plasma-poor environments. This illustrates the critical role of the biomolecular corona in determining nanoparticle bioactivity and highlights the importance of testing nanoparticle effects under conditions that closely mimic the in vivo environment.

Quantitative assessment of cytokine and chemokine secretion profiles serves as a critical tool for evaluating the immunological safety of novel nanomaterials. Elevated levels of these mediators can act as early biomarkers of dysregulated immune activation, including the onset of cytokine storms, and may predict adverse outcomes such as chronic inflammation, autoimmune activation, or irreversible tissue injury. While no

https://doi.org/10.1021/acsami.5c12952
ACS Appl. Mater. Interfaces 2026, 18, 11671−11686

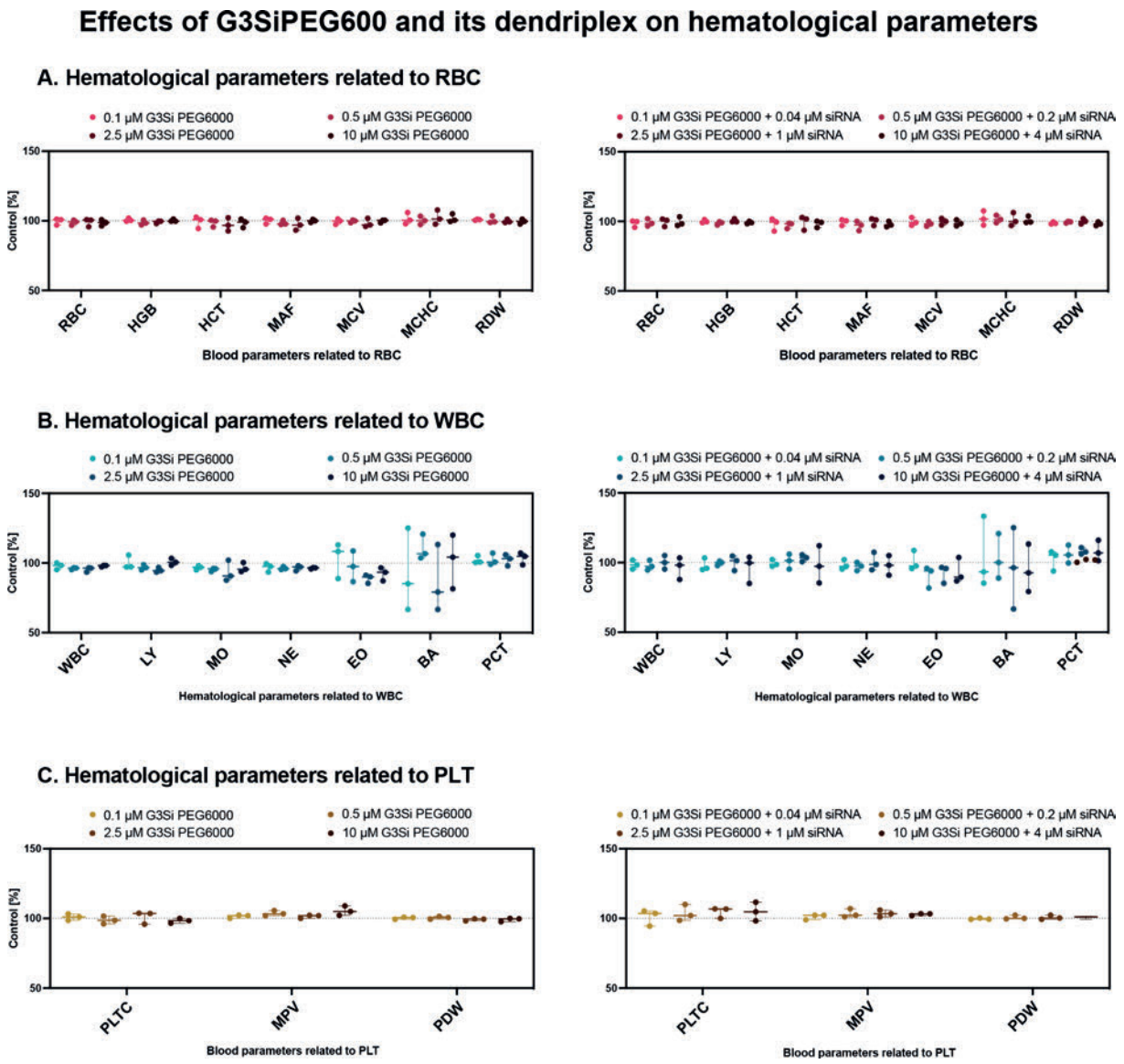


Figure 8. Effects of the G3Si PEG6000 dendrimer and its dendriplexes on various hematological parameters, expressed as a percentage relative to the negative control. Each panel pair in the figure represents parameters associated with RBC (A), WBC (B), and PLT (C). Individual data points correspond to measurements from single patients, and the horizontal line within each panel indicates the median value of the respective parameter.

statistically significant elevations in cytokine or chemokine levels were observed when compared to negative controls, subtle yet reproducible shifts in expression patterns were detected. These findings suggest that the G3Si PEG6000 dendrimer and its dendriplex formulation may exert a mild immunostimulatory effect, indicating that they are not completely immunologically inert. Within this framework, PEG on G3Si PEG6000 may exert mixed effects. Under plasma-rich conditions, steric shielding by the biocompatible polymer can significantly reduce recognition and clearance of nanoparticles by the RES, which blunts some pro-inflammatory readouts.[78] Conversely, PEG can also participate in complement-linked responses via anti-PEG antibodies, whose prevalence appears boosted in some populations after mRNA-LNP vaccination, potentially amplifying cytokine release in a donor-dependent manner.[79] Nonetheless, owing to interdonor variation in anti-PEG antibodies and complex complement triggers, our data cannot predict the intensity of any anti-PEG response in vivo. The minimal pro-inflammatory signature observed here is a desirable characteristic for translational nanomedicine applications, as it supports the potential for prolonged systemic circulation and reduced risk of off-target immunotoxicity in vivo. Importantly, these findings lay a strong foundation for subsequent in vivo evaluations, where a subdued innate immune response is often a prerequisite for clinical feasibility.

Hematological Blood Parameters

Building on the analyses conducted under simplified conditions, we expanded our investigation to evaluate the hemocompatibility of the G3Si PEG6000 dendrimer and its dendriplex in the complex environment of whole human blood. To achieve this, we utilized an advanced automatic hematology analyzer to study the effects of G3Si PEG6000 and its dendriplex on a comprehensive range of hematological parameters associated with RBCs, WBCs, and platelets (PLTs) over a 3 h incubation period.

The RBC parameters assessed—including RBC count (RBCC), hemoglobin (HGB), hematocrit (HCT), microcytic

https://doi.org/10.1021/acsami.5c12952
ACS Appl. Mater. Interfaces 2026, 18, 11671−11686

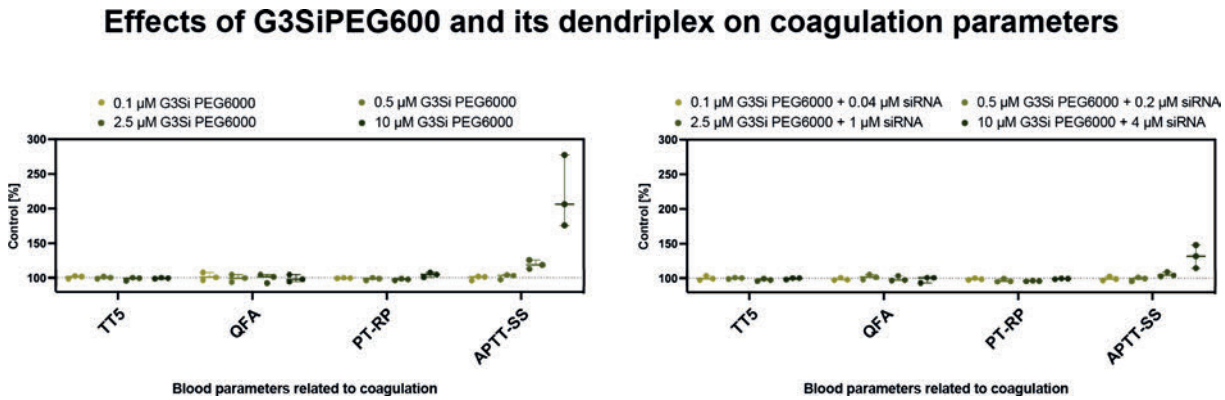


Figure 9. Effects of the G3Si PEG6000 dendrimer and its dendriplex on coagulation parameters, expressed as a percentage relative to the negative control. The panel on the left displays the effects of the dendrimer, while the panel on the right shows the effects of the dendriplex. Individual data points correspond to measurements from single patients, while the horizontal line within each panel indicates the median value of the respective parameter.

anemia factor (MAF), mean corpuscular volume (MCV), mean corpuscular hemoglobin concentration (MCHC), and red cell distribution width (RDW)—are critical indicators of erythrocyte health and function. In our study, the observation that these parameters remain within normal ranges, with minimal deviation from control samples, suggests that the introduction of G3Si PEG6000 dendrimers and their dendriplexes does not adversely affect red blood cells (Figure 8). Specifically, the unaltered RBC count and HGB, HCT, and MAF levels suggest the absence of eryptosis and agree with the results obtained in the hemotoxicity experiment in the presence of plasma. Stable MCV, MCHC, and RDW values further imply that the dendrimer exposure does not cause pronounced morphological alterations or cellular heterogeneity in RBC.

The evaluation of WBC parameters—including total WBC count (WBCC), neutrophils (NE), lymphocytes (LY), monocytes (MO), eosinophils (EO), basophils (BA), and procalcitonin (PCT) levels—revealed that most values remained within normal ranges. However, the observed variability in eosinophil and basophil counts may be attributed to analytical imprecision inherent in automated hematology analyzers. Basophils, being the least abundant WBC, present a challenge for precise quantification. Several studies have indicated that automated analyzers often exhibit high analytical imprecision and poor specificity in basophil counting and, to a lesser extent, for eosinophils.[80,81] Therefore, the scattered results observed for basophil and eosinophil counts in this study likely reflect the known limitations in the precision of automated hematology analyzers rather than an actual effect of dendrimer or dendriplex exposure. These results are in line with the results obtained in PBMC toxicity. Additionally, PCT levels remained within normal ranges, indicating that the nanovector exposure did not elicit a systemic inflammatory response, mimicking systemic bacterial infection.

The evaluation of PLT parameters—including PLT count (PLTC), mean platelet volume (MPV), and platelet distribution width (PDW)—revealed that all values remained within normal ranges, exhibiting minimal deviation from control samples. This consistency suggests that introducing G3Si PEG6000 dendrimers and their dendriplexes into whole blood does not adversely affect PLT function or morphology. Nanovectors may exert diverse effects on platelet behavior. Nanoparticles with negative surface charges, smaller sizes, and lower molecular weights have been shown to inhibit PLT aggregation. Conversely, cationic dendrimers are known to stimulate platelet aggregation due to the electrostatic interaction between their positively charged surfaces and the negatively charged platelet membrane. The observed stability of platelet parameters in the presence of positively charged G3Si PEG6000 dendrimers and its dendriplex may be attributed to the nanovector's PEGylation. It is well established in the scientific literature that surface modification reduces interactions with platelets and other blood components while enhancing biocompatibility, thereby minimizing the risk of adverse effects.[82]

Coagulation Blood Parameters

Advanced optical automatic hemostasis analyzer was utilized to evaluate the effect of the G3Si PEG6000 dendrimer and its dendriplex on coagulation parameters—including thrombin time (TT), quantitative fibrinogen assay (QFA), prothrombin time (PT), and activated partial thromboplastin time (aPTT)—demonstrated that TT, QFA, and PT values remained within normal ranges, exhibiting minimal deviation from control samples (Figure 9). However, a notable finding was the concentration-dependent prolongation of aPTT observed with the addition of both the G3Si PEG6000 dendrimer and its dendriplex. The isolated prolongation of aPTT, with physiologically normal values of TT, QFA, and PT, suggests the impact of the tested nanosystem on the intrinsic pathway of the coagulation cascade. The control aPTT median was 35.2 s, which increased to 42.9 s in samples containing 2.5 μM dendrimer and further to 74.4 s at a dendrimer concentration of 10 μM. In comparison, the aPTT prolongation was less pronounced in samples containing the dendriplex. The median aPTT for samples with 2.5 μM G3Si PEG6000 dendrimer and 1 μM siRNA rose to 37.5 s, while those with 10 μM G3Si PEG6000 dendrimer and 2.5 μM siRNA exhibited a median aPTT of 47.6 s. Prolongation of the aPTT by the tested nanovector may result from its interaction with coagulation factors specific to the intrinsic pathway. This interaction likely involves binding these factors to the dendrimer surface, leading to their depletion or functional inhibition. Multiple studies have demonstrated that nanoparticles can affect the coagulation pathways in various ways. Similar aPTT-biased anticoagulant effects are reported for polydopamine nanoparticles and ZIF-8 MOFs, reinforcing that nanosurface interactions can sequester intrinsic-pathway

https://doi.org/10.1021/acsami.5c12952
ACS Appl. Mater. Interfaces 2026, 18, 11671−11686

Table 1. Summary of Selected Hemocompatibility Parameter Readouts for the G3Si PEG6000 Dendrimer and Its siRNA Dendriplexes, Chosen from a Broader Panel of Parameters Evaluated in This Manuscript[a]

		Hemolysis [% of positive control]		Viscosity [% of control]		Fluorescence anistotropy [% of control]		PBMC viability [% of control]	Coagulation Parameters [% of control]
		without addition of plasma	with addition of plasma	1 s^{-1} shear rate	100 s^{-1} shear rate	DPH	TMA-DPH		APTT-SS
dendrimer	0.1 μM G3Si	1.74	1.60	↑ 105.19	107.66	98.40	99.32	106.18	99.68
	0.5 μM G3Si	3.40	1.53	↑ 108.36	111.90	↓ 91.97	↓ 92.13	101.93	101.49
	2.5μM G3Si	↑ 11.07	1.49	↑ 109.97	↑ 116.83	↓ 90.05	↓ 84.95	102.28	119.21
	10μM G3Si	↑ 27.46	1.71	↑ 110.51	↑ 120.52	↓ 89.70	↓ 84.21	93.44	↑ 219.90
dendriplex	0.1 μM G3Si + 0,04μM siRNA	1.10	1.60	↑ 113.01	103.41	100.02	97.34	101.61	99.24
	0.5 μM G3Si + 0,2μM siRNA	1.34	1.57	↑ 117.23	↑ 108.13	96.69	96.36	100.28	98.54
	2.5μM G3Si + 1μM siRNA	2.39	1.46	↑ 123.89	↑ 112.92	96.11	↓ 91.09	96.78	105.26
	10μM G3Si + 4μM siRNA	↑ 3.53	1.51	↑ 115.96	↑ 115.02	↓ 87.96	↓ 88.25	94.21	↑ 131.59

[a]Hemolysis and PBMC viability shown here were measured after 24 h of incubation; hemolysis is expressed as % of the positive control (100% RBC lysis), whereas viscosity (1 and 100 s^{-1}), fluorescence anisotropy (DPH, TMA-DPH), PBMC viability, and APTT-SS are expressed as % of the negative control. Blue arrows (↑/↓) indicate the direction of statistically significant changes relative to the corresponding control.

factors without broad extrinsic disturbance.[83,84] Notably, cationic amine-terminated PAMAM dendrimers were found to induce disseminated intravascular coagulation (DIC)-like effects in vivo at high doses.[85] The ability of nanovectors, such as PAMAM dendrimers, to interact with coagulation pathways underscores the critical importance of comprehensive safety testing in nanomedicine development. The mechanism of DIC itself is highly complex, involving coagulation factors, leukocytes, endothelial cells, and platelets, which collectively drive the pathological cascade. While the tested dendrimer G3Si PEG6000 and its dendriplex demonstrated no substantial effects on these critical components, suggesting a low likelihood of DIC development, future study designs and analyses must account for the likelihood of resulting in interruption of the intrinsic coagulation pathway to ensure their safety for effective application.

CONCLUSIONS

Given the increasing number of nanotechnology-based products in the development, evaluating the effects of nanoparticles on blood components is essential, as these interactions can significantly influence both the fate and efficacy of the nanovectors and constitute risks to hematological balance. Our comprehensive in vitro investigation of dendrimer G3Si PEG6000 and its dendriplex provides critical insights into the interactions between the nanovector and blood elements, highlighting the importance of biomolecular corona formation. The study conclusively demonstrates that dendrimer complexation with siRNA and biomolecular corona formation effectively mitigates direct hemolytic damage. Increasing concentrations of dendrimer G3Si PEG6000 and its dendriplex induce a modest, concentration-dependent increase in blood viscosity, most notably at lower shear rates. While the viscosity rise is comparable between the two formulations, the observed changes remain below thresholds typically associated with significant cardiovascular risks. Fluorescence spectroscopy analysis revealed that exposure to G3Si PEG6000 dendrimer and its dendriplex increases erythrocyte membrane fluidity, as evidenced by a decrease in fluorescence anisotropy. The uncomplexed dendrimer exerts a pronounced effect on membrane dynamics, whereas siRNA complexation attenuates this effect, thereby reducing dendrimers impacts membrane integrity. These findings align with hemotoxicity studies and suggest the hemorheology changes likely arise from enhanced cell-to-cell adhesion. In vitro cytotoxicity assays confirm that both the dendrimer and its dendriplex exhibit minimal effects on PBMC viability over 24 and 48 h incubation periods relative to the negative control, with only transient, nonsignificant variations observed at the highest concentrations. Modest immunomodulatory responses were observed, particularly reflected in cytokine expression profiles such as IL-6, IL-8, and TNFα; however, these remained within ranges unlikely to trigger severe systemic immune reactions. Notably, the magnitude and nature of these responses were strongly influenced by the presence of plasma and the siRNA cargo, highlighting the critical role of both the biological milieu and therapeutic payload in shaping the immunological behavior of the nanocarrier—an essential consideration for the design and clinical translation of any nanosystem. Advanced hematological analyses indicate that the nanovectors do not adversely alter RBC, WBC, or PLT parameters. Notably, most coagulation parameters remained within physiological limits, except for a nonsignificant, concentration-dependent prolongation of the aPTT, which suggests a mild impact on the intrinsic coagulation cascade. This effect was less pronounced in samples incubated with the dendriplex, likely due to siRNA complexation mitigating direct interactions with coagulation factors. A summary of the key findings is presented in Table 1. Ultimately, our data also highlight specific areas of concern that warrant further investigation in future studies, ensuring comprehensive safety profiling is necessary for effective clinical translation. Collectively, these results underscore the translational potential of this nanosystem for therapeutic applications and emphasize the importance of therapeutic cargo and biomolecular corona formation in assessing nanocarriers' safety and efficacy.

https://doi.org/10.1021/acsami.5c12952
ACS Appl. Mater. Interfaces 2026, 18, 11671−11686

AUTHOR INFORMATION

Corresponding Authors

Serafin Zawadzki − *Department of General Biophysics, Faculty of Biology and Environmental Protection, University of Lodz, Lodz 90-236, Poland; Bio-Med-Chem Doctoral School of the University of Lodz and Lodz Institutes of the Polish Academy of Sciences, University of Lodz, Lodz 90-237, Poland;* orcid.org/0000-0002-3093-5945; Email: serafin.zawadzki@edu.uni.lodz.pl

Katarzyna Miłowska − *Department of General Biophysics, Faculty of Biology and Environmental Protection, University of Lodz, Lodz 90-236, Poland;* orcid.org/0000-0002-4050-2756; Email: katarzyna.milowska@biol.uni.lodz.pl

Authors

Simon Suty − *Department of Nuclear Physics and Biophysics, Faculty of Mathematics, Physics and Informatics, Comenius University, Bratislava 842 48, Slovakia*

Elżbieta Okła − *Department of General Biophysics, Faculty of Biology and Environmental Protection, University of Lodz, Lodz 90-236, Poland*

Paula Ortega López − *Department of Organic and Inorganic Chemistry, IQAR, University of Alcalá, Madrid 28805, Spain; Networking Research Center on Bioengineering, Biomaterials and Nanomedicine (CIBER-BBN), Madrid 28029, Spain; Ramón y Cajal Health Research Institute (IRYCIS), Madrid 28034, Spain;* orcid.org/0000-0003-0377-5429

F. Javier de la Mata − *Department of Organic and Inorganic Chemistry, IQAR, University of Alcalá, Madrid 28805, Spain; Networking Research Center on Bioengineering, Biomaterials and Nanomedicine (CIBER-BBN), Madrid 28029, Spain; Ramón y Cajal Health Research Institute (IRYCIS), Madrid 28034, Spain;* orcid.org/0000-0003-0418-3935

Iveta Waczulikova − *Department of Nuclear Physics and Biophysics, Faculty of Mathematics, Physics and Informatics, Comenius University, Bratislava 842 48, Slovakia*

Maksim Ionov − *Department of General Biophysics, Faculty of Biology and Environmental Protection, University of Lodz, Lodz 90-236, Poland; Faculty of Medicine, Collegium Medicum, Mazovian Academy in Plock, Plock 09-402, Poland;* orcid.org/0000-0001-7227-6864

Maria Bryszewska − *Department of General Biophysics, Faculty of Biology and Environmental Protection, University of Lodz, Lodz 90-236, Poland*

Complete contact information is available at: https://pubs.acs.org/10.1021/acsami.5c12952

Author Contributions

S.Z.: Conceptualization, Methodology, Validation, Formal analysis, Investigation, Writing—Original Draft, Writing—Review and Editing, Visualization; E.O.: Investigation; S.S.: Investigation; P.O.L.: Resources; F.J.d.M.: Resources; I.W.: Methodology, Writing—Review and Editing; M.I.: Methodology, Writing—Review and Editing; M.B.: Conceptualization, Methodology, Resources, Writing—Review and Editing, Project administration, Funding acquisition; K.M.: Conceptualization, Methodology, Formal analysis, Data Curation, Writing—Review and Editing, Supervision, Project administration.

Notes

The authors declare no competing financial interest.

ACKNOWLEDGMENTS

This work was supported by grant 2018/30/Z/NZ1/00911 of the Project "NanoTENDO" financed by the National Science Centre, under the M-ERA.NET 2, which has received funding from the European Union's Horizon 2020 research. This research was also funded by grants from PID2020-112924RB-I00 (MINECO) and CIBER-BBN from ISCIII with assistance from the European Regional Development Fund. This research was also funded by the EU NextGenerationEU through the Recovery and Resilience Plan for Slovakia under the project No. 09I03-03-V04-00375. Additional support was provided by the Scientific Grant Agency of the Ministry of Education, Science, Research and Sport of the Slovak Republic and Slovak Academy of Sciences (VEGA), project registration number 1/0634/25 The authors would like to thank Hanna Jerczyńska, PhD from the Research Laboratory CoreLab of the Medical University of Lodz for her invaluable advice and technical assistance during the course of this study.

ABBREVIATIONS

APOE4,apolipoprotein E 4; aPTT,activated partial thromboplastin time; BA,basophils; BBB,blood−brain barrier; CNS,central nervous system; DAMPs,damage-associated molecular patterns; DIC,disseminated intravascular coagulation; DPH,1,6-diphenyl- 1,3,5-hexatriene; EMA,European Medicines Agency; EO,eosinophils; FBS,fetal bovine serum; FDA,Food and Drug Administration; HCT,hematocrit; HGB,hemoglobin; LY,lymphocytes; MAF,microcytic anemia factor; MCHC,mean corpuscular hemoglobin concentration; MCV,mean corpuscular volume; MO,monocytes; MPS,mononuclear phagocytic system; MPV,mean platelet volume; NE,neutrophils; PAMPs,pathogen-associated molecular patterns; PBMC,peripheral blood mononuclear cell; PBS,phosphate-buffered saline; PCT,procalcitonin; PDW,platelet distribution width; PEG,polyethylene glycol; PLTC,PLT count; PLT,platelets; PRRs,pattern recognition receptors; PT,prothrombin time; QFA,quantitative fibrinogen assay; RBCC,RBC count; RBC,red blood cells; RDW,red cell distribution width; RES,reticuloendothelial system; TMA-DPH,N,N,N-trimethyl-4-(6-phenyl-1,3,5-hexa-triene-1-yl); TT,thrombin time; WBCC,total WBC count; WBC,white blood cell

REFERENCES

(1) Sriram, K.; Intaglietta, M.; Tartakovsky, D. M. Non-Newtonian Flow of Blood in Arterioles: Consequences for Wall Shear Stress Measurements. *Microcirculation* **2014**, *21* (7), 628−639.

(2) Du, V.; Huskens, D.; Maas, C.; Al Dieri, R.; De Groot, P.; De Laat, B. New Insights into the Role of Erythrocytes in Thrombus Formation. *Semin Thromb Hemost* **2014**, *40* (01), 072−080.

(3) Davenport, R. D. Pathophysiology of Hemolytic Transfusion Reactions. *Seminars in Hematology* **2005**, *42* (3), 165−168.

(4) L'Acqua, C.; Hod, E. New Perspectives on the Thrombotic Complications of Haemolysis. *Br. J. Hamaetol.* **2015**, *168* (2), 175−185.

(5) Ataga, K. I. Hypercoagulability and Thrombotic Complications in Hemolytic Anemias. *Haematologica* **2009**, *94* (11), 1481−1484.

(6) Rother, R. P.; Bell, L.; Hillmen, P.; Gladwin, M. T. The Clinical Sequelae of Intravascular Hemolysis and Extracellular Plasma Hemoglobin: A Novel Mechanism of Human Disease. *JAMA* **2005**, *293* (13), 1653.

(7) Michalczuk, U.; Przekop, R.; Moskal, A. The Effect of Selected Nanoparticles on Rheological Properties of Human Blood. *Bulletin of the Polish Academy of Sciences Technical Sciences* **2022**, No. 140437.
(8) Lin, Y.-C. The Influence of Nanodiamond on the Oxygenation States and Micro Rheological Properties of Human Red Blood Cells in Vitro. *J. Biomed. Opt* **2012**, *17* (10), No. 101512.
(9) Weisel, J. W.; Litvinov, R. I. Red Blood Cells: The Forgotten Player in Hemostasis and Thrombosis. *Journal of Thrombosis and Haemostasis* **2019**, *17* (2), 271−282.
(10) Ran, Q.; Xiang, Y.; Liu, Y.; Xiang, L.; Li, F.; Deng, X.; Xiao, Y.; Chen, L.; Chen, L.; Li, Z. Eryptosis Indices as a Novel Predictive Parameter for Biocompatibility of Fe3O4Magnetic Nanoparticles on Erythrocytes. *Sci. Rep* **2015**, *5* (1), 16209.
(11) Pan, D. C.; Myerson, J. W.; Brenner, J. S.; Patel, P. N.; Anselmo, A. C.; Mitragotri, S.; Muzykantov, V. Nanoparticle Properties Modulate Their Attachment and Effect on Carrier Red Blood Cells. *Sci. Rep* **2018**, *8* (1), 1615.
(12) Kim, E.-H.; Choi, S.; Kim, D.; Park, H. J.; Bian, Y.; Choi, S. H.; Chung, H. Y.; Bae, O.-N. Amine-Modified Nanoplastics Promote the Procoagulant Activation of Isolated Human Red Blood Cells and Thrombus Formation in Rats. *Part Fibre Toxicol* **2022**, *19* (1), 60.
(13) Bian, Y.; Kim, K.; Ngo, T.; Kim, I.; Bae, O.-N.; Lim, K.-M.; Chung, J.-H. Silver Nanoparticles Promote Procoagulant Activity of Red Blood Cells: A Potential Risk of Thrombosis in Susceptible Population. *Part Fibre Toxicol* **2019**, *16* (1), 9.
(14) Bian, Y.; Chung, H.-Y.; Bae, O.-N.; Lim, K.-M.; Chung, J.-H.; Pi, J. Titanium Dioxide Nanoparticles Enhance Thrombosis through Triggering the Phosphatidylserine Exposure and Procoagulant Activation of Red Blood Cells. *Part Fibre Toxicol* **2021**, *18* (1), 28.
(15) Holinstat, M. Normal Platelet Function. *Cancer Metastasis Rev.* **2017**, *36* (2), 195−198.
(16) Mancuso, M. E.; Santagostino, E. Platelets: Much More than Bricks in a Breached Wall. *Br. J. Hamaetol.* **2017**, *178* (2), 209−219.
(17) Radomska, A.; Leszczyszyn, J.; Radomski, M. W. The Nanopharmacology and Nanotoxicology of Nanomaterials: New Opportunities and Challenges. *Adv. Clin Exp Med.* **2016**, *25* (1), 151−162.
(18) Brandt, E.; Petersen, F.; Ludwig, A.; Ehlert, J. E.; Bock, L.; Flad, H.-D. The *β*-Thromboglobulins and Platelet Factor 4: Blood Platelet-Derived CXC Chemokines with Divergent Roles in Early Neutrophil Regulation. *Journal of Leukocyte Biology* **2000**, *67* (4), 471−478.
(19) Fröhlich, E. Action of Nanoparticles on Platelet Activation and Plasmatic Coagulation. *CMC* **2016**, *23* (5), 408−430.
(20) Frenette, P. S.; Denis, C. V.; Weiss, L.; Jurk, K.; Subbarao, S.; Kehrel, B.; Hartwig, J. H.; Vestweber, D.; Wagner, D. D. P-Selectin Glycoprotein Ligand 1 (Psgl-1) Is Expressed on Platelets and Can Mediate Platelet−Endothelial Interactions in Vivo. *Journal of Experimental Medicine* **2000**, *191* (8), 1413−1422.
(21) Pallardy, M. J.; Turbica, I.; Biola-Vidamment, A. Why the Immune System Should Be Concerned by Nanomaterials? *Front. Immunol.* **2017**, *8*, 544.
(22) Rampado, R.; Crotti, S.; Caliceti, P.; Pucciarelli, S.; Agostini, M. Recent Advances in Understanding the Protein Corona of Nanoparticles and in the Formulation of "Stealthy" Nanomaterials. *Front. Bioeng. Biotechnol.* **2020**, *8*, 166.
(23) De La Harpe, K.; Kondiah, P.; Choonara, Y.; Marimuthu, T.; Du Toit, L.; Pillay, V. The Hemocompatibility of Nanoparticles: A Review of Cell−Nanoparticle Interactions and Hemostasis. *Cells* **2019**, *8* (10), 1209.
(24) Zawadzki, S.; Martín-Serrano, Á.; Okła, E.; Kędzierska, M.; Garcia-Gallego, S.; López, P. O.; De La Mata, F. J.; Michlewska, S.; Makowski, T.; Ionov, M.; Pędziwiatr-Werbicka, E.; Bryszewska, M.; Miłowska, K. Synthesis and Biophysical Evaluation of Carbosilane Dendrimers as Therapeutic siRNA Carriers. *Sci. Rep* **2024**, *14* (1), 1615.
(25) Raulin, A.-C.; Doss, S. V.; Trottier, Z. A.; Ikezu, T. C.; Bu, G.; Liu, C.-C. ApoE in Alzheimer's Disease: Pathophysiology and Therapeutic Strategies. *Mol. Neurodegeneration* **2022**, *17* (1), 72.
(26) Zawadzki, S.; Okła, E.; Michlewska, S.; Makowski, T.; Buczkowski, A.; López, P. O.; de la Mata, F. J.; Ionov, M.; Bryszewska, M.; Miłowska, K. Structural and Conformational Rearrangements of Human Serum Albumin, Transferrin, and Blood Plasma Induced by Carbosilane Dendrimer Therapeutic Delivery System. *Sci. Rep.* **2025**, *15*, 39650.
(27) Böhmert, L.; Voß, L.; Stock, V.; Braeuning, A.; Lampen, A.; Sieg, H. Isolation Methods for Particle Protein Corona Complexes from Protein-Rich Matrices. *Nanoscale Adv.* **2020**, *2* (2), 563−582.
(28) Hewson, W.; Gulliver, G. *The Works of William Hewson, F.R.S.*; The Sydenham Society [Publications]; Printed for the Sydenham Society: London, 1846.
(29) Virchow, R. *Gesammelte Abhandlungen Zur Wissenschaftlichen Medicin.*; Meidinger: Frankfurt a. M., 1856.
(30) Baier, R. E.; Kurusz, M. Understanding Blood/Material Interactions: Contributions From the Columbia University Biomaterials Seminar. *ASAIO Journal* **2012**, *58* (5), 450−454.
(31) Gurland, H. J.; Davison, A. M.; Bonomini, V.; Falkenhagen, D.; Hansen, S.; Kishimoto, T.; Lisaght, M. J.; Moran, J.; Valek, A. Definitions and Terminology in Biocompatibility. *Nephrol. dial. transplant. (Print)* **1994**, *9*, 4−10.
(32) Biological Evaluation of Medical Devices—Part 4: Selection of Tests for Interactions with Blood. In *ANSI/AAMI/ISO 10993−4:2017; Biological evaluation of medical devices—Part 4: Selection of tests for interactions with blood*; AAMI: 2020.
(33) Pfaller, T.; Colognato, R.; Nelissen, I.; Favilli, F.; Casals, E.; Ooms, D.; Leppens, H.; Ponti, J.; Stritzinger, R.; Puntes, V.; Boraschi, D.; Duschl, A.; Oostingh, G. J. The Suitability of Different Cellular *in Vitro* Immunotoxicity and Genotoxicity Methods for the Analysis of Nanoparticle-Induced Events. *Nanotoxicology* **2010**, *4* (1), 52−72.
(34) Gioria, S.; Caputo, F.; Urbán, P.; Maguire, C. M.; Bremer-Hoffmann, S.; Prina-Mello, A.; Calzolai, L.; Mehn, D. Are Existing Standard Methods Suitable for the Evaluation of Nanomedicines: Some Case Studies. *Nanomedicine (London)* **2018**, *13* (5), 539−554.
(35) Shi, L.; Zhang, J.; Zhao, M.; Tang, S.; Cheng, X.; Zhang, W.; Li, W.; Liu, X.; Peng, H.; Wang, Q. Effects of Polyethylene Glycol on the Surface of Nanoparticles for Targeted Drug Delivery. *Nanoscale* **2021**, *13* (24), 10748−10764.
(36) Padnya, P.; Shiabiev, I.; Pysin, D.; Gerasimova, T.; Ranishenka, B.; Stanavaya, A.; Abashkin, V.; Shcharbin, D.; Shi, X.; Shen, M.; Nazarova, A.; Stoikov, I. Non-Viral Systems Based on PAMAM-Calix-Dendrimers for Regulatory siRNA Delivery into Cancer Cells. *IJMS* **2024**, *25* (23), 12614.
(37) Chang, P. K. C.; Prestidge, C. A.; Bremmell, K. E. PAMAM versus PEI Complexation for siRNA Delivery: Interaction with Model Lipid Membranes and Cellular Uptake. *Pharm. Res.* **2022**, *39* (6), 1151−1163.
(38) Pang, Y. T.; Ge, Z.; Zhang, B.; Xiu, P.; Li, Q.; Wang, Y. Pore Formation Induced by Nanoparticles Binding to a Lipid Membrane. *Nanoscale* **2020**, *12* (14), 7902−7913.
(39) Xiao, Q.; Zoulikha, M.; Qiu, M.; Teng, C.; Lin, C.; Li, X.; Sallam, M. A.; Xu, Q.; He, W. The Effects of Protein Corona on in Vivo Fate of Nanocarriers. *Adv. Drug Delivery Rev.* **2022**, *186*, No. 114356.
(40) Önal Acet, B.; Gül, D.; Stauber, R. H.; Odabaşı, M.; Acet, Ö. A Review for Uncovering the "Protein-Nanoparticle Alliance": Implications of the Protein Corona for Biomedical Applications. *Nanomaterials* **2024**, *14* (10), 823.
(41) Saha, K.; Moyano, D. F.; Rotello, V. M. Protein Coronas Suppress the Hemolytic Activity of Hydrophilic and Hydrophobic Nanoparticles. *Mater. Horiz.* **2014**, *1* (1), 102−105.
(42) Ma, Z.; Bai, J.; Wang, Y.; Jiang, X. Impact of Shape and Pore Size of Mesoporous Silica Nanoparticles on Serum Protein Adsorption and RBCs Hemolysis. *ACS Appl. Mater. Interfaces* **2014**, *6* (4), 2431−2438.
(43) Paula, A. J.; Martinez, D. S. T.; Araujo Júnior, R. T.; Souza Filho, A. G.; Alves, O. L. Suppression of the Hemolytic Effect of Mesoporous Silica Nanoparticles after Protein Corona Interaction:

Independence of the Surface Microchemical Environment. *J. Braz. Chem. Soc.* **2012**, *23* (10), 1807−1814.
(44) Tenzer, S.; Docter, D.; Kuharev, J.; Musyanovych, A.; Fetz, V.; Hecht, R.; Schlenk, F.; Fischer, D.; Kiouptsi, K.; Reinhardt, C.; Landfester, K.; Schild, H.; Maskos, M.; Knauer, S. K.; Stauber, R. H. Rapid Formation of Plasma Protein Corona Critically Affects Nanoparticle Pathophysiology. *Nat. Nanotechnol.* **2013**, *8* (10), 772−781.
(45) Zhu, W.; Zhou, Y.; Guo, L.; Feng, S. Biological Function of Sialic Acid and Sialylation in Human Health and Disease. *Cell Death Discovery* **2024**, *10* (1), 415.
(46) Avsievich, T.; Popov, A.; Bykov, A.; Meglinski, I. Mutual Interaction of Red Blood Cells Influenced by Nanoparticles. *Sci. Rep* **2019**, *9* (1), 5147.
(47) Tran, H. D. N.; Moonshi, S. S.; Xu, Z. P.; Ta, H. T. Influence of Nanoparticles on the Haemostatic Balance: Between Thrombosis and Haemorrhage. *Biomater. Sci.* **2021**, *10* (1), 10−50.
(48) Beris, A. N.; Horner, J. S.; Jariwala, S.; Armstrong, M. J.; Wagner, N. J. Recent Advances in Blood Rheology: A Review. *Soft Matter* **2021**, *17* (47), 10591−10613.
(49) Lanotte, L.; Mauer, J.; Mendez, S.; Fedosov, D. A.; Fromental, J.-M.; Claveria, V.; Nicoud, F.; Gompper, G.; Abkarian, M. Red Cells' Dynamic Morphologies Govern Blood Shear Thinning under Microcirculatory Flow Conditions. *Proc. Natl. Acad. Sci. U.S.A.* **2016**, *113* (47), 13289−13294.
(50) Brust, M.; Schaefer, C.; Doerr, R.; Pan, L.; Garcia, M.; Arratia, P. E.; Wagner, C. Rheology of Human Blood Plasma: Viscoelastic Versus Newtonian Behavior. *Phys. Rev. Lett.* **2013**, *110* (7), No. 078305.
(51) Watts, T.; Barigou, M.; Nash, G. B. Comparative Rheology of the Adhesion of Platelets and Leukocytes from Flowing Blood: Why Are Platelets so Small? *American Journal of Physiology-Heart and Circulatory Physiology* **2013**, *304* (11), H1483−H1494.
(52) Aarts, P. A.; Van Den Broek, S. A.; Prins, G. W.; Kuiken, G. D.; Sixma, J. J.; Heethaar, R. M. Blood Platelets Are Concentrated near the Wall and Red Blood Cells, in the Center in Flowing Blood. *Arteriosclerosis* **1988**, *8* (6), 819−824.
(53) Cooley, M.; Sarode, A.; Hoore, M.; Fedosov, D. A.; Mitragotri, S.; Sen Gupta, A. Influence of Particle Size and Shape on Their Margination and Wall-Adhesion: Implications in Drug Delivery Vehicle Design across Nano-to-Micro Scale. *Nanoscale* **2018**, *10* (32), 15350−15364.
(54) Kroll, M. H.; Hellums, J. D.; McIntire, L. V.; Schafer, A. I.; Moake, J. L. Platelets and Shear Stress. *Blood* **1996**, *88* (5), 1525−1541.
(55) Farina, A.; Rosso, F.; Fasano, A. A Continuum Mechanics Model for the Fåhræus-Lindqvist Effect. *J. Biol. Phys.* **2021**, *47* (3), 253−270.
(56) Fåhræus, R.; Lindqvist, T. THE VISCOSITY OF THE BLOOD IN NARROW CAPILLARY TUBES. *American Journal of Physiology-Legacy Content* **1931**, *96* (3), 562−568.
(57) Devereux, R. B.; Case, D. B.; Alderman, M. H.; Pickering, T. G.; Chien, S.; Laragh, J. H. Possible Role of Increased Blood Viscosity in the Hemodynamics of Systemic Hypertension. *American Journal of Cardiology* **2000**, *85* (10), 1265−1268.
(58) Gal, R.; Praksch, D.; Kenyeres, P.; Rabai, M.; Toth, K.; Halmosi, R.; Habon, T. Hemorheological Alterations in Patients with Heart Failure with Reduced Ejection Fraction Treated by Resveratrol. *Cardiovascular Therapeutics* **2020**, *2020*, 1−8.
(59) Akcaboy, M.; Nazliel, B.; Goktas, T.; Kula, S.; Celik, B.; Buyan, N. Whole Blood Viscosity and Cerebral Blood Flow Velocities in Obese Hypertensive or Obese Normotensive Adolescents. *Journal of Pediatric Endocrinology and Metabolism* **2018**, *31* (3), 275−281.
(60) Connes, P.; Alexy, T.; Detterich, J.; Romana, M.; Hardy-Dessources, M.-D.; Ballas, S. K. The Role of Blood Rheology in Sickle Cell Disease. *Blood Reviews* **2016**, *30* (2), 111−118.
(61) Veliskova, M.; Zvarik, M.; Suty, S.; Jacko, J.; Mydla, P.; Cechova, K.; Dzubinska, D.; Morvova, M.; Ionov, M.; Terehova, M.; Majoral, J.-P.; Bryszewska, M.; Waczulikova, I. In Vitro Interactions of Amphiphilic Phosphorous Dendrons with Liposomes and Exosomes—Implications for Blood Viscosity Changes. *Pharmaceutics* **2022**, *14* (8), 1596.
(62) Tian, Y.; Tian, Z.; Dong, Y.; Wang, X.; Zhan, L. Current Advances in Nanomaterials Affecting Morphology, Structure, and Function of Erythrocytes. *RSC Adv.* **2021**, *11* (12), 6958−6971.
(63) Gupta, R.; Badhe, Y.; Mitragotri, S.; Rai, B. Permeation of Nanoparticles across the Intestinal Lipid Membrane: Dependence on Shape and Surface Chemistry Studied through Molecular Simulations. *Nanoscale* **2020**, *12* (11), 6318−6333.
(64) Dimova, R.; Marques, C. M. *The Giant Vesicle Book*; CRC press, Taylor & Francis group: Boca Raton, FL, 2020.
(65) Kim, J.; Lee, H.; Shin, S. Advances in the Measurement of Red Blood Cell Deformability: A Brief Review. *JCB* **2015**, *1* (1), 63−79.
(66) Kleiveland, C. R. Peripheral Blood Mononuclear Cells. In *The Impact of Food Bioactives on Health*; Verhoeckx, K.; Cotter, P.; López-Expósito, I.; Kleiveland, C.; Lea, T.; Mackie, A.; Requena, T.; Swiatecka, D.; Wichers, H., Eds.; Springer International Publishing: Cham, 2015; pp 161−167.
(67) Candeias, L. P.; MacFarlane, D. P. S.; McWhinnie, S. L. W.; Maidwell, N. L.; Roeschlaub, C. A.; Sammes, P. G.; Whittlesey, R. The Catalysed NADH Reduction of Resazurin to Resorufin. *J. Chem. Soc., Perkin Trans. 2* **1998**, *11*, 2333−2334.
(68) Zhang, H.; Du, G.; Zhang, J. Assay of Mitochondrial Functions by Resazurin in Vitro. *Acta Pharmacol. Sin.* **2004**, *25*, 385.
(69) David, C. A. W.; Barrow, M.; Murray, P.; Rosseinsky, M. J.; Owen, A.; Liptrott, N. J. In Vitro Determination of the Immunogenic Impact of Nanomaterials on Primary Peripheral Blood Mononuclear Cells. *IJMS* **2020**, *21* (16), 5610.
(70) Silva, A. L.; Peres, C.; Conniot, J.; Matos, A. I.; Moura, L.; Carreira, B.; Sainz, V.; Scomparin, A.; Satchi-Fainaro, R.; Préat, V.; Florindo, H. F. Nanoparticle Impact on Innate Immune Cell Pattern-Recognition Receptors and Inflammasomes Activation. *Seminars in Immunology* **2017**, *34*, 3−24.
(71) Brun, E.; Sicard-Roselli, C. Could Nanoparticle Corona Characterization Help for Biological Consequence Prediction? *Cancer Nanotechnol.* **2014**, *5* (1), 7.
(72) Lesniak, A.; Salvati, A.; Santos-Martinez, M. J.; Radomski, M. W.; Dawson, K. A.; Åberg, C. Nanoparticle Adhesion to the Cell Membrane and Its Effect on Nanoparticle Uptake Efficiency. *J. Am. Chem. Soc.* **2013**, *135* (4), 1438−1444.
(73) Carnovale, C.; Bryant, G.; Shukla, R.; Bansal, V. Identifying Trends in Gold Nanoparticle Toxicity and Uptake: Size, Shape, Capping Ligand, and Biological Corona. *ACS Omega* **2019**, *4* (1), 242−256.
(74) Zhang, X.; Si, S.; Lieberwirth, I.; Landfester, K.; Mailänder, V. Engineered Protein Corona Sustains Stealth Functionality of Nanocarriers in Plasma. *J. Nanobiotechnol* **2025**, *23* (1), 512.
(75) Rivera, A.; Siracusa, M. C.; Yap, G. S.; Gause, W. C. Innate Cell Communication Kick-Starts Pathogen-Specific Immunity. *Nat. Immunol* **2016**, *17* (4), 356−363.
(76) Kaczorowski, K. J.; Shekhar, K.; Nkulikiyimfura, D.; Dekker, C. L.; Maecker, H.; Davis, M. M.; Chakraborty, A. K.; Brodin, P. Continuous Immunotypes Describe Human Immune Variation and Predict Diverse Responses. *Proc. Natl. Acad. Sci. U. S. A.* **2017**, *114* (30), E6097−E6106.
(77) Kanasty, R. L.; Whitehead, K. A.; Vegas, A. J.; Anderson, D. G. Action and Reaction: The Biological Response to siRNA and Its Delivery Vehicles. *Molecular Therapy* **2012**, *20* (3), 513−524.
(78) Estapé Senti, M.; De Jongh, C. A.; Dijkxhoorn, K.; Verhoef, J. J. F.; Szebeni, J.; Storm, G.; Hack, C. E.; Schiffelers, R. M.; Fens, M. H.; Boross, P. Anti-PEG Antibodies Compromise the Integrity of PEGylated Lipid-Based Nanoparticles via Complement. *J. Controlled Release* **2022**, *341*, 475−486.
(79) Li, C.; Li, T.; Tian, X.; An, W.; Wang, Z.; Han, B.; Tao, H.; Wang, J.; Wang, X. Research Progress on the PEGylation of Therapeutic Proteins and Peptides (TPPs). *Front. Pharmacol.* **2024**, *15*, 1353626.

https://doi.org/10.1021/acsami.5c12952
ACS Appl. Mater. Interfaces 2026, 18, 11671−11686

(80) Hoffmann, J. J. M. L. Basophil Counting in Hematology Analyzers: Time to Discontinue? *Clinical Chemistry and Laboratory Medicine (CCLM)* **2021**, *59* (5), 813−820.
(81) Åstrand, A.; Wingren, C.; Walton, C.; Mattsson, J.; Agrawal, K.; Lindqvist, M.; Odqvist, L.; Burmeister, B.; Eck, S.; Hughes, G.; Luporini Saraiva, G.; Schantz, A.; Psallidas, I.; McCrae, C. A Comparative Study of Blood Cell Count in Four Automated Hematology Analyzers: An Evaluation of the Impact of Preanalytical Factors. *PLoS One* **2024**, *19* (5), No. e0301845.
(82) Mehrizi, T. Z.; Kafiabad, S. A.; Eshghi, P. Effects and Treatment Applications of Polymeric Nanoparticles on Improving Platelets' Storage Time: A Review of the Literature from 2010 to 2020. *Blood Res.* **2021**, *56* (4), 215−228.
(83) Li, S.; Yan, S.-M.; Zhang, L.-W.; Yang, X.-Y.; Guo, Z. Blood Compatibility Evaluation of Polydopamine Nanoparticles. *Front. Pharmacol.* **2025**, *16*, 1530650.
(84) Lin, J.; Huang, L.; Ou, H.; Chen, A.; Xiang, R.; Liu, Z. Effects of ZIF-8 MOFs on Structure and Function of Blood Components. *RSC Adv.* **2021**, *11* (35), 21414−21425.
(85) Ilinskaya, A. N.; Dobrovolskaia, M. A. Nanoparticles and The Blood Coagulation System. Part II: Safety Concerns. *Nanomedicine* **2013**, *8* (6), 969−981.



https://doi.org/10.1021/acsami.5c12952
ACS Appl. Mater. Interfaces 2026, 18, 11671−11686

Multilevel Assessment of Carbosilane Dendrimer–siRNA Nanoplatform: Cellular Compatibility, Blood–Brain Barrier Model Integrity, and Murine Model Biodistribution

Serafin Zawadzki [1,2,] (serafin.zawadzki@edu.uni.lodz.pl), Elżbieta Okła [1] (elzbieta.okla@biol.uni.lodz.pl), Paula Ortega López [3,4,5] (paula.ortega@uah.es), F. Javier de la Mata [3,4,5] (javier.delamata@uah.es), Maksim Ionov [1,6] (maksim.ionov@biol.uni.lodz.pl), Madara Kreišmane [7] (madara.kreismane@rsu.lv), Dace Skrastiņa [7] (daceskr@biomed.lu.lv), Juris Jansons [7] (jansons@biomed.lu.lv) Maria Bryszewska [1] (maria.bryszewska@biol.uni.lodz.pl) and Katarzyna Miłowska [1,**] (katarzyna.milowska@biol.uni.lodz.pl)*

1. Department of General Biophysics, Faculty of Biology and Environmental Protection, University of Lodz, 141/143 Pomorska St., 90-236 Lodz, Poland; 2. Bio-Med-Chem Doctoral School of the University of Lodz and Lodz Institutes of the Polish Academy of Sciences, University of Lodz Matejki 21/23, Lodz 90-237, Poland; 3. Department of Organic and Inorganic Chemistry, IQAR, University of Alcalá, 28805 Madrid, Spain; 4. Networking Research Center on Bioengineering, Biomaterials and Nanomedicine (CIBER-BBN), 28029 Madrid, Spain; 5. Ramón y Cajal Health Research Institute (IRYCIS), 28034 Madrid, Spain; 6. Faculty of Medicine, Collegium Medicum, Mazovian Academy in Plock, 2 Dabrowskiego Sq, 09-402

Plock, Poland; 7. Latvian Biomedical Research and Study Centre, Ratsupites street1 k-1, Riga LV-1067, Latvia

KEYWORDS: Carbosilane Dendrimer, Nanoparticles, siRNA, BBB Model, Biodistribution

ABSTRACT

The tight regulation of bidirectional solute flux between the systemic circulation and neural tissue by the blood–brain barrier (BBB) remains a principal obstacle to effective pharmacotherapy of the central nervous system. In this study, we evaluate the biocompatibility and biodistribution of a novel third-generation PEGylated carbosilane dendrimer (G3Si PEG6000) and its siRNA dendriplex using a tiered, upstream strategy that progresses from BBB-relevant monocultures to a capillary-weighted BBB model, and *in vivo/ex vivo* biodistribution in mice, in accordance with current recommendations for nanomaterial testing. In endothelial cells, pericytes, and astrocytes, mitochondrial/redox profiling (MTT, DCF-ROS, JC-1 ΔΨm) defined tolerated exposure ranges. Complexation with siRNA consistently attenuated apparent cytotoxicity across cell types, yet both free and complexed formulations elicited modest ROS and dose-dependent ΔΨm depolarization, indicating persistent mitochondrial stress. In the BBB model, responses were concentration- and formulation-dependent: high-dose free dendrimer produced sustained impedance and nuclear confluence loss with sheet-like detachment, whereas lower doses and the dendriplex induced transient, recoverable perturbations or increases in impedance and proliferation. *In vivo*, whole-body IVIS imaging demonstrated prolonged systemic exposure for the dendriplex and an ex vivo kidney-dominant, liver-secondary distribution; brain fluorescence was below planar NIR-I detection limits. Collectively, these data indicate that siRNA complexation broadens the functional window at the BBB and improves

pharmacokinetic behavior, providing a mechanistically informed basis for dose optimization and efficacy testing of this dendrimer–siRNA platform in CNS indications. The results provide a scientific basis for advancing this platform in further investigations targeting Alzheimer's disease.

INTRODUCTION

The central nervous system (CNS) is the most structurally and functionally complex organ system in higher metazoans. Although constituting only approximately 2% of total body mass, the human brain accounts for approximately 20% of the organism's total glucose and oxygen consumption, reflecting its exceptionally high metabolic demand [1,2]. Due to its limited capacity to store metabolic substrates, the CNS relies on a continuous, tightly regulated supply of vital nutrients derived from systemic circulation. The human cerebral vasculature facilitates not only the delivery of oxygen, metabolic substrates, and essential nutrients but also the removal of carbon dioxide and neurotoxic metabolites. The vascular architecture is aligned with the spatial and energetic demands of approximately 86 billion neurons and a similar number of non-neuronal cells, which, collectively with astrocytes and pericytes, occupy almost 80% of brain volume. The extracellular space accounts for 15–30% of brain volume, while the cerebral vasculature constitutes only about 3% of brain volume. Brain capillaries range 7–10 μm in diameter and are spaced about 40 μm apart, ensuring that neuronal somata are typically situated 10–20 μm from a capillary [3,4]. This pervasive microvasculature ensures proper neurovascular coupling by maintaining the chemical composition of brain interstitial fluid (ISF), which is critical for proper synaptic functioning, information processing, and neuronal connectivity. Disruption of cerebral vascular integrity increases permeability, perturbs cerebral blood flow (CBF), impairs synaptic activity and network function, while permitting the entry of neurotoxic

blood-derived molecules, immune cells, and microbial agents that initiate an inflammatory cascade and contribute to neurodegeneration. Loss of cerebral perfusion leads to rapid neuronal injury, and neuronal necrosis initiates within minutes, with irreversible brain damage occurring within hours after cessation of CBF [5,6]. To maintain strict physical and functional compartmentalization between the systemic circulation and the cerebral parenchyma, vertebrates have evolved critical barrier systems: the blood-brain barrier (BBB), blood-spinal cord barrier (BSCB), blood-cerebrospinal fluid barrier (BCSFB), and the arachnoid barrier (AB), with circumventricular organs (CVO) playing a unique role in this compartmentalization. Among these systems, the BBB stands out as the primary interface between the systemic circulation and the brain parenchyma. The BBB is a specialized, highly selective, and dynamic interface comprised mainly of endothelial cells that regulates the molecular and cellular influx and efflux of fluids, thereby preserving the brain's homeostatic environment [7].

Bidirectional molecular exchanges between blood-and-brain and brain-and-blood proceed via discrete, solute-selective pathways determined by each molecule's physicochemical attributes. Under physiological conditions, tight junctions (TJ) formed by claudins and occludin effectively restrict the penetration of solutes through paracellular diffusion, so most movement occurs through transcellular diffusion. Lipid-soluble compounds and gases may cross predominantly by passive transcellular diffusion through the cell plasma whereas the membrane majority of substrates use regulated endothelial mechanisms: solute-carrier–mediated transport (CMT) for carbohydrates, amino acids, monocarboxylates, hormones, fatty acids, nucleotides, organic anions and cations, amines, choline, and vitamins; receptor-mediated transcytosis (RMT) for proteins such as transferrin, insulin, leptin, arginine vasopressin, amyloid-β, and apolipoproteins E and J; and ion transport pathways like ATPases, uniporters, exchangers, and symporters move

Na+, K+, Cl−, HCO3−, H+, and Ca2+; ATP-binding cassette efflux pumps return xenobiotics, drugs, drug conjugates, and nucleosides to the blood [7–9]. While essential for homeostasis, the tightly regulated molecular trafficking remains a major impediment to the effective delivery of drugs and therapeutic nucleic acids for treating brain disorders. The BBB excludes from entering the brain parenchyma approximately 98% of small molecule drugs prevent systemically administered drugs achieving therapeutically relevant unbound concentrations, underscoring the need to re-evaluate prevailing strategies and to leverage opportunities for mechanism-informed delivery platforms [10,11]. Advances in understanding BBB physiology, including delineation of transporter systems, tight-junction regulation, and neurovascular unit dynamics, together with increasingly predictive *in vitro* and microphysiological models, now enable design and rigorous preclinical evaluation of brain-targeted delivery systems [12]. In this context, nanoparticle platforms offer modular carriers whose size, morphology, and surface chemistry can be precisely engineered. Surface functionalization with peptide ligands can exploit receptor- or carrier-mediated transcytosis, whereas cationic or amphiphilic coatings facilitate adsorptive-mediated transcytosis. Stealth strategies such as PEGylation modulate biomolecular corona composition reduce opsonization, and stimuli-responsive or biomimetic designs can enhance endosomal escape and target engagement while optimizing hemocompatibility, therapeutic index, circulation half-life, biodistribution, BBB penetration, and spatiotemporally controlled release within the CNS [13–21]. A broad array of nanomaterials, including dendrimers, carbon nanotubes, quantum dots, polymeric and metallic nanoparticles, nanocrystals, nanoemulsions, and lipid-based systems, have been investigated for CNS delivery to achieve therapeutically relevant concentrations at the site of action. Dendrimers are among the most versatile and structurally well-defined nanocarriers, consisting of a symmetrical core with radially branching repeat

monomer units that define the generation number. Their architecture enables precise control over their size, shape, and surface chemistry, termed “synthetic identity”, that also defines their biomolecular corona composition, forming their "biological identity". All the factors collectively determine their biocompatibility, immunogenicity, colloidal stability, membrane interaction, cellular uptake, and intracellular trafficking [22–24]. Dendrimers are predominantly internalized via clathrin-mediated endocytosis, with additional contributions from macropinocytosis, then act as a proton sponge, making endosomes and lysosomes easier to rupture and release the trapped dendrimers and carried therapeutics [25]. The unique dendrimer properties have allowed to engineer formulations that have demonstrated the capacity to traverse major physiological barriers, including the skin, pulmonary airway mucosa, the oral and intestinal epithelium, ocular surfaces, placenta barrier and BBB [26–31]. Multiple dendrimer-based systems have been evaluated *in vitro* using static and dynamic BBB models as well as *in vivo* models and proven potential for brain delivery of chemotherapeutics, anti-inflammatory agents, neuroprotective small molecules, and nucleic acid cargos [32–37]. The accumulating evidence base and rapid progress in functionalized dendrimer designs continue to expand their translational potential for targeted CNS therapy. Within this space, carbosilane dendrimers are emerging as attractive siRNA carriers with favorable safety–efficiency trade-offs and physicochemical profiles suited for variety of applications [38–42].

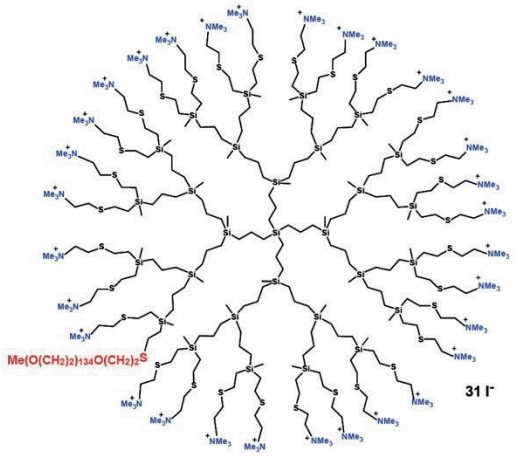
Guided by advances in understanding of cerebrovascular biology, experimental methodologies, and nanotechnology, in the article, we evaluate a third-generation, PEGylated cationic carbosilane dendrimer as a carrier for apolipoprotein E4 (APOE4) directed siRNA as a rational delivery platform for Alzheimer's disease therapy [43]. Our study was conducted under a weight-of-evidence, intelligent testing strategy (ITS/IATA) framework in line with OECD guidance and

ISO/TR 16197 recommendations for toxicological screening of manufactured nanomaterials. We first established the nanocarrier's synthetic identity in our prior work where we comprehensively characterizing the carbosilane dendrimer and its complex with siRNA (dendriplex) biophysical parameters and evaluated interactions with model proteins to anticipate formation of a biologically relevant biomolecullar corona, together with hemocompatibility testing using recognized practices for blood-contacting materials [44–46]. Building on that foundation, the present article integrates cell viability and cytotoxicity profiling (MTT), reactive oxygen species (ROS) quantification, and mitochondrial membrane potential ($\Delta\Psi m$) assessment, with a tri-culture BBB model characterized barrier integrity by real-time impedance and fluorescence microscopy. For translational context, we further performed *in vivo* whole-body fluorescence imaging in mice (IVIS) to analyze biodistribution, followed by ex vivo IVIS of excised organs after necropsy to assess the nanosystem's organ-level distribution.

MATERIALS AND METHODS

Dendrimer

Dendrimer with a silicon atom core, surface tertiary ammonium groups, and single polyethylene glycol (PEG) (6000) – G3Si PEG6000 with chemical formula $C_{601}H_{1324}I_{30}N_{31}O_{135}S_{32}Si_{29}$ and molar weight of 16794.81 g/mol is presented in Figure 1. The studied dendrimer was diluted in a phosphate buffer solution of 7.4 pH. The synthesis and biophysical characterization of the dendrimer, along with its complex with siRNA, was described in previous work [44].



G3Si PEG6000

Figure 1. Structure of the studied dendrimer G3Si PEG6000.

siRNA

The following siRNA was used in the present study (Revvity Inc, Waltham, Massachusetts, USA):

Sense: 5'-GAUUACCUGCGCUGGGUGCUU

Antisense: 5'-P GCACCCAGCGCAGGUAAUCUU

Dendriplex formation

Our prior research provides insights into the dendrimer/siRNA complexation process. We characterized Dendrimer G3Si PEG6000 and determined its optimal dendriplex saturation at a molar ratio of dendrimer to siRNA of 2.5:1 [44]. In this research, we chose dendrimer G3Si PEG6000 concentrations ranging from 0.1 to 10 μM and 0.04 to 4 μM for the siRNA in dendriplex. The dendrimer/siRNA complexes were incubated in PBS (Sigma-Aldrich, Saint Louis, MO, USA) at room temperature for 20 minutes to ensure complex formation.

Cell Lines

Human brain microvascular endothelial cells (HBEC-5i; ATCC, Manassas, VA, USA) were cultured on tissue culture flasks pre-coated with 1% gelatin coated flasks in Dulbecco's Modified Eagle Medium/Nutrient Mixture F-12 (DMEM/F-12; Biowest, Nuaillé, France) supplemented with 10% heat-inactivated fetal bovine serum (FBS; Biowest, Nuaillé, France), 1% penicillin–streptomycin (P/S; Sigma-Aldrich, Saint Louis, MO, USA), endothelial cell growth supplement (ECGS; Sigma-Aldrich, Darmstadt, Germany), and 1 μg/mL hydrocortisone (MP Biomedicals, Santa Ana, CA, USA). Cells were maintained at 37 °C in a humidified 5% CO_2 incubator.

Human brain vascular pericytes (HBVP; ScienCell Research Laboratories, Carlsbad, CA, USA) were cultured on flasks coated with 2 μg/cm² poly-L-lysine (PLL) in pericyte medium supplemented with FBS, pericyte growth supplement (PGS), and P/S (all from ScienCell Research Laboratories, Carlsbad, CA, USA). Cells were maintained at 37 °C in a humidified 5% CO_2 incubator.

Human astrocytes (HA; ScienCell Research Laboratories) were grown on flasks coated with 2 μg/cm² PLL in astrocyte medium supplemented with FBS, astrocyte growth supplement (AGS), and P/S (all from ScienCell Research Laboratories, Carlsbad, CA, USA). Cells were maintained at 37 °C in a humidified 5% CO_2 incubator.

Cytotoxicity Profiling

Human astrocytes (HA), Human Brain Vascular Pericytes (HBVP), and Human Brain Endothelial Cell (HBEC-5i) cells were seeded into 96-well plates at 1×10^4 cells/well (37 °C, 5% CO_2). To evaluate the effects of G3Si-PEG6000 and its dendriplex across the three cell lines,

cells were exposed to each formulation for 24 h. After incubation, cells were washed in PBS and incubated with 0.5 mg/mL of MTT at 37 °C for 3 h. Then the MTT was discarded carefully, and DMSO (both sourced from Avantor, Radnor, PA, USA) was added to solubilize the formazan crystals [47]. Finally, the absorbance was measured for each well at a wavelength of 570 nm using a Bio-Tek Synergy HT Microplate Reader (Bio-Tek Instruments, Winooski, VT, USA). Cell viability was calculated as the percent ratio of absorbance of the samples to the reference control (untreated). The experiment was performed in 6 repetitions for the HBEC-5i cell line and 3 repetitions for the HA and HBVP cell lines.

Reactive Oxygen Species (ROS) Quantification

HBEC-5i cells were seeded in black 96-well plates at 1.5×10^4 cells/well and cultured for 24 h (37 °C, 5% CO_2). Cells were then exposed to G3Si PEG6000 or its dendriplex and assessed after 1, 3, and 24 h. After the incubation, cells were washed with PBS and loaded with 2 μM 2′,7′-dichlorodihydrofluorescein diacetate (H2DCF-DA, Thermo Fisher Scientific, Waltham, MA, USA) probe for 15 min at 37 °C, 5% CO_2. The non-fluorescent H2DCF-DA probe, which diffuses into cells, is deacetylated by intracellular esterases to non-fluorescent DCFH and is oxidized by ROS to fluorescent DCF, which was read fluorometrically at λ_{ex} = 485 nm and λ_{em} = 530 nm on a plate reader (BioTek PowerWave HT, BioTek Instruments, Inc., Winooski, VT, USA). The experiment was performed in 3 repetitions.

Mitochondrial Membrane Potential (ΔΨm) and Function Assessment

HBEC-5i cells were seeded in black 96-well plates at 1.5×10^4 cells/well and cultured for 24 h (37 °C, 5% CO_2). Cells were then exposed to G3Si PEG6000 or its dendriplex and assessed after

1, 3, and 24 h. After the incubation, cells were washed with PBS and loaded with 5 μM JC-1 (Thermo Fisher Scientific, Waltham, MA, USA) for 20 min at 37 °C under 5% CO_2 (light-protected). JC-1 accumulates in mitochondria in a membrane-potential–dependent manner: at low ΔΨm it remains monomeric and fluoresces green, whereas at high ΔΨm it forms red-emitting J-aggregates. The fluorescence was measured at λ_{ex}=485nm, λ_{em} = 530 nm for monomers and λ_{ex} = 528 nm, λ_{em} = 590 nm for dimers on the multiwell plate reader (BioTek PowerWave HT, BioTek Instruments, Inc., Winooski, VT, USA) and ΔΨm was expressed as the red/green (590/530 nm) ratio. The experiment was performed in 3 repetitions.

Real-Time Blood–Brain Barrier (BBB) Model Integrity by Impedance Measurement

A human triculture BBB model (astrocytes–pericytes–endothelium) was established on electrode-integrated 96- (E-Plate VIEW 96, Agilent), which were pre-coated with poly-L-lysine (PLL, 10 μg/mL, 50 μL/well, 3 h), rinsed twice with sterile water, and equilibrated with complete medium before background impedance was recorded. Astrocytes were seeded first at 2.0×10^4 cells/cm², allowed to settle for 30 min at room temperature, and then transferred to the xCELLigence RTCA eSight system (Agilent Technologies, Inc., Santa Clara, USA) housed in a humidified incubator at 37°C and 5% CO_2 and cultured further for 48 h. Pericytes were then added at 2.0×10^4 cells/cm² and cultured a further 48 h, after which HBEC-5i endothelial cells were plated at 8.0×10^4 cells/cm² to complete the triculture (Fig. 2). From endothelial seeding onward, cultures were maintained in complete HBEC-5i medium supplemented with amphotericin B (1 μg/mL; Thermo Fisher Scientific, Germany), with medium exchanges every 48 h. Impedance was acquired every 30 min and reported as Cell Index (CI) and normalised (NCI) relative to the time immediately before addition of tested formulations and further

contextualized as a percentage of untreated control, yielding NCI (% of control) calculated in Agilent xCELLigence RTCA eSight Software version 1.2.1. G3Si PEG6000 dendrimer and its dendriplex were added on the 13th day of the experiment, once a stable plateau had formed, and monitoring continued at 30 min intervals. To minimize artifacts, spaces between wells were filled with sterile water to reduce evaporation, and plates were inspected for bubbles prior to runs. Experiments were performed in 3 independent replicates.

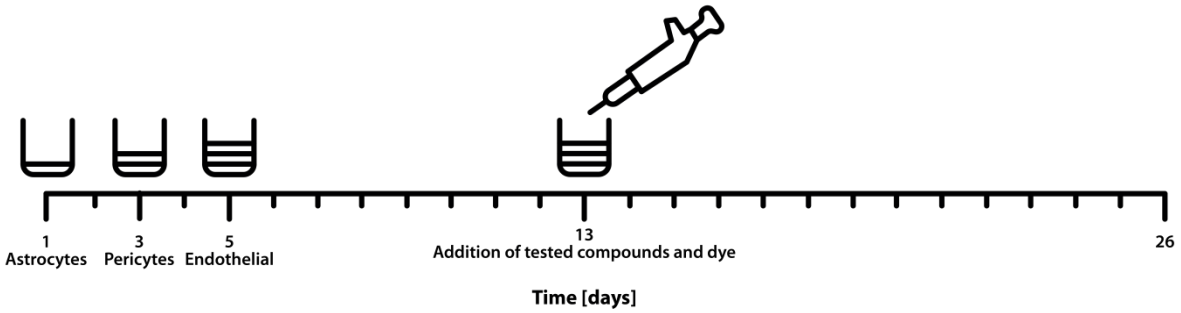


Figure 2. Schematic overview of the experimental schedule for the BBB model. Astrocytes were seeded on day 1, followed by pericytes on day 3 and brain microvascular endothelial cells on day 5. The BBB model was allowed to mature until day 13, when the G3Si PEG6000 dendrimer, its siRNA dendriplex, and the fluorescent nuclear dye eLive Red were added. Impedance and imaging readouts of BBB model integrity were then acquired longitudinally up to day 26.

Fluorescence Microscopy of the Blood–Brain Barrier (BBB) Model Integrity Assessment

In parallel with impedance, barrier status was monitored by real-time imaging on the RTCA eSight using E-Plate VIEW 96 microplates and the eLive Red nuclear label (Agilent Technologies, Inc., Santa Clara, USA). eLive Red is a membrane-permeant nuclear dye that diffuses into live cells and becomes fluorescent only upon binding to DNA, enabling red-channel

nuclear imaging during time-lapse acquisition. Following the manufacturer's protocol, eLive Red was diluted at 1× in assay medium, added to the wells before addition of the dendrimer G3Si PEG6000 and its dendriplex and maintained throughout the imaging (Fig. 2). Two non-overlapping fields per well were acquired on the red channel (excitation 584–605 nm; emission 621–720 nm) with a 10× objective at 120-min intervals, with exposure set to ~300 ms; field-level values were averaged to a single per-well value before downstream analysis. The images were analyzed with xCELLigence RTCA eSight Software version 1.2.1 to compute red confluence, which was then normalised to the pre-dose baseline, yielding NRC (%) as an imaging metric. Experiments were performed in 3 independent replicates.

Animals

All procedures complied with the bioethical principles adopted by the European Convention for the Protection of Vertebrate Animals Used for Experimental and Other Scientific Purposes (Strasbourg, 1986), Order of the Ministry of Health of the Russian Federation of 23 August 2010 "Establishment of the Rules of Laboratory Practice" No. 708n. The ethical permit Nr. 142 /2023 for the described experiments was obtained from the Latvian Food and Veterinary Service Ethics Commission. Female C57BL/6 mice (8–10 weeks; Charles River, Germany) were group-housed (5–8 per cage) in environmentally-enriched cages at 22 °C on a 12 h light/12 h dark cycle with ad libitum access to food and water. Animals were regularly monitored for food and water intake, weight gain, skin and fur changes, and microscopic alterations at the injection site. All animals were acclimatized for one week before starting the experiments. For invasive procedures, mice were anesthetized with inhalation of isoflurane in oxygen (induction with 4% of isoflurane in box, maintenance with 2.5% of isoflurane delivered via a nose cones), with peri-

procedural monitoring; analgesia was provided as indicated by the procedure-specific welfare assessment. Mice were humanely euthanized by cervical dislocation following deep anesthesia. Procedures were performed by trained personnel.

In Vivo Whole-Body Fluorescence Imaging in Mice (IVIS) Biodistribution Analysis

Female C57BL/6 mice (8–10 weeks; n = 4 per group) received five intravenous tail-vein administrations over 7 days (Fig. 3) of Cy5-labeled siRNA formulated as G3Si-PEG6000 dendriplex; control groups received naked siRNA or PBS, with injection route/volume matched across groups. Based on preliminary dose-range finding, the safe dose was estimated at 80 μg of nanoformulation per 50 μL injection, prepared as described in *dendriplex formation* section. The fur was removed from the abdominal skin of the mice prior to imaging. Mice were imaged supine on a temperature-controlled stage using isoflurane anesthesia as described above on an IVIS Spectrum system (PerkinElmer, Waltham, MA, USA) in 2D epi-illumination mode using the Cy5 filter set (Ex ≈ 640 nm / Em ≈ 680 nm). Acquisition parameters (exposure time, f/stop, binning, field of view) were optimized to avoid pixel saturation and then held constant across samples. Whole-body images were acquired 1.5 h after the final dose (day 7) and 24 h later (day 8). Fluorescence was quantified in Living Image software as total radiant efficiency and reported in calibrated units (p/s/cm^2/sr). At 24 h post-final dose, mice were euthanized as described above.

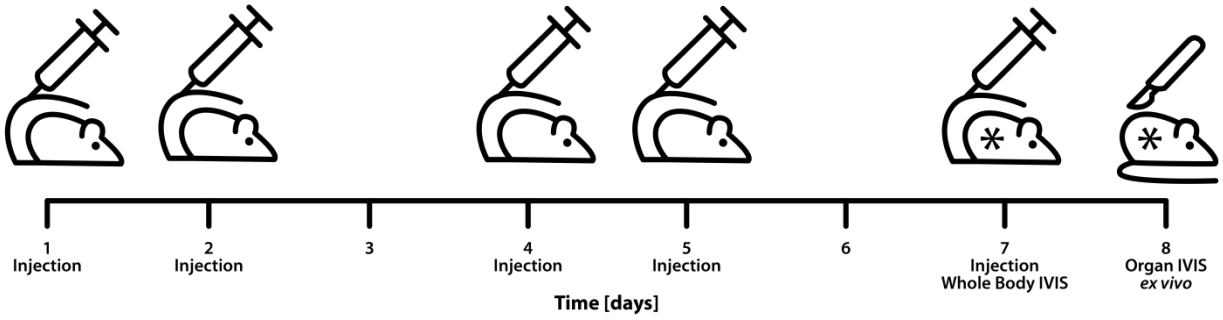


Figure 3. Schematic overview of the in vivo IVIS biodistribution study. Mice received intravenous injections of the G3Si PEG6000 dendrimer or its siRNA dendriplex on days 1, 2, 4, 5, and 7. Whole-body IVIS imaging was performed on day 7 (1.5 h after the final injection) and on day 8 (24 h after the final injection). On day 8, following the 24-h imaging session, animals were euthanized and major organs were collected for ex vivo IVIS analysis.

Ex Vivo Mice Organ Fluorescence Imaging (IVIS) and Biodistribution Analysis

At the experimental endpoint (24 h after the final dose; day 7), female C57BL/6 mice (8–10 weeks; n = 4 per group) were anesthetized and euthanized as described above. Liver, spleen, kidneys, heart, lungs, and brain were excised, rinsed in ice-cold PBS, blotted dry, and placed one organ per well in a black 24-well plate for imaging. *Ex vivo* fluorescence was acquired on an IVIS Spectrum (PerkinElmer, Waltham, MA, USA) in 2D epi-illumination mode using the Cy5 filter set (Ex ≈ 640 nm / Em ≈ 680 nm). Acquisition parameters (exposure time, f/stop, binning, field of view) were optimized to avoid pixel saturation and then held constant across samples. Fluorescence was quantified in Living Image software as radiant efficiency units $(p \cdot cm^{-2} \cdot sr^{-1})/(\mu W \cdot cm^{-2})$.

Statistical analyses

Statistical analyses and data visualization were performed using Prism version 10.4.2 (GraphPad Software, Boston, MA, USA). The Shapiro–Wilk test was used to assess the normality of data distributions. For factorial designs, multiple-way ANOVA was applied to assess differences in group means. Where ANOVA indicated statistically significant main effects, appropriate post hoc multiple comparison tests were selected based on the structure of the comparisons: Tukey's test was used for evaluating all pairwise group differences, Dunnett's test for comparisons of multiple treatments against a single control group, and Šidák's test for a limited set of planned comparisons. For non-normally distributed data or ordinal outcomes, pairwise differences were assessed using the nonparametric Mann–Whitney test. All tests were two-tailed and performed at a significance level $\alpha = 0.05$. In our graphical representations, significance is denoted by asterisks: one asterisk (*) indicates a p-value < 0.05, two asterisks (**) represent a p-value < 0.01, and three asterisks (***) denote a p-value < 0.001.

RESULTS AND DISCUSSION

The concept of a selective barrier between blood and brain emerged gradually, evolving from early anatomic observations and dye studies into the modern notion of the blood–brain barrier (BBB) into a coherent physiological concept that now anchors CNS pharmacology. Electron microscopy, combined with intravascular tracers subsequently attributed this barrier function to endothelial tight junctions, transforming a phenomenological idea into a defined cellular structure. At the start of this century term "the neurovascular unit" (NVU) was introduced to describe an integrated system linking brain parenchymal and vascular elements, emphasizing the intimate physical and functional association of neurons, glia, and the cerebral microvasculature

[48,49]. Subsequent literature often operationalized the NVU as comprising endothelial cells, pericytes, astrocytes, neurons, and extracellular matrix into an interacting module that coordinates permeability. Contemporary single-cell and spatial analyses now reveal pronounced heterogeneity across regions and along the arteriovenous axis, directly shaping uptake, transcytosis, and efflux of therapeutic agents [50]. Consequently, NVU and models alike are best treated as a pragmatic operational abstraction for organizing assumptions and measurements prior to *in vitro* to *in vivo* extrapolation, rather than as a literal, uniform template. The development and evaluation of BBB-penetrant nanovectors should be anchored in a physiologically based approach that integrates rigorous Design of Experiments (DoE) with transparent model progression across scales. The informed study design and interpretation, which helps avoid broad pitfalls, aligns nanovector chemistry with BBB biology, ensures that measurements reflect pharmacologically relevant exposure at the action site, and supports credible translation from *in vitro* models to *in vivo* performance. The current article integrates evidence from single-cell-based assays, through multicellular *in vitro* models, to *in vivo* animal studies, progressively evaluating the therapeutic delivery potential of the G3Si PEG6000 nanosystem.

Cytotoxicity Profiling

Consistent with international standards for nanomaterial safety evaluation, we initiated the examination with cell-based assays to rapidly identify potential hazards and define exposure ranges for downstream experiments. We selected the MTT assay as our primary readout for the G3Si PEG6000 dendrimer and its dendriplex, as it is the most sensitive indicator of toxicity for cationic dendrimers. A decrease in mitochondrial reductive capacity is an early and sensitive

indicator of the tested positively charged cationic nanosystem, as these are attracted to the negatively charged mitochondrial membrane, resulting in their selective accumulation in these organelles. Thus, the quantification of mitochondrial reductive capacity can report early losses in mitochondrial function [51,52]. Using the previously established dendrimer:siRNA saturation ratio (2.5:1) and concentration ranges (dendrimer 0.1–10 μM; siRNA 0.04–4 μM in dendriplex), we profiled BBB-relevant cell types: human brain microvascular endothelial cells (EC), pericytes (PC), and astrocytes (AC). Astrocytes displayed the highest tolerance to the non-complexed dendrimer exposures (IC_{50} = 8.97 μM; IC_{20} = 3.74 μM), endothelial cells showed comparable viability (IC_{50} = 7.84 μM; IC_{20} = 2.34 μM), and pericytes were the most susceptible (IC_{50} = 2.48 μM; IC_{20} = 1.66 μM) (Fig. 4). These findings are congruent with cell-specific physiology. Astrocytes maintain a high antioxidant capacity through convergent IL-1β/NF-κB-driven glutathione pathways and robust Nrf2 program control, with p21Ras acting as a redox-responsive signaling hub. Collectively, the pathways enable the attenuation of oxidative stress and may contribute to the relatively greater astrocyte viability observed during cationic-dendrimer exposure [53,54]. In contrast, pericytes exhibit intrinsic redox vulnerability, with NOX4 providing a dominant source of superoxide and TRPM2 functioning as an oxidative/nitrosative-stress-gated channel linked to nanoparticle–induced injury [55,56]. Complexation of the studied nanovector with siRNA reduced cytotoxicity across all cell lines. We attribute this protective effect to partial neutralization of the dendrimer's positive charges by the siRNA polyanion, which reduces the amount of the dendrimer's functional groups available to interact nonspecifically with cell membranes and organelles. With rising concentration, the protective effect of complexation diminishes, the absolute cationic exposure per cell rises, and ultimately approaches that of the free dendrimer IC_{50} in ECs. Finally, because nanomaterials can interfere with MTT readouts, we

interpret these findings alongside orthogonal endpoints (ROS and ΔΨm) in endothelial cells, following best-practice recommendations from nanosafety method reviews [57,58].

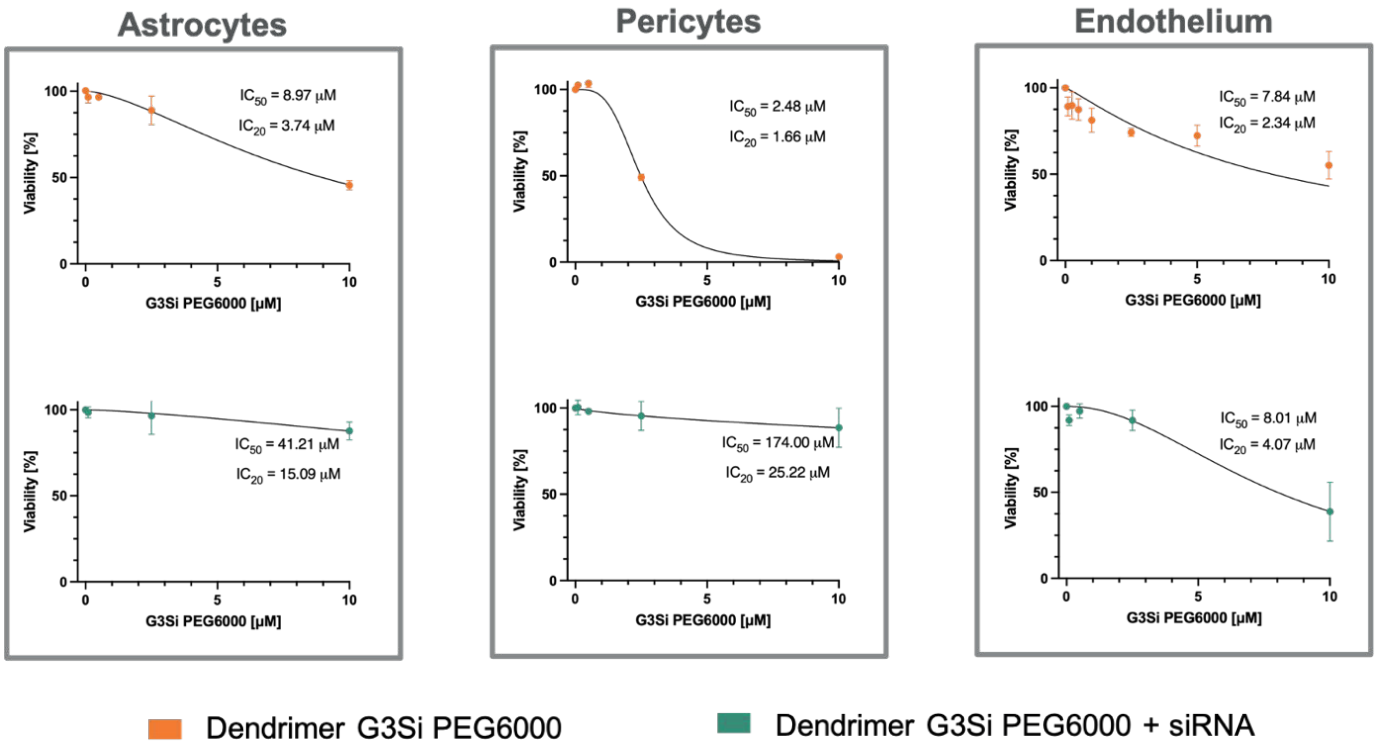


Figure 4. IC50 and IC20 values of actrocytes, pericytes, and endothelial cell lines treated with dendrimers and their complexes with siRNA were determined by MTT assay after 24 h incubation. The results are presented as the mean and standard deviation for 3 repetitions. The astrocytes and pericytes IC values exceeded the highest concentrations tested; therefore, we report right-censored estimates calculated from the available data points. (*p<0.05; **p<0.01; ***p<0.001).

Reactive Oxygen Species (ROS) Quantification

Positively charged dendrimers typically elicit oxidative stress-mediated cytotoxicity via a shared cascade: avid membrane association and cellular uptake, endolysosomal escape,

subsequent mitochondrial engagement, ROS generation, depolarization of the ΔΨm, and ultimately, cell death [59]. In this context, oxidative-stress liability reflects a set of physicochemical attributes of the G3Si PEG6000 carbosilane dendrimer: moderately positive surface charge, nanometric size, near-spherical architecture, while PEG6000 grafting and siRNA complexation partially mitigate effective surface charge and can alter intracellular routing [44,59]. Consistent with this mechanism, $DCFH_2$-DA/DCFDA assays demonstrated a modest, concentration-dependent increase in ROS for both the free dendrimer and its dendriplex (Fig. 5). At the highest concentration, the non-complexed dendrimer resulted in ROS generation of ~117% of control after 1- and 3-hour incubation and ~112% after 24-hour incubation period, while the dendriplex yielded ~120% after 1- and 3-hour incubation and ~112% after 24-hour incubation period, indicating an early increase with partial normalisation by 24 hours. The time of incubation did not result in a statistically significant difference in ROS generation, with early peaks subsiding to still-elevated readouts. Notably, siRNA complexation did not attenuate ROS generation. Overall, complexation mitigated the MTT response at low effect levels (IC_{20} shift), but the modest ROS elevations weren't comparably attenuated, indicating that mitochondrial injury persists despite improved metabolic readouts. To determine whether this redox burden translated into mitochondrial dysfunction, indicated by mitochondrial depolarization, we next quantified mitochondrial membrane potential changes with the JC-1 assay.

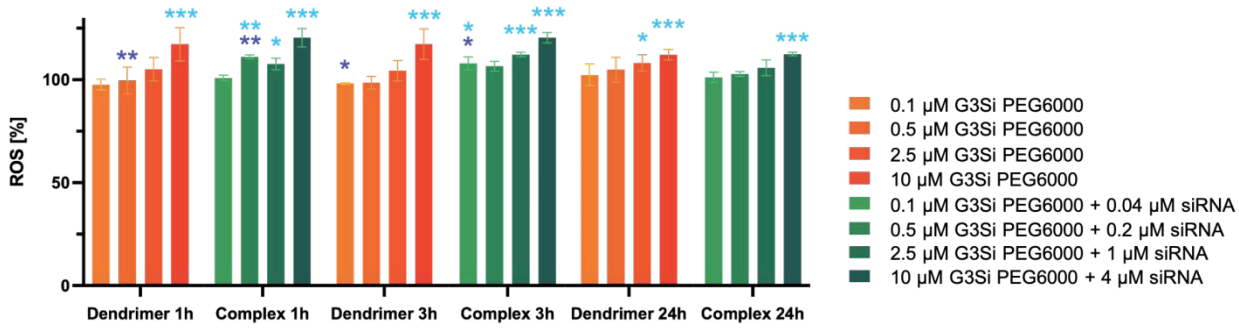


Figure 5. Changes in reactive oxygen species (ROS) production in endothelial cells following 1, 3, and 24 h incubation with the G3Si PEG6000 dendrimer and its dendriplex. ROS levels in untreated control cells were set at 100%. The results are presented as the mean and standard deviation for 3 repetitions. A blue asterisk marks significant differences relative to the control, and a violet asterisk indicates significant differences due to dendrimer-siRNA complexation (*p<0.05; **p<0.01; ***p<0.001).

Mitochondrial Membrane Potential (ΔΨm) and Function Assessment

We assessed mitochondrial function with the dye JC-1, where a decrease in the red-to-green fluorescence ratio indicates mitochondrial depolarization (ΔΨm loss) due to the dye's potential-dependent J-aggregate behavior. After 24 hours, both studied agents produced a statistically significant depolarization at concentrations of ≥ 0.5 μM, indicating mitochondrial malfunction at concentrations below the EC IC_{20} (Fig. 6). After 24 h exposure, the non-complexed dendrimer preserved ΔΨm at ~97% of control at 0.5 μM, while the dendriplex was ~84%; at 2.5 μM, ΔΨm was ~55% and ~58%, respectively. The observed ΔΨm collapse is mechanistically important, as mitochondrial depolarization is an early event on the intrinsic apoptotic pathway and provides a plausible bridge between the modest early rise in ROS and the later decline in metabolic activity,

as captured by MTT. This pattern is consistent with nanotoxicology reports in endothelial models, where mitochondrial depolarization is a common injury mode [60–62].

Evidence from amine-modified polystyrene nanoparticles demonstrates that significant, charge-driven redox and mitochondrial liabilities can outweigh otherwise attractive attributes. In epithelial and macrophage systems, amine-modified polystyrene nanoparticles elevate ROS, reduce mitochondrial membrane potential, and induce ultrastructural swelling with disruption of the mitochondrial network. In the same systems, neutral or carboxylated polystyrene increases ROS without compromising mitochondrial integrity or viability. Taken together, these findings constitute sufficient grounds to discontinue further development of the amine-modified polystyrene variant [63]. A parallel pattern is observed with the cationic gene-delivery polyethylenimine platform, despite favorable delivery performance, due to time-dependent mitochondrial membrane potential loss and mitochondrial liability, which narrows the tolerability window irrespective of transfection performance. Additionally, the authors caution that MTT alone can understate mitochondrial liabilities and advise incorporating time-resolved mitochondrial readouts when setting safe exposure limits [64]. Taken together, these examples support a practical development guide in which advancement is conditional on meeting prospectively defined ROS and ΔΨm thresholds, applying conservative exposure limits, and prioritizing design modifications when mitochondrial safety margins are not met. The G3Si PEG6000 nanosystem studied in this manuscript meets continuation criteria for exploratory development within a mitochondria-centered safety framework: oxidative signals are modest and stabilize over time, complexation improves low-effect metabolic tolerance, and ΔΨm findings are present yet actionable as design targets rather than exclusionary outcomes.

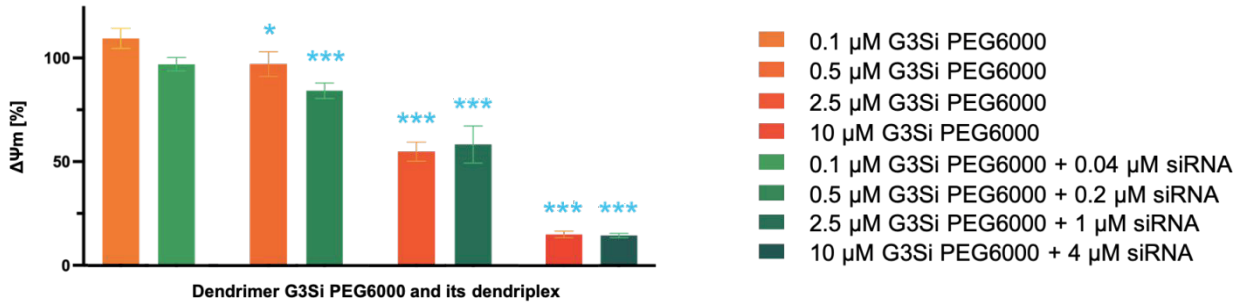


Figure 6. Changes in mitochondrial potential in endothelial cells following 24 h incubation with the G3Si PEG6000 dendrimer and its dendriplex. The untreated control cells were set at 100%. The results are presented as the mean and standard deviation for 3 repetitions. A blue asterisk marks significant differences relative to the control (*p<0.05; **p<0.01; ***p<0.001).

Real-Time Blood–Brain Barrier (BBB) Model Integrity by Impedance Measurement

To extend single-cell metabolic screening to barrier-relevant outcomes, we adopted a multicellular BBB model that captures the NVU context in which barrier properties emerge. Anatomical and molecular zonation produce segment-specific BBB phenotypes. Given that capillaries comprise ~85% of total vessel length in the human brain, a capillary-weighted triculture is the most relevant stage for assessing pharmacological exposure and barrier disruption [8]. To mimic the capillary architecture, we employed a direct-contact, layered tri-culture with astrocytes, then pericytes, and brain capillary endothelial cells on the apical face of the well, which recapitulates the *in vivo* orientation of the capillary wall and its abluminal support, also allowing crosstalk between the three cell types (Fig. 7). Building on this rationale, we configured the model to approximate capillary-weighted cell ratios, reflecting endothelial dominance with high pericyte representation and robust astrocytic ensheathment, as reported *in vivo* and in accordance with current best practices on barrier modeling, which are appropriate for

detecting compound-induced barrier disruption [65]. Taken together, this configuration establishes the biological context necessary to interpret subsequent quantitative evaluations of treatment-evoked changes, allowing for suitable screening tools in neurotherapeutic development.

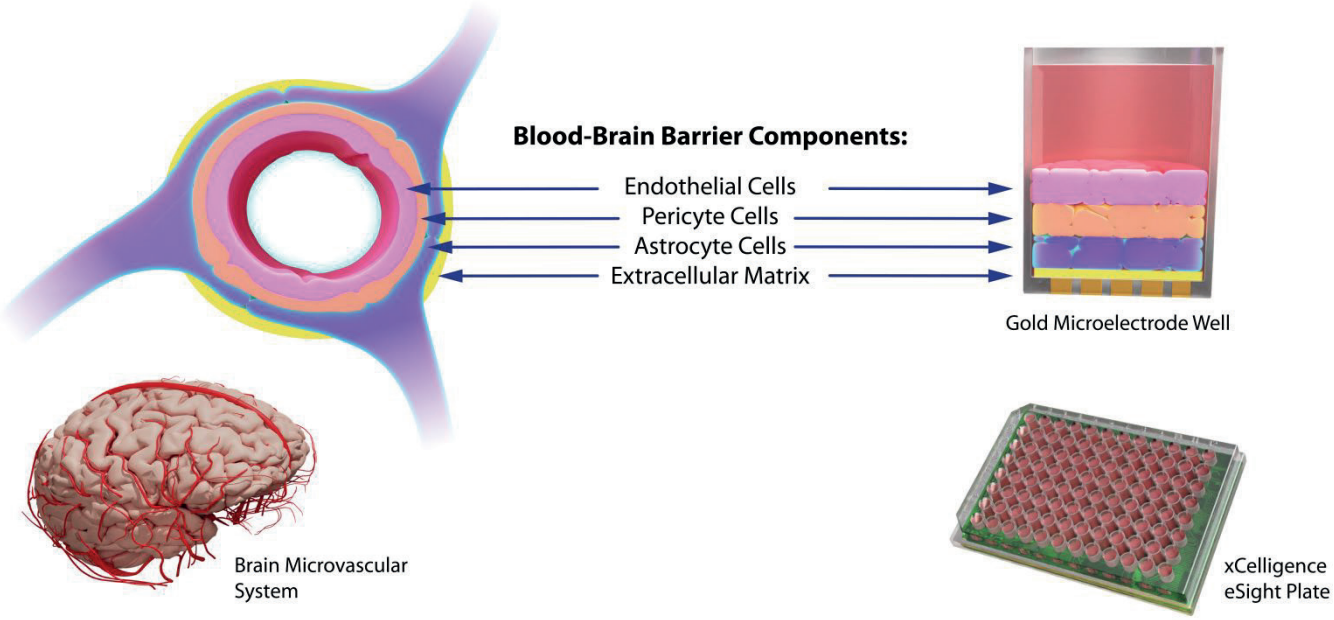


Figure 7. Illustration depicts a schematic cross section of the Blood–Brain Barrier (BBB) on the left and the corresponding *in vitro* barrier model established in the xCELLigence eSight plate on the right.

The effects of G3SiPEG 6000 dendrimer and its dendriplex on the BBB-model were quantified by label-free electrical impedance using a Real-Time Cell Analyzer (RTCA) xCELLigence RTCA eSight system. Cells adhering to the interdigitated gold microelectrodes in E-Plate wells increase the measured impedance. This change, quantified as the dimensionless Cell Index (CI) parameter, reflects cell proliferation, adhesion, and the extent of well surface coverage. CI is calculated as the relative impedance difference between cell-free and cell-covered electrodes. To

enable comparisons of treatment kinetics, raw CI traces were converted to Normalised Cell Index (NCI) by dividing each time point by the pre-dose baseline, which in this study was the day-13 plateau and further contextualized as a percentage of untreated control, yielding NCI (% of control) as the primary readout of barrier dynamics over time (Fig. 8). Compounds were added only after the plateau to avoid confounding maturation with treatment effects. At the highest concentration of the free G3Si-PEG6000 dendrimer, NCI (% of control) decreased progressively. After approximately 24 hours of constant exposure to the dendrimer, NCI (% of control) sharply fell, ultimately reaching a baseline-subtracted value of zero. The result is consistent with persistent barrier failure and/or loss of cell adhesion/viability rather than a transient response. At matched exposures, complexation with siRNA shifted the biological response toward transient and recoverable behavior. The dendriplex at the highest tested concentration showed a similar profile but with greater heterogeneity. 40% of the tested barrier samples treated with the highest dendriplex concentration failed to recover after the sudden drop, whereas the remaining 60% exhibited a transient dip, followed by recovery and exceeded the control levels within 20 minutes after the introduction of the compound. Functionally, this indicates that complexation improves the safety profile in the BBB model, favoring remodeling and rapid restoration of barrier tone over persistent collapse. Continuous exposure to ≤2.5 μM of the G3Si PEG6000 dendrimer resulted in a concentration-dependent increase in NCI (% control). In contrast, the concentration-matched dendriplex exhibited a biphasic profile, with an initial decline in NCI and a subsequent increase above 100%. This trend aligns with the concept of hormesis, wherein low doses of a potentially cytotoxic agent induce an adaptive cellular response that enhances cellular performance. At these concentrations, for the initial exposure period, the dendriplex may cause a

mild perturbation of homeostasis, activating stress-response pathways that promote cell adhesion and/or proliferation [66].

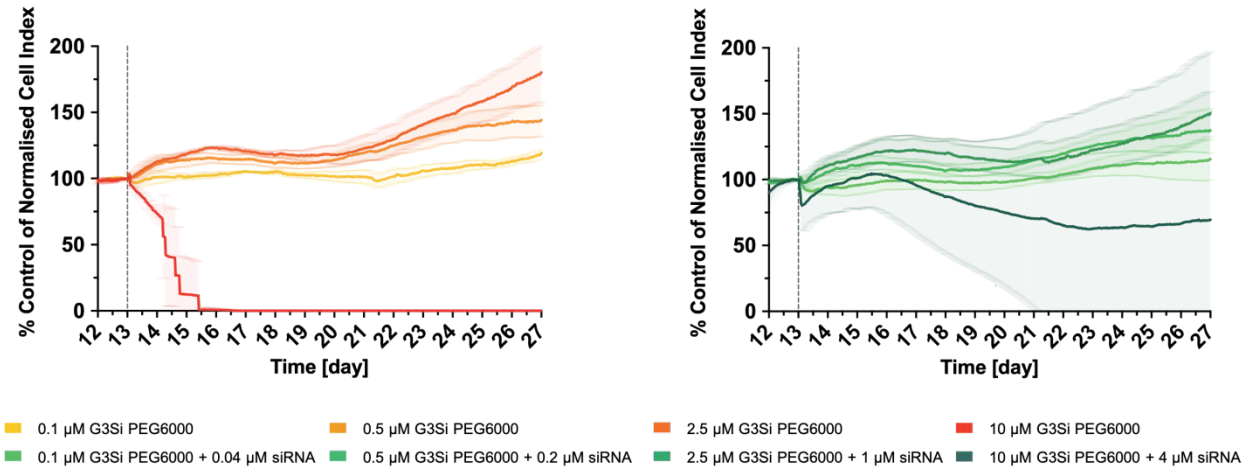


Figure 8. Real-time impedance monitoring of the Blood–Brain Barrier (BBB) model following exposure to G3Si PEG6000 dendrimer and its dendriplex, initiated after establishment of the plateau on day 13 (indicated by the horizontal dashed line). Data are presented as the mean and standard deviation for 5 repetitions, reported as Normalised Cell Index (NCI; % of control).

Fluorescence Microscopy of the Blood–Brain Barrier (BBB) Model Integrity Assessment

In parallel with impedance, barrier responses were interpreted alongside real-time live-cell imaging using eLive Red, a membrane-permeable, DNA-binding nuclear dye formulated for continuous use in culture media, enabling time-resolved viable-cell coverage. Image series were acquired on a fixed schedule and analyzed to compute red confluence, which we then normalised to the day-13 pre-dose baseline, yielding NRC (%) as an imaging metric. Mirroring the impedance results, the highest dose of free G3Si PEG6000, which produced a rapid NCI decline, was accompanied by a parallel fall in NRC (%), consistent with barrier collapse (Fig. 9). The

microscopic images show detachment in large sheets, indicating a severe cytotoxic response for the highest tested concentrations (Fig. 10). These findings are further corroborated by time-lapse imaging that captures the barrier disruption (Supplementary Video S1). In our BBB model, detachment suggests the preservation of cell–cell cohesion during detachment, causing sheets of cells to peel away together rather than as individual cells. The sequence of changes in our tri-culture suggests that the weak link disrupted by the nanoparticle occurs at cell–matrix adhesions rather than cell–cell junctions. Basal focal adhesions are integrin-based, multi-protein hubs that couple the extracellular matrix to the actin cytoskeleton and integrate mechano-chemical signals to maintain anchorage [67–69]. We hypothesize that, as intracellular nanovector burden accumulates over time, the nanovector-generated ROS may oxidatively remodel adhesion and junctional scaffolds, weakening basal cell adhesion while temporarily preserving cell–cell cohesion and predisposing to cell–matrix detachment.

Any sustained loss of BBB tightness compromises neural homeostasis and is linked to neurodegenerative conditions such as Alzheimer's and Parkinson's disease. Even though it is often assumed in clinical practice that disease-related BBB breakdown might present an opportunity for aid drug entry, authoritative reviews warn the opposite that pathological BBB degeneration impairs delivery by diverting solutes into enlarged perivascular spaces, disrupting extracellular diffusion and interstitial fluid flow, and thereby limiting CNS-wide distribution [70]. At sub-toxic doses, the concurrent rise in NCI (% of control) and the NRC (%) reflects proliferation-driven rather than stronger adhesion per cell. By day 6 of exposure, NRC (%) peaked, with the dendrimer alone exceeding 170 NRC (%) at 0.1 and 0.5 μM, whereas the dendriplex reached a comparable NRC (%) at 0.5 μM only.

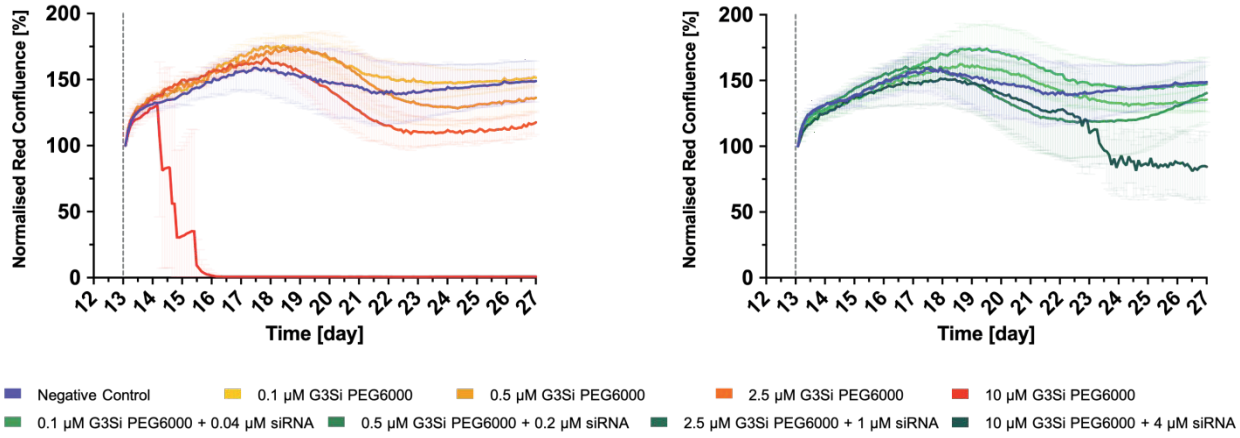


Figure 9. Real-time red object confluence monitoring of the Blood–Brain Barrier (BBB) model following exposure to G3Si PEG6000 dendrimer and its dendriplex, initiated after establishment of the plateau on day 13 (indicated by the horizontal dashed line). Nuclei, visualized as red objects, were stained with eLive Red dye. Data are presented as the mean and standard deviation for 5 repetitions, reported as Normalised Red Confluence - NRC (%).

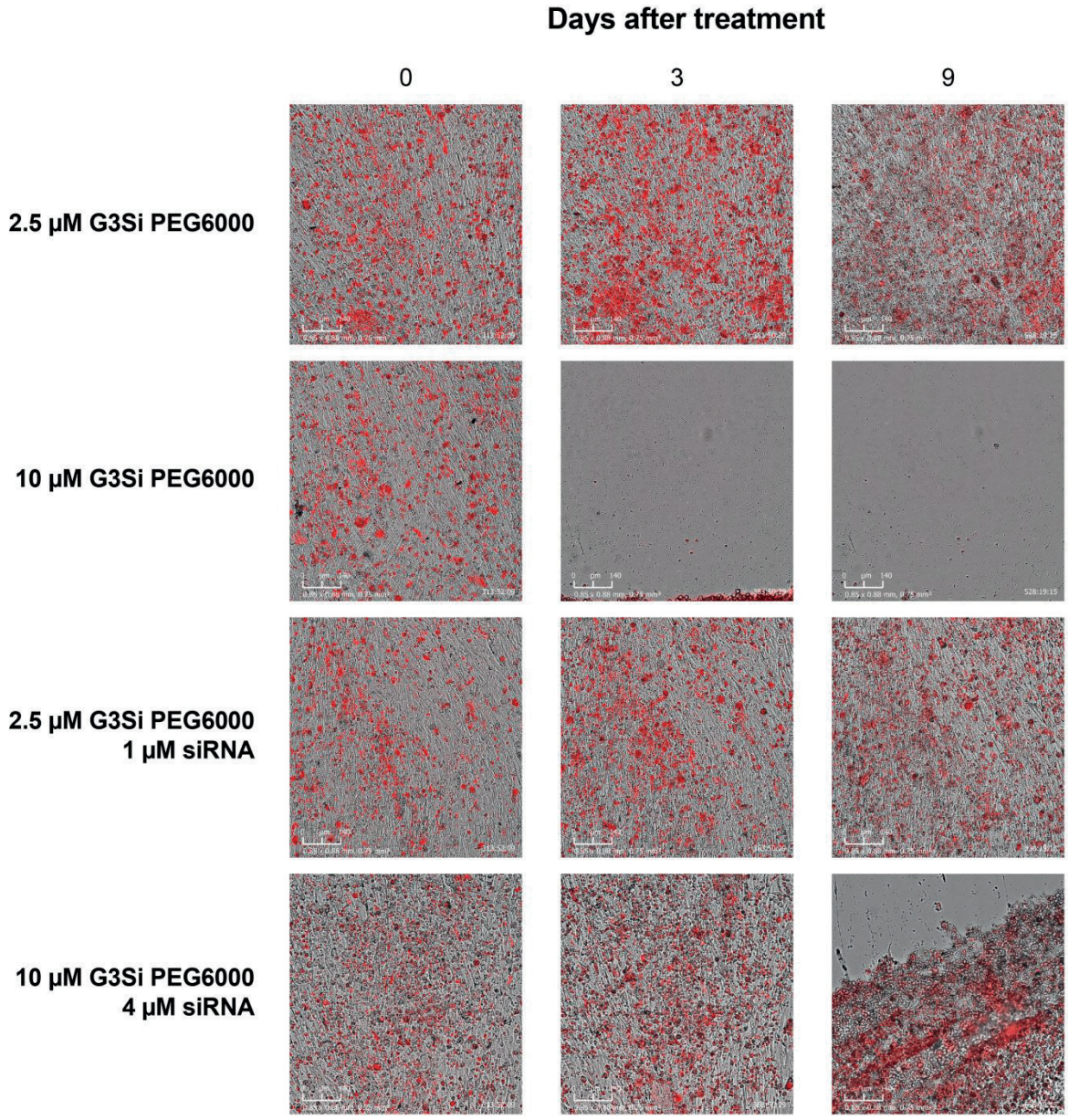


Figure 10. Composite brightfield and fluorescence images of the Blood–Brain Barrier (BBB) model acquired before treatment (day 13 of the experiment) and at days 3 and 9 following exposure to the two highest tested concentrations of G3Si-PEG6000 dendrimer and its dendriplex. The red fluorescent signal marks cell nuclei (stained with eLive Red dye), illustrating temporal changes in cellular distribution and morphology under each treatment condition. Time-

lapse recording of BBB model morphology and cellular organization across the entire tested concentration range for both compounds is provided in Supplementary Video S1.

In Vivo Whole-Body Fluorescence Imaging in Mice (IVIS) Biodistribution Analysis

The applied *in vitro* assays are indispensable for mechanism and screening; however, all current cell-based models cannot yet reproduce the full physiological complexity of the brain microvasculature. A multitude of physiological processes, including blood flow, biomolecular corona formation, and systemic clearance pathways, are likely to influence these interactions *in vivo*. Consequently, animal studies remain necessary to build confidence in BBB transport, biodistribution, and dose-setting safety. We therefore performed whole-body IVIS to quantify the biodistribution of uncomplexed Cy5–siRNA and Cy5–siRNA complexed with the G3Si PEG6000 dendrimer in mice and to resolve accumulation over time (Fig. 11). IVIS enables longitudinal, whole-animal imaging with millimeter-scale spatial resolution.

At 1.5 h after the last injection, the total whole-body flux for the dendriplex was 4.6-fold higher than for uncomplexed siRNA, indicating prolonged systemic exposure and earlier organ sequestration relative to the rapidly cleared oligonucleotide. By 24 h, the free siRNA signal converged to the PBS baseline, whereas the dendriplex remained 1.7-fold higher (Fig. 12). Unmodified siRNA is quickly degraded and filtered, resulting in transient plasma exposure of minutes to ~0.5 h, in contrast to nanocarrier-mediated exposure extension [71]. These kinetics demonstrate that the G3Si PEG6000 formulation extends circulation and reduces early renal elimination, thereby increasing the total-body signal relative to uncomplexed siRNA. In both formulations, a strong, ovoid midline hotspot was observed in the caudal abdomen/pelvis, whose

position and shape match the murine urinary bladder, indicating urinary accumulation of he labeled material [72].

Signals from Cy5–siRNA (Cy5 ex/em ~649/667 nm) are recorded in the first near-infrared window (NIR-I; ~650–900 nm), where hemoglobin absorption and scattering by scalp and skull substantially attenuate excitation and emission. Consequently, head-region planar IVIS is surface-weighted and has limited sensitivity to small parenchymal fractions through an intact cranium. Moreover, cyanine-dye photophysics are microenvironment-dependent: Cy5 can brighten upon protein/membrane binding or higher microviscosity and dim via aggregation/self-quenching, so intensity is not necessarily proportional to local analyte concentration. Under these constraints, head-region signals are most consistent with vascular or superficial tissues (e.g., scalp/cranial sinuses, ocular and lacrimal/Harderian structures) rather than brain parenchyma on their own [73].

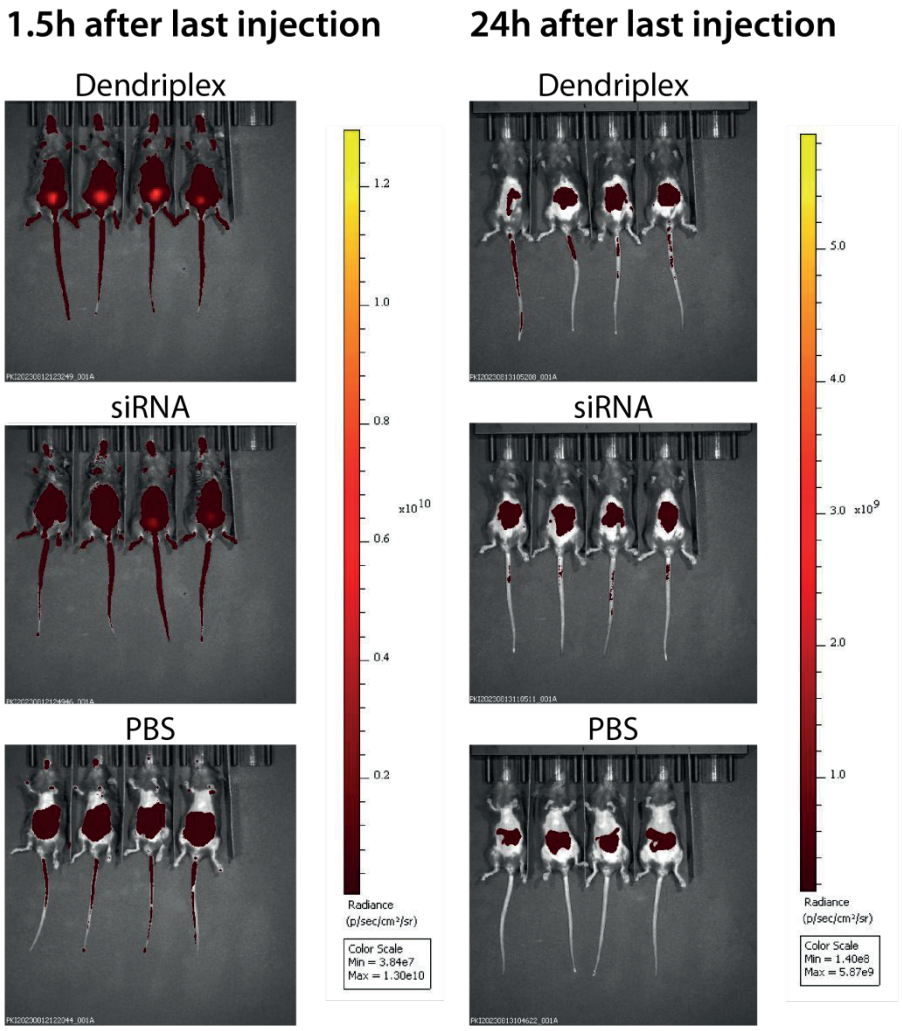


Figure 11. Whole-animal images of mice administered dendriplex (Cy5–siRNA dendrimer complex), uncomplexed Cy5–siRNA, and PBS (negative control) were acquired 1.5 h and 24 h after the last injection. Fluorescence is shown as a red pseudocolor radiance overlay on the photographic reference and reported in calibrated units (p/s/cm^2/sr). Individual LUTs and scale bars are displayed for each panel. Quantitative whole-animal total flux and between-group comparisons are provided in Fig. 12.

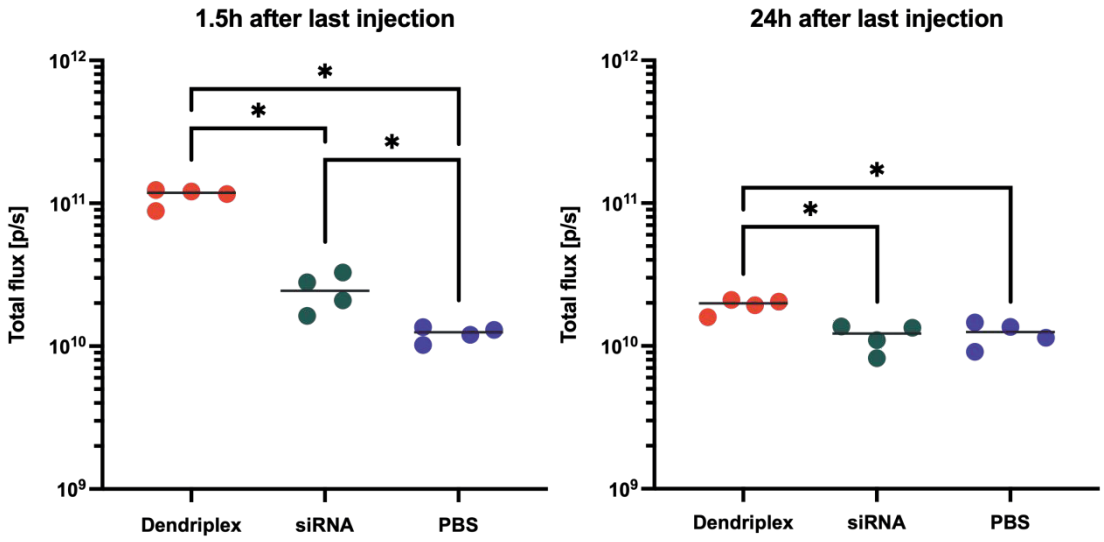


Figure 12. Whole-animal total flux ($p \cdot s^{-1}$) of mice administered dendriplex (Cy5–siRNA dendrimer complex), uncomplexed Cy5–siRNA, and PBS (negative control) was acquired 1.5 h and 24 h after the last injection. Points represent individual animals (n=4), and horizontal bars denote the group median. Asterisks indicate the between-group difference (*$p<0.05$).

Ex Vivo Mice Organ Fluorescence Imaging (IVIS) and Biodistribution Analysis

Whole-body *in vivo* fluorescence imaging is confounded by tissue-dependent attenuation and autofluorescence, so raw signals are not directly comparable across organs [74]. To improve cross-organ comparability, we excised organs enabling *ex vivo* organ-specific background subtraction and spectral unmixing during quantification, which improves cross-tissue biodistribution accuracy (Fig. 13).

At 24 h post last injection, no robust brain Cy5–siRNA signal was detected *ex vivo*. Given residual organ-specific absorption/scatter even after tissue removal, we conclude that the lack of gross accumulation by planar *ex vivo* IVIS indicates that concentrations fall below the assay's detection limit in highly complex biological environments, rather than to a complete

absence of delivery. This interpretation is consistent with IVIS technical guidance and protocols that emphasize tissue-dependent background attenuation and recommend *ex vivo* organ imaging mainly to confirm gross signals source location [75]. Accordingly, the following results focus on cross-organ patterns that are robust under the specified acquisition and analysis settings.

In our study, both the siRNA dendriplex and non-complexed siRNA exhibited kidney-dominant distribution with a secondary hepatic accumulation (Figure 14). Quantitatively, the kidneys accounted for ~67% of total fluorescence for the dendriplex and ~75% for the non-complexed siRNA (Fig. 15). Based on our size characterization, the dendriplex modestly exceeds the glomerular filtration barrier (GFB) [44]. We therefore hypothesize that the strong renal fluorescence may reflect GBM-mediated (glomerular basement membrane) disassembly of dendriplex. Cationic polyplexes can bind to the negatively charged GBM and disassemble *in situ*, releasing fluorescently labeled siRNA that is then freely filtered, producing a strong fluorescent signal in the kidneys, even though the carrier itself may be retained. This mechanism has been demonstrated *in vivo* for cationic polymer-siRNA nanoparticles [76].

The major biodistribution divergence between the two formulations occurred in the liver, where the dendriplex yielded a 1.5-fold higher absolute hepatic signal than naked siRNA, corresponding to 24% versus 16% of total flux, respectively. Consistent with prior reports, the preferential liver accumulation of circulating nanoparticles is well-documented and arises from the adsorption of a biomolecular corona that promotes opsonization and capture by liver-resident macrophages (Kupffer cells) within the mononuclear phagocyte system (MPS). The composition of this corona, and thus MPS engagement, is sensitive to particle size/charge and surface chemistry, including PEG grafting. Collectively, these findings suggest that, under our dosing

conditions, the dendriplex engages the MPS more strongly than uncomplexed siRNA, yielding a higher absolute liver signal despite only a modest shift in fractional distribution.

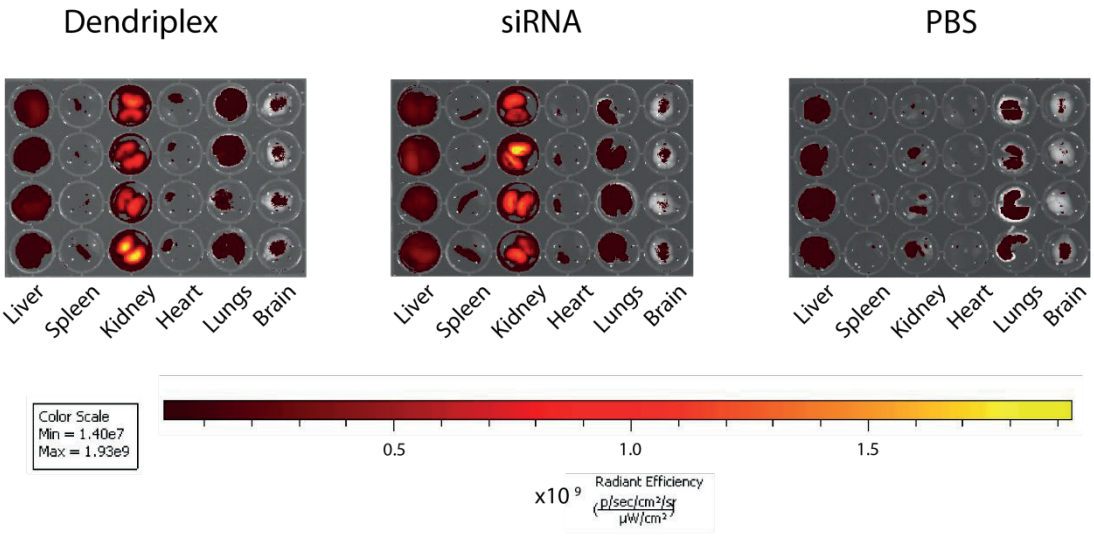


Figure 13. *Ex vivo* fluorescence images of liver, spleen, kidneys, heart, lungs, and brain harvested from mice administered dendriplex (Cy5–siRNA dendrimer complex), uncomplexed Cy5–siRNA, or PBS (negative control) 24 h after the final injection. Organs were imaged immediately after necropsy under identical acquisition parameters. Fluorescence is displayed as a red pseudocolor radiance overlay on the photographic reference and reported in calibrated radiant efficiency units $(p \cdot cm^{-2} \cdot sr^{-1})/(\mu W \cdot cm^{-2})$; common LUTs/scale bars are shown for panel-to-panel comparability. Quantitative organ between-group comparisons are provided in Fig. 14.

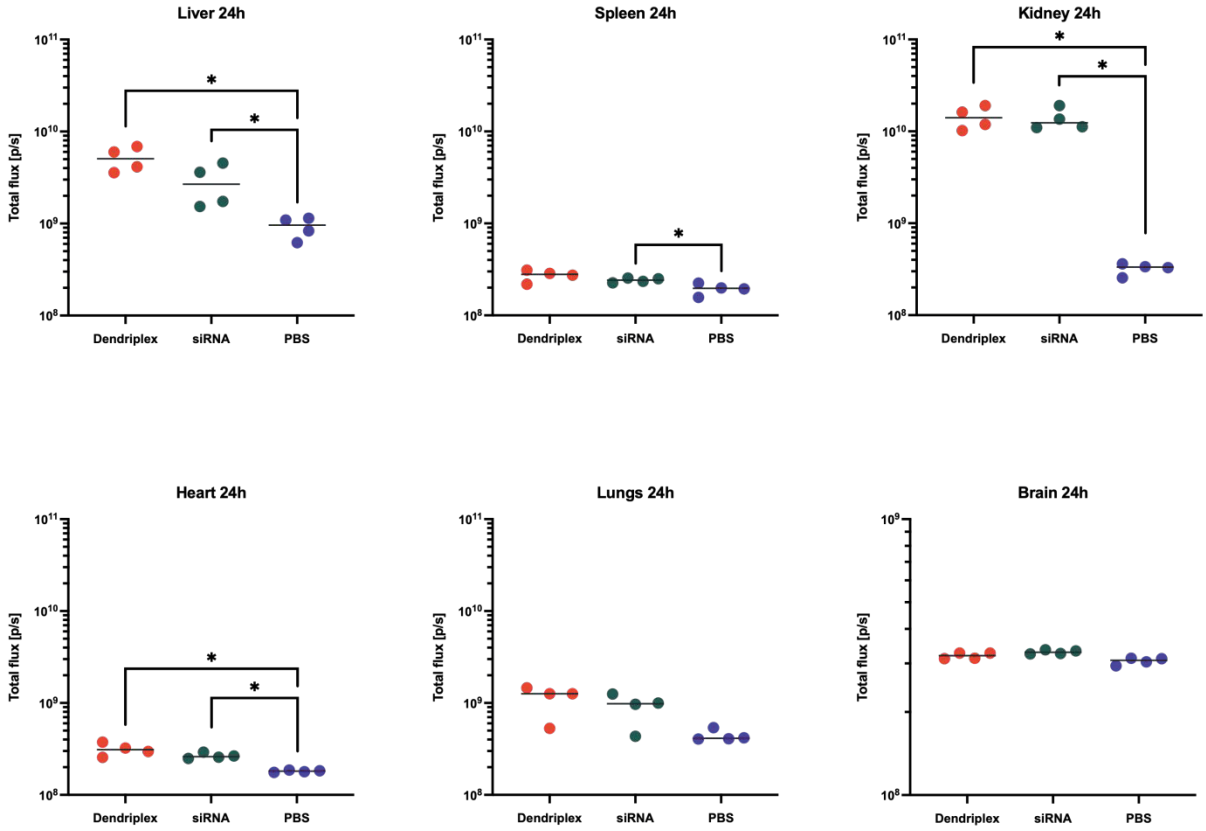


Figure 14. Per-organ Total Flux ($p \cdot s^{-1}$) for liver, spleen, kidneys, heart, lungs, and brain harvested from mice administered dendriplex (Cy5–siRNA dendrimer complex), uncomplexed Cy5–siRNA, or PBS (negative control) 24 h after the final injection. Points represent individual organs; horizontal bars denote the group median. Asterisks indicate between-group differences (*$p<0.05$).

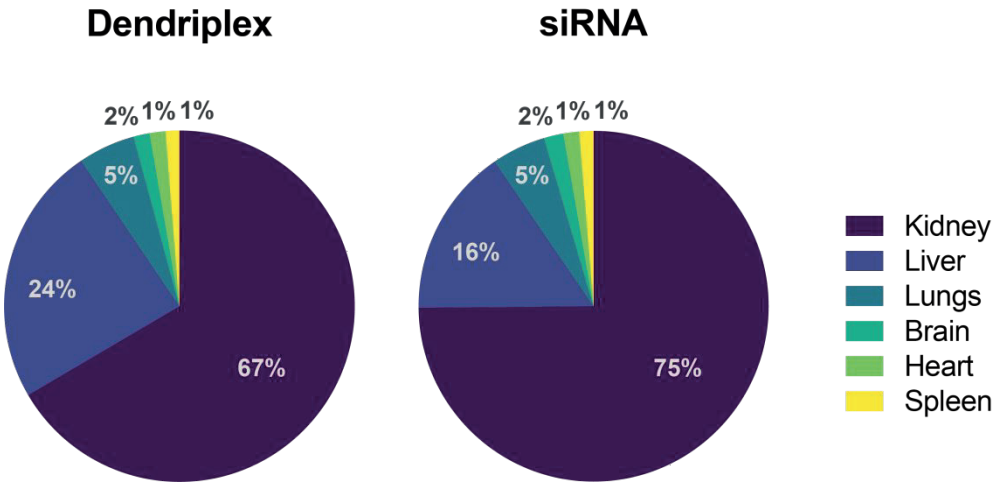


Figure 15. Fractional allocation (%) of *ex vivo* fluorescence IVIS measurements across liver, spleen, kidneys, heart, lungs, and brain for mice administered dendriplex (Cy5–siRNA dendrimer complex) and uncomplexed Cy5–siRNA 24 h after the final injection. Each wedge represents the mean percentage contribution of the indicated organ to the summed Total Flux ($p \cdot s^{-1}$) across the listed organs for that group.

CONCLUSIONS

Across progressively more complex systems, from individual NVU cell types, through a capillary-weighted BBB model, to mouse biodistribution imaging, we characterized the biocompatibility and biodistribution patterns of the G3Si-PEG6000 platform. In BBB-relevant cells (brain endothelial cells, pericytes, astrocytes), mitochondrial performance profiling delineated exposure ranges suitable for subsequent in-depth evaluation. Pericytes emerged as the most vulnerable population, whereas astrocytes and endothelial cells were more tolerant. Complexation with siRNA consistently attenuated apparent cytotoxicity (dendriplex IC_{20} = 4.07–25.22 μM), and both formulations evoked modest ROS but a dose-dependent ΔΨm

depolarization, consistent with ΔΨm acting as an early indicator of injury upstream of overt cytotoxicity.

The BBB model integrity was concentration- and formulation-dependent: at the highest concentration, the non-complexed dendrimer caused sustained drops in impedance and nuclear confluence, while lower doses and the dendriplex produced transient, recoverable perturbations, indicating a wider functional window for the complex in a barrier context. Time-lapse fluorescence microscopy mirrored the impedance dynamics and suggested preferential loss of cell–matrix adhesion with preserved cell–cell contacts. Among several plausible mechanisms, this pattern is consistent with nanovector-generated ROS and associated signaling remodeling focal-adhesion and junctional scaffolds.

In vivo, whole-body IVIS demonstrated prolonged systemic exposure for the dendriplex (4.6-fold higher total flux at 1.5 h; 1.7-fold at 24 h of dendriplex vs. naked siRNA) and a kidney-dominant, secondarily hepatic *ex vivo* distribution. Brain fluorescence was not robustly detected by planar NIR-I IVIS at 24 h after the last injection; in accordance with known limitations of this modality, we interpret this as signal falling below the detection limit rather than evidence of absent CNS delivery, highlighting the need for future compartment-resolved brain assays and molecular quantification.

In a BBB drug-delivery field increasingly shaped by refined structural, functional, and disease-state data and by conceptual and technological roadmaps that narrow the gap between experimental models and clinical translation, our demonstration that the G3Si-PEG6000 dendrimer exhibits promising compatibility in BBB-relevant cells and barrier models, manageable and mechanistically interpretable mitochondrial signals, and a well-defined renal/hepatic biodistribution with extended systemic exposure as a dendriplex. Considered

alongside earlier biophysical characterization and complexation profiling, plasma interaction and remodeling, and hemocompatibility profiling across blood components, these findings position the dendrimer–siRNA platform as a well-characterized, mechanistically informed basis for further evaluation and for next-generation nanocarrier designs intended to safely and reproducibly cross the human BBB in CNS indications.

Supporting Information

The following Supporting Information is available free of charge at the ACS website.

Supplementary Video S1. Time-lapse composite of brightfield and fluorescence images documenting blood–brain barrier (BBB) model assembly, maturation, and subsequent morphological and organizational changes following exposure to the G3Si PEG6000 dendrimer or its dendriplex across the tested concentration range.

ACKNOWLEDGMENT

This work was supported by grant 2018/30/Z/NZ1/00911 of the Project “NanoTENDO” financed by the National Science Centre, under the M-ERA.NET 2, which has received funding from the European Union’s Horizon 2020 research. This research was also funded by grants from PID2020-112924RB-I00 (MINECO) and CIBER-BBN from ISCIII with assistance from the European Regional Development Fund.

AUTHOR INFORMATION

Corresponding Author

*Serafin Zawadzki - Department of General Biophysics, Faculty of Biology and Environmental Protection, University of Lodz, 141/143 Pomorska St., 90-236 Lodz, Poland;
Email: serafin.zawadzki@edu.uni.lodz.pl
**Katarzyna Miłowska - Department of General Biophysics, Faculty of Biology and Environmental Protection, University of Lodz, 141/143 Pomorska St., 90-236 Lodz, Poland;
Email: katarzyna.milowska@biol.uni.lodz.pl

Author Contributions

Serafin Zawadzki: Conceptualization, Methodology, Validation, Formal analysis, Investigation, Writing - Original Draft, Writing - Review & Editing, Visualization; **Elżbieta Okła:** Investigation; **Paula Ortega López:** Resources; **F. Javier de la Mata:** Resources; **Maksim Ionov:** Methodology, Writing - Review & Editing; **Juris Jansons:** Methodology, Investigation; **Dace Skrastiņa:** Methodology, Investigation, Project administration; **Madara Kreišmane:** Investigation; **Maria Bryszewska:** Conceptualization, Methodology, Resources, Project administration, Funding acquisition; **Katarzyna Miłowska:** Conceptualization, Methodology, Formal analysis, Data Curation, Writing - Review & Editing, Supervision, Project administration.

ABBREVIATIONS

APOE4, apolipoprotein E4; AB, arachnoid barrier; AC, Astrocyte cells; AGS, astrocyte growth supplement; BSCB, blood-spinal cord barrier; BCSFB, blood-cerebrospinal fluid barrier; BBB, blood–brain barrier; CI, Cell Index; CNS, central nervous system; CBF, cerebral blood flow; CVO, circumventricular organs; DoE, Design of Experiments; H2DCF-DA, dichlorodihydrofluorescein diacetate; ECGS, endothelial cell growth supplement; EC,

endothelial cells; FBS, fetal bovine serum; GBM, Glomerular basement membrane; IVIS, In Vivo Imaging System; ITS/IATA, intelligent testing strategy; ISF, interstitial fluid; ΔΨm, mitochondrial membrane potential; MPS, Mononuclear phagocyte system; NIR, Near-infrared window; NVU, Neurovascular Unit; NCI, Normalised Cell Index; NRC, Normalised Red Confluence; P/S, penicillin–streptomycin; PC, Pericyte cells; PGS, pericyte growth supplement; PLL, poly-L-lysine; ROS, reactive oxygen species; RTCA, Real-Time Cell Analyzer; RMT, receptor-mediated transcytosis; CMT, solute-carrier–mediated transport; TJ, tight junctions.

REFERENCES

(1) Jain, V.; Langham, M. C.; Wehrli, F. W. MRI Estimation of Global Brain Oxygen Consumption Rate. *J Cereb Blood Flow Metab* **2010**, *30* (9), 1598–1607. https://doi.org/10.1038/jcbfm.2010.49.

(2) Mergenthaler, P.; Lindauer, U.; Dienel, G. A.; Meisel, A. Sugar for the Brain: The Role of Glucose in Physiological and Pathological Brain Function. *Trends in Neurosciences* **2013**, *36* (10), 587–597. https://doi.org/10.1016/j.tins.2013.07.001.

(3) Azevedo, F. A. C.; Carvalho, L. R. B.; Grinberg, L. T.; Farfel, J. M.; Ferretti, R. E. L.; Leite, R. E. P.; Filho, W. J.; Lent, R.; Herculano-Houzel, S. Equal Numbers of Neuronal and Nonneuronal Cells Make the Human Brain an Isometrically Scaled-up Primate Brain. *J of Comparative Neurology* **2009**, *513* (5), 532–541. https://doi.org/10.1002/cne.21974.

(4) Nicholson, C. Diffusion and Related Transport Mechanisms in Brain Tissue. *Rep. Prog. Phys.* **2001**, *64* (7), 815–884. https://doi.org/10.1088/0034-4885/64/7/202.

(5) Lo, E. H.; Dalkara, T.; Moskowitz, M. A. Mechanisms, Challenges and Opportunities in Stroke. *Nat Rev Neurosci* **2003**, *4* (5), 399–414. https://doi.org/10.1038/nrn1106.

(6) Hossmann, K.-A. Pathophysiology and Therapy of Experimental Stroke. *Cell Mol Neurobiol* **2006**, *26* (7–8), 1055–1081. https://doi.org/10.1007/s10571-006-9008-1.

(7) Abbott, N. J.; Patabendige, A. A. K.; Dolman, D. E. M.; Yusof, S. R.; Begley, D. J. Structure and Function of the Blood–Brain Barrier. *Neurobiology of Disease* **2010**, *37* (1), 13–25. https://doi.org/10.1016/j.nbd.2009.07.030.

(8) Sweeney, M. D.; Zhao, Z.; Montagne, A.; Nelson, A. R.; Zlokovic, B. V. Blood-Brain Barrier: From Physiology to Disease and Back. *Physiological Reviews* **2019**, *99* (1), 21–78. https://doi.org/10.1152/physrev.00050.2017.

(9) Pardridge, W. M. BLOOD-BRAIN BARRIER DRUG TARGETING: THE FUTURE OF BRAIN DRUG DEVELOPMENT. *Molecular Interventions* **2003**, *3* (2), 90–105. https://doi.org/10.1124/mi.3.2.90.

(10) Ghose, A. K.; Viswanadhan, V. N.; Wendoloski, J. J. A Knowledge-Based Approach in Designing Combinatorial or Medicinal Chemistry Libraries for Drug Discovery. 1. A

Qualitative and Quantitative Characterization of Known Drug Databases. *J. Comb. Chem.* **1999**, *1* (1), 55–68. https://doi.org/10.1021/cc9800071.
(11) Pardridge, W. M. The Blood-Brain Barrier: Bottleneck in Brain Drug Development. *NeuroRx* **2005**, *2* (1), 3–14. https://doi.org/10.1602/neurorx.2.1.3.
(12) Cader, Z. Human Blood-Brain-Barrier In Vitro Models: Overview and Applications. In *Physiology, Pharmacology and Pathology of the Blood-Brain Barrier*; Cader, Z., Neuhaus, W., Eds.; Springer International Publishing: Cham, 2022; pp 205–222. https://doi.org/10.1007/164_2021_562.
(13) Baghirov, H. Mechanisms of Receptor-Mediated Transcytosis at the Blood-Brain Barrier. *Journal of Controlled Release* **2025**, *381*, 113595. https://doi.org/10.1016/j.jconrel.2025.113595.
(14) Ding, S.; Khan, A. I.; Cai, X.; Song, Y.; Lyu, Z.; Du, D.; Dutta, P.; Lin, Y. Overcoming Blood–Brain Barrier Transport: Advances in Nanoparticle-Based Drug Delivery Strategies. *Materials Today* **2020**, *37*, 112–125. https://doi.org/10.1016/j.mattod.2020.02.001.
(15) Rampado, R.; Crotti, S.; Caliceti, P.; Pucciarelli, S.; Agostini, M. Recent Advances in Understanding the Protein Corona of Nanoparticles and in the Formulation of "Stealthy" Nanomaterials. *Front. Bioeng. Biotechnol.* **2020**, *8*, 166. https://doi.org/10.3389/fbioe.2020.00166.
(16) Jokerst, J. V.; Lobovkina, T.; Zare, R. N.; Gambhir, S. S. Nanoparticle PEGylation for Imaging and Therapy. *Nanomedicine* **2011**, *6* (4), 715–728. https://doi.org/10.2217/nnm.11.19.
(17) Shi, D.; Beasock, D.; Fessler, A.; Szebeni, J.; Ljubimova, J. Y.; Afonin, K. A.; Dobrovolskaia, M. A. To PEGylate or Not to PEGylate: Immunological Properties of Nanomedicine's Most Popular Component, Polyethylene Glycol and Its Alternatives. *Advanced Drug Delivery Reviews* **2022**, *180*, 114079. https://doi.org/10.1016/j.addr.2021.114079.
(18) Patching, S. G. Glucose Transporters at the Blood-Brain Barrier: Function, Regulation and Gateways for Drug Delivery. *Mol Neurobiol* **2017**, *54* (2), 1046–1077. https://doi.org/10.1007/s12035-015-9672-6.
(19) Liu, J.; Wang, T.; Dong, J.; Lu, Y. The Blood–Brain Barriers: Novel Nanocarriers for Central Nervous System Diseases. *J Nanobiotechnol* **2025**, *23* (1), 146. https://doi.org/10.1186/s12951-025-03247-8.
(20) Suk, J. S.; Xu, Q.; Kim, N.; Hanes, J.; Ensign, L. M. PEGylation as a Strategy for Improving Nanoparticle-Based Drug and Gene Delivery. *Advanced Drug Delivery Reviews* **2016**, *99*, 28–51. https://doi.org/10.1016/j.addr.2015.09.012.
(21) Liu, L.; Bai, X.; Martikainen, M.-V.; Kårlund, A.; Roponen, M.; Xu, W.; Hu, G.; Tasciotti, E.; Lehto, V.-P. Cell Membrane Coating Integrity Affects the Internalization Mechanism of Biomimetic Nanoparticles. *Nat Commun* **2021**, *12* (1), 5726. https://doi.org/10.1038/s41467-021-26052-x.
(22) Monopoli, M. P.; Åberg, C.; Salvati, A.; Dawson, K. A. Biomolecular Coronas Provide the Biological Identity of Nanosized Materials. *Nature Nanotech* **2012**, *7* (12), 779–786. https://doi.org/10.1038/nnano.2012.207.
(23) Pearson, R. M.; Juettner, V. V.; Hong, S. Biomolecular Corona on Nanoparticles: A Survey of Recent Literature and Its Implications in Targeted Drug Delivery. *Front. Chem.* **2014**, *2*. https://doi.org/10.3389/fchem.2014.00108.

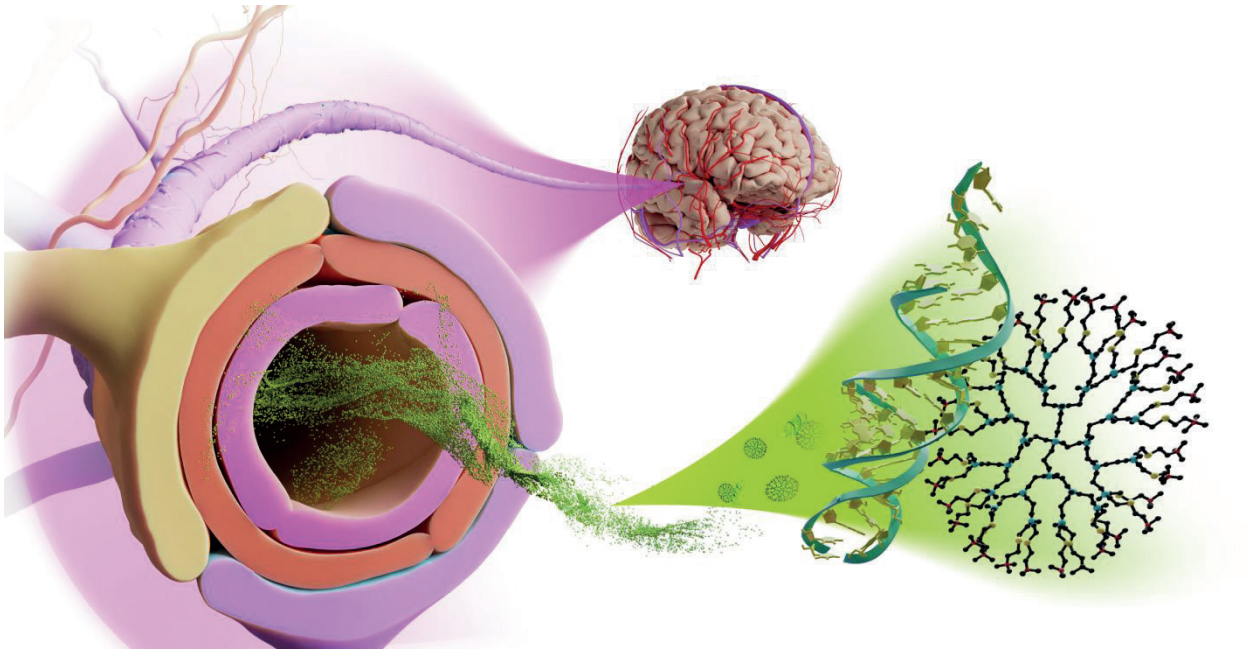
(24) Ghosh, G.; Panicker, L. Protein–Nanoparticle Interactions and a New Insight. *Soft Matter* **2021**, *17* (14), 3855–3875. https://doi.org/10.1039/D0SM02050H.
(25) Albertazzi, L.; Serresi, M.; Albanese, A.; Beltram, F. Dendrimer Internalization and Intracellular Trafficking in Living Cells. *Mol. Pharmaceutics* **2010**, *7* (3), 680–688. https://doi.org/10.1021/mp9002464.
(26) Kuhn, E.; Srinageshwar, B.; Story, D. T.; Swanson, D.; Sharma, A.; Dunbar, G. L.; Rossignol, J. Delivery of PAMAM Dendrimers and Dendriplexes across Natural Barriers (Blood–Brain Barrier and Placental Barrier) in Healthy Pregnant Mice. *Discover Nano* **2024**, *19* (1), 148. https://doi.org/10.1186/s11671-024-04105-6.
(27) Goldberg, D. S.; Vijayalakshmi, N.; Swaan, P. W.; Ghandehari, H. G3.5 PAMAM Dendrimers Enhance Transepithelial Transport of SN38 While Minimizing Gastrointestinal Toxicity. *Journal of Controlled Release* **2011**, *150* (3), 318–325. https://doi.org/10.1016/j.jconrel.2010.11.022.
(28) Oliveira, J. M.; Salgado, A. J.; Sousa, N.; Mano, J. F.; Reis, R. L. Dendrimers and Derivatives as a Potential Therapeutic Tool in Regenerative Medicine Strategies—A Review. *Progress in Polymer Science* **2010**, *35* (9), 1163–1194. https://doi.org/10.1016/j.progpolymsci.2010.04.006.
(29) D'Emanuele, A.; Jevprasesphant, R.; Penny, J.; Attwood, D. The Use of a Dendrimer-Propranolol Prodrug to Bypass Efflux Transporters and Enhance Oral Bioavailability. *Journal of Controlled Release* **2004**, *95* (3), 447–453. https://doi.org/10.1016/j.jconrel.2003.12.006.
(30) Mehta, P.; Kadam, S.; Pawar, A.; Bothiraja, C. Dendrimers for Pulmonary Delivery: Current Perspectives and Future Challenges. *New J. Chem.* **2019**, *43* (22), 8396–8409. https://doi.org/10.1039/C9NJ01591D.
(31) Manikkath, J.; Hegde, A. R.; Kalthur, G.; Parekh, H. S.; Mutalik, S. Influence of Peptide Dendrimers and Sonophoresis on the Transdermal Delivery of Ketoprofen. *International Journal of Pharmaceutics* **2017**, *521* (1–2), 110–119. https://doi.org/10.1016/j.ijpharm.2017.02.002.
(32) He, H.; Li, Y.; Jia, X.-R.; Du, J.; Ying, X.; Lu, W.-L.; Lou, J.-N.; Wei, Y. PEGylated Poly(Amidoamine) Dendrimer-Based Dual-Targeting Carrier for Treating Brain Tumors. *Biomaterials* **2011**, *32* (2), 478–487. https://doi.org/10.1016/j.biomaterials.2010.09.002.
(33) Xu, Z.; Wang, Y.; Ma, Z.; Wang, Z.; Wei, Y.; Jia, X. A Poly(Amidoamine) Dendrimer-Based Nanocarrier Conjugated with Angiopep-2 for Dual-Targeting Function in Treating Glioma Cells. *Polym. Chem.* **2016**, *7* (3), 715–721. https://doi.org/10.1039/C5PY01625H.
(34) Li, Z.; Yang, J.; Li, J.; Zhao, S.; Jiang, S.; Liu, W.; Li, X.; Zhang, S.; Du, H.; Ni, J.; Huang, Y.; Qing, H.; Ruan, S. Targeted Delivery of BACE1 siRNA for Synergistic Treatment of Alzheimer's Disease. *Transl Neurodegener* **2025**, *14* (1), 41. https://doi.org/10.1186/s40035-025-00503-7.
(35) Gothwal, A.; Kumar, H.; Nakhate, K. T.; Ajazuddin; Dutta, A.; Borah, A.; Gupta, U. Lactoferrin Coupled Lower Generation PAMAM Dendrimers for Brain Targeted Delivery of Memantine in Aluminum-Chloride-Induced Alzheimer's Disease in Mice. *Bioconjugate Chem.* **2019**, *30* (10), 2573–2583. https://doi.org/10.1021/acs.bioconjchem.9b00505.
(36) Nance, E.; Kambhampati, S. P.; Smith, E. S.; Zhang, Z.; Zhang, F.; Singh, S.; Johnston, M. V.; Kannan, R. M.; Blue, M. E.; Kannan, S. Dendrimer-Mediated Delivery of N-Acetyl Cysteine to Microglia in a Mouse Model of Rett Syndrome. *J Neuroinflammation* **2017**, *14* (1), 252. https://doi.org/10.1186/s12974-017-1004-5.

(37) Pérez-Carrión, M. D.; Posadas, I. Dendrimers in Neurodegenerative Diseases. *Processes* **2023**, *11* (2), 319. https://doi.org/10.3390/pr11020319.
(38) Rabiee, N.; Ahmadvand, S.; Ahmadi, S.; Fatahi, Y.; Dinarvand, R.; Bagherzadeh, M.; Rabiee, M.; Tahriri, M.; Tayebi, L.; Hamblin, M. R. Carbosilane Dendrimers: Drug and Gene Delivery Applications. *Journal of Drug Delivery Science and Technology* **2020**, *59*, 101879. https://doi.org/10.1016/j.jddst.2020.101879.
(39) Serramía, M. J.; Álvarez, S.; Fuentes-Paniagua, E.; Clemente, M. I.; Sánchez-Nieves, J.; Gómez, R.; de la Mata, J.; Muñoz-Fernández, M. Á. In Vivo Delivery of siRNA to the Brain by Carbosilane Dendrimer. *J Control Release* **2015**, *200*, 60–70. https://doi.org/10.1016/j.jconrel.2014.12.042.
(40) Müllerová, M.; Tarach, P.; Strašák, T.; Cuřínová, P.; Petrickovic, R.; Závodná, T.; Topinka, J.; Janaszewska, A.; Klajnert-Maculewicz, B.; Červenková Šťastná, L. Comparative Study of Functionalized Carbosilane Dendrimers for siRNA Delivery: Synthesis, Cytotoxicity, and Biophysical Properties. *ACS Omega* **2025**, *10* (1), 1047–1060. https://doi.org/10.1021/acsomega.4c08314.
(41) Herma, R.; Wrobel, D.; Liegertová, M.; Müllerová, M.; Strašák, T.; Maly, M.; Semerádtová, A.; Štofik, M.; Appelhans, D.; Maly, J. Carbosilane Dendrimers with Phosphonium Terminal Groups Are Low Toxic Non-Viral Transfection Vectors for siRNA Cell Delivery. *International Journal of Pharmaceutics* **2019**, *562*, 51–65. https://doi.org/10.1016/j.ijpharm.2019.03.018.
(42) Grodzicka, M.; Michlewska, S.; Blasiak, J.; Ortega, P.; de la Mata, F. J.; Bryszewska, M.; Ionov, M. Polyphenolic Dendrimers as Carriers of Anticancer siRNA. *International Journal of Pharmaceutics* **2024**, *658*, 124199. https://doi.org/10.1016/j.ijpharm.2024.124199.
(43) Raulin, A.-C.; Doss, S. V.; Trottier, Z. A.; Ikezu, T. C.; Bu, G.; Liu, C.-C. ApoE in Alzheimer's Disease: Pathophysiology and Therapeutic Strategies. *Mol Neurodegeneration* **2022**, *17* (1), 72. https://doi.org/10.1186/s13024-022-00574-4.
(44) Zawadzki, S.; Martín-Serrano, Á.; Okła, E.; Kędzierska, M.; Garcia-Gallego, S.; López, P. O.; De La Mata, F. J.; Michlewska, S.; Makowski, T.; Ionov, M.; Pędziwiatr-Werbicka, E.; Bryszewska, M.; Miłowska, K. Synthesis and Biophysical Evaluation of Carbosilane Dendrimers as Therapeutic siRNA Carriers. *Sci Rep* **2024**, *14* (1), 1615. https://doi.org/10.1038/s41598-024-51238-w.
(45) Zawadzki, S.; Okła, E.; Michlewska, S.; Makowski, T.; Buczkowski, A.; López, P. O.; de la Mata, F. J.; Ionov, M.; Bryszewska, M.; Miłowska, K. Structural and Conformational Rearrangements of Human Serum Albumin, Transferrin, and Blood Plasma Induced by Carbosilane Dendrimer Therapeutic Delivery System. *Sci Rep* **2025**, In Press. https://doi.org/10.1038/s41598-025-23355-7.
(46) Zawadzki, S.; Suty, S.; Okła, E.; López, P. O.; de la Mata, F. J.; Waczulikova, I.; Ionov, M.; Bryszewska, M.; Miłowska, K. Hemocompatibility of Carbosilane Dendrimers as Therapeutic siRNA Delivery System Across Blood-Brain Barrier. *ACS Appl. Mater. Interfaces* **2026**. (in press).
(47) Mosmann, T. Rapid Colorimetric Assay for Cellular Growth and Survival: Application to Proliferation and Cytotoxicity Assays. *J Immunol Methods* **1983**, *65* (1–2), 55–63. https://doi.org/10.1016/0022-1759(83)90303-4.
(48) Liddelow, S. A. Fluids and Barriers of the CNS: A Historical Viewpoint. *Fluids Barriers CNS* **2011**, *8* (1), 2. https://doi.org/10.1186/2045-8118-8-2.

(49) Iadecola, C. The Neurovascular Unit Coming of Age: A Journey through Neurovascular Coupling in Health and Disease. *Neuron* **2017**, *96* (1), 17–42. https://doi.org/10.1016/j.neuron.2017.07.030.
(50) Schaeffer, S.; Iadecola, C. Revisiting the Neurovascular Unit. *Nat Neurosci* **2021**, *24* (9), 1198–1209. https://doi.org/10.1038/s41593-021-00904-7.
(51) Mukherjee, S. P.; Davoren, M.; Byrne, H. J. In Vitro Mammalian Cytotoxicological Study of PAMAM Dendrimers – Towards Quantitative Structure Activity Relationships. *Toxicology in Vitro* **2010**, *24* (1), 169–177. https://doi.org/10.1016/j.tiv.2009.09.014.
(52) Mukherjee, S. P.; Lyng, F. M.; Garcia, A.; Davoren, M.; Byrne, H. J. Mechanistic Studies of in Vitro Cytotoxicity of Poly(Amidoamine) Dendrimers in Mammalian Cells. *Toxicology and Applied Pharmacology* **2010**, *248* (3), 259–268. https://doi.org/10.1016/j.taap.2010.08.016.
(53) McBean, G. J. Astrocyte Antioxidant Systems. *Antioxidants* **2018**, *7* (9), 112. https://doi.org/10.3390/antiox7090112.
(54) Baxter, P. S.; Hardingham, G. E. Adaptive Regulation of the Brain's Antioxidant Defences by Neurons and Astrocytes. *Free Radical Biology and Medicine* **2016**, *100*, 147–152. https://doi.org/10.1016/j.freeradbiomed.2016.06.027.
(55) Kuroda, J.; Ago, T.; Nishimura, A.; Nakamura, K.; Matsuo, R.; Wakisaka, Y.; Kamouchi, M.; Kitazono, T. Nox4 Is a Major Source of Superoxide Production in Human Brain Pericytes. *J Vasc Res* **2014**, *51* (6), 429–438. https://doi.org/10.1159/000369930.
(56) Jiang, Q.; Gao, Y.; Wang, C.; Tao, R.; Wu, Y.; Zhan, K.; Liao, M.; Lu, N.; Lu, Y.; Wilcox, C. S.; Luo, J.; Jiang, L.-H.; Yang, W.; Han, F. Nitration of TRPM2 as a Molecular Switch Induces Autophagy During Brain Pericyte Injury. *Antioxidants & Redox Signaling* **2017**, *27* (16), 1297–1316. https://doi.org/10.1089/ars.2016.6873.
(57) El Yamani, N.; Rundén-Pran, E.; Varet, J.; Beus, M.; Dusinska, M.; Fessard, V.; Moschini, E.; Serchi, T.; Cimpan, M. R.; Lynch, I.; Vinković Vrček, I. Hazard Assessment of Nanomaterials Using in Vitro Toxicity Assays: Guidance on Potential Assay Interferences and Mitigating Actions to Avoid Biased Results. *Nano Today* **2024**, *55*, 102215. https://doi.org/10.1016/j.nantod.2024.102215.
(58) Kroll, A.; Pillukat, M. H.; Hahn, D.; Schnekenburger, J. Interference of Engineered Nanoparticles with in Vitro Toxicity Assays. *Arch Toxicol* **2012**, *86* (7), 1123–1136. https://doi.org/10.1007/s00204-012-0837-z.
(59) Fu, P. P.; Xia, Q.; Hwang, H.-M.; Ray, P. C.; Yu, H. Mechanisms of Nanotoxicity: Generation of Reactive Oxygen Species. *Journal of Food and Drug Analysis* **2014**, *22* (1), 64–75. https://doi.org/10.1016/j.jfda.2014.01.005.
(60) Grossini, E.; Venkatesan, S.; Ola Pour, M. M. Mitochondrial Dysfunction in Endothelial Cells: A Key Driver of Organ Disorders and Aging. *Antioxidants* **2025**, *14* (4), 372. https://doi.org/10.3390/antiox14040372.
(61) Wang, Y.; Wu, J.; Wang, J.; He, L.; Lai, H.; Zhang, T.; Wang, X.; Li, W. Mitochondrial Oxidative Stress in Brain Microvascular Endothelial Cells: Triggering Blood-Brain Barrier Disruption. *Mitochondrion* **2023**, *69*, 71–82. https://doi.org/10.1016/j.mito.2023.01.007.
(62) Ghasemi, M.; Turnbull, T.; Sebastian, S.; Kempson, I. The MTT Assay: Utility, Limitations, Pitfalls, and Interpretation in Bulk and Single-Cell Analysis. *IJMS* **2021**, *22* (23), 12827. https://doi.org/10.3390/ijms222312827.
(63) Ruenraroengsak, P.; Tetley, T. D. Differential Bioreactivity of Neutral, Cationic and Anionic Polystyrene Nanoparticles with Cells from the Human Alveolar Compartment:

Robust Response of Alveolar Type 1 Epithelial Cells. *Part Fibre Toxicol* **2015**, *12* (1), 19. https://doi.org/10.1186/s12989-015-0091-7.
(64) Moghimi, S. M.; Symonds, P.; Murray, J. C.; Hunter, A. C.; Debska, G.; Szewczyk, A. A Two-Stage Poly(Ethylenimine)-Mediated Cytotoxicity: Implications for Gene Transfer/Therapy. *Molecular Therapy* **2005**, *11* (6), 990–995. https://doi.org/10.1016/j.ymthe.2005.02.010.
(65) Knipp, G. T.; Lubin, K. E. Design of Experiment Based Optimization of an in Vitro Direct Contact Triculture Blood Brain Barrier Model for Permeability Screening. *PPIJ* **2021**, *9* (4), 143–158. https://doi.org/10.15406/ppij.2021.09.00340.
(66) Calabrese, V.; Cornelius, C.; Dinkova-Kostova, A. T.; Calabrese, E. J.; Mattson, M. P. Cellular Stress Responses, The Hormesis Paradigm, and Vitagenes: Novel Targets for Therapeutic Intervention in Neurodegenerative Disorders. *Antioxidants & Redox Signaling* **2010**, *13* (11), 1763–1811. https://doi.org/10.1089/ars.2009.3074.
(67) Hebbar, S.; Knust, E. Reactive Oxygen Species (ROS) Constitute an Additional Player in Regulating Epithelial Development. *BioEssays* **2021**, *43* (8), 2100096. https://doi.org/10.1002/bies.202100096.
(68) Mavrakis, M.; Juanes, M. A. The Compass to Follow: Focal Adhesion Turnover. *Current Opinion in Cell Biology* **2023**, *80*, 102152. https://doi.org/10.1016/j.ceb.2023.102152.
(69) Murthy, S. K.; Radisic, M. Cell Adhesion and Detachment. In *Encyclopedia of Microfluidics and Nanofluidics*; Li, D., Ed.; Springer US: Boston, MA, 2013; pp 1–9. https://doi.org/10.1007/978-3-642-27758-0_177-2.
(70) Sweeney, M. D.; Sagare, A. P.; Zlokovic, B. V. Blood–Brain Barrier Breakdown in Alzheimer Disease and Other Neurodegenerative Disorders. *Nat Rev Neurol* **2018**, *14* (3), 133–150. https://doi.org/10.1038/nrneurol.2017.188.
(71) Ranasinghe, P.; Addison, M. L.; Dear, J. W.; Webb, D. J. Small Interfering RNA: Discovery, Pharmacology and Clinical Development—An Introductory Review. *British J Pharmacology* **2023**, *180* (21), 2697–2720. https://doi.org/10.1111/bph.15972.
(72) Treuting, P. M.; Dintzis, S. M.; Montine, K. S. Comparative Anatomy and Histology.
(73) Fan, F.; Povedailo, V. A.; Lysenko, I. L.; Seviarynchyk, T. P.; Sharko, O. L.; Mazunin, I. O.; Shmanai, V. V. Fluorescent Properties of Cyanine Dyes as a Matter of the Environment. May 22, 2023. https://doi.org/10.21203/rs.3.rs-2942963/v1.
(74) Hong, G.; Diao, S.; Chang, J.; Antaris, A. L.; Chen, C.; Zhang, B.; Zhao, S.; Atochin, D. N.; Huang, P. L.; Andreasson, K. I.; Kuo, C. J.; Dai, H. Through-Skull Fluorescence Imaging of the Brain in a New near-Infrared Window. *Nature Photon* **2014**, *8* (9), 723–730. https://doi.org/10.1038/nphoton.2014.166.
(75) Triguero, D.; Buciak, J.; Pardridge, W. M. Capillary Depletion Method for Quantification of Blood–Brain Barrier Transport of Circulating Peptides and Plasma Proteins. *Journal of Neurochemistry* **1990**, *54* (6), 1882–1888. https://doi.org/10.1111/j.1471-4159.1990.tb04886.x.
(76) Zuckerman, J. E.; Choi, C. H. J.; Han, H.; Davis, M. E. Polycation-siRNA Nanoparticles Can Disassemble at the Kidney Glomerular Basement Membrane. *Proc. Natl. Acad. Sci. U.S.A.* **2012**, *109* (8), 3137–3142. https://doi.org/10.1073/pnas.1200718109.

Graphical abstract



The graphical abstract illustrates siRNA-loaded dendrimers within the context of the blood–brain barrier, emphasizing the barrier's complex, multi-component organization.

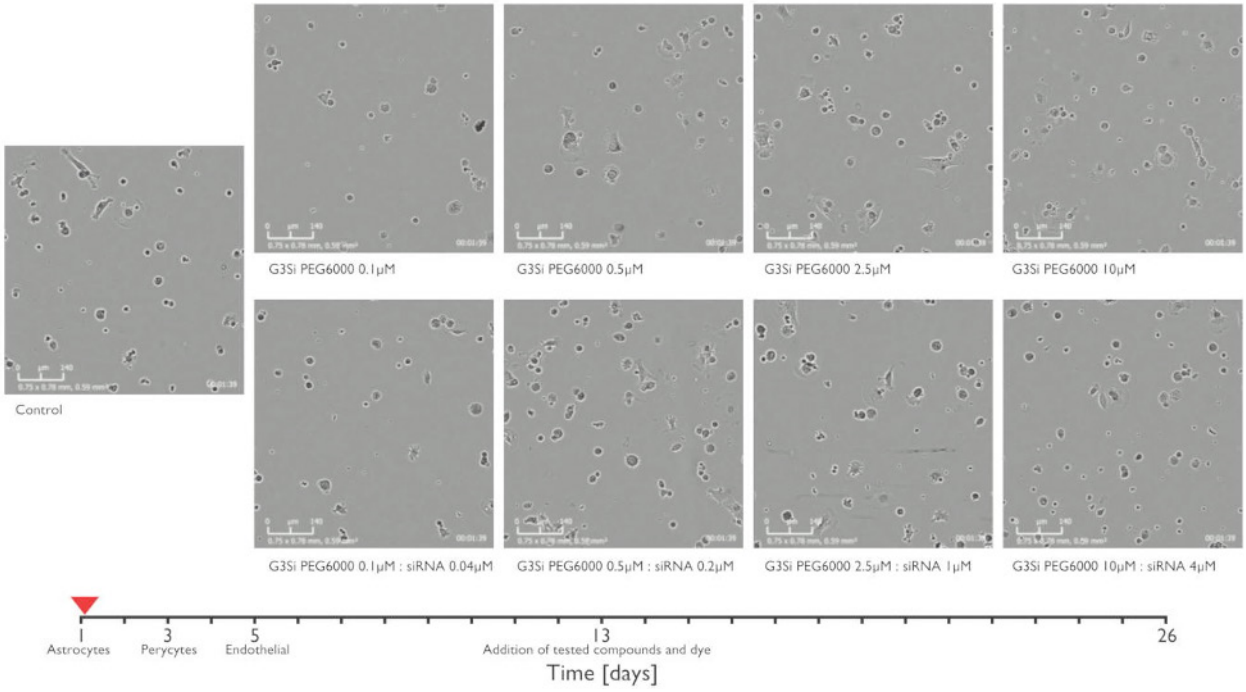
Supplementary information for:

Multilevel Assessment of Carbosilane Dendrimer–siRNA Nanoplatform: Cellular Compatibility, Blood–Brain Barrier Model Integrity, and Murine Model Biodistribution

Serafin Zawadzki [1,2,] (serafin.zawadzki@edu.uni.lodz.pl), Elżbieta Okła [1] (elzbieta.okla@biol.uni.lodz.pl), Paula Ortega López [3,4,5] (paula.ortega@uah.es), F. Javier de la Mata [3,4,5] (javier.delamata@uah.es), Maksim Ionov [1,6] (maksim.ionov@biol.uni.lodz.pl), Madara Kreišmane [7] (madara.kreismane@rsu.lv), Dace Skrastiņa [7] (daceskr@biomed.lu.lv), Juris Jansons [7] (jansons@biomed.lu.lv), Maria Bryszewska [1] (maria.bryszewska@biol.uni.lodz.pl) and Katarzyna Miłowska [1,**] (katarzyna.milowska@biol.uni.lodz.pl)*

1. Department of General Biophysics, Faculty of Biology and Environmental Protection, University of Lodz, 141/143 Pomorska St., 90-236 Lodz, Poland; 2. Bio-Med-Chem Doctoral School of the University of Lodz and Lodz Institutes of the Polish Academy of Sciences, University of Lodz Matejki 21/23, Lodz 90-237, Poland; 3. Department of Organic and Inorganic Chemistry, IQAR, University of Alcalá, 28805 Madrid, Spain; 4. Networking Research Center on Bioengineering, Biomaterials and Nanomedicine

(CIBER-BBN), 28029 Madrid, Spain; 5. Ramón y Cajal Health Research Institute (IRYCIS), 28034 Madrid, Spain; 6. Faculty of Medicine, Collegium Medicum, Mazovian Academy in Plock, 2 Dabrowskiego Sq, 09-402 Plock, Poland; 7. Latvian Biomedical Research and Study Centre, Ratsupites street1 k-1, Riga LV-1067, Latvia



Supplementary Video S1. Time-lapse composite of brightfield and fluorescence images documenting blood–brain barrier (BBB) model assembly, maturation, and subsequent morphological and organizational changes following exposure to the G3Si PEG6000 dendrimer or its dendriplex across the tested concentration range. The red fluorescent signal marks cell nuclei (stained with eLive Red dye). The timeline at the bottom tracks experiment progression.

Materiał wideo **Supplementary Video S1** uzupełniający wyniki przedstawione w pracy „Multilevel Assessment of Carbosilane Dendrimer–siRNA Nanoplatform: Cellular Compatibility, Blood–Brain Barrier Model Integrity, and Murine Model Biodistribution” został załączony do rozprawy w formie elektronicznej.

Tiered Evaluation of Carbosilane Dendrimer – siRNA Nanoplatform from Single-Cell Biocompatibility to Blood-Brain Barrier Model Dynamics, and Murine Alzheimer Model Behavior Assessment

Serafin Zawadzki [1,2,] (serafin.zawadzki@edu.uni.lodz.pl), Elżbieta Okła [1](elzbieta.okla@biol.uni.lodz.pl), Sylwia Michlewska [3] (sylwia.michlewska@biol.uni.lodz.pl), Radosław Bednarek [4] (radoslaw.bednarek@umed.lodz.pl), Paula Ortega López [5,6,7] (paula.ortega@uah.es), F. Javier de la Mata [5,6,7] (javier.delamata@uah.es), Juris Jansons[8] (jansons@biomed.lu.lv), Dace Skrastina[8] (daceskr@biomed.lu.lv), Madara Kreišmane[8] (madara.kreismane@rsu.lv), Vladimirs Piļipenko[9] (vladimirs.pilipenko@ut.ee), Baiba Jansone[9] (baiba.jansone@lu.lv), Maksim Ionov [1,10] (maksim.ionov@biol.uni.lodz.pl), Maria Bryszewska [1] (maria.bryszewska@biol.uni.lodz.pl) and Katarzyna Miłowska [1,**] (katarzyna.milowska@biol.uni.lodz.pl)*

1. Department of General Biophysics, Faculty of Biology and Environmental Protection, University of Lodz, 141/143 Pomorska St., 90-236 Lodz, Poland; 2. Bio-Med-Chem Doctoral School of the University of Lodz and Lodz Institutes of the Polish Academy of Sciences,

University of Lodz, Matejki 21/23, Lodz 90-237, Poland; 3. Laboratory of Microscopic Imaging and Specialized Biological Techniques, Faculty of Biology and Environmental Protection, University of Lodz, Banacha 12/16, 90-237 Lodz, Poland; 4. Department of Cytobiology and Proteomics, Medical University of Lodz, 92-215 Lodz, Poland; 5. Department of Organic and Inorganic Chemistry, IQAR, University of Alcalá, 28805 Madrid, Spain; 6. Networking Research Center on Bioengineering, Biomaterials and Nanomedicine (CIBER-BBN), 28029 Madrid, Spain; 7. Ramón y Cajal Health Research Institute (IRYCIS), 28034 Madrid, Spain; 8 Latvian Biomedical Research and Study Centre, Ratsupites str 1 k-1, Riga, Latvia; 9 Department of Neuromedicine and Neuroscience, Faculty of Medicine and Life Sciences, University of Latvia, Jelgavas street 3, Riga, Latvia; 10. Faculty of Medicine, Collegium Medicum, Mazovian Academy in Plock, 2 Dabrowskiego Sq, 09-402 Plock, Poland

KEYWORDS: Carbosilane Dendrimer, Nanoparticles, siRNA, Blood–Brain Barrier Model, Behavioral Assessment, Alzheimer's disease

ABSTRACT

Blood–brain barrier (BBB) transport remains a primary constraint on achieving predictable central nervous system (CNS) exposure for Alzheimer's disease (AD) therapeutics, motivating the evaluation of delivery platforms with barrier-resolved and functionally relevant endpoints. We assessed a carbosilane dendrimer (G3Si PEG6000) and its siRNA dendriplex using a tiered, upstream strategy spanning cell internalization, DNA damage screening, BBB model integrity and permeability, and *in vivo* AD-relevant murine model learning. At the cellular level, the dendrimer enhanced intracellular siRNA-associated signal with predominantly cytoplasmic

localization, and siRNA complexation attenuated genotoxicity relative to the non-complexed carrier. In a BBB tri-culture model, barrier function was preserved without sustained transendothelial electrical resistance (TEER) loss, and complementary tracer flux readouts showed time- and formulation-dependent, non-monotonic changes, including TEER–permeability decoupling consistent with non-uniform perturbation and adaptive remodeling of paracellular organization. In APOE4 knock-in mice, dendriplex treatment improved spatial learning, as evidenced by increased platform zone crossings in the Morris water maze test. Collectively, these integrated results indicate that siRNA complexation improves the BBB-relevant safety-performance balance of G3Si PEG6000 and supports further studies that directly link brain exposure and target engagement to cognitive outcomes.

INTRODUCTION

Contemporary models describe Alzheimer's disease (AD) as a multifactorial disorder in which genetic susceptibility (e.g., APOE and APP variants) and environmental or ageing-related stressors converge on partially overlapping biological cascades that ultimately drive synaptic failure, progressive neurodegeneration, and dementia. In the amyloid-centered pathway, amyloid precursor protein (APP) is cleaved sequentially by beta-site APP cleaving enzyme 1 (BACE1) and gamma-secretase, generating amyloid-beta (Aβ) peptides that can oligomerize and deposit as extracellular plaques. In parallel, Aβ and APP-derived fragments are proposed to amplify kinase and phosphatase imbalance and inflammatory signaling, thereby promoting tau hyperphosphorylation, secretion, cellular uptake, and propagation along synaptically connected neuronal pathways. These processes convert tau from a microtubule-stabilizing protein into an aggregation-prone species that forms neurofibrillary tangles (NFTs) and disrupts axonal and

synaptic communication. Together, amyloid- and tau-linked pathways, coupled with chronic neuroinflammation and vascular dysfunction, contribute to synaptic failure, neuronal loss, brain atrophy, resulting in clinical dementia that primarily manifests as memory loss, aphasia, agnosia, visuospatial impairment, deficits in critical thinking and calculation, along with personality and behavioral changes [1–3]. An increasingly supported hypothesis posits that early cerebrovascular impairment, particularly the blood-brain barrier (BBB) dysfunction, acts as an upstream contributor to the disease continuum rather than merely a downstream consequence. Multiple independent lines of evidence identify BBB breakdown as an early vascular abnormality in AD, documented by neuroimaging and corroborated by both animal models and post-mortem human tissue analyses [4–14]. In this context, the two-hit vascular hypothesis proposes that an initial insult driven by vascular risk factors and ageing results in BBB disruption, capillary hypoperfusion, and impaired microvascular function, thereby permitting the entry of blood-derived neurotoxic/pro-inflammatory factors into the brain. This altered milieu is then proposed to facilitate a second insult marked by Aβ accumulation, tau pathology, and progressive neurodegeneration [15,16].

Despite major advances in mechanistic understanding, approved pharmacotherapies remain largely symptomatic. Acetylcholinesterase inhibitors (donepezil, rivastigmine, galantamine) reversibly increase synaptic acetylcholine and transiently enhance cholinergic signaling. These agents can yield modest improvements or short-term stabilization in cognition and daily function for some patients, but they do not modify underlying disease biology [17–22]. Memantine, an N-methyl-D-aspartate (NMDA) receptor antagonist approved for moderate-to-severe AD, acts as an uncompetitive, voltage-dependent blocker that preferentially attenuates sustained pathological NMDA receptor activation and calcium-mediated excitotoxicity while

largely preserving physiological glutamatergic transmission [23,24]. Consequently, current standard-of-care medicines can provide limited symptomatic benefit but do not halt disease progression. In contrast, the clinical trial landscape spans multiple mechanistic-centered strategies, including therapies directed at neuroinflammation, synaptic resilience and neuroprotection, oxidative injury, and amyloid- and tau-linked processes. As a snapshot of the ClinicalTrials.gov registry on February 2026 identified 164 active, interventional AD studies across Phases 1 to 4, with 13 listed as Phase 1, 38 as Phase 2, 22 as Phase 3, and 6 as Phase 4. Within the field, anti-Aβ monoclonal antibodies such as aducanumab (Aduhelm®), lecanemab (Leqembi®), and donanemab (Kisunla™) have received accelerated or conditional approvals, representing the first wave of FDA-approved anti-Aβ immunotherapeutics [25–27]. The anti-amyloid beta monoclonal antibodies reduce plaque burden and have yielded statistically significant modest clinical slowing in early AD, yet analyses of their pharmacokinetics emphasize that the blood-brain barrier severely limits effective CNS exposure. The aducanumab was reported to cross the BBB because brain concentrations appeared to track plasma levels in mice, yet the reported brain-to-plasma ratio of approximately 1 μL/g is more than tenfold lower than the estimated cerebral plasma volume of about 10 to 15 μL/g [28,29]. This quantitative mismatch implies that much of the measured signal can be explained by antibody confined to the residual blood volume rather than parenchymal penetration. Consequently, without correcting for residual blood volume, brain uptake estimates risk overestimating effective delivery across the BBB and may foster the misconception that no dedicated BBB transport technology is required for CNS biologics. Rational therapeutic design in AD increasingly shifted toward strategies that explicitly incorporate the BBB not as a passive backdrop but as a central design parameter.

Accounting for this complexity, BBB critically shapes not only whether therapeutics enter the CNS, but also how they distribute within brain tissue. Accordingly, explicit consideration of BBB architecture and CNS compartmentalization should be central to therapeutic design. Contrary to the intuitive assumption that disease-driven BBB disruption would passively enhance access of therapeutics to degenerating brain regions, vascular injury and BBB pathology introduce profound hindrance to effective drug distribution. Reported features of neurodegenerative vascular injury include endothelial degeneration, altered tight and adherens junction protein expression, increased non-specific transcytosis, transporter dysregulation, pericyte loss, perivascular accumulation of blood-derived proteins, and sustained neuroinflammation, all of which can perturb solute handling and tissue microenvironment properties [30–33]. Under these conditions, water and solutes accumulate in enlarged perivascular spaces, impairing normal interstitial fluid formation, convection and diffusion through the extracellular space, so that exogenous therapeutics tend to be sequestered with blood-borne debris rather than reaching neuronal targets at effective concentrations [34,35]. In addition, dysfunction or downregulation of carrier-mediated and receptor-mediated transport pathways can further limit delivery for substrates that rely on these routes [30]. Consequently, while transient and spatially controlled BBB opening, for example by focused ultrasound in the presence of intravenously administered microbubbles, can enhance regional drug or gene delivery in selected settings such as brain tumours, chronic or diffuse BBB disruption appears to promote neurodegenerative cascades and compromise therapeutic distribution rather than a reliable facilitator of delivery [36,37].

Considering the increasing recognition that BBB dysfunction can act as an upstream contributor to neurodegeneration, we prioritized targets that mechanistically link Alzheimer's

disease risk to neurovascular unit pathology. Multiple AD-associated risk genes have functions relevant to vascular biology, endocytosis, and barrier maintenance (e.g., PICALM, BIN1, CD2AP, RIN3, FMNL2), supporting BBB-oriented target selection [38–40]. In particular, APOE ε4 is the strongest common genetic risk factor for late-onset AD and has been associated with structural and functional vascular abnormalities, including altered basement membrane morphology and leakage of plasma-derived proteins in affected brain regions, with evidence that these changes can contribute to blood flow dysregulation and cognitive decline independent of canonical AD lesions [8,41,42]. Mechanistic studies report that APOE ε4 can promote BBB breakdown, reduce cerebral blood flow, and contribute to neuronal injury independently of Aβ, in part through pericyte-linked cyclophilin A and matrix metalloproteinase 9 signalling with downstream effects on junctional proteins such as ZO-1 and occludin, supported by complementary findings in post-mortem tissue and cerebrospinal fluid biomarkers in ε4 carriers [14,42,43]. In parallel, the APOE ε4 isoform can impair amyloid homeostasis through receptor-mediated mechanisms that slow Aβ clearance [44]. Together, these lines of evidence motivate our allele-selective RNA interference (RNAi) approach in which siRNA is used to preferentially silence apolipoprotein E4 (APOE4), with the goal of mitigating AD-relevant pathology at the neurovascular interface and within the brain parenchyma.

In this context, nanoparticle platforms offer modular carriers whose size, architecture, and surface chemistry can be rationally engineered guided by BBB permeability and its underlying architecture and physiology, enabling therapeutic strategies to influence both the BBB and brain parenchyma. Surface ligands can be used to engage receptor- or carrier-mediated transcytosis, while cationic or amphiphilic coatings may support adsorptive-mediated transcytosis [45]. A broad range of nanomaterials has been explored for central nervous system

delivery, including dendrimers, polymeric and metallic nanoparticles, nanoemulsions, nanocrystals, and lipid-based systems, with the shared goal of achieving therapeutically relevant brain exposure. Among these, dendrimer nanoparticles have gained attention for their high versatility and structurally well-defined nanocarriers, consisting of a symmetrical core with radially branching repeat monomer units that define the generation number. With the nanoformulation design constraints imposed by BBB architecture in mind, we synthesized a third-generation carbosilane dendrimer with a silicon core and PEG6000 graft (Dendrimer G3Si PEG6000). This nanosystem is designed to provide a size distribution compatible with transcytosis-based transport mechanisms and a high density of terminal groups suitable for conjugation or complexation of nucleic acid cargo while limiting excessive surface charge that could compromise biocompatibility. PEGylation is intended to improve colloidal stability in biological media, reduce opsonisation and non-specific protein binding, and prolong systemic circulation, thereby increasing the probability of brain exposure while limiting peripheral off-target interactions [46].

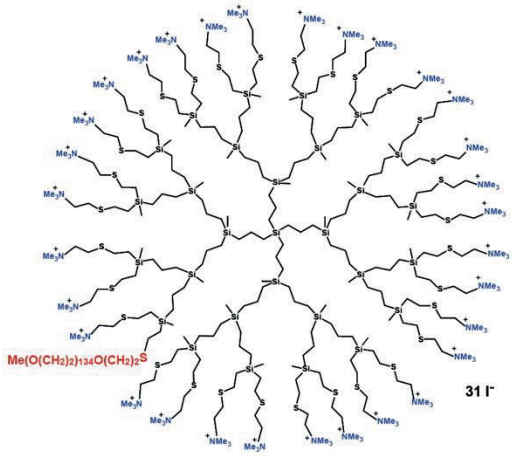
These design expectations require validation through a decision-guided, multi-method validation framework that integrates and translates evidence from multiple sources into transparent safety–performance conclusions. We first established the nanocarrier's synthetic identity in prior work by comprehensively characterizing the carbosilane dendrimer nanosystem biophysical parameters and evaluating interactions with model proteins to anticipate formation of a biologically relevant biomolecular corona, together with hemocompatibility testing using recognized practices for blood-contacting materials [47–49]. Our study was conducted under a weight-of-evidence intelligent testing strategy and an integrated approach to testing and assessment (ITS/IATA) framework, in line with OECD guidance and ISO/TR 16197

recommendations for toxicological screening of manufactured nanomaterials. Building on that foundation, the present article integrates a coordinated endpoint set spanning genotoxicity assessment, cellular uptake, BBB model integrity assessed by transendothelial electrical resistance (TEER), BBB paracellular permeability, spatial learning, and memory in an Alzheimer's disease murine model. Collectively, this structured framework is intended to support a transparent, fit-for-purpose appraisal of the nanocarrier's biological interactions, BBB-relevant performance, and *in vivo* functional readouts within a single, reproducible assessment framework.

MATERIALS AND METHODS

Dendrimer

Dendrimer with a silicon atom core, surface tertiary ammonium groups, and single polyethylene glycol (PEG) (6000) – G3Si PEG6000 with chemical formula $C_{601}H_{1324}I_{30}N_{31}O_{135}S_{32}Si_{29}$ and molar weight of 16794.81 g/mol is presented in Figure 1. The studied dendrimer was diluted in a phosphate buffer solution of 7.4 pH. The synthesis and biophysical characterization of the dendrimer, along with its complex with siRNA, was described in previous work [47].



G3Si PEG6000

Figure 1. Structure of the studied dendrimer G3Si PEG6000.

siRNA

The following siRNA was used in the present study (Dharmacon Inc., Lafayette, CO, USA):

Sense: 5'-GAUUACCUGCGCUGGGUGCUU

Antisense: 5'-P GCACCCAGCGCAGGUAAUCUU

Dendriplex formation

Our prior research provides insights into the dendrimer/siRNA complexation process. We characterized dendrimer G3Si PEG6000 and determined its optimal dendriplex saturation at a molar ratio of dendrimer to siRNA of 2.5:1 [47]. In this research, we chose dendrimer G3Si PEG6000 concentrations ranging from 0.1 to 10 μM and 0.04 to 4 μM for the siRNA in dendriplex. The dendrimer/siRNA complexes were incubated in PBS (Sigma-Aldrich, Saint Louis, MO, USA) at room temperature for 20 minutes to ensure complex formation.

Cell Lines

Human brain microvascular endothelial cells (HBEC-5i; ATCC, Manassas, VA, USA) were cultured on tissue culture flasks pre-coated with 1% gelatin coated flasks in Dulbecco's Modified Eagle Medium/Nutrient Mixture F-12 (DMEM/F-12; Biowest, Nuaillé, France) supplemented with 10% heat-inactivated fetal bovine serum (FBS; Biowest, Nuaillé, France), 1% penicillin–streptomycin (P/S; Sigma-Aldrich, Saint Louis, MO, USA), endothelial cell growth supplement (ECGS; Sigma-Aldrich, Darmstadt, Germany), and 1 μg/mL hydrocortisone (MP Biomedicals, Santa Ana, CA, USA). Cells were maintained at 37 °C in a humidified incubator with 5% CO_2.

Human brain vascular pericytes (HBVP; ScienCell Research Laboratories, Carlsbad, CA, USA) were cultured on flasks coated with 2 μg/cm² poly-L-lysine (PLL) in pericyte medium supplemented with FBS, pericyte growth supplement (PGS), and P/S (all from ScienCell Research Laboratories, Carlsbad, CA, USA). Cells were maintained at 37 °C in a humidified incubator with 5% CO_2.

Human astrocytes (HA; ScienCell Research Laboratories) were grown on flasks coated with 2 μg/cm² PLL in astrocyte medium supplemented with FBS, astrocyte growth supplement (AGS), and P/S (all from ScienCell Research Laboratories, Carlsbad, CA, USA). Cells were maintained at 37 °C in a humidified incubator with 5% CO_2.

Genotoxicity Assessment

DNA strand-break–associated damage in HBEC-5i cells was screened using the Fast Halo Assay (FHA) as described by Sestili et al. The assay quantifies radial diffusion of alkali-solubilized DNA fragments from nucleoids at the single-cell level following alkaline extraction and fluorescent DNA staining [50]. Cells were seeded into 24-well plates at 5×10^4 cells/well and cultured for 24 h (37 °C, 5% CO2). To evaluate the effects of G3Si-PEG6000 and its dendriplex,

cells were exposed to each formulation for 24 h. Cells were collected by trypsinization, resuspended in cold PBS, washed twice, and embedded in a 1% low-melting-point agarose solution (Sigma-Aldrich, Darmstadt, Germany). A small amount of the cell suspension was applied to a glass slide precoated with normal-melting-point agarose (Sigma-Aldrich, Darmstadt, Germany) and covered with a coverslip. After the agarose had solidified on ice, the coverslip was removed, and the slides were incubated for 15 min in 0.3 M NaOH (pH ≥ 13.0) at room temperature. Ethidium bromide was added during the final 5 min to a final concentration of 25 μg/mL, followed by destaining in distilled water for up to 15 min. Slides were immediately examined under a Zeiss Axio Scope A1 fluorescence microscope (Carl Zeiss, Germany) with exposure settings fixed across conditions. Images were analysed using ImageJ software and HaloJ plugin [51]. The results are expressed as the nuclear diffusion factor (NDF), which is the ratio of the total area of the halo plus the nucleus to the area of the nucleus. The experiment was performed at least 4 repetitions.

Cellular Uptake by Confocal Microscopy

HBEC-5i cells were seeded at 1×10^4 cells per well in glass-bottom imaging plates (Ibidi GmbH, Gräfelfing, Germany) and cultured under standard conditions (37 °C, 5% CO_2) for 24 h. Cells were then incubated with the G3Si PEG6000 dendrimer labelled with FITC, the siRNA labelled with Cy5, and their dendriplex complexes for 3 h or 24 h. After incubation, cells were washed with PBS, fixed with 4% formaldehyde (Avantor Performance Materials Poland S.A., Gliwice, Poland), followed by washing with PBS and staining with DAPI (4′,6-diamidino-2-phenylindole) (Thermo Scientific TM, ThermoFischer Scientific, Waltham, MA, USA) at 0.5 μg/mL for 5 min.

Images were acquired on a Leica TCS SP8 confocal microscope (Leica Microsystems, Wetzlar, Germany) equipped with a 63×/1.40 oil objective (HC PL APO CS2, Leica Microsystems, Germany). Fluorescence was acquired using the following channel settings: DAPI (405 nm excitation, 430–470 nm emission), FITC (489 nm excitation, 500–530 nm emission), and Cy5 (650 nm excitation, 660–720 nm emission).

Blood–Brain Barrier Model Integrity by Transendothelial Electrical Resistance (TEER)

A human tri-culture BBB model comprising astrocytes, pericytes, and brain endothelial cells was established on permeable membrane inserts (ThinCert, Greiner Bio-One) with 1.0 μm pores and a membrane growth area of 33.6 mm² in 24-well plates. Inserts were pre-coated with poly-L-lysine (PLL, 10 μg/mL; 50 μL per insert; 3 h), then rinsed twice with sterile water. Astrocytes were seeded first at 2.0×10^4 cells/cm², allowed to attach for 30 min at room temperature, and subsequently maintained at 37°C and 5% CO_2 for 48 h. Pericytes were then added at 2.0×10^4 cells/cm² and cultured for an additional 48 h. Finally, HBEC-5i endothelial cells were seeded at 8.0×10^4 cells/cm² to complete the tri-culture (Fig. 2). From the time of endothelial seeding onward, cultures were maintained in complete HBEC-5i medium supplemented with amphotericin B (1 μg/mL), with medium exchanges every 48 h in both apical and basolateral compartments. G3Si PEG6000 dendrimer and its dendriplex were added on the 13th day of the experiment, once a stable plateau had formed. Monitoring continued at 24 h intervals, with medium exchanges every 48 h only in the basolateral compartments. TEER was measured using an EVOM3 epithelial volt-ohmmeter (World Precision Instruments, FL, USA) connected to an EndOhm-6G chamber electrode. The measurement principle is based on a four-electrode configuration in which a known constant current is driven through the sample on one electrode

pair and the voltage drop is sensed on the other pair, after which resistance is computed from Ohm's law. For each experiment, blank resistance (R_{BLANK}) was measured using coated inserts containing medium but no cells, capturing background contributions. The total resistance across cell-seeded inserts (R_{TOTAL}) comprises the cell-layer component together with these background terms, and the cell-specific resistance (R_{TISSUE}) was obtained by subtraction:

$$R_{TISSUE} = R_{TOTAL} - R_{BLANK}$$

TEER was then area-normalized and reported as $TEER_{REPORTED}$ in Ω·cm² using the equation:

$$TEER_{REPORTED} = R_{TISSUE} - M_{AREA}$$

where M_{AREA} is the membrane growth area in cm². Accordingly, $TEER_{REPORTED}$ represents the area-averaged, blank-corrected electrical resistance across the cell layer on the insert and is inversely related to net ionic conductance across the cell barrier. The experiment was performed in 3 repetitions.

Blood–Brain Barrier Paracellular Permeability

The BBB tri-culture model was established as described above. Paracellular macromolecular permeability was assessed by quantifying the translocation of 40 kDa FITC dextran across the barrier using a Transwell flux assay. G3Si PEG6000 dendrimer and its dendriplex were added on day 13 to the apical compartment, after formation of a stable TEER plateau.

Once a stable TEER plateau had formed, G3Si PEG6000 dendrimer and its dendriplex were added on day 13 to the apical compartment (Fig. 2). Permeability measurements were performed 3 days and 5 days after compound addition. 40 kDa FITC–dextran (Invitrogen, MA, USA) was added to the upper compartment to a final concentration of 400 μg/mL. Receiver-well

fluorescence was read directly in the black 24-well plate without sampling at t = 0 and 15, 30, 45, 60, 90, and 120 min using a BioTek microplate reader (BioTek Instruments Inc., VT, USA) with excitation at 485 nm and emission at 530 nm. Permeability was expressed as a percentage of the untreated control at each time point according to:

$$\%Permeability = (\frac{F_s}{F_c}) \times 100\%$$

Where F_s is the fluorescence of cells treated with dendrimer or dendriplex, and F_c is the fluorescence of control cells (untreated). The experiment was performed in 3 repetitions.

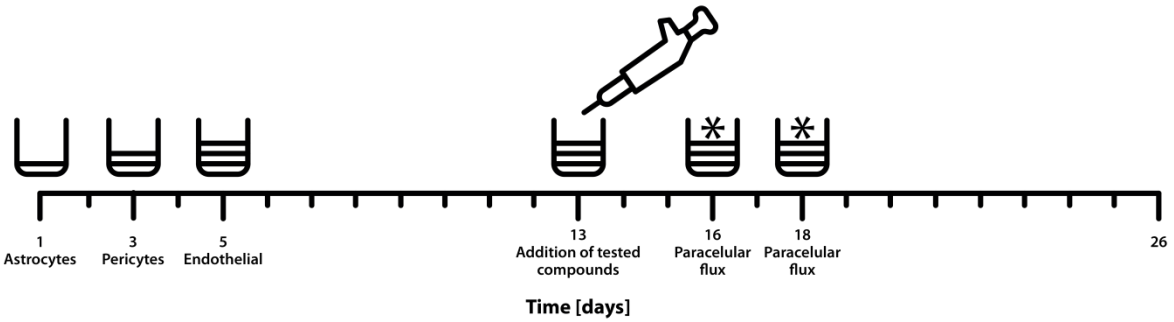


Figure 2. Schematic overview of the experimental schedule for the BBB model. Astrocytes were seeded on day 1, followed by pericytes on day 3 and brain microvascular endothelial cells on day 5. The BBB model was allowed to mature until day 13, when the G3Si PEG6000 dendrimer or its siRNA dendriplex was added. Permeability of 40 kDa FITC-dextran through the BBB model was measured on days 16th and 18th.

Animals

All procedures complied with the bioethical principles adopted by the European Convention for the Protection of Vertebrate Animals Used for Experimental and Other Scientific Purposes (Strasbourg, 1986), Order of the Ministry of Health of the Russian Federation of 23 August 2010 "Establishment of the Rules of Laboratory Practice" No. 708n. The ethical permit Nr. 142 /2023 for the described experiments was obtained from the Latvian Food and Veterinary Service Ethics Commission. Female C57BL/6 mice (8–10 weeks; Charles River, Germany) and APOE4 knock-in (APOE4 KI) mice (B6(SJL)-*Apoe*$^{tm1.1(APOE*4)Adiuj}$/J; 8–10 weeks; The Jackson Laboratory) were group-housed (5–8 per cage) in environmentally-enriched cages at 22 °C on a 12 h light/12 h dark cycle with ad libitum access to food and water. Animals were regularly monitored for food and water intake, weight gain, skin and fur changes, and microscopic alterations at the injection site. All animals were acclimatized for 1 week before the experiments began. For invasive procedures, mice were anesthetized with isoflurane in oxygen (induction 4%, maintenance 2.3%) delivered via facial masks or by ether inhaled from the gauze-soaked nose cones, with peri-procedural monitoring; analgesia was provided as indicated by the procedure-specific welfare assessment. Mice were humanely euthanized by cervical dislocation following deep anesthesia. Procedures were performed by trained personnel.

Spatial Learning and Memory in Alzheimer's Disease Murine Model

Spatial learning and reference memory were assessed at the experimental endpoint using the Morris Water Maze (MWM). Female APOE4 KI mice and C57BL/6 mice were assigned to the following experimental groups (n = 12 per group): 1) APOE4 KI mice treated with G3Si-PEG6000 dendriplex, 2) APOE4 KI mice treated with naked anti-APOE4 siRNA, 3) APOE4 KI mice treated with PBS, and 4) C57BL/6 mice treated with PBS. Beginning at 8 weeks of age,

mice received once-weekly injections for 63 days (nine total injections) according to group allocation, after which behavioral testing was performed. The MWM consisted of a circular pool (diameter 150 cm, height 60 cm) filled with water maintained at approximately 25 °C and rendered opaque to conceal the escape platform. A submerged 10 × 10 cm platform was positioned ~2 cm below the water surface in a fixed target quadrant. Stationary geometric cues were placed along the maze's cardinal axes and remained constant throughout the experiment. Animal trajectories were recorded using an overhead camera connected to EthoVision XT 11 software (Noldus, The Netherlands). Spatial learning tests were performed over three consecutive days with two daily sessions separated by 4 h. For each trial, the mouse was released from a pseudorandom start position in a quadrant that did not contain the platform. If a mouse failed to locate the platform within 60 s, the trial ended, and the mouse was guided to the platform and allowed to stay on it for 15 s. Escape latency, the time elapsed since the mouse was submerged in the water until it found and climbed onto a hidden platform, was quantified. A probe trial was performed 24 h after the final spatial learning test with the platform removed. Probe trial performance was quantified as time spent in the target quadrant and the number of crossings across the former platform zone.

Statistical analyses

Statistical analyses and data visualization were performed using Prism version 10.4.2 (GraphPad Software, Boston, MA, USA). The Shapiro–Wilk test was used to assess the normality of data distributions. For factorial designs, multiple-way ANOVA was applied to assess differences in group means. Where ANOVA indicated statistically significant main effects, appropriate post hoc multiple comparison tests were selected based on the structure of the comparisons: Tukey’s

test was used for evaluating all pairwise group differences, Dunnett's test for comparisons of multiple treatments against a single control group, and Šidák's test for a limited set of planned comparisons. For non-normally distributed data or ordinal outcomes, pairwise differences were assessed using the nonparametric Mann–Whitney test, with effect sizes reported as rank-biserial correlation (r_{rb}). All tests were two-tailed and performed at a significance level $\alpha = 0.05$. In our graphical representations, significance is denoted by asterisks: one asterisk (*) indicates a p-value < 0.05, two asterisks (**) represent a p-value < 0.01, and three asterisks (***) denote a p-value < 0.001.

RESULTS AND DISCUSSION

RNA interference (RNAi) emerged from transgene-induced co-suppression in plants and post-transcriptional gene silencing in fungi into a unified mechanism, culminating in the discovery that double-stranded RNA elicits potent, sequence-specific silencing in *Caenorhabditis elegans* and later in *Drosophila* and mammalian systems through small interfering RNAs [52–57]. Recognition of this mechanism by the 2006 Nobel Prize marked a turning point, and subsequent efforts accelerated the translation of RNAi into therapeutics. This is now reflected in the first wave of FDA-approved siRNA therapeutics, which demonstrate that RNAi is clinically feasible. To date, six siRNA therapeutics have been approved by the FDA, namely patisiran (Onpattro), givosiran (Givlaari), lumasiran (Oxlumo), inclisiran (Leqvio), vutrisiran (Amvuttra), and nedosiran (Rivfloza). These agents must overcome multiple extracellular and intracellular barriers and therefore rely on chemical modification and/or specialized delivery systems to achieve efficient delivery. Patisiran is the first up-to-date FDA-approved only nanocarrier

formulation to enable siRNA delivery, whereas subsequent approvals primarily use covalent triantennary N-acetylgalactosamine (GalNAc) conjugation to exploit efficient hepatocyte uptake after subcutaneous dosing [58,59]. A defining feature of this portfolio is that the clinical success has so far been built around a relatively narrow, hepatocyte-optimized set of delivery solutions. At the same time, the broader RNAi therapeutic landscape has expanded substantially, with 139 (14 active, not recruiting) siRNA-related projects listed on ClinicalTrials.gov as of February 2026, reflecting a diverse and growing pipeline beyond currently approved drugs. Against this backdrop, the present article integrates evidence from single-cell-based assays, through multicellular *in vitro* models, to *in vivo* animal studies, progressively evaluating the therapeutic potential of the G3Si PEG6000 nanosystem for safe and effective delivery of siRNA in the context of CNS disease.

Cellular Uptake by Confocal Microscopy

Efficient intracellular delivery is a prerequisite for RNAi-mediated gene silencing, making the cellular uptake of the G3Si PEG6000 dendrimer-siRNA nanosystem a critical determinant of its functional relevance. We therefore used confocal microscopy in human brain endothelial cells, labeling the dendrimer with FITC and the siRNA with Cy5, and additionally counterstaining nuclei with DAPI to distinguish cytoplasmic from nuclear accumulation of the internalized carrier and cargo. This approach allows independent quantification of carrier and cargo signals and provides a direct assessment of how complexation influences the effective cellular delivery of siRNA.

In the uptake experiments, we used 2.5 μM FITC–G3Si PEG6000, 1 μM Cy5–siRNA, and the corresponding dendriplex because this carrier concentration provides a biologically

relevant near-threshold exposure that enables robust fluorescence detection while minimizing confounding effects from overt cytotoxicity. As expected for carrier-free delivery, Cy5–siRNA alone produced near-background red fluorescence at 3 h (0.19 ± 0.17) and low, highly variable redout by 24 h (0.78 ± 1.69) (Fig. 3). In contrast, FITC–G3Si PEG6000 alone showed strong, time-dependent green fluorescence (4.46 ± 1.41 at 3 h; 8.81 ± 2.11 at 24 h), indicative of efficient carrier uptake. Complexation of Cy5–siRNA with FITC–G3Si PEG6000 significantly increased red signal relative to free siRNA already at 3 h (dendriplex: red 4.71 ± 2.40; green 4.75 ± 3.01), with a further ~1.6-fold rise in siRNA-associated red fluorescence at 24 h (7.43 ± 3.34) and a more moderate ~1.3-fold increase in dendrimer-associated green fluorescence (6.10 ± 2.30). Together, these trends support robust time-dependent cellular uptake of the dendriplex and demonstrate that association with G3Si PEG6000 substantially enhances the effective cellular delivery of Cy5–siRNA compared with the free oligonucleotide. Confocal uptake imaging further showed that, although the bulk of the non-complexed dendrimer signal remained extranuclear, a small fraction of puncta was detectable within the nuclear compartment, whereas in the dendriplex condition, both Cy5–siRNA and dendrimer fluorescence were restricted to the cytoplasm, consistent with targeting the subcellular domain in which RNAi is executed (Fig. 4).

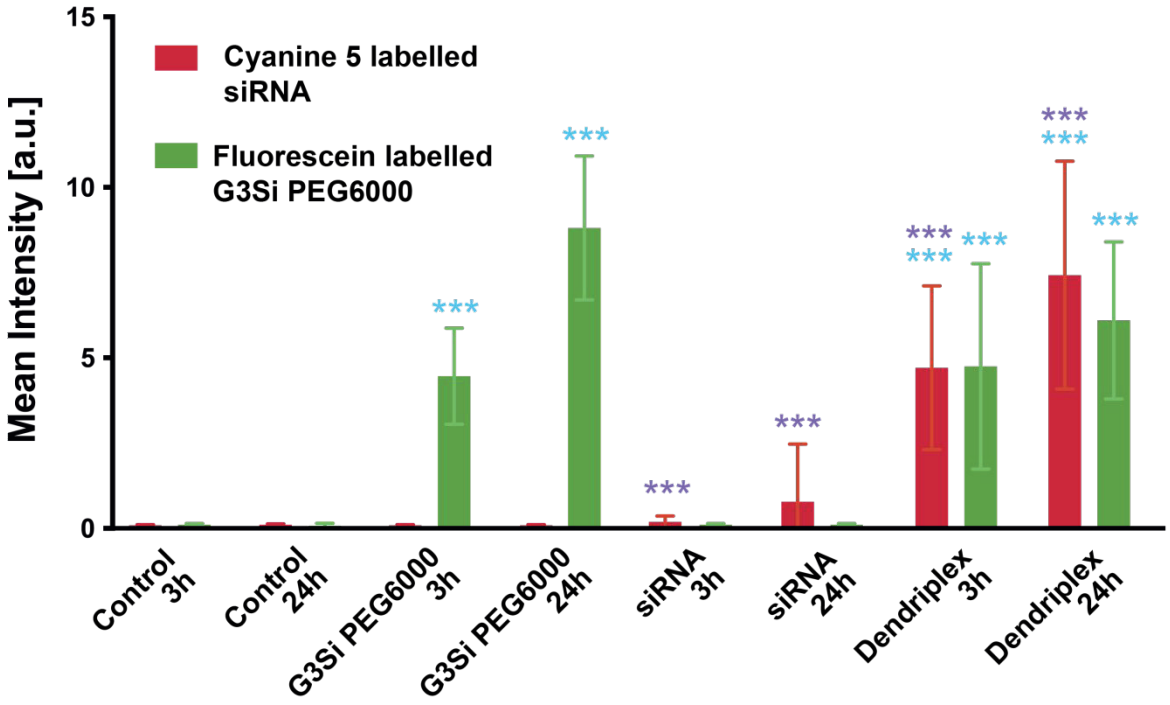


Figure 3. Cellular internalization of 2.5 μM FITC–G3Si PEG6000 dendrimer and 1 μM Cy5–siRNA at 3 h and 24 h incubation times. Uptake was quantified as per-cell mean fluorescence intensity (MFI) in the FITC and Cy5 channels. A blue asterisk marks significant differences relative to the control, and a violet asterisk indicates significant differences between the dendrimer and its complex at the corresponding concentration (***$p<0.001$). Data are presented as the mean and standard deviation for 5 repetitions.

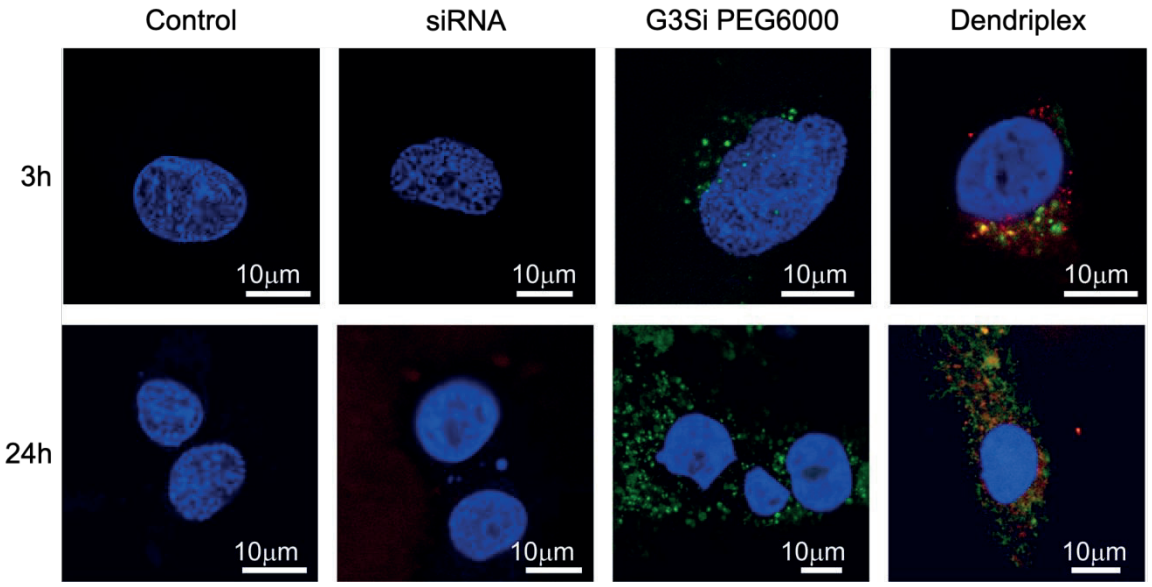


Figure 4. Cellular uptake and subcellular distribution of FITC-G3Si PEG6000 (green) and Cy5–siRNA (red) and their dendriplex in HBEC-5i cells. Representative confocal micrographs of HBEC-5i cells incubated with FITC–G3Si PEG6000 (2.5 μM), Cy5–siRNA (1 μM), or the corresponding dendriplex for 3 h or 24 h. Nuclei were counterstained with DAPI (blue). Images were acquired on a confocal microscope using a 63×/1.40 and identical acquisition settings across conditions. Scale bar, 10 μm.

Genotoxicity Assessment

DNA damage was screened using the Fast Halo Assay, a rapid single-cell nucleoid diffusion method in which DNA radial dispersion and relaxation arising from strand discontinuities, where alkali-labile sites diffuse radially under alkaline conditions and are quantified by image analysis, here reported as the Nuclear Diffusion Factor (NDF). Relative to the negative control (1.16 ± 0.41), cell exposure to the non-complexed dendrimer produced a pronounced, dose-dependent increase in NDF, reaching 3.2 ± 0.21 at 0.5 μM, 6.91 ± 1.74 at 2.5 μM, and 16.85 ± 0.20 at 10 μM (Fig. 5). FHA can capture DNA fragmentation arising from apoptosis or other forms of cell

death in addition to genotoxic lesions. This consideration is particularly pertinent at concentrations 2.5 μM and above, which approximates the previously reported IC20 (2.34 μM) for this nanocarrier in the endothelial cell line [47]. At near-subcytotoxic exposures, even a small fraction of dying cells can disproportionately inflate mean strand-break readouts. Accordingly, we interpret the DNA-damage data in conjunction with cytotoxicity metrics using commonly applied ~25% cytotoxicity as a pragmatic upper-bound threshold to reduce the risk of false-positive DNA-damage classification [60]. Notably, a clear FHA signal emerges at 0.5 μM, well below the previously reported IC20 (2.34 μM) for the G3Si PEG6000 nanocarrier, indicating that the response cannot be attributed solely to widespread overt cytotoxicity.

Confocal uptake imaging in the present work revealed that while most non-complexed dendrimer signal localized outside the nucleus, a small number of entities were detectable within the nuclear compartment, indicating that direct primary interactions with genetic material are at least plausible for a minority fraction (Fig. 4). Sporadic nuclear localization of cationic dendrimers has been reported previously in confocal studies, supporting plausibility of a nanoparticle induced genotoxicity [61,62]. Given that nanomaterials can induce genotoxicity through direct and/or indirect mechanisms, the rare intranuclear dendrimer signal is best treated as a supportive context rather than a mechanistic discriminator [63,64]. siRNA complexation markedly mitigated the DNA damage signal, as dendriplex-treated cells remained below 3 NDF and did not reach statistical significance, supporting the conclusion that complexation reduces the cationic carrier fraction and attenuates the pathways that culminate in strand-break readouts.

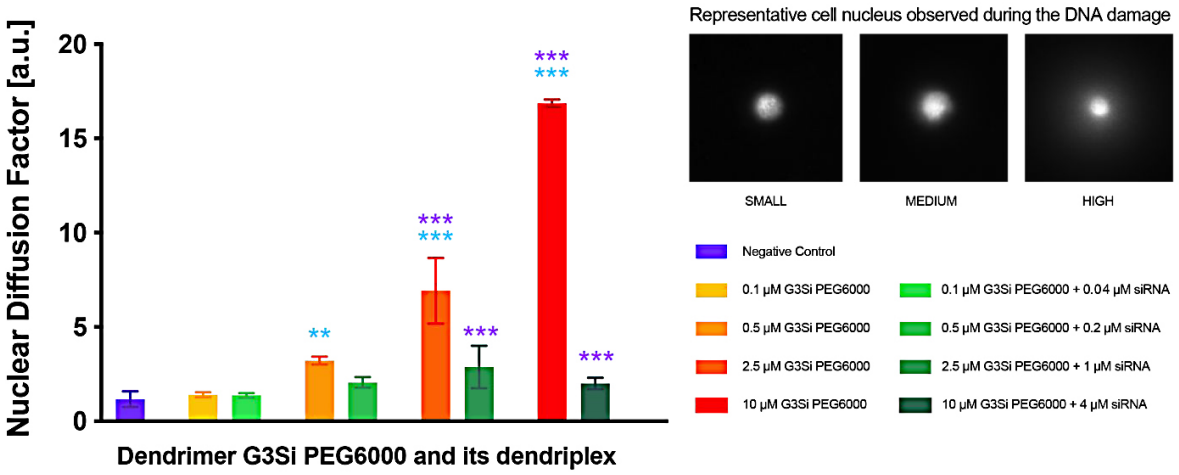


Figure 5. DNA strand-break–associated damage screening by Fast Halo Assay after 24 h exposure to G3Si PEG6000 dendrimer or dendriplex. Photographs of a representative cell nucleus observed during the DNA damage test. Representative ethidium bromide-stained increasing halo area reflects greater alkali-induced DNA relaxation consistent with increased strand-break–associated damage. A blue asterisk marks significant differences relative to the control, and a violet asterisk indicates significant differences between the dendrimer and its complex at the corresponding concentration (**$p<0.01$; ***$p<0.001$). Data are presented as the mean and standard deviation for at least 4 repetitions. Images were acquired at 400× total magnification.

Blood–Brain Barrier Model Integrity by Transendothelial Electrical Resistance (TEER)

To extend single-cell screening to barrier-relevant evaluations, we employed a multicellular BBB model that captures essential neurovascular unit (NVU) interactions in which barrier properties emerge. BBB properties vary across the vascular tree due to anatomical and molecular zonation, with practical implications for how nanocarrier exposure translates into changes in barrier integrity and permeability. Cerebral capillaries account for approximately 85%

of the total cerebral blood vessels' length and provide the dominant endothelial exchange surface of about 12 m² in the adult human brain, indicating that most blood-to-brain interfaces encountered by circulating therapeutics are capillary interfaces [65]. On this basis, we employed a direct-contact, tri-culture with capillary-weighted cellular composition, reproducing an endothelial-dominant barrier layer on the apical face of the well supported by high pericyte representation and robust astrocytic ensheathment (Fig. 6). This arrangement mirrors key structural features of the *in vivo* capillary wall and preserves reciprocal BBB signaling, providing sensitive detection of compound-induced changes in barrier integrity [66].

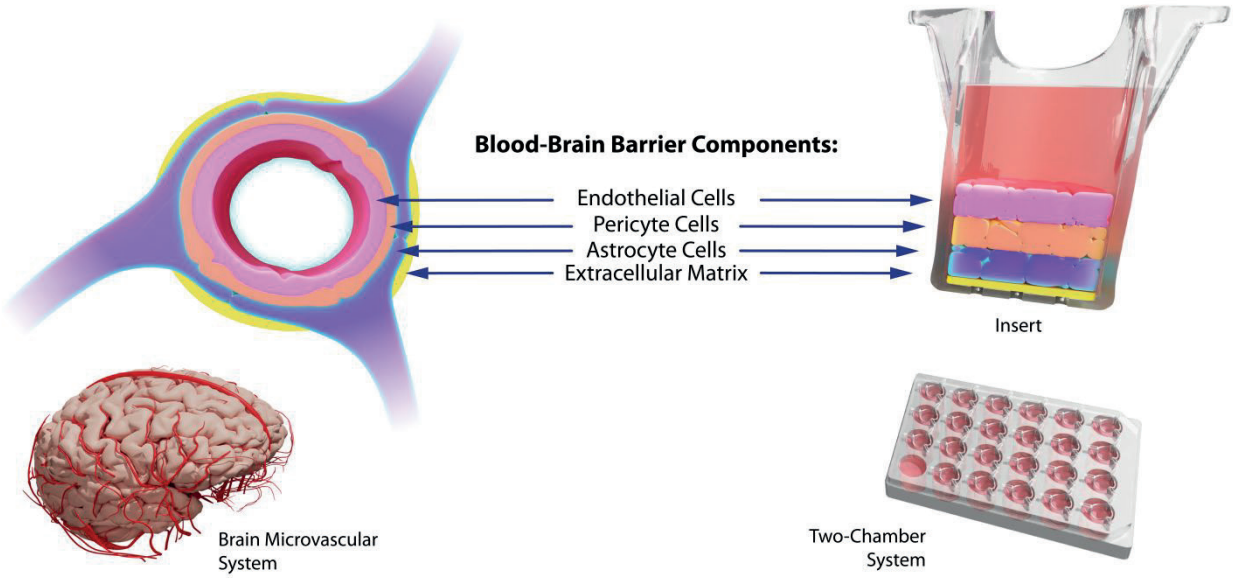


Figure 6. Illustration depicts a schematic cross section of the Blood–Brain Barrier (BBB) on the left and the corresponding *in vitro* barrier model established in the insert of the two-chamber system on the right.

The effects of the G3SiPEG 6000 dendrimer and its dendriplex on the BBB model integrity were quantified by monitoring transendothelial electrical resistance (TEER). TEER is a

widely used, label-free, noninvasive electrophysiological readout and serves as a quantitative proxy for barrier integrity *in vitro.* The approach is grounded in early in vivo microelectrode studies of brain surface microvessels by Crone and colleagues, and TEER has since become a routine quality-control attribute for BBB models [67]. The measurement is obtained by applying a low alternating current (AC) conducted by small inorganic ions in the culture media between the electrodes placed in the apical and basolateral compartments. The measured resistance reflects the overall ionic resistance across the cellular barrier. Compounds were added only after the readout plateau on day 13 was reached to avoid confounding maturation with treatment effects. The not-complexed G3Si PEG6000 dendrimer elicited a concentration-dependent, non-monotonic TEER response (Fig. 7). 24 h after the addition of the compounds, the highest concentration of the non-complexed dendrimer elicited a modest, transient TEER decline (90.25% ± 6.71 of control), followed by recovery on the subsequent measurement (111.79% ± 13.02) and a progressive overshoot above baseline that peaked at day 5 (136.85% ± 26.14) and remained elevated through day 12 (124.56% ± 21.60). By contrast, at an equivalent concentration, the dendriplex did not induce an early decrease (101.45% ± 22.12 at 24 h) and produced progressive (143.32% ± 16.24 at day 5) and statistically significant sustained elevation in TEER in the later stages of the experiment (149.00% ± 9.62 at day 12) (Fig. 8). Notably, none of the tested formulations produced a prolonged TEER decline.

The early divergence between formulations is plausibly attributable to reduced bioavailable cationic surface activity upon siRNA complexation, which decreases the free dendrimer fraction that can drive acute membrane perturbation and stress responses. The sustained elevation in TEER observed at later time points likely reflects adaptive, mesoscopic remodeling of the tri-culture BBB, including enhanced intercellular adhesion, junctional

organization, in-cell-substrate adhesion, and proliferation that improve coverage of the insert surface and reduce microheterogeneity, which can increase the net resistive path sensed by TEER [68,69]. Reinforcement of BBB integrity is particularly relevant in the conditions such as the AD, where barrier disruption contributes to neuroinflammation and accelerates neurodegenerative processes [70–72]. By maintaining or enhancing barrier integrity, the dendrimer-based formulations indicate a favorable profile for preserving the barrier function.

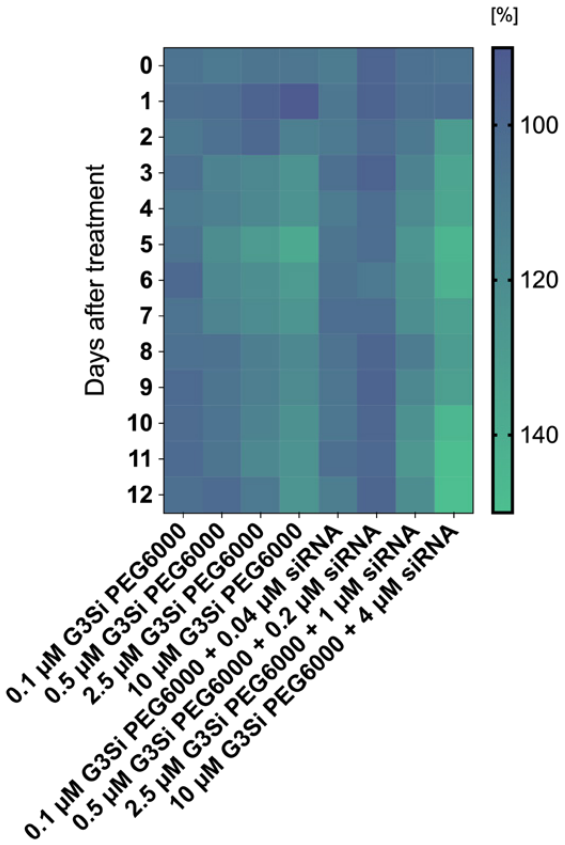


Figure 7. TEER dynamics of the Blood–Brain Barrier (BBB) model following exposure to G3Si PEG6000 dendrimer and its dendriplex. Data are expressed as a percentage of the untreated control from 3 repetitions. The $TEER_{REPORTED}$ data at days 3, 5, 10, and 12 post-treatment are summarized in Fig. 8.

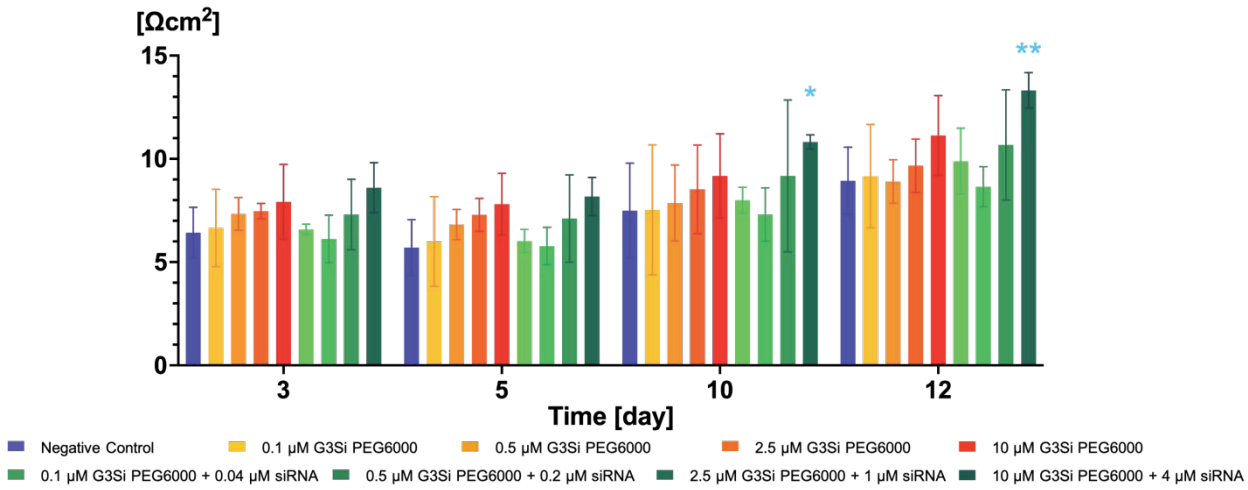


Figure 8. Changes of $TEER_{REPORTED}$ [$\Omega \cdot cm^2$] of the Blood–Brain Barrier (BBB) model following exposure to G3Si PEG6000 dendrimer and its dendriplex. A blue asterisk marks significant differences relative to the control (*$p<0.05$; **$p<0.01$). Data are presented as the mean and standard deviation for 3 repetitions. A heatmap summarizing all post-treatment days is shown in Fig. 7.

Blood–Brain Barrier Paracellular Permeability

The effects of the G3Si PEG6000 dendrimer and its dendriplex on BBB-model paracellular transport were quantified using a 40 kDa FITC–dextran flux assay. Fluorescent dextran tracers of defined nominal molecular weight are widely used in Transwell barrier models to quantify macromolecular paracellular permeability, and they are commonly paired with TEER because tracer flux and electrical resistance provide complementary readouts of barrier performance [73,74]. Interpretation of these orthogonal permeability methods requires emphasizing that TEER and dextran flux, also termed the macromolecular tracer assay, provide complementary but non-interchangeable measures of barrier performance. TEER reports area-averaged translayer electrical resistance and primarily reflects net ionic conductance across the barrier. In contrast,

FITC–dextran permeability reports macromolecular passage and can be disproportionately influenced by spatially restricted routes that can contribute relatively little to global ionic conductance.

At day 3 after exposure, the paracellular flux data revealed an early divergence from TEER, indicating a decoupling between these orthogonal measures of barrier function. Specifically, the highest tested concentration of the not-complexed dendrimer increased macromolecular permeability to 175.51% ± 28.90 of control, while the matched dendriplex concentration increased permeability to 163.71% ± 32.40 of control (Fig. 9). In the corresponding conditions, TEER was not significantly reduced, despite the increased macromolecular flux. We hypothesize that the observed decoupling reflects a non-uniform perturbation of paracellular organization, with a transient increase in a macromolecule-permissive leak pathway occurring in the absence of a commensurate change in the pathway that predominantly determines ionic resistance. This pattern is consistent with permeability being governed by spatially restricted or short-lived high-permeability routes that can disproportionately increase 40 kDa FITC–dextran flux while contributing minimally to the area-averaged TEER signal. Plausible microstructural contributors include transient bicellular discontinuities and tricellular junction-associated transport [75,76]. Mechanistic interpretation remains tentative and should be evaluated by imaging-based quantification of junction continuity together with analysis of tight-junction marker localization and organization.

By day 5, dextran permeability in the highest tested concentration of the non-complexed dendrimer returned to near-baseline levels at 97.03% ± 27.87 of control, whereas the highest concentration of dendriplex reduced dextran flux to 61.00% ± 4.37 of control, coinciding with

the TEER overshoot observed at later time points. The concurrent TEER overshoot and reduction in 40 kDa FITC–dextran flux is consistent with a delayed barrier tightening response. A plausible hypothesis is that dendriplex exposure promotes the reinforcement and reorganization of intercellular junctions and endothelial adhesion, which can decrease the effective paracellular leak of macromolecules and thereby suppresses dextran passage. This interpretation aligns with findings from BBB microfluidic models, in which the tested nanoparticle led to concurrent increases in TEER and enhanced expression of junctional markers ZO-1 and VE-cadherin, signifying a reinforcement of tight junctions and a subsequent reduction in barrier permeability [68].

At lower concentrations, short-term exposure to sub-cytotoxic levels of the not-complexed dendrimer preserved macromolecular permeability, whereas prolonged exposure produced a concentration-dependent increase in dextran flux. On day 5, the 2.5 μM concentration elevated dextran flux to 164.70% ± 25.60 of control, and the 0.5 μM concentration elevated dextran flux to 144.25% ± 31.51 of control. These time-dependent and concentration-dependent changes are consistent with a delayed adverse effect of the not-complexed dendrimer on paracellular macromolecular transport under prolonged exposure. In contrast, the corresponding dendriplex formulations did not increase dextran permeability and maintained macromolecular permeability at or near control levels.

Accounting for key *in vivo* determinants of BBB function that are not fully recapitulated in static transwell systems, the *in vitro* profile suggests that subtoxic dendriplex concentrations do not increase macromolecular leak or impair ion pathway function, thus suggesting they are unlikely to compromise BBB integrity *in vivo*. This prediction is particularly relevant in AD,

where BBB dysfunction can be regionally heterogeneous and influenced by local vascular pathology rather than reflecting a uniform, global loss of barrier function [77,78].

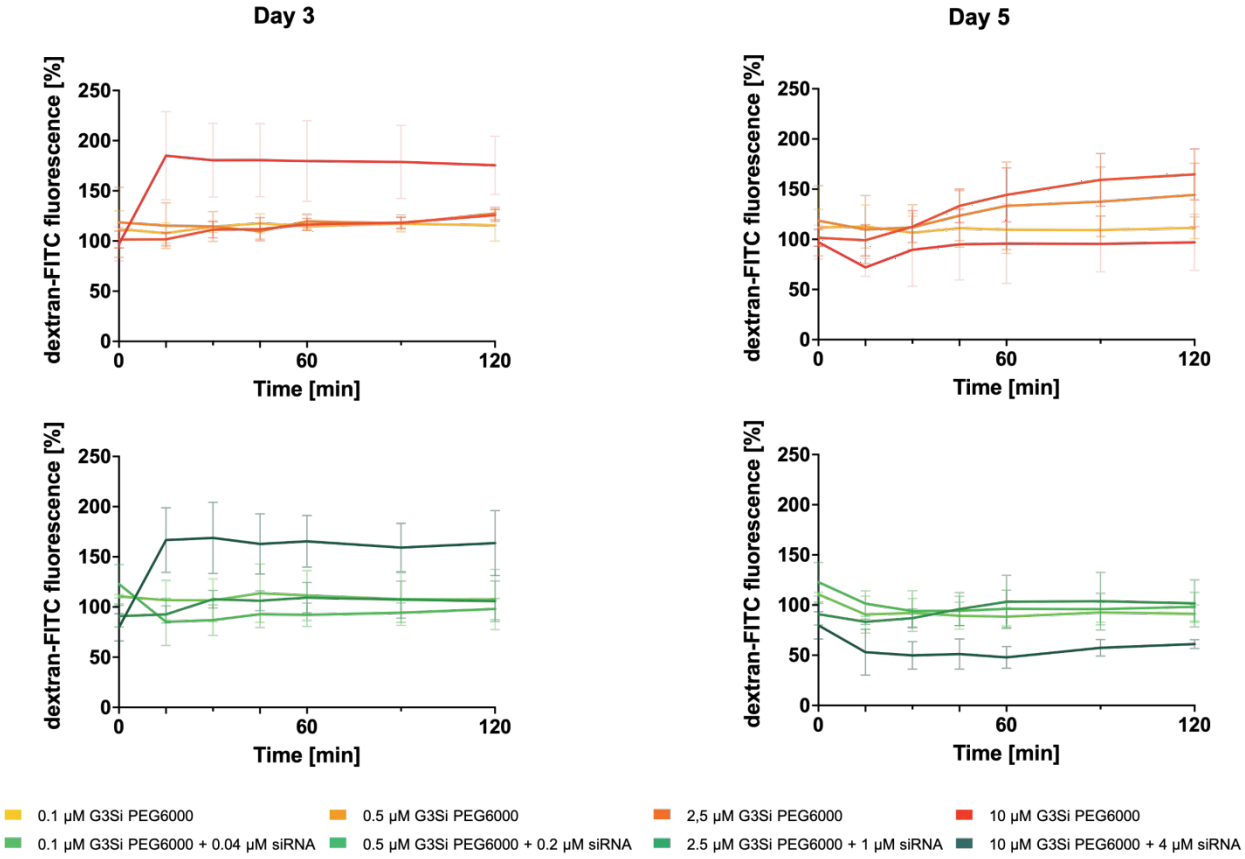


Figure 9. Accumulation of 40 kDa FITC-dextran in the basolateral compartment of the Blood–Brain Barrier (BBB) Transwell model measured 3 and 5 days after exposure to G3Si PEG6000 dendrimer or its dendriplex. Fluorescence intensity in the basolateral compartment was recorded at 0, 15, 30, 45, 60, 90, and 120 min after addition of FITC-dextran. Data are expressed as a percentage of untreated control at each time point for 3 repetitions.

Spatial Learning and Memory in Alzheimer's Disease Murine Model

Applied *in vitro* assays are indispensable for mechanism and screening, however their predictive value for CNS delivery and safety ultimately depends on how well key *in vivo* modifiers are represented. We therefore interpreted the subsequent *in vivo* study as an essential translational step positioned to test whether the formulation-dependent patterns observed *in vitro* translate into disease relevant performance in a whole organism setting.

Cognitive performance was assessed using the Morris Water Maze, a well-established test of spatial learning and reference memory in which rodents learn across repeated trials to locate a submerged escape platform in a circular pool by using stable distal cues in the testing room. Reference memory is assessed in a probe trial, during which the platform is removed, and search behavior is quantified by the animal's preference for the former platform location. Probe-trial outcomes were summarized as time spent in the target quadrant and the number of crossings through the former platform zone, which provide complementary readouts of spatial bias and the precision of searching around the learned goal location (Fig. 10).

There were no significant changes in escape latencies between any of the tested groups (data not shown). In both probe-trial endpoints, APOE4 knock-in (KI) mice receiving PBS performed worse than C57BL/6 PBS controls, supporting the suitability of the experimental conditions for detecting APOE4-associated cognitive vulnerability relative to the healthy counterparts [79]. In the APOE4 KI cohort, treatment with the G3Si PEG6000 dendriplex resulted in a significant increase in platform-zone crossings compared with the APOE4 PBS group. In contrast, only a trend towards increased time spent in the target quadrant was observed in the APOE4 KI group, and the accompanying rank-based effect size ($r_{rb} \approx 0.22$) indicated only a modest shift with substantial overlap between group distributions, consistent with a partial or

heterogeneous behavioral benefit rather than a robust normalization of sustained spatial bias. This dissociation is plausible because crossings reflect how precisely the animal searches the small spatial region, whereas quadrant time is a broader measure that can be diluted by mixed search strategies variability between animals, including non-cognitive contributors that are well recognized in water maze probe analyses [80,81]. This pattern is consistent with published reports on APOE4 knock-in mice, in which Morris water maze deficits are generally modest and endpoint-dependent rather than uniformly detected across all measures [79]. This pattern is consistent with the broader literature indicating that APOE4-associated cognitive dysfunction emerges early but remains relatively subtle and endpoint-dependent in young APOE4 targeted-replacement mice, whereas more robust and reproducible probe-trial deficits become apparent in middle-aged animals [82–84].

Collectively, the dendriplex profile is most consistent with a partial improvement in spatial search precision in APOE4 KI mice, which supports the premise that formulation-mediated delivery can translate into measurable functional benefit. By contrast, APOE4 KI mice receiving naked siRNA showed no improvement across probe endpoints, consistent with well-established *in vivo* limitations of unformulated siRNA, including rapid nuclease degradation and rapid systemic clearance, which together reduce tissue exposure and cellular internalization.

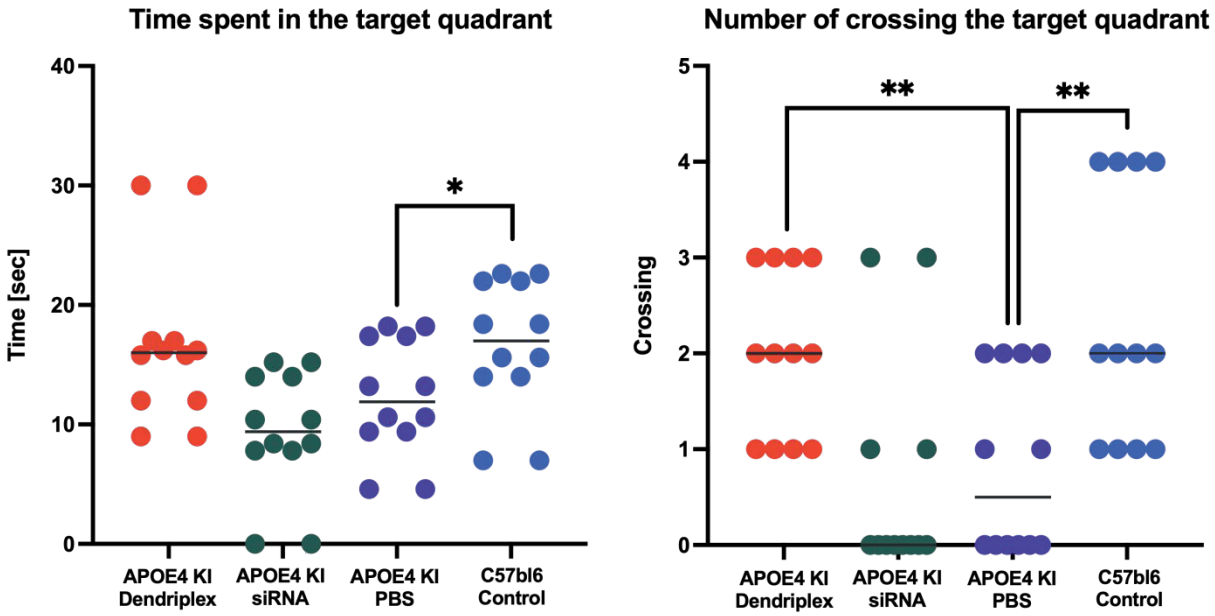


Figure 10. Spatial memory performance of APOE4 KI and C57bl6 in the Morris water maze probe trial. Left panel: cumulative amount of time animals swam in the target quadrant; Right panel: total amount of platform zone crossings. An asterisk marks significant differences relative to the APOE KI control (*$p<0.05$; **$p<0.01$). Data shown as individual values and group median (horizontal lines).

SUMMARY AND CONCLUSIONS

Clinical progress in Alzheimer's disease has advanced without a widely transferable approach that reliably delivers predictable, compartment-appropriate CNS exposure under BBB constraints, reflecting both momentum and persistent limitations in neurological disease interventions. The sustained entry of biologics into CNS trials suggests that clinical feasibility is often achieved by accepting constrained exposure or relying on routes that are practical only in specific contexts, rather than indicating that the broader delivery challenge has been resolved. As

mechanistic insight increasingly incorporates neurovascular biology and disease-associated BBB remodeling, greater emphasis is being placed on BBB architecture, transport-route constraints, and safety–performance tradeoffs at the BBB interface as design inputs, alongside evaluating performance with functionally meaningful endpoints. In this study, we used a stepwise progression of models to link cellular responses, barrier integrity metrics, and *in vivo* outcomes to assess an RNAi nanosystem within this broader translational framework.

At the cellular level, the dendrimer served as an efficient delivery vehicle, significantly enhancing intracellular siRNA accumulation compared to free oligonucleotides. While the non-complexed carrier signal was mainly extranuclear with rare puncta overlapping the nuclear compartment, the dendriplex showed both carrier and siRNA fluorescence, only restricted to the cytoplasm, consistent with delivery into the mechanistically relevant domain for RNAi. DNA damage screening by Fast Halo Assay showed a pronounced, dose-dependent increase in NDF following exposure to the non-complexed dendrimer. Because FHA can also capture DNA fragmentation associated with apoptosis or cytotoxicity-related DNA relaxation, interpretation at concentrations near or above cytotoxicity thresholds requires caution; however, the presence of a clear FHA signal already at 0.5 μM non-complexed dendrimer suggests that the response cannot be explained solely by widespread overt cell death. Importantly, siRNA complexation attenuated the FHA signal, with dendriplex-treated cells remaining below ~3 NDF and not reaching statistical significance. This pattern is consistent with the fact that complexation reduces the bioavailable cationic fraction and thereby limits damage pathways that culminate in strand-break readouts. Rare intranuclear carrier signal observed by confocal microscopy provides plausibility for direct nuclear interaction in a minority fraction.

In a capillary-weighted, direct-contact BBB tri-culture model, neither formulation caused a sustained decline in TEER. The non-complexed dendrimer produced a non-monotonic TEER trajectory at the highest dose, with an early transient decrease at 24 hours, followed by recovery and overshoot. In contrast, the dendriplex avoided the early TEER drop and exhibited a progressive, statistically significant, sustained increase in TEER at later time points. Macromolecular flux assays refine interpretation by demonstrating an early decoupling at day 3, where both the highest tested non-complexed dendrimer concentration and the matched dendriplex increased dextran permeability without a significant TEER reduction, indicating a functional decoupling between ionic resistance and macromolecular leak at this early time point. By day 5, the highest tested dendriplex concentration reduced dextran passage to 61.00% ± 4.37 at 10 μM, whereas lower dendriplex concentrations remained at or near control levels. Dextran permeability in the highest tested concentration of the non-complexed dendrimer returned to near-baseline levels, whereas sub-cytotoxic non-complexed dendrimer increased dextran flux (e.g., 164.70% ± 25.60 at 2.5 μM). Collectively, these results are most consistent with a broader functional window for the dendriplex in barrier-relevant conditions and supporting a barrier-tightening trajectory, while also indicating that early, spatially restricted macromolecular perturbations remain plausible and warrant direct junctional imaging and marker quantification.

In vivo, Morris Water Maze probe-trial analysis demonstrated that the APOE4 KI mice cohort treated with dendriplex improved performance, as quantified by platform-zone crossings, whereas time in the target quadrant increased only numerically and did not reach statistical significance. This dissociation is most likely due to platform-zone crossings being more sensitive to precise search focus, while quadrant time can be diluted by heterogeneous strategies and non-cognitive contributors. Definitive mechanistic linkage will require brain exposure measurements

and target engagement assays. Nevertheless, the functional signal observed with dendriplex treatment supports the premise that formulation-dependent delivery properties can translate into measurable behavioral benefit in a disease-relevant setting. Direct brain biodistribution and knockdown evidence are required to connect phenotype to mechanism.

Taken together, the results position the G3Si PEG6000 dendriplex formulation as allowing intracellular siRNA uptake with cytoplasmic distribution, attenuated genotoxicity signals relative to the free carrier, and BBB-model compatibility characterized by preserved or enhanced barrier integrity with a time-dependent tightening signature.

Corresponding Author

*Serafin Zawadzki - Department of General Biophysics, Faculty of Biology and Environmental Protection, University of Lodz, 141/143 Pomorska St., 90-236 Lodz, Poland;
Email: serafin.zawadzki@edu.uni.lodz.pl
**Katarzyna Miłowska - Department of General Biophysics, Faculty of Biology and Environmental Protection, University of Lodz, 141/143 Pomorska St., 90-236 Lodz, Poland;
Email: katarzyna.milowska@biol.uni.lodz.pl

Author Contributions

Serafin Zawadzki: Conceptualization, Methodology, Validation, Formal analysis, Investigation, Writing - Original Draft, Writing - Review & Editing, Visualization; **Elżbieta Okła:** Investigation; **Sylwia Michlewska:** Investigation; **Radosław Bednarek:** Methodology; **Paula Ortega López:** Resources; **F. Javier de la Mata:** Resources; **Juris Jansons:** Methodology, Investigation; **Dace Skrastiņa:** Methodology, Investigation, Project administration; **Madara Kreišmane:** Investigation; **Vladimirs Piļipenko:** Formal analysis; **Baiba Jansone:** Methodology, Project administration; **Maksim Ionov:** Methodology, Writing - Review &

Editing; **Maria Bryszewska:** Conceptualization, Methodology, Resources, Project administration, Funding acquisition; **Katarzyna Miłowska:** Conceptualization, Methodology, Formal analysis, Data Curation, Writing - Review & Editing, Supervision, Project administration.

ACKNOWLEDGMENT

This work was supported by grant 2018/30/Z/NZ1/00911 of the Project "NanoTENDO" financed by the National Science Centre, under the M-ERA.NET 2, which has received funding from the European Union's Horizon 2020 research. This research was also funded by grants from PID2020-112924RB-I00 (MINECO) and CIBER-BBN from ISCIII with assistance from the European Regional Development Fund.

ABBREVIATIONS

AC, alternating current; AD, Alzheimer's disease; AGS, astrocyte growth supplement; AP, amyloid precursor protein; APOE4, apolipoprotein E4; Aβ, amyloid β; BACE1, beta-site APP cleaving enzyme 1; BBB, Blood–Brain Barrier; CNS, central nervous system; ECGS, endothelial cell growth supplement; FBS, fetal bovine serum; FHA, Fast Halo Assay; GalNAc, triantennary N-acetylgalactosamine; IATA, Integrated Approaches to Testing and Assessment; ITS, Integrated Testing Strategies; KI, knock-in; MFI, mean fluorescence intensity; MWM, Morris Water Maze; NDF, nuclear diffusion factor; NFTs, neurofibrillary tangles; NMDA, N-methyl-D-aspartate; NVU, neurovascular unit; P/S, penicillin–streptomycin; PBS, Phosphate buffered saline; PEG, polyethylene glycol; PGS, pericyte growth supplement; PLL, poly-L-lysine; RNAi, RNA interference; TEER, transendothelial electrical resistance

REFERENCES

(1) Takahashi, R. H.; Nagao, T.; Gouras, G. K. Plaque Formation and the Intraneuronal Accumulation of B-amyloid in Alzheimer's Disease. *Pathology International* **2017**, *67* (4), 185–193. https://doi.org/10.1111/pin.12520.
(2) Das, U.; Wang, L.; Ganguly, A.; Saikia, J. M.; Wagner, S. L.; Koo, E. H.; Roy, S. Visualizing APP and BACE-1 Approximation in Neurons Yields Insight into the Amyloidogenic Pathway. *Nat Neurosci* **2016**, *19* (1), 55–64. https://doi.org/10.1038/nn.4188.
(3) Zhang, J.; Zhang, Y.; Wang, J.; Xia, Y.; Zhang, J.; Chen, L. Recent Advances in Alzheimer's Disease: Mechanisms, Clinical Trials and New Drug Development Strategies. *Sig Transduct Target Ther* **2024**, *9* (1), 211. https://doi.org/10.1038/s41392-024-01911-3.
(4) Protas, H. D.; Chen, K.; Langbaum, J. B. S.; Fleisher, A. S.; Alexander, G. E.; Lee, W.; Bandy, D.; De Leon, M. J.; Mosconi, L.; Buckley, S.; Truran-Sacrey, D.; Schuff, N.; Weiner, M. W.; Caselli, R. J.; Reiman, E. M. Posterior Cingulate Glucose Metabolism, Hippocampal Glucose Metabolism, and Hippocampal Volume in Cognitively Normal, Late-Middle-Aged Persons at 3 Levels of Genetic Risk for Alzheimer Disease. *JAMA Neurol* **2013**, *70* (3), 320. https://doi.org/10.1001/2013.jamaneurol.286.
(5) Bailly, M.; Destrieux, C.; Hommet, C.; Mondon, K.; Cottier, J.-P.; Beaufils, E.; Vierron, E.; Vercouillie, J.; Ibazizene, M.; Voisin, T.; Payoux, P.; Barré, L.; Camus, V.; Guilloteau, D.; Ribeiro, M.-J. Precuneus and Cingulate Cortex Atrophy and Hypometabolism in Patients with Alzheimer's Disease and Mild Cognitive Impairment: MRI and^{18} F-FDG PET Quantitative Analysis Using FreeSurfer. *BioMed Research International* **2015**, *2015*, 1–8. https://doi.org/10.1155/2015/583931.
(6) Montagne, A.; Barnes, S. R.; Sweeney, M. D.; Halliday, M. R.; Sagare, A. P.; Zhao, Z.; Toga, A. W.; Jacobs, R. E.; Liu, C. Y.; Amezcua, L.; Harrington, M. G.; Chui, H. C.; Law, M.; Zlokovic, B. V. Blood-Brain Barrier Breakdown in the Aging Human Hippocampus. *Neuron* **2015**, *85* (2), 296–302. https://doi.org/10.1016/j.neuron.2014.12.032.
(7) Niwa, K.; Kazama, K.; Younkin, S. G.; Carlson, G. A.; Iadecola, C. Alterations in Cerebral Blood Flow and Glucose Utilization in Mice Overexpressing the Amyloid Precursor Protein. *Neurobiology of Disease* **2002**, *9* (1), 61–68. https://doi.org/10.1006/nbdi.2001.0460.
(8) Salloway, S.; Gur, T.; Berzin, T.; Zipser, B.; Correia, S.; Hovanesian, V.; Fallon, J.; Kuo-Leblanc, V.; Glass, D.; Hulette, C.; Rosenberg, C.; Vitek, M.; Stopa, E. Effect of APOE Genotype on Microvascular Basement Membrane in Alzheimer's Disease. *Journal of the Neurological Sciences* **2002**, *203–204*, 183–187. https://doi.org/10.1016/S0022-510X(02)00288-5.
(9) Ryu, J. K.; McLarnon, J. G. A Leaky Blood–Brain Barrier, Fibrinogen Infiltration and Microglial Reactivity in Inflamed Alzheimer's Disease Brain. *J Cellular Molecular Medi* **2009**, *13* (9a), 2911–2925. https://doi.org/10.1111/j.1582-4934.2008.00434.x.
(10) Bell, R. D.; Winkler, E. A.; Sagare, A. P.; Singh, I.; LaRue, B.; Deane, R.; Zlokovic, B. V. Pericytes Control Key Neurovascular Functions and Neuronal Phenotype in the Adult Brain and during Brain Aging. *Neuron* **2010**, *68* (3), 409–427. https://doi.org/10.1016/j.neuron.2010.09.043.
(11) Hultman, K.; Strickland, S.; Norris, E. H. The *APOE* E4/E4 Genotype Potentiates Vascular Fibrin(Ogen) Deposition in Amyloid-Laden Vessels in the Brains of Alzheimer's Disease Patients. *J Cereb Blood Flow Metab* **2013**, *33* (8), 1251–1258.

https://doi.org/10.1038/jcbfm.2013.76.
(12) Sengillo, J. D.; Winkler, E. A.; Walker, C. T.; Sullivan, J. S.; Johnson, M.; Zlokovic, B. V. Deficiency in Mural Vascular Cells Coincides with Blood–Brain Barrier Disruption in A Lzheimer's Disease. *Brain Pathology* **2013**, *23* (3), 303–310. https://doi.org/10.1111/bpa.12004.
(13) Zenaro, E.; Pietronigro, E.; Bianca, V. D.; Piacentino, G.; Marongiu, L.; Budui, S.; Turano, E.; Rossi, B.; Angiari, S.; Dusi, S.; Montresor, A.; Carlucci, T.; Nanì, S.; Tosadori, G.; Calciano, L.; Catalucci, D.; Berton, G.; Bonetti, B.; Constantin, G. Neutrophils Promote Alzheimer's Disease–like Pathology and Cognitive Decline via LFA-1 Integrin. *Nat Med* **2015**, *21* (8), 880–886. https://doi.org/10.1038/nm.3913.
(14) Halliday, M. R.; Rege, S. V.; Ma, Q.; Zhao, Z.; Miller, C. A.; Winkler, E. A.; Zlokovic, B. V. Accelerated Pericyte Degeneration and Blood–Brain Barrier Breakdown in Apolipoprotein E4 Carriers with Alzheimer's Disease. *J Cereb Blood Flow Metab* **2016**, *36* (1), 216–227. https://doi.org/10.1038/jcbfm.2015.44.
(15) Zlokovic, B. V. Neurovascular Pathways to Neurodegeneration in Alzheimer's Disease and Other Disorders. *Nat Rev Neurosci* **2011**, *12* (12), 723–738. https://doi.org/10.1038/nrn3114.
(16) Zhu, W. M.; Neuhaus, A.; Beard, D. J.; Sutherland, B. A.; DeLuca, G. C. Neurovascular Coupling Mechanisms in Health and Neurovascular Uncoupling in Alzheimer's Disease. *Brain* **2022**, *145* (7), 2276–2292. https://doi.org/10.1093/brain/awac174.
(17) Birks, J. S.; Harvey, R. J. Donepezil for Dementia Due to Alzheimer's Disease. *Cochrane Database of Systematic Reviews* **2018**, *2018* (6). https://doi.org/10.1002/14651858.CD001190.pub3.
(18) Cui, X.; Guo, Y.; Fang, J.; Shi, C.; Suo, N.; Zhang, R.; Xie, X. Donepezil, a Drug for Alzheimer's Disease, Promotes Oligodendrocyte Generation and Remyelination. *Acta Pharmacol Sin* **2019**, *40* (11), 1386–1393. https://doi.org/10.1038/s41401-018-0206-4.
(19) Feldman, H. H.; Lane, R.; on behalf of the Study 304 Group. Rivastigmine: A Placebo Controlled Trial of Twice Daily and Three Times Daily Regimens in Patients with Alzheimer's Disease. *Journal of Neurology, Neurosurgery & Psychiatry* **2007**, *78* (10), 1056–1063. https://doi.org/10.1136/jnnp.2006.099424.
(20) Rösler, M.; Anand, R.; Cicin-Sain, A.; Gauthier, S.; Agid, Y.; Dal-Bianco, P.; Stähelin, H. B.; Hartman, R. Efficacy and Safety of Rivastigmine in Patients with Alzheimer's Disease: International Randomised Controlled Trial. **1999**, *318*.
(21) Coyle, J.; Kershaw, P. Galantamine, a Cholinesterase Inhibitor That Allosterically Modulates Nicotinic Receptors: Effects on the Course of Alzheimer's Disease. *Biological Psychiatry* **2001**, *49* (3), 289–299. https://doi.org/10.1016/S0006-3223(00)01101-X.
(22) Scott, L. J.; Goa, K. L. Galantamine: A Review of Its Use in Alzheimer??S Disease. *Drugs* **2000**, *60* (5), 1095–1122. https://doi.org/10.2165/00003495-200060050-00008.
(23) Robinson, D. M.; Keating, G. M. Memantine: A Review of Its Use in Alzheimer??S Disease. *Drugs* **2006**, *66* (11), 1515–1534. https://doi.org/10.2165/00003495-200666110-00015.
(24) Reisberg, B.; Schmitt, F.; Möbius, H. J. Memantine in Moderate-to-Severe Alzheimer's Disease. *n engl j med* **2003**.
(25) Dhillon, S. Aducanumab: First Approval. *Drugs* **2021**, *81* (12), 1437–1443. https://doi.org/10.1007/s40265-021-01569-z.
(26) Van Dyck, C. H.; Swanson, C. J.; Aisen, P.; Bateman, R. J.; Chen, C.; Gee, M.; Kanekiyo, M.; Li, D.; Reyderman, L.; Cohen, S.; Froelich, L.; Katayama, S.; Sabbagh, M.; Vellas, B.; Watson, D.; Dhadda, S.; Irizarry, M.; Kramer, L. D.; Iwatsubo, T. Lecanemab in Early Alzheimer's Disease. *N Engl J Med* **2023**, *388* (1), 9–21.

https://doi.org/10.1056/NEJMoa2212948.
(27) Shcherbinin, S.; Evans, C. D.; Lu, M.; Andersen, S. W.; Pontecorvo, M. J.; Willis, B. A.; Gueorguieva, I.; Hauck, P. M.; Brooks, D. A.; Mintun, M. A.; Sims, J. R. Association of Amyloid Reduction After Donanemab Treatment With Tau Pathology and Clinical Outcomes: The TRAILBLAZER-ALZ Randomized Clinical Trial. *JAMA Neurol* **2022**, *79* (10), 1015. https://doi.org/10.1001/jamaneurol.2022.2793.
(28) Sevigny, J.; Chiao, P.; Bussière, T.; Weinreb, P. H.; Williams, L.; Maier, M.; Dunstan, R.; Salloway, S.; Chen, T.; Ling, Y.; O'Gorman, J.; Qian, F.; Arastu, M.; Li, M.; Chollate, S.; Brennan, M. S.; Quintero-Monzon, O.; Scannevin, R. H.; Arnold, H. M.; Engber, T.; Rhodes, K.; Ferrero, J.; Hang, Y.; Mikulskis, A.; Grimm, J.; Hock, C.; Nitsch, R. M.; Sandrock, A. The Antibody Aducanumab Reduces Aβ Plaques in Alzheimer's Disease. *Nature* **2016**, *537* (7618), 50–56. https://doi.org/10.1038/nature19323.
(29) Pardridge, W. M. Alzheimer's Disease: Future Drug Development and the Blood-Brain Barrier. *Expert Opinion on Investigational Drugs* **2019**, *28* (7), 569–572. https://doi.org/10.1080/13543784.2019.1627325.
(30) Custodia, A.; Ouro, A.; Romaus-Sanjurjo, D.; Pías-Peleteiro, J. M.; De Vries, H. E.; Castillo, J.; Sobrino, T. Endothelial Progenitor Cells and Vascular Alterations in Alzheimer's Disease. *Front. Aging Neurosci.* **2022**, *13*, 811210. https://doi.org/10.3389/fnagi.2021.811210.
(31) Sun, B.; Li, L.; Harris, O. A.; Luo, J. Blood–Brain Barrier Disruption: A Pervasive Driver and Mechanistic Link between Traumatic Brain Injury and Alzheimer's Disease. *Transl Neurodegener* **2025**, *14* (1), 16. https://doi.org/10.1186/s40035-025-00478-5.
(32) Fernandes, F.; Dias-Teixeira, M.; Delerue-Matos, C.; Grosso, C. Critical Review of Lipid-Based Nanoparticles as Carriers of Neuroprotective Drugs and Extracts. *Nanomaterials* **2021**, *11* (3), 563. https://doi.org/10.3390/nano11030563.
(33) Chen, Y.; He, Y.; Han, J.; Wei, W.; Chen, F. Blood-Brain Barrier Dysfunction and Alzheimer's Disease: Associations, Pathogenic Mechanisms, and Therapeutic Potential. *Front. Aging Neurosci.* **2023**, *15*, 1258640. https://doi.org/10.3389/fnagi.2023.1258640.
(34) Zhou, L.; Nguyen, T. D.; Chiang, G. C.; Keil, S. A.; Wang, X. H.; Hu, T.-W.; Lan, H.; Xi, K.; Costa, A. P.; Tanzi, E. B.; Glodzik, L.; Wegiel, J.; Butler, T.; de Leon, M. J.; Li, Y. Brain Glymphatic Fluid Mapping in Alzheimer's Disease: A Human MRI and PET Study. *Brain Commun* **2025**, *7* (3), fcaf200. https://doi.org/10.1093/braincomms/fcaf200.
(35) Harrison, I. F.; Ismail, O.; Machhada, A.; Colgan, N.; Ohene, Y.; Nahavandi, P.; Ahmed, Z.; Fisher, A.; Meftah, S.; Murray, T. K.; Ottersen, O. P.; Nagelhus, E. A.; O'Neill, M. J.; Wells, J. A.; Lythgoe, M. F. Impaired Glymphatic Function and Clearance of Tau in an Alzheimer's Disease Model. *Brain* **2020**, *143* (8), 2576–2593. https://doi.org/10.1093/brain/awaa179.
(36) Todd, N.; Angolano, C.; Ferran, C.; Devor, A.; Borsook, D.; McDannold, N. Secondary Effects on Brain Physiology Caused by Focused Ultrasound-Mediated Disruption of the Blood–Brain Barrier. *Journal of Controlled Release* **2020**, *324*, 450–459. https://doi.org/10.1016/j.jconrel.2020.05.040.
(37) Chen, S.; Nazeri, A.; Baek, H.; Ye, D.; Yang, Y.; Yuan, J.; Rubin, J. B.; Chen, H. A Review of Bioeffects Induced by Focused Ultrasound Combined with Microbubbles on the Neurovascular Unit. *J Cereb Blood Flow Metab* **2022**, *42* (1), 3–26. https://doi.org/10.1177/0271678X211046129.
(38) Juul Rasmussen, I.; Tybjærg-Hansen, A.; Rasmussen, K. L.; Nordestgaard, B. G.; Frikke-Schmidt, R. Blood–Brain Barrier Transcytosis Genes, Risk of Dementia and Stroke: A Prospective Cohort Study of 74,754 Individuals. *Eur J Epidemiol* **2019**, *34* (6), 579–590.

https://doi.org/10.1007/s10654-019-00498-2.
(39) Lee, A. J.; Raghavan, N. S.; Bhattarai, P.; Siddiqui, T.; Sariya, S.; Reyes-Dumeyer, D.; Flowers, X. E.; Cardoso, S. A. L.; De Jager, P. L.; Bennett, D. A.; Schneider, J. A.; Menon, V.; Wang, Y.; Lantigua, R. A.; Medrano, M.; Rivera, D.; Jiménez-Velázquez, I. Z.; Kukull, W. A.; Brickman, A. M.; Manly, J. J.; Tosto, G.; Kizil, C.; Vardarajan, B. N.; Mayeux, R. FMNL2 Regulates Gliovascular Interactions and Is Associated with Vascular Risk Factors and Cerebrovascular Pathology in Alzheimer's Disease. *Acta Neuropathol* **2022**, *144* (1), 59–79. https://doi.org/10.1007/s00401-022-02431-6.
(40) Rajabli, F.; Benchek, P.; Tosto, G.; Kushch, N.; Sha, J.; Bazemore, K.; Zhu, C.; Lee, W.-P.; Haut, J.; Hamilton-Nelson, K. L.; Wheeler, N. R.; Zhao, Y.; Farrell, J. J.; Grunin, M. A.; Leung, Y. Y.; Kuksa, P. P.; Li, D.; Da Fonseca, E. L.; Mez, J. B.; Palmer, E. L.; Pillai, J.; Sherva, R. M.; Song, Y. E.; Zhang, X.; Ikeuchi, T.; Iqbal, T.; Pathak, O.; Valladares, O.; Reyes-Dumeyer, D.; Kuzma, A. B.; Abner, E.; Adams, L. D.; Adams, P. M.; Aguirre, A.; Albert, M. S.; Albin, R. L.; Allen, M.; Alvarez, L.; Apostolova, L. G.; Arnold, S. E.; Asthana, S.; Atwood, C. S.; Auerbach, S.; Ayres, G.; Baldwin, C. T.; Barber, R. C.; Barnes, L. L.; Barral, S.; Beach, T. G.; Becker, J. T.; Beecham, G. W.; Beekly, D.; Benitez, B. A.; Bennett, D.; Bertelson, J.; Bird, T. D.; Blacker, D.; Boeve, B. F.; Bowen, J. D.; Boxer, A.; Brewer, J.; Burke, J. R.; Burns, J. M.; Buxbaum, J. D.; Cairns, N. J.; Cantwell, L. B.; Cao, C.; Carlson, C. S.; Carlsson, C. M.; Carney, R. M.; Carrasquillo, M. M.; Chasse, S.; Chesselet, M.-F.; Chin, N. A.; Chui, H. C.; Chung, J.; Craft, S.; Crane, P. K.; Cribbs, D. H.; Crocco, E. A.; Cruchaga, C.; Cuccaro, M. L.; Cullum, M.; Darby, E.; Davis, B.; De Jager, P. L.; DeCarli, C.; DeToledo, J.; Dick, M.; Dickson, D. W.; Dombroski, B. A.; Doody, R. S.; Duara, R.; Ertekin-Taner, Ni.; Evans, D. A.; Faber, K. M.; Fairchild, T. J.; Fallon, K. B.; Fardo, D. W.; Farlow, M. R.; Fernandez-Hernandez, V.; Ferris, S.; Friedland, R. P.; Foroud, T. M.; Frosch, M. P.; Fulton-Howard, B.; Galasko, D. R.; Gamboa, A.; Gearing, M.; Geschwind, D. H.; Ghetti, B.; Gilbert, J. R.; Go, R. C. P.; Goate, A. M.; Grabowski, T. J.; Graff-Radford, N. R.; Green, R. C.; Growdon, J. H.; Hakonarson, H.; Hall, J.; Hamilton, R. L.; Harari, O.; Hardy, J.; Harrell, L. E.; Head, E.; Henderson, V. W.; Hernandez, M.; Hohman, T.; Honig, L. S.; Huebinger, R. M.; Huentelman, M. J.; Hulette, C. M.; Hyman, B. T.; Hynan, L. S.; Ibanez, L.; Jarvik, G. P.; Jayadev, S.; Jin, L.-W.; Johnson, K.; Johnson, L.; Kamboh, M. I.; Karydas, A. M.; Katz, M. J.; Kauwe, J. S.; Kaye, J. A.; Keene, C. D.; Khaleeq, A.; Kikuchi, M.; Kim, R.; Knebl, J.; Kowall, N. W.; Kramer, J. H.; Kukull, W. A.; LaFerla, F. M.; Lah, J. J.; Larson, E. B.; Lerner, A.; Leverenz, J. B.; Levey, A. I.; Lieberman, A. P.; Lipton, R. B.; Logue, M.; Lopez, O. L.; Lunetta, K. L.; Lyketsos, C. G.; Mains, D.; Margaret, F. E.; Marson, D. C.; Martin, E. Rr.; Martiniuk, F.; Mash, D. C.; Masliah, E.; Massman, P.; Masurkar, A.; McCormick, W. C.; McCurry, S. M.; McDavid, A. N.; McDonough, S.; McKee, A. C.; Mesulam, M.; Miller, B. L.; Miller, C. A.; Miller, J. W.; Montine, T. J.; Monuki, E. S.; Morris, J. C.; Mukherjee, S.; Myers, A. J.; Nguyen, T.; Obisesan, T.; O'Bryant, S.; Olichney, J. M.; Ory, M.; Palmer, R.; Parisi, J. E.; Paulson, H. L.; Pavlik, V.; Paydarfar, D.; Perez, V.; Peskind, E.; Petersen, R. C.; Petrovitch, H.; Pierce, A.; Polk, M.; Poon, W. W.; Potter, H.; Qu, L.; Quiceno, M.; Quinn, J. F.; Raj, A.; Raskind, M.; Reiman, E. M.; Reisberg, B.; Reisch, J. S.; Ringman, J. M.; Roberson, E. D.; Rodriguear, M.; Rogaeva, E.; Rosen, H. J.; Rosenberg, R. N.; Royall, D. R.; Sabbagh, M.; Sadovnick, A. D.; Sager, M. A.; Sano, M.; Saykin, A. J.; Schneider, J. A.; Schneider, L. S.; Seeley, W. W.; Slifer, S. H.; Small, S.; Smith, A. G.; Smith, J. P.; Sonnen, J. A.; Spina, S.; George-Hyslop, P. S.; Starks, T. D.; Stern, R. A.; Stevens, A. B.; Strittmatter, S. M.; Sultzer, D.; Swerdlow, R. H.; Tanzi, R. E.; Tilson, J. L.; Trojanowski, J. Q.; Troncoso, J. C.; Tsolaki, M.; Tsuang, D. W.; Van Deerlin, V. M.; Van Eldik, L. J.; Vance, J. M.; Vardarajan, B.

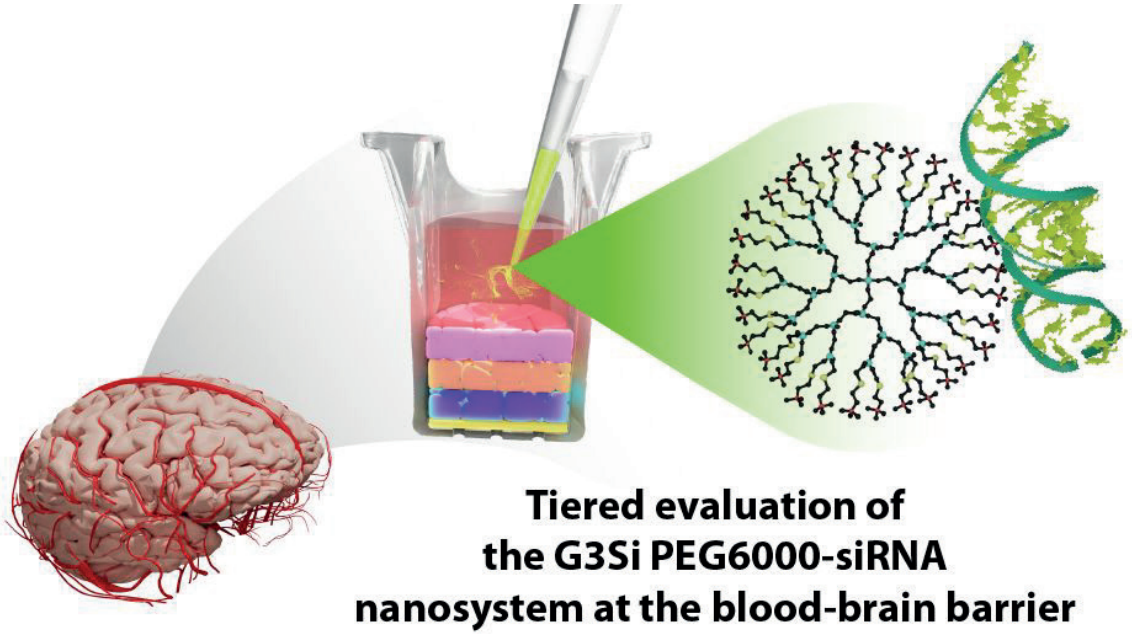
N.; Vassar, R.; Vinters, H. V.; Vonsattel, J.-P.; Weintraub, S.; Welsh-Bohmer, K. A.; Whitehead, P. L.; Wijsman, E. M.; Wilhelmsen, K. C.; Williams, B.; Williamson, J.; Wilms, H.; Wingo, T. S.; Wisniewski, T.; Woltjer, R. L.; Woon, M.; Wright, C. B.; Wu, C.-K.; Younkin, S. G.; Yu, C.-E.; Yu, L.; Zhu, X.; Kunkle, B. W.; Bush, W. S.; Miyashita, A.; Byrd, G. S.; Wang, L.-S.; Farrer, L. A.; Haines, J. L.; Mayeux, R.; Pericak-Vance, M. A.; Schellenberg, G. D.; Jun, G. R.; Reitz, C.; Naj, A. C.; on behalf of Alzheimer's Disease Genetics Consortium (ADGC). Multi-Ancestry Genome-Wide Meta-Analysis of 56,241 Individuals Identifies Known and Novel Cross-Population and Ancestry-Specific Associations as Novel Risk Loci for Alzheimer's Disease. *Genome Biol* **2025**, *26* (1), 210. https://doi.org/10.1186/s13059-025-03564-z.
(41) Farrer, L. A. Effects of Age, Sex, and Ethnicity on the Association Between Apolipoprotein E Genotype and Alzheimer Disease: A Meta-Analysis. *JAMA* **1997**, *278* (16), 1349. https://doi.org/10.1001/jama.1997.03550160069041.
(42) Montagne, A.; Nation, D. A.; Sagare, A. P.; Barisano, G.; Sweeney, M. D.; Chakhoyan, A.; Pachicano, M.; Joe, E.; Nelson, A. R.; D'Orazio, L. M.; Buennagel, D. P.; Harrington, M. G.; Benzinger, T. L. S.; Fagan, A. M.; Ringman, J. M.; Schneider, L. S.; Morris, J. C.; Reiman, E. M.; Caselli, R. J.; Chui, H. C.; Tcw, J.; Chen, Y.; Pa, J.; Conti, P. S.; Law, M.; Toga, A. W.; Zlokovic, B. V. APOE4 Leads to Blood–Brain Barrier Dysfunction Predicting Cognitive Decline. *Nature* **2020**, *581* (7806), 71–76. https://doi.org/10.1038/s41586-020-2247-3.
(43) Montagne, A.; Nikolakopoulou, A. M.; Huuskonen, M. T.; Sagare, A. P.; Lawson, E. J.; Lazic, D.; Rege, S. V.; Grond, A.; Zuniga, E.; Barnes, S. R.; Prince, J.; Sagare, M.; Hsu, C.-J.; LaDu, M. J.; Jacobs, R. E.; Zlokovic, B. V. APOE4 Accelerates Advanced-Stage Vascular and Neurodegenerative Disorder in Old Alzheimer's Mice via Cyclophilin A Independently of Amyloid-β. *Nat Aging* **2021**, *1* (6), 506–520. https://doi.org/10.1038/s43587-021-00073-z.
(44) Deane, R.; Sagare, A.; Hamm, K.; Parisi, M.; Lane, S.; Finn, M. B.; Holtzman, D. M.; Zlokovic, B. V. apoE Isoform–Specific Disruption of Amyloid β Peptide Clearance from Mouse Brain. *J. Clin. Invest.* **2008**, *118* (12), 4002–4013. https://doi.org/10.1172/JCI36663.
(45) Ding, S.; Khan, A. I.; Cai, X.; Song, Y.; Lyu, Z.; Du, D.; Dutta, P.; Lin, Y. Overcoming Blood–Brain Barrier Transport: Advances in Nanoparticle-Based Drug Delivery Strategies. *Materials Today* **2020**, *37*, 112–125. https://doi.org/10.1016/j.mattod.2020.02.001.
(46) Rampado, R.; Crotti, S.; Caliceti, P.; Pucciarelli, S.; Agostini, M. Recent Advances in Understanding the Protein Corona of Nanoparticles and in the Formulation of "Stealthy" Nanomaterials. *Front. Bioeng. Biotechnol.* **2020**, *8*, 166. https://doi.org/10.3389/fbioe.2020.00166.
(47) Zawadzki, S.; Martín-Serrano, Á.; Okła, E.; Kędzierska, M.; Garcia-Gallego, S.; López, P. O.; De La Mata, F. J.; Michlewska, S.; Makowski, T.; Ionov, M.; Pędziwiatr-Werbicka, E.; Bryszewska, M.; Miłowska, K. Synthesis and Biophysical Evaluation of Carbosilane Dendrimers as Therapeutic siRNA Carriers. *Sci Rep* **2024**, *14* (1), 1615. https://doi.org/10.1038/s41598-024-51238-w.
(48) Zawadzki, S.; Okła, E.; Michlewska, S.; Makowski, T.; Buczkowski, A.; López, P. O.; de la Mata, F. J.; Ionov, M.; Bryszewska, M.; Miłowska, K. Structural and Conformational Rearrangements of Human Serum Albumin, Transferrin, and Blood Plasma Induced by Carbosilane Dendrimer Therapeutic Delivery System. *Sci Rep* **2025**, In Press. https://doi.org/10.1038/s41598-025-23355-7.
(49) Zawadzki, S.; Suty, S.; Okła, E.; Ortega López, P.; De La Mata, F. J.; Waczulikova, I.; Ionov, M.; Bryszewska, M.; Miłowska, K. Hemocompatibility of Carbosilane Dendrimers as a Therapeutic siRNA Delivery System across Blood–Brain Barrier. *ACS Appl. Mater. Interfaces*

2026, *18* (7), 11671–11686. https://doi.org/10.1021/acsami.5c12952.
(50) Sestili, P.; Calcabrini, C.; Diaz, A. R.; Fimognari, C.; Stocchi, V. The Fast-Halo Assay for the Detection of DNA Damage. In *Fast Detection of DNA Damage*; Didenko, V. V., Ed.; Methods in Molecular Biology; Springer New York: New York, NY, 2017; Vol. 1644, pp 75–93. https://doi.org/10.1007/978-1-4939-7187-9_6.
(51) Maurya, D. K. HaloJ: An ImageJ Program for Semiautomatic Quantification of DNA Damage at Single-Cell Level. *Int J Toxicol* **2014**, *33* (5), 362–366. https://doi.org/10.1177/1091581814549961.
(52) Napoli, C.; Lemieux, C.; Jorgensen, R. Introduction of a Chimeric Chalcone Synthase Gene into Petunia Results in Reversible Co-Suppression of Homologous Genes in Trans. *Plant Cell* **1990**, *2* (4), 279–289. https://doi.org/10.1105/tpc.2.4.279.
(53) Romano, N.; Macino, G. Quelling: Transient Inactivation of Gene Expression in *Neurospora Crassa* by Transformation with Homologous Sequences. *Molecular Microbiology* **1992**, *6* (22), 3343–3353. https://doi.org/10.1111/j.1365-2958.1992.tb02202.x.
(54) Fire, A.; Xu, S.; Montgomery, M. K.; Kostas, S. A.; Driver, S. E.; Mello, C. C. Potent and Specific Genetic Interference by Double-Stranded RNA In. **1998**, *391*.
(55) Hamilton, A. J.; Baulcombe, D. C. A Species of Small Antisense RNA in Posttranscriptional Gene Silencing in Plants. *Science, New Series* **1999**, *286* (5441), 950–952.
(56) Zamore, P. D.; Tuschl, T.; Sharp, P. A.; Bartel, D. P. RNAi: Double-Stranded RNA Directs the ATP-Dependent Cleavage of mRNA at 21 to 23 Nucleotide Intervals. *Cell* **2000**, *101* (1), 25–33. https://doi.org/10.1016/S0092-8674(00)80620-0.
(57) Elbashir, S. M.; Harborth, J.; Lendeckel, W.; Yalcin, A.; Weber, K.; Tuschl, T. Duplexes of 21-Nucleotide RNAs Mediate RNA Interference in Cultured Mammalian Cells. *Nature* **2001**, *411* (6836), 494–498. https://doi.org/10.1038/35078107.
(58) Adams, D.; Gonzalez-Duarte, A.; O'Riordan, W. D.; Yang, C.-C.; Ueda, M.; Kristen, A. V.; Tournev, I.; Schmidt, H. H.; Coelho, T.; Berk, J. L.; Lin, K.-P.; Vita, G.; Attarian, S.; Planté-Bordeneuve, V.; Mezei, M. M.; Campistol, J. M.; Buades, J.; Brannagan, T. H.; Kim, B. J.; Oh, J.; Parman, Y.; Sekijima, Y.; Hawkins, P. N.; Solomon, S. D.; Polydefkis, M.; Dyck, P. J.; Gandhi, P. J.; Goyal, S.; Chen, J.; Strahs, A. L.; Nochur, S. V.; Sweetser, M. T.; Garg, P. P.; Vaishnaw, A. K.; Gollob, J. A.; Suhr, O. B. Patisiran, an RNAi Therapeutic, for Hereditary Transthyretin Amyloidosis. *N Engl J Med* **2018**, *379* (1), 11–21. https://doi.org/10.1056/NEJMoa1716153.
(59) Nair, J. K.; Willoughby, J. L. S.; Chan, A.; Charisse, K.; Alam, Md. R.; Wang, Q.; Hoekstra, M.; Kandasamy, P.; Kel'in, A. V.; Milstein, S.; Taneja, N.; O'Shea, J.; Shaikh, S.; Zhang, L.; Van Der Sluis, R. J.; Jung, M. E.; Akinc, A.; Hutabarat, R.; Kuchimanchi, S.; Fitzgerald, K.; Zimmermann, T.; Van Berkel, T. J. C.; Maier, M. A.; Rajeev, K. G.; Manoharan, M. Multivalent *N* -Acetylgalactosamine-Conjugated siRNA Localizes in Hepatocytes and Elicits Robust RNAi-Mediated Gene Silencing. *J. Am. Chem. Soc.* **2014**, *136* (49), 16958–16961. https://doi.org/10.1021/ja505986a.
(60) Azqueta, A.; Stopper, H.; Zegura, B.; Dusinska, M.; Møller, P. Do Cytotoxicity and Cell Death Cause False Positive Results in the in Vitro Comet Assay? *Mutation Research/Genetic Toxicology and Environmental Mutagenesis* **2022**, *881*, 503520. https://doi.org/10.1016/j.mrgentox.2022.503520.
(61) Uram, Ł.; Szuster, M.; Filipowicz, A.; Gargasz, K.; Wołowiec, S.; Wałajtys-Rode, E. Different Patterns of Nuclear and Mitochondrial Penetration by the G3 PAMAM Dendrimer and Its Biotin–Pyridoxal Bioconjugate BC-PAMAM in Normal and Cancer Cells in Vitro.

IJN **2015**, 5647. https://doi.org/10.2147/IJN.S87307.
(62) Flores-Mejía, R.; Fragoso-Vázquez, M. J.; Pérez-Blas, L. G.; Parra-Barrera, A.; Hernández-Castro, S. S.; Estrada-Pérez, A. R.; Rodrígues, J.; Lara-Padilla, E.; Ortiz-Morales, A.; Correa-Basurto, J. Chemical Characterization (LC–MS–ESI), Cytotoxic Activity and Intracellular Localization of PAMAM G4 in Leukemia Cells. *Sci Rep* **2021**, *11* (1), 8210. https://doi.org/10.1038/s41598-021-87560-w.
(63) Gutleb, A. C.; Murugadoss, S.; Stępnik, M.; SenGupta, T.; El Yamani, N.; Longhin, E. M.; Olsen, A.-K. H.; Wyrzykowska, E.; Jagiello, K.; Judzinska, B.; Cambier, S.; Honza, T.; McFadden, E.; Shaposhnikov, S.; Puzyn, T.; Serchi, T.; Weber, P.; Arnesdotter, E.; Skakalova, V.; Jirsova, K.; Grudzinski, I. P.; Collins, A.; Rundén-Pran, E.; Dusinska, M. New Approach Methods (NAMs) for Genotoxicity Assessment of Nano- and Advanced Materials; Advantages and Challenges. *Mutation Research - Genetic Toxicology and Environmental Mutagenesis* **2025**, *904*, 503867. https://doi.org/10.1016/j.mrgentox.2025.503867.
(64) Shukla, R. K.; Badiye, A.; Vajpayee, K.; Kapoor, N. Genotoxic Potential of Nanoparticles: Structural and Functional Modifications in DNA. *Front. Genet.* **2021**, *12*, 728250. https://doi.org/10.3389/fgene.2021.728250.
(65) Sweeney, M. D.; Zhao, Z.; Montagne, A.; Nelson, A. R.; Zlokovic, B. V. Blood-Brain Barrier: From Physiology to Disease and Back. *Physiological Reviews* **2019**, *99* (1), 21–78. https://doi.org/10.1152/physrev.00050.2017.
(66) Knipp, G. T.; Lubin, K. E. Design of Experiment Based Optimization of an in Vitro Direct Contact Triculture Blood Brain Barrier Model for Permeability Screening. *PPIJ* **2021**, *9* (4), 143–158. https://doi.org/10.15406/ppij.2021.09.00340.
(67) Srinivasan, B.; Kolli, A. R.; Esch, M. B.; Abaci, H. E.; Shuler, M. L.; Hickman, J. J. TEER Measurement Techniques for In Vitro Barrier Model Systems. *SLAS Technology* **2015**, *20* (2), 107–126. https://doi.org/10.1177/2211068214561025.
(68) Palma-Florez, S.; López-Canosa, A.; Moralez-Zavala, F.; Castaño, O.; Kogan, M. J.; Samitier, J.; Lagunas, A.; Mir, M. BBB-on-a-Chip with Integrated Micro-TEER for Permeability Evaluation of Multi-Functionalized Gold Nanorods against Alzheimer's Disease. *J Nanobiotechnol* **2023**, *21* (1), 115. https://doi.org/10.1186/s12951-023-01798-2.
(69) Benson, K.; Cramer, S.; Galla, H.-J. Impedance-Based Cell Monitoring: Barrier Properties and Beyond. *Fluids Barriers CNS* **2013**, *10* (1), 5. https://doi.org/10.1186/2045-8118-10-5.
(70) Liu, W.; Wang, Z.; Zhang, L.; Wei, X.; Li, L. Tight Junction in Blood-Brain Barrier: An Overview of Structure, Regulation, and Regulator Substances. *CNS Neuroscience & Therapeutics* **2012**, *18* (8), 609–615. https://doi.org/10.1111/j.1755-5949.2012.00340.x.
(71) Desai, B. S.; Monahan, A. J.; Carvey, P. M.; Hendey, B. Blood–Brain Barrier Pathology in Alzheimer's and Parkinson's Disease: Implications for Drug Therapy. *Cell Transplant* **2007**, *16* (3), 285–299. https://doi.org/10.3727/000000007783464731.
(72) Algotsson, A.; Winblad, B. The Integrity of the Blood?Brain Barrier in Alzheimer?S Disease. *Acta Neurol Scand* **2007**, *115* (6), 403–408. https://doi.org/10.1111/j.1600-0404.2007.00823.x.
(73) Nozohouri, S.; Noorani, B.; Al-Ahmad, A.; Abbruscato, T. J. Estimating Brain Permeability Using In Vitro Blood-Brain Barrier Models. In *Permeability Barrier*; Turksen, K., Ed.; Methods in Molecular Biology; Springer US: New York, NY, 2020; Vol. 2367, pp 47–72. https://doi.org/10.1007/7651_2020_311.
(74) Bednarek, R. In Vitro Methods for Measuring the Permeability of Cell Monolayers. *MPs*

2022, *5* (1), 17. https://doi.org/10.3390/mps5010017.
(75) Tervonen, A.; Ihalainen, T. O.; Nymark, S.; Hyttinen, J. Structural Dynamics of Tight Junctions Modulate the Properties of the Epithelial Barrier. *PLoS ONE* **2019**, *14* (4), e0214876. https://doi.org/10.1371/journal.pone.0214876.
(76) Monaco, A.; Ovryn, B.; Axis, J.; Amsler, K. The Epithelial Cell Leak Pathway. *IJMS* **2021**, *22* (14), 7677. https://doi.org/10.3390/ijms22147677.
(77) Denkinger, M.; Baker, S.; Inglis, B.; Kobayashi, S.; Juarez, A.; Mason, S.; Jagust, W. Associations between Regional Blood-Brain Barrier Permeability, Aging, and Alzheimer's Disease Biomarkers in Cognitively Normal Older Adults. *PLoS ONE* **2024**, *19* (6), e0299764. https://doi.org/10.1371/journal.pone.0299764.
(78) Nehra, G.; Bauer, B.; Hartz, A. M. S. Blood-Brain Barrier Leakage in Alzheimer's Disease: From Discovery to Clinical Relevance. *Pharmacology & Therapeutics* **2022**, *234*, 108119. https://doi.org/10.1016/j.pharmthera.2022.108119.
(79) Van Heuvelen, M. J. G.; Van Der Lei, M. B.; Alferink, P. M.; Roemers, P.; Van Der Zee, E. A. Cognitive Deficits in Human ApoE4 Knock-in Mice: A Systematic Review and Meta-Analysis. *Behavioural Brain Research* **2024**, *471*, 115123. https://doi.org/10.1016/j.bbr.2024.115123.
(80) Maei, H. R. What Is the Most Sensitive Measure of Water Maze Probe Test Performance? *Front. Integr. Neurosci.* **2009**, *3*. https://doi.org/10.3389/neuro.07.004.2009.
(81) Puzzo, D.; Lee, L.; Palmeri, A.; Calabrese, G.; Arancio, O. Behavioral Assays with Mouse Models of Alzheimer's Disease: Practical Considerations and Guidelines. *Biochemical Pharmacology* **2014**, *88* (4), 450–467. https://doi.org/10.1016/j.bcp.2014.01.011.
(82) Bour, A.; Grootendorst, J.; Vogel, E.; Kelche, C.; Dodart, J.-C.; Bales, K.; Moreau, P.-H.; Sullivan, P. M.; Mathis, C. Middle-Aged Human apoE4 Targeted-Replacement Mice Show Retention Deficits on a Wide Range of Spatial Memory Tasks. *Behavioural Brain Research* **2008**, *193* (2), 174–182. https://doi.org/10.1016/j.bbr.2008.05.008.
(83) Rodriguez, G. A.; Burns, M. P.; Weeber, E. J.; Rebeck, G. W. Young APOE4 Targeted Replacement Mice Exhibit Poor Spatial Learning and Memory, with Reduced Dendritic Spine Density in the Medial Entorhinal Cortex. *Learn. Mem.* **2013**, *20* (5), 256–266. https://doi.org/10.1101/lm.030031.112.
(84) Salomon-Zimri, S.; Boehm-Cagan, A.; Liraz, O.; Michaelson, D. M. Hippocampus-Related Cognitive Impairments in Young apoE4 Targeted Replacement Mice. *Neurodegener Dis* **2013**, *13* (2–3), 86–92. https://doi.org/10.1159/000354777.

Graphical abstract



XVI. Oświadczenia współautorów prac wchodzących w skład rozprawy doktorskiej

UNIWERSYTET ŁÓDZKI

Wydział Biologii i Ochrony Środowiska,
Katedra Biofizyki Ogólnej,
ul. Pomorska 141/143, 90-236 Łódź
e-mail.: serafin.zawadzki@edu.uni.lodz.pl

mgr Serafin Zawadzki

Łódź, dnia 27.03.26

Oświadczenie

Oświadczam, że mój udział w pracy:

Zawadzki S., Martín-Serrano Á., Okła E., Kędzierska M., Garcia-Gallego S., López P.O., de la Mata F.J., Michlewska S., Makowski T., Ionov M., Pędziwiatr-Werbicka E., Bryszewska M., Miłowska K., Synthesis and biophysical evaluation of carbosilane dendrimers as therapeutic siRNA carriers. Sci. Rep. 2024, 14, 1615. https://doi.org/10.1038/s41598-024-51238-w obejmował:

- współudział w opracowaniu koncepcji pracy
- współudział w projektowaniu badań
- wykonanie pomiarów biofizycznych (potencjał zeta, średnica hydrodynamiczna, elektroforeza w żelu agarozowym, dichroizm kołowy)
- wykonanie testów biokompatybilności komórkowej (test cytotoksyczności MTT)
- współudział w obrazowaniu próbek techniką transmisyjnej mikroskopii elektronowej, obrazowaniu próbek techniką mikroskopii sił atomowych
- opracowanie, analiza statystyczna i interpretacja wyników badań
- przygotowanie pierwotnej wersji manuskryptu
- przygotowanie rycin
- współudział w odpowiedzi na recenzje
- redakcja i przygotowanie pracy do druku

Serafin Zawadzki

UNIWERSYTET ŁÓDZKI

Wydział Biologii i Ochrony Środowiska,
Katedra Biofizyki Ogólnej,
ul. Pomorska 141/143, 90-236 Łódź
e-mail.: serafin.zawadzki@edu.uni.lodz.pl

mgr Serafin Zawadzki

Łódź, dnia 27.03.26

Oświadczenie

Oświadczam, że mój udział w pracy:

Zawadzki S., Okła E., Michlewska S., Makowski T., Buczkowski A., O. López P., de la Mata F.J., Ionov M., Bryszewska M., Miłowska K., Structural and conformational rearrangements of human serum albumin, transferrin, and blood plasma induced by carbosilane dendrimer therapeutic delivery system. Sci. Rep. 2025, 15, 39650. https://doi.org/10.1038/s41598-025-23355-7 obejmował:

- współudział w opracowaniu koncepcji pracy
- współudział w projektowaniu badań
- wykonanie pomiarów biofizycznych (wygaszanie fluorescencji, dichroizm kołowy)
- współudział w obrazowaniu próbek techniką transmisyjnej mikroskopii elektronowej, obrazowaniu próbek techniką mikroskopii sił atomowych
- opracowanie, analiza statystyczna i interpretacja wyników badań
- przygotowanie pierwotnej wersji manuskryptu
- przygotowanie rycin
- współudział w odpowiedzi na recenzje
- redakcja i przygotowanie pracy do druku

Serafin Zawadzki

UNIWERSYTET ŁÓDZKI

Wydział Biologii i Ochrony Środowiska,
Katedra Biofizyki Ogólnej,
ul. Pomorska 141/143, 90-236 Łódź
e-mail.: serafin.zawadzki@edu.uni.lodz.pl

mgr Serafin Zawadzki

Łódź, dnia 27.03.26

Oświadczenie

Oświadczam, że mój udział w pracy:

Zawadzki S., Suty S., Okła E., Ortega López P., de la Mata F.J., Waczulikova I., Ionov M., Bryszewska M., Miłowska K., Hemocompatibility of Carbosilane Dendrimers as a Therapeutic siRNA Delivery System across Blood–Brain Barrier. ACS Appl. Mater. Interfaces 2026, 18, 11671−11686 https://doi.org/10.1021/acsami.5c12952, obejmował:

- współudział w opracowaniu koncepcji pracy
- współudział w projektowaniu badań
- wykonanie pomiarów biofizycznych (płynność błon erytrocytarnych)
- wykonanie testów hemokompatybilności (hemoliza, aktywność metaboliczna PBMC oraz profil cytokin i chemokin)
- współudział w badaniach właściwości hemoreologicznych, parametrów hemostatycznych i morfologii krwi
- opracowanie, analiza statystyczna i interpretacja wyników badań
- przygotowanie pierwotnej wersji manuskryptu
- przygotowanie rycin
- współudział w odpowiedzi na recenzje
- redakcja i przygotowanie pracy do druku

Serafin Zawadzki

UNIWERSYTET ŁÓDZKI

Wydział Biologii i Ochrony Środowiska, Katedra Biofizyki Ogólnej,
Instytut Biofizyki
ul. Pomorska 141/143, 90-236 Łódź
e-mail.: serafin.zawadzki@edu.uni.lodz.pl

mgr Serafin Zawadzki

Łódź, dnia 27.03.26..

Oświadczenie

Oświadczam, że mój udział w manuskrypcie wysłanym do czasopisma:

Zawadzki S., Okła E., Ortega López P., de la Mata F.J., Ionov M., Kreišmane M., Skrastina D., Jansons J., Bryszewska M., Miłowska K., Multilevel Assessment of Carbosilane Dendrimer–siRNA Nanoplatform: Cellular Compatibility, Blood–Brain Barrier Model Integrity, and Murine Model Biodistribution, obejmował:

- współudział w opracowaniu koncepcji pracy
- współudział w projektowaniu badań
- wykonanie testów biokompatybilności komórkowej (test cytotoksyczności MTT, oznaczanie reaktywnych form tlenu i potencjału błony mitochondrialnej)
- opracowanie modelu eksperymentalnego bariery krew-mózg
- wykonanie testów integralności oraz funkcjonalności modelu bariery krew-mózg (monitorowanie impedancji w czasie rzeczywistym, oceny konfluencji mikroskopią fluorescencyjną)
- opracowanie, analiza statystyczna i interpretacja wyników badań (w tym analiza biodystrybucji IVIS *in vivo* oraz *ex vivo* w modelu mysim)
- przygotowanie pierwotnej wersji manuskryptu
- przygotowanie rycin

Serafin Zawadzki

UNIWERSYTET ŁÓDZKI

Wydział Biologii i Ochrony Środowiska,
Katedra Biofizyki Ogólnej,
ul. Pomorska 141/143, 90-236 Łódź
e-mail.: serafin.zawadzki@edu.uni.lodz.pl

mgr Serafin Zawadzki

Łódź, dnia 27.03.26.

Oświadczenie

Oświadczam, że mój udział w w manuskrypcie:

Zawadzki S., Okła E., Michlewska S., Bednarek R., Jansons J., Skrastiņa D., Kreišmane M., Piļipenko V., Jansone B., Ortega López P., de la Mata F.J., Ionov M., Bryszewska M., Miłowska K. Tiered Evaluation of Carbosilane–siRNA Nanoplatform from Single-Cell Biocompatibility to Blood-Brain Barrier Model Dynamics, and Murine Alzheimer Model Behavior Assessment, obejmował:

- współudział w opracowaniu koncepcji pracy
- współudział w projektowaniu badań
- wykonanie testów biokompatybilności komórkowej (test genotoksyczności FHA, oznaczanie reaktywnych form tlenu i potencjału błony mitochondrialnej)
- opracowanie modelu eksperymentalnego bariery krew-mózg
- wykonanie testów integralności oraz funkcjonalności modelu bariery krew-mózg (monitorowanie oporu elektrycznego TEER, test przepuszczalności makromolekularnej)
- współudział w obrazowaniu próbek techniką transmisyjnej mikroskopii konfokalnej
- opracowanie i interpretacja wyników badań
  (w tym analiza eksperymentów labiryntu wodnego Morrisa (MWM) w modelu mysim)
- przygotowanie pierwotnej wersji manuskryptu
- przygotowanie rycin

Serafin Zawadzki

UNIWERSYTET ŁÓDZKI

Wydział Biologii i Ochrony Środowiska,
Katedra Biofizyki Ogólnej,
ul. Pomorska 141/143, 90-236 Łódź
e-mail.: katarzyna.milowska@biol.uni.lodz.pl

dr hab. Katarzyna Miłowska, prof. UŁ

Łódź, dnia 23.03.2026

Oświadczenie

Oświadczam, że mój udział w pracy:

1. Zawadzki S., Martín-Serrano Á., Okła E., Kędzierska M., Garcia-Gallego S., López P.O., de la Mata F.J., Michlewska S., Makowski T., Ionov M., Pędziwiatr-Werbicka E., Bryszewska M., **Miłowska K.,** Synthesis and biophysical evaluation of carbosilane dendrimers as therapeutic siRNA carriers. Sci. Rep. 2024, 14, 1615. https://doi.org/10.1038/s41598-024-51238-w obejmował:

- współudział w opracowaniu koncepcji pracy
- współudział w projektowaniu badań
- korektę manuskryptu
- współudział w odpowiedzi na recenzje

2. Zawadzki S., Okła E., Michlewska S., Makowski T., Buczkowski A., O. López P., de la Mata F.J., Ionov M., Bryszewska M., **Miłowska K.,** Structural and conformational rearrangements of human serum albumin, transferrin, and blood plasma induced by carbosilane dendrimer therapeutic delivery system. Sci. Rep. 2025, 15, 39650. https://doi.org/10.1038/s41598-025-23355-7 obejmował:

- współudział w opracowaniu koncepcji pracy
- współudział w projektowaniu badań
- korektę manuskryptu
- współudział w odpowiedzi na recenzje

3. Zawadzki S., Suty S., Okła E., Ortega López P., de la Mata F.J., Waczulikova I., Ionov M., Bryszewska M., **Miłowska K.,** Hemocompatibility of Carbosilane Dendrimers as a Therapeutic siRNA Delivery System across Blood–Brain Barrier. ACS Appl. Mater. Interfaces 2026, 18, 11671−11686 https://doi.org/10.1021/acsami.5c12952, obejmował:

- współudział w opracowaniu koncepcji pracy
- współudział w projektowaniu badań
- korektę manuskryptu
- współudział w odpowiedzi na recenzje

Kmiłowska

UNIWERSYTET ŁÓDZKI

Wydział Biologii i Ochrony Środowiska, Katedra Biofizyki Ogólnej,
Instytut Biofizyki
ul. Pomorska 141/143, 90-236 Łódź
e-mail.: katarzyna.milowska@biol.uni.lodz.pl

dr hab. Katarzyna Miłowska, prof. UŁ

Łódź, dnia 23.03.2026 r.

Oświadczenie

Oświadczam, że mój udział w manuskrypcie wysłanym do czasopisma:

1. Zawadzki S., Okła E., Ortega López P., de la Mata F.J., Ionov M., Kreišmane M., Skrastina D., Jansons J., Bryszewska M., **Miłowska K.,** Multilevel Assessment of Carbosilane Dendrimer–siRNA Nanoplatform: Cellular Compatibility, Blood–Brain Barrier Model Integrity, and Murine Model Biodistribution, obejmował:

- współudział w opracowaniu koncepcji pracy
- współudział w projektowaniu badań
- korektę manuskryptu

2. Zawadzki S., Okła E., Michlewska S., Bednarek R., Jansons J., Skrastiņa D., Kreišmane M., Piļipenko V., Jansone B., Ortega López P., de la Mata F.J., Ionov M., Bryszewska M., Miłowska K. Tiered Evaluation of Carbosilane–siRNA Nanoplatform from Single-Cell Biocompatibility to Blood-Brain Barrier Model Dynamics, and Murine Alzheimer Model Behavior Assessment, obejmował:

- współudział w opracowaniu koncepcji pracy
- współudział w projektowaniu badań
- korektę manuskryptu

Kkiłowska

Dr hab. n. med. Radosław Bednarek
Uniwersytet Medyczny w Łodzi
Wydział Nauk o Zdrowiu
Zakład Cytobiologii i Proteomiki
ul. Mazowiecka 6/8, 92-215 Łódź,
e-mail.: radoslaw.bednarek@umed.lodz.pl

Łódź, dnia 25.03.2026

Oświadczenie

Oświadczam, że mój udział w manuskrypcie:

Zawadzki S., Okła E., Michlewska S., **Bednarek R.**, Jansons J., Skrastiņa D., Kreišmane M., Piļipenko V., Jansone B., Ortega López P., de la Mata F.J., Ionov M., Bryszewska M., Miłowska K. Tiered Evaluation of Carbosilane–siRNA Nanoplatform from Single-Cell Biocompatibility to Blood-Brain Barrier Model Dynamics, and Murine Alzheimer Model Behavior Assessment, obejmował:

- pomoc w zaprojektowaniu eksperymentu w wykorzystaniem techniki TEER
- konsultacji w zakresie analizy i opisu wyników uzyskanych techniką

ADIUNKT
Zakładu Cytobiologii i Proteomiki
Uniwersytet Medyczny w Łodzi
dr hab. n. med. Radosław Bednarek

UNIWERSYTET ŁÓDZKI

Wydział Biologii i Ochrony Środowiska, Katedra Biofizyki Ogólnej,
ul. Pomorska 141/143, 90-236 Łódź
e-mail.: maria.bryszewska@biol.uni.lodz.pl

Prof. dr hab. Maria Bryszewska

Łódź, dnia 16/03/2026

Oświadczenie

Oświadczam, że mój udział w pracy:

1. Zawadzki S., Martín-Serrano Á., Okła E., Kędzierska M., Garcia-Gallego S., López P.O., de la Mata F.J., Michlewska S., Makowski T., Ionov M., Pędziwiatr-Werbicka E., **Bryszewska M.**, Miłowska K., Synthesis and biophysical evaluation of carbosilane dendrimers as therapeutic siRNA carriers. Sci. Rep. 2024, 14, 1615. https://doi.org/10.1038/s41598-024-51238-w polegał na:

- finansowaniu badań uwzględnionych w pracy,
- korekcie ostatecznej wersji manuskryptu.

2. Zawadzki S., Okła E., Michlewska S., Makowski T., Buczkowski A., O. López P., de la Mata F.J., Ionov M., **Bryszewska M.**, Miłowska K., Structural and conformational rearrangements of human serum albumin, transferrin, and blood plasma induced by carbosilane dendrimer therapeutic delivery system. Sci. Rep. 2025, 15, 39650. https://doi.org/10.1038/s41598-025-23355-7 polegał na:

- finansowaniu badań uwzględnionych w pracy,
- korekcie ostatecznej wersji manuskryptu.

3. Zawadzki S., Suty S., Okła E., Ortega López P., de la Mata F.J., Waczulikova I., Ionov M., **Bryszewska M.**, Miłowska K., Hemocompatibility of Carbosilane Dendrimers as a Therapeutic siRNA Delivery System across Blood–Brain Barrier. ACS Appl. Mater. Interfaces 2026, 18, 11671−11686 https://doi.org/10.1021/acsami.5c12952, polegał na:

- finansowaniu badań uwzględnionych w pracy,
- korekcie ostatecznej wersji manuskryptu.

.....

UNIWERSYTET ŁÓDZKI

Wydział Biologii i Ochrony Środowiska, Katedra Biofizyki Ogólnej,
ul. Pomorska 141/143, 90-236 Łódź
e-mail.: maria.bryszewska@biol.uni.lodz.pl

Prof. dr hab. Maria Bryszewska

Łódź, dnia 16/03/2026

Oświadczenie

Oświadczam, że mój udział w manuskrypcie wysłanym do czasopisma:

1. Zawadzki S., Okła E., Ortega López P., de la Mata F.J., Ionov M., Kreišmane M., Skrastina D., Jansons J., **Bryszewska M.**, Miłowska K., Multilevel Assessment of Carbosilane Dendrimer–siRNA Nanoplatform: Cellular Compatibility, Blood–Brain Barrier Model Integrity, and Murine Model Biodistribution, polegał na:

- finansowaniu badań uwzględnionych w pracy,
- korekcie ostatecznej wersji manuskryptu.

2. Zawadzki S., Okła E., Michlewska S., Bednarek R., Jansons J., Skrastiņa D., Kreišmane M., Piļipenko V., Jansone B., Ortega López P., de la Mata F.J., Ionov M., **Bryszewska M.**, Miłowska K. Tiered Evaluation of Carbosilane–siRNA Nanoplatform from Single-Cell Biocompatibility to Blood-Brain Barrier Model Dynamics, and Murine Alzheimer Model Behavior Assessment, polegał na:

- finansowaniu badań uwzględnionych w pracy,
- korekcie ostatecznej wersji manuskryptu.

.....

WYDZIAŁ CHEMII
Uniwersytet Łódzki

UNIC

UNIWERSYTET ŁÓDZKI

Wydział Chemii, Katedra Chemii Fizycznej, Zakład Chemii Biofizycznej
ul. Pomorska 165, 90-236 Łódź
e-mail.: adam.buczkowski@chemia.uni.lodz.pl

Dr hab. Adam Buczkowski, prof. UŁ

Łódź, dnia 24.09.2026

Oświadczenie

Oświadczam, że mój udział w pracy:

Zawadzki S., Okła E., Michlewska S., Makowski T., **Buczkowski A.**, O. López P., de la Mata F.J., Ionov M., Bryszewska M., Miłowska K., Structural and conformational rearrangements of human serum albumin, transferrin, and blood plasma induced by carbosilane dendrimer therapeutic delivery system. Sci. Rep. 2025, 15, 39650, https://doi.org/10.1038/s41598-025-23355-7 obejmował:

- przygotowanie i wykonanie pomiarów na izotermicznym kalorymetrze miareczkującym
- przygotowanie i analizę wyników

ABuczkowski

UNIWERSYTET ŁÓDZKI

Wydział Biologii i Ochrony Środowiska, Katedra Biofizyki Ogólnej,
Instytut Biofizyki
ul. Pomorska 141/143, 90-236 Łódź
e-mail.: maksim.ionov@biol.uni.lodz.pl

Prof. dr hab. Maksim Ionov

Łódź, dnia 26.03.2026 r.

Oświadczenie

Oświadczam, że mój udział w pracy:

1. Zawadzki S., Martín-Serrano Á., Okła E., Kędzierska M., Garcia-Gallego S., López P.O., de la Mata F.J., Michlewska S., Makowski T., **Ionov M.**, Pędziwiatr-Werbicka E., Bryszewska M., Miłowska K., Synthesis and biophysical evaluation of carbosilane dendrimers as therapeutic siRNA carriers. Sci. Rep. 2024, 14, 1615. https://doi.org/10.1038/s41598-024-51238-w obejmował:

- współudział w opracowaniu części eksperymentów,
- korektę ostatecznej wersji manuskryptu

2. Zawadzki S., Okła E., Michlewska S., Makowski T., Buczkowski A., O. López P., de la Mata F.J., **Ionov M.**, Bryszewska M., Miłowska K., Structural and conformational rearrangements of human serum albumin, transferrin, and blood plasma induced by carbosilane dendrimer therapeutic delivery system. Sci. Rep. 2025, 15, 39650. https://doi.org/10.1038/s41598-025-23355-7 obejmował:

- współudział w opracowaniu części eksperymentów,
- korektę ostatecznej wersji manuskryptu

3. Zawadzki S., Suty S., Okła E., Ortega López P., de la Mata F.J., Waczulikova I., **Ionov M.**, Bryszewska M., Miłowska K., Hemocompatibility of Carbosilane Dendrimers as a Therapeutic siRNA Delivery System across Blood–Brain Barrier. ACS Appl. Mater. Interfaces 2026, 18, 11671−11686 https://doi.org/10.1021/acsami.5c12952, obejmował:

- współudział w opracowaniu części eksperymentów,
- korektę ostatecznej wersji manuskryptu

.....

UNIWERSYTET ŁÓDZKI

Wydział Biologii i Ochrony Środowiska, Katedra Biofizyki Ogólnej,
Instytut Biofizyki
ul. Pomorska 141/143, 90-236 Łódź
e-mail.: maksim.ionov@biol.uni.lodz.pl

Prof. dr hab. Maksim Ionov

Łódź, dnia 26.03.2026

Oświadczenie

Oświadczam, że mój udział w manuskrypcie wysłanym do czasopisma:

1. Zawadzki S., Okła E., Ortega López P., de la Mata F.J., **Ionov M.**, Kreišmane M., Skrastina D., Jansons J., Bryszewska M., Miłowska K., Multilevel Assessment of Carbosilane Dendrimer–siRNA Nanoplatform: Cellular Compatibility, Blood–Brain Barrier Model Integrity, and Murine Model Biodistribution, obejmował:

- współudział w opracowaniu części eksperymentów,
- korektę ostatecznej wersji manuskryptu

2. Zawadzki S., Okła E., Michlewska S., Bednarek R., Jansons J., Skrastiņa D., Kreišmane M., Piļipenko V., Jansone B., Ortega López P., de la Mata F.J., Ionov M., Bryszewska M., Miłowska K. Tiered Evaluation of Carbosilane–siRNA Nanoplatform from Single-Cell Biocompatibility to Blood-Brain Barrier Model Dynamics, and Murine Alzheimer Model Behavior Assessment, obejmował:

- współudział w opracowaniu części eksperymentów,
- korektę ostatecznej wersji manuskryptu

WYDZIAŁ BIOLOGII
i OCHRONY ŚRODOWISKA
Uniwersytet Łódzki

UNIC

Dr Marta Kędzierska
Uniwersytet Medyczny w Łodzi
Zakład Mikrobiologii, Genetyki i Immunologii Doświadczalnej
e-mail: marta.kedzierska@umed.lodz.pl

Łódź, dnia 27.03.2026

Oświadczenie

Oświadczam, że mój udział w pracy:

Zawadzki S., Martín-Serrano Á., Okła E., **Kędzierska M.**, Garcia-Gallego S., López P.O., de la Mata F.J., Michlewska S., Makowski T., Ionov M., Pędziwiatr-Werbicka E., Bryszewska M., Miłowska K., Synthesis and biophysical evaluation of carbosilane dendrimers as therapeutic siRNA carriers. Sci. Rep. 2024, 14, 1615. https://doi.org/10.1038/s41598-024-51238-w obejmował:

- współudział w wykonaniu pomiarów polaryzacji fluorescencji oraz udział w analizie otrzymanych wyników

Marta Kędzierska

Dr hab. Tomasz Makowski, prof. Instytutu
Centrum Badań Molekularnych i Makromolekularnych
Polskiej Akademii Nauk
Zespół Struktury Powierzchni Materii Miękkiej
ul. Sienkiewicza 112, 90-363 Łódź
e-mail.: tomasz.makowski@cbmm.lodz.pl

Łódź, dnia 24.03.2026

Oświadczenie

Oświadczam, że mój udział w pracy:

1. Zawadzki S., Martín-Serrano Á., Okła E., Kędzierska M., Garcia-Gallego S., López P.O., de la Mata F.J., Michlewska S., **Makowski T.**, Ionov M., Pędziwiatr-Werbicka E., Bryszewska M., Miłowska K., Synthesis and biophysical evaluation of carbosilane dendrimers as therapeutic siRNA carriers. Sci. Rep. 2024, 14, 1615. https://doi.org/10.1038/s41598-024-51238-w obejmował:

   - obrazowanie próbek techniką mikroskopii sił elektronowych (AFM)
   - współudział w przygotowaniu i analizie wyników AFM

2. Zawadzki S., Okła E., Michlewska S., **Makowski T.**, Buczkowski A., O. López P., de la Mata F.J., Ionov M., Bryszewska M., Miłowska K., Structural and conformational rearrangements of human serum albumin, transferrin, and blood plasma induced by carbosilane dendrimer therapeutic delivery system. Sci. Rep. 2025, 15, 39650. https://doi.org/10.1038/s41598-025-23355-7 obejmował:

   - obrazowanie próbek techniką mikroskopii sił elektronowych (AFM)
   - współudział w przygotowaniu i analizie wyników AFM

Makowski

UNIWERSYTET ŁÓDZKI

Wydział Biologii i Ochrony Środowiska, Pracownia Obrazowania Mikroskopowego
i Specjalistycznych Technik Biologicznych,
ul. Pomorska 141/143, 90-236 Łódź
e-mail.: sylwia.michlewska@biol.uni.lodz.pl

Dr hab. Sylwia Michlewska

Łódź, dnia 26-03-2026 r.

Oświadczenie

Oświadczam, że mój udział w pracy:

1. Zawadzki S., Martín-Serrano Á., Okła E., Kędzierska M., Garcia-Gallego S., López P.O., de la Mata F.J., **Michlewska S.**, Makowski T., Ionov M., Pędziwiatr-Werbicka E., Bryszewska M., Miłowska K., Synthesis and biophysical evaluation of carbosilane dendrimers as therapeutic siRNA carriers. Sci. Rep. 2024, 14, 1615. https://doi.org/10.1038/s41598-024-51238-w polegał na:

- obrazowanie próbek techniką transmisyjnej mikroskopii elektronowej (TEM)
- współudział w przygotowaniu i analizie wyników TEM

2. Zawadzki S., Okła E., **Michlewska S.**, Makowski T., Buczkowski A., O. López P., de la Mata F.J., Ionov M., Bryszewska M., Miłowska K., Structural and conformational rearrangements of human serum albumin, transferrin, and blood plasma induced by carbosilane dendrimer therapeutic delivery system. Sci. Rep. 2025, 15, 39650. https://doi.org/10.1038/s41598-025-23355-7 polegał na:

- obrazowanie próbek techniką transmisyjnej mikroskopii elektronowej (TEM)
- współudział w przygotowaniu i analizie wyników TEM

PODPIS ZAUFANY
SYLWIA
MICHLEWSKA

UNIWERSYTET ŁÓDZKI

Wydział Biologii i Ochrony Środowiska, Pracownia Obrazowania Mikroskopowego
i Specjalistycznych Technik Biologicznych,
ul. Pomorska 141/143, 90-236 Łódź
e-mail.: sylwia.michlewska@biol.uni.lodz.pl

Dr hab. Sylwia Michlewska **Łódź, dnia 26-03-2026 r.**

Oświadczenie

Oświadczam, że mój udział w manuskrypcie:

Zawadzki S., Okła E., Michlewska S., Bednarek R., Jansons J., Skrastiņa D., Kreišmane M., Piļipenko V., Jansone B., Ortega López P., de la Mata F.J., Ionov M., Bryszewska M., Miłowska K. Tiered Evaluation of Carbosilane–siRNA Nanoplatform from Single-Cell Biocompatibility to Blood-Brain Barrier Model Dynamics, and Murine Alzheimer Model Behavior Assessment, polegał na:

- wykonaniu pomiarów oraz obrazowania za pomocą techniki mikroskopii konfokalnej

PODPIS ZAUFANY
SYLWIA
MICHLEWSKA

UNIWERSYTET ŁÓDZKI

Wydział Biologii i Ochrony Środowiska, Katedra Biofizyki Ogólnej,
Instytut Biofizyki
ul. Pomorska 141/143, 90-236 Łódź
e-mail.: elzbieta.okla@biol.uni.lodz.pl

mgr Elżbieta Okła

Łódź, dnia 27/03/2026

Oświadczenie

Oświadczam, że mój udział w pracy:

1. Zawadzki S., Martín-Serrano Á., **Okła E.**, Kędzierska M., Garcia-Gallego S., López P.O., de la Mata F.J., Michlewska S., Makowski T., Ionov M., Pędziwiatr-Werbicka E., Bryszewska M., Miłowska K., Synthesis and biophysical evaluation of carbosilane dendrimers as therapeutic siRNA carriers. Sci. Rep. 2024, 14, 1615. https://doi.org/10.1038/s41598-024-51238-w obejmował:

- Współudział w przeprowadzeniu części eksperymentów biofizycznych

2. Zawadzki S., **Okła E.**, Michlewska S., Makowski T., Buczkowski A., O. López P., de la Mata F.J., Ionov M., Bryszewska M., Miłowska K., Structural and conformational rearrangements of human serum albumin, transferrin, and blood plasma induced by carbosilane dendrimer therapeutic delivery system. Sci. Rep. 2025, 15, 39650. https://doi.org/10.1038/s41598-025-23355-7 obejmował:

- współudział w przeprowadzeniu części eksperymentów biofizycznych

3. Zawadzki S., Suty S., **Okła E.**, Ortega López P., de la Mata F.J., Waczulikova I., Ionov M., Bryszewska M., Miłowska K., Hemocompatibility of Carbosilane Dendrimers as a Therapeutic siRNA Delivery System across Blood–Brain Barrier. ACS Appl. Mater. Interfaces 2026, 18, 11671−11686 https://doi.org/10.1021/acsami.5c12952,
obejmował:

- współudział w realizacji eksperymentów z wykorzystaniem komórek jednojądrzastych krwi obwodowej (PBMC)

Okła Elżbieta

UNIWERSYTET ŁÓDZKI

Wydział Biologii i Ochrony Środowiska, Katedra Biofizyki Ogólnej,
Instytut Biofizyki
ul. Pomorska 141/143, 90-236 Łódź
e-mail.: elzbieta.okla@biol.uni.lodz.pl

mgr Elżbieta Okła

Łódź, dnia 27/03/2026

Oświadczenie

Oświadczam, że mój udział w manuskrypcie wysłanym do czasopisma:

1. Zawadzki S., **Okła E.**, Ortega López P., de la Mata F.J., Ionov M., Kreišmane M., Skrastina D., Jansons J., Bryszewska M., Miłowska K., Multilevel Assessment of Carbosilane Dendrimer–siRNA Nanoplatform: Cellular Compatibility, Blood–Brain Barrier Model Integrity, and Murine Model Biodistribution,
obejmował:

- współudział w części prac eksperymentalnych obejmujących badania komórkowe

2. Zawadzki S., **Okła E.**, Michlewska S., Bednarek R., Jansons J., Skrastiņa D., Kreišmane M., Piļipenko V., Jansone B., Ortega López P., de la Mata F.J., Ionov M., Bryszewska M., Miłowska K. Tiered Evaluation of Carbosilane–siRNA Nanoplatform from Single-Cell Biocompatibility to Blood-Brain Barrier Model Dynamics, and Murine Alzheimer Model Behavior Assessment, obejmował:

- współudział w części prac eksperymentalnych obejmujących badania komórkowe

Okła Elżbieta

UNIWERSYTET ŁÓDZKI

Wydział Biologii i Ochrony Środowiska
Katedra Biofizyki Ogólnej
ul. Pomorska 141/143, 90-236 Łódź
e-mail.: elzbieta.pedziwiatr@biol.uni.lodz.pl

dr Elżbieta Pędziwiatr-Werbicka

Łódź, dnia 23.03.2026

Oświadczenie

Oświadczam, że mój udział w pracy:

Zawadzki S., Martín-Serrano Á., Okła E., Kędzierska M., Garcia-Gallego S., López P.O., de la Mata F.J., Michlewska S., Makowski T., Ionov M., **Pędziwiatr-Werbicka E.**, Bryszewska M., Miłowska K., Synthesis and biophysical evaluation of carbosilane dendrimers as therapeutic siRNA carriers. Sci. Rep. 2024, 14, 1615, https://doi.org/10.1038/s41598-024-51238-w obejmował:

- współudział w opracowaniu części eksperymentów
- korektę manuskryptu

Elżbieta Pędziwiatr-Werbicka

UNIVERSIDAD DE ALCALÁ

Departamento de Química Orgánica y Química Inorgánica
Facultad de Farmacia
Alcalá de Henares, Spain
e-mail.: javier.delamata@uah.es

Prof. Francisco Javier de la Mata Alcalá de Henares, 18.03.2026

Statement of contribution

I am co-author of following publications:

1. Zawadzki S., Martín-Serrano Á., Okła E., Kędzierska M., Garcia-Gallego S., Ortega López P., **de la Mata F.J.**, Michlewska S., Makowski T., Ionov M., Pędziwiatr-Werbicka E., Bryszewska M., Miłowska K., Synthesis and biophysical evaluation of carbosilane dendrimers as therapeutic siRNA carriers. Sci. Rep. 2024, 14, 1615. https://doi.org/10.1038/s41598-024-51238-w
I participated in:

- the supervision and coordination of dendrimer synthesis.
- consultation and manuscript edition

2. Zawadzki S., Okła E., Michlewska S., Makowski T., Buczkowski A., Ortega López P., **de la Mata F.J.**, Ionov M., Bryszewska M., Miłowska K., Structural and conformational rearrangements of human serum albumin, transferrin, and blood plasma induced by carbosilane dendrimer therapeutic delivery system. Sci. Rep. 2025, 15, 39650. https://doi.org/10.1038/s41598-025-23355-7
I participated in:

- the supervision and coordination of dendrimer synthesis.

3. Zawadzki S., Suty S., Okła E., Ortega López P., **de la Mata F.J.**, Waczulikova I., Ionov M., Bryszewska M., Miłowska K., Hemocompatibility of Carbosilane Dendrimers as a Therapeutic siRNA Delivery System across Blood–Brain Barrier. ACS Appl. Mater. Interfaces 2026, 18, 11671−11686 https://doi.org/10.1021/acsami.5c12952
I participated in:

- the supervision and coordination of dendrimer synthesis.

DE LA MATA DE LA MATA FRANCISCO JAVIER - DNI 08969382A

Firmado digitalmente por DE LA MATA DE LA MATA FRANCISCO JAVIER - DNI 08969382A
Fecha: 2026.03.25 12:38:12 +01'00'

Universidad de Alcalá

UNIVERSIDAD DE ALCALÁ

Departamento de Química Orgánica y Química Inorgánica
Facultad de Farmacia
Alcalá de Henares, Spain
e-mail.: javier.delamata@uah.es

Prof. Francisco Javier de la Mata

Alcalá de Henares, 18.03.2026

Statement of contribution

I am co-author of following manuscript:

1. Zawadzki S., Okła E., Ortega López P., **de la Mata F.J.**, Ionov M., Kreišmane M., Skrastina D., Jansons J., Bryszewska M., Miłowska K., Multilevel Assessment of Carbosilane Dendrimer–siRNA Nanoplatform: Cellular Compatibility, Blood–Brain Barrier Model Integrity, and Murine Model
I participated in:

- the supervision and coordination of dendrimer synthesis.

Zawadzki S., Okła E., Michlewska S., Bednarek R., Jansons J., Skrastiņa D., Kreišmane M., Piļipenko V., Jansone B., Ortega López P., **de la Mata F.J.**, Ionov M., Bryszewska M., Miłowska K. Tiered Evaluation of Carbosilane–siRNA Nanoplatform from Single-Cell Biocompatibility to Blood-Brain Barrier Model Dynamics, and Murine Alzheimer Model Behavior Assessment
I participated in:

- the supervision and coordination of dendrimer synthesis.

DE LA MATA DE LA MATA FRANCISCO JAVIER - DNI 08969382A

Firmado digitalmente por DE LA MATA DE LA MATA FRANCISCO JAVIER - DNI 08969382A
Fecha: 2026.03.25 12:39:25 +01'00'

.....

UNIVERSIDAD DE ALCALÁ

Departamento de Química Orgánica y Química Inorgánica
Facultad de Farmacia
Alcalá de Henares, Spain
e-mail.: sandra.garciagallego@uah.es

Prof. Sandra García Gallego

Alcalá de Henares, 18.03.2026

Statement of contribution

I am co-author of following publication:

1. Zawadzki S., Martín-Serrano Á., Okła E., Kędzierska M., **Garcia-Gallego S.**, Ortega López P., de la Mata F.J., Michlewska S., Makowski T., Ionov M., Pędziwiatr-Werbicka E., Bryszewska M., Miłowska K., Synthesis and biophysical evaluation of carbosilane dendrimers as therapeutic siRNA carriers. Sci. Rep. 2024, 14, 1615. https://doi.org/10.1038/s41598-024-51238-w

I participated in:

- dendrimers synthesis and preparation

GARCIA GALLEGO SANDRA - 03133892G

Firmado digitalmente por GARCIA GALLEGO SANDRA - 03133892G
Fecha: 2026.03.24 22:07:04 +01'00'

.....

UNIVERSIDAD DE ALCALÁ

Departamento de Química Orgánica y Química Inorgánica
Facultad de Farmacia
Alcalá de Henares, Spain
e-mail.: angela.martins@uah.es

Dr Ángela Martín-Serrano

Alcalá de Henares, 18.03.2026

Statement of contribution

I am co-author of following publication:

1. Zawadzki S., **Martín-Serrano Á.**, Okła E., Kędzierska M., Garcia-Gallego S., Ortega López P., de la Mata F.J., Michlewska S., Makowski T., Ionov M., Pędziwiatr-Werbicka E., Bryszewska M., Miłowska K., Synthesis and biophysical evaluation of carbosilane dendrimers as therapeutic siRNA carriers. Sci. Rep. 2024, 14, 1615. https://doi.org/10.1038/s41598-024-51238-w

I participated in:

- dendrimers synthesis and preparation

MARTIN-SERRANO ORTIZ ANGELA - DNI 71720314N

Firmado digitalmente por MARTIN-SERRANO ORTIZ ANGELA - DNI 71720314N
Fecha: 2026.03.23 15:14:13 +01'00'

.....

Universidad de Alcalá

UNIVERSIDAD DE ALCALÁ

Departamento de Química Orgánica y Química Inorgánica
Facultad de Farmacia
Alcalá de Henares, Spain
e-mail.: paula.ortega@uah.es

Prof. Paula Ortega López

Alcalá de Henares, 18.03.2026

Statement of contribution

I am co-author of following publications:

1. Zawadzki S., Martín-Serrano Á., Okła E., Kędzierska M., Garcia-Gallego S., **Ortega López P.**, de la Mata F.J., Michlewska S., Makowski T., Ionov M., Pędziwiatr-Werbicka E., Bryszewska M., Miłowska K., Synthesis and biophysical evaluation of carbosilane dendrimers as therapeutic siRNA carriers. Sci. Rep. 2024, 14, 1615. https://doi.org/10.1038/s41598-024-51238-w
I participated in:

- dendrimers synthesis and preparation
- consultation and manuscript edition

2. Zawadzki S., Okła E., Michlewska S., Makowski T., Buczkowski A., **Ortega López P.**, de la Mata F.J., Ionov M., Bryszewska M., Miłowska K., Structural and conformational rearrangements of human serum albumin, transferrin, and blood plasma induced by carbosilane dendrimer therapeutic delivery system. Sci. Rep. 2025, 15, 39650. https://doi.org/10.1038/s41598-025-23355-7
I participated in:

- dendrimers synthesis and preparation

3. Zawadzki S., Suty S., Okła E., **Ortega López P.**, de la Mata F.J., Waczulikova I., Ionov M., Bryszewska M., Miłowska K., Hemocompatibility of Carbosilane Dendrimers as a Therapeutic siRNA Delivery System across Blood–Brain Barrier. ACS Appl. Mater. Interfaces 2026, 18, 11671−11686 https://doi.org/10.1021/acsami.5c12952
I participated in:

- dendrimers synthesis and preparation

.....

Código Seguro De Verificación	tXWqnTeNzMH+K6rTNvIVRg==	Estado	Fecha y hora
Firmado Por	Paula Ortega López	Firmado	25/03/2026 12:44:08
Observaciones		Página	1/1
Url De Verificación	https://vfirma.uah.es/vfirma/code/tXWqnTeNzMH%2BK6rTNvIVRg%3D%3D		
Normativa	Este informe tiene carácter de copia electrónica auténtica con validez y eficacia administrativa de ORIGINAL (art. 27 Ley 39/2015).		

Universidad de Alcalá

UNIVERSIDAD DE ALCALÁ

Departamento de Química Orgánica y Química Inorgánica
Facultad de Farmacia
Alcalá de Henares, Spain
e-mail.: paula.ortega@uah.es

Prof. Paula Ortega López

Alcalá de Henares, 18.03.2026

Statement of contribution

I am co-author of following publications:

1. Zawadzki S., Martín-Serrano Á., Okła E., Kędzierska M., Garcia-Gallego S., **Ortega López P.**, de la Mata F.J., Michlewska S., Makowski T., Ionov M., Pędziwiatr-Werbicka E., Bryszewska M., Miłowska K., Synthesis and biophysical evaluation of carbosilane dendrimers as therapeutic siRNA carriers. Sci. Rep. 2024, 14, 1615. https://doi.org/10.1038/s41598-024-51238-w
I participated in:

- dendrimers synthesis and preparation
- consultation and manuscript edition

2. Zawadzki S., Okła E., Michlewska S., Makowski T., Buczkowski A., **Ortega López P.**, de la Mata F.J., Ionov M., Bryszewska M., Miłowska K., Structural and conformational rearrangements of human serum albumin, transferrin, and blood plasma induced by carbosilane dendrimer therapeutic delivery system. Sci. Rep. 2025, 15, 39650. https://doi.org/10.1038/s41598-025-23355-7
I participated in:

- dendrimers synthesis and preparation

3. Zawadzki S., Suty S., Okła E., **Ortega López P.**, de la Mata F.J., Waczulikova I., Ionov M., Bryszewska M., Miłowska K., Hemocompatibility of Carbosilane Dendrimers as a Therapeutic siRNA Delivery System across Blood–Brain Barrier. ACS Appl. Mater. Interfaces 2026, 18, 11671−11686 https://doi.org/10.1021/acsami.5c12952
I participated in:

- dendrimers synthesis and preparation

.....

Código Seguro De Verificación	tXWqnTeNzMH+K6rTNvIVRg==	Estado	Fecha y hora
Firmado Por	Paula Ortega López	Firmado	25/03/2026 12:44:08
Observaciones		Página	1/1
Url De Verificación	https://vfirma.uah.es/vfirma/code/tXWqnTeNzMH%2BK6rTNvIVRg%3D%3D		
Normativa	Este informe tiene carácter de copia electrónica auténtica con validez y eficacia administrativa de ORIGINAL (art. 27 Ley 39/2015).		

COMENIUS UNIVERSITY BRATISLAVA

FACULTY OF MATHEMATICS, PHYSICS AND INFORMATICS
Comenius University
Bratislava

COMENIUS UNIVERSITY

Department of Nuclear Physics and Biophysics
Faculty of Mathematics, Physics and Informatics
Bratislava, Slovakia
e-mail.: simon.suty@fmph.uniba.sk

Dr Šimon Šutý

Bratislava, Slovakia,18.03.2026

Statement of contribution

I am co-author of following publication:

1. Zawadzki S., **Suty S.,** Okła E., Ortega López P., de la Mata F.J., Waczulikova I., Ionov M., Bryszewska M., Miłowska K., Hemocompatibility of Carbosilane Dendrimers as a Therapeutic siRNA Delivery System across Blood−Brain Barrier. ACS Appl. Mater. Interfaces 2026, 18, 11671−11686 https://doi.org/10.1021/acsami.5c12952

I participated in:

- conducting the hemorheology and the hematological and coagulation blood parameter experiments.

.....

COMENIUS UNIVERSITY BRATISLAVA

FACULTY OF MATHEMATICS, PHYSICS AND INFORMATICS
Comenius University
Bratislava

COMENIUS UNIVERSITY

Department of Nuclear Physics and Biophysics
Faculty of Mathematics, Physics and Informatics
Bratislava, Slovakia
e-mail.: waczulikova@fmph.uniba.sk

Prof. Iveta Waczulikova

Bratislava, Slovakia,18.03.2026

Statement of contribution

I am co-author of following publication:

1. Zawadzki S., Suty S., Okła E., Ortega López P., de la Mata F.J., **Waczulikova I.**, Ionov M., Bryszewska M., Miłowska K., Hemocompatibility of Carbosilane Dendrimers as a Therapeutic siRNA Delivery System across Blood–Brain Barrier. ACS Appl. Mater. Interfaces 2026, 18, 11671−11686 https://doi.org/10.1021/acsami.5c12952

I participated in:

- participation in the conceptualization, methodological design of hemorheology and hematological and coagulation blood parameters experiments
- consultation and manuscript edition